Wake affected offshore tower and foundation loads

Gunner C. Larsen, Torben J. Larsen, Mads M. Pedersen, Karen Enevoldsen and Helge Aa. Madsen

Project Final Report

Energinet.dk project no. 10546

Funded by PSO ForskEL

Table of Contents

1 Overview of project objectives and report structure

The objectives of this project are:

- To instrument 6 offshore wind turbines (WT's) in the Nysted II wind farm (WF) with strain-gauges in order to resolve WT *tower loads*;
- To establish a data base with such load measurements as well as with inter-related wind field measurements from a nearby meteorological tower (located in one corner of the Nysted II WF) covering a time span of at least one year;
- Based on the recorded data to identify, characterize and model the basic mechanisms driving the increased loading experienced by WT's operating in offshore wind farm conditions as compared to solitary wind turbines subjected to an identical ambient wind climate;
- Investigate potential implications of the data analysis on the present standard for calculation of foundation and tower loads.

The last item is reported separately. The present project report covers the first 3 of the above listed items, and it is structured as follows: Chapter 2 describes the experimental setup, encountered challenges, data availability, data processing and experimental results. Chapter 3 deals with numerical simulations of measured results including single wake cases as well as multi-wake cases with focus on the effect of both WT interspacing and ambient turbulence intensity. Based on the results obtained in Chapter 2 and Chapter 3, respectively, Chapter 4 synthesize measured and simulated results to validate the Dynamic Wake Meandering simulation approach with particular focus on the fatigue load level of wake affected WT towers for both single- and multi-wake cases. Finally, Chapter 5 summarizes the achieved results. The report Chapters are supplemented by 5 Appendices containing detailed "catalogs" of both measured and simulated results as well as a description of a proposed yaw-dependent calibration approach for WT tower mounted strain-gauges.

2 Measurements

The established measurement data base contains WT load data as well as simultaneous recorded meteorological data and has involved the merger and synchronization of a number of independent recording systems – i.e. 6 individual but identical WT recording systems; 2 different meteorological recording systems; and 16 individual but identical WT SCADA recording systems.

2 .1 Experimental setup

Available measurements resulting from the experimental campaign can be divided into 5 data classes, each with their own characteristics, data coverage and time stamp reference. The 5 classes are: 1) High frequency sampled meteorological data; 2) High frequency sampled WT structural strain-gauge data; 3) Time series data from WT Supervisory Control And Data Acquisition (SCADA) systems; 4) Statistical 10-minute meteorological data; and 5) Statistical data from the WT SCADA systems.

The high frequency sampled (i.e. 20 Hz) *meteorological data* consist of recordings from 3 Sonic's mounted on an off-shore meteorological mast nearby the WF in altitudes 17m, 40m and 57m above mean sea level (AMSL), respectively. Each Sonic resolves the 3D wind vector and provides in addition a temperature scalar, thus facilitating computation of mean wind direction, mean wind speed, turbulence intensity and atmospheric boundary layer (ABL) stability characteristics expressed in terms of Monin-Obukhov length. Including a status signal for each Sonic (i.e. error flag) and a common (DAU) time signal for all Sonic's, this adds up to a total of *up to* 16 channels depending on sensor availability.

The high sampled (i.e. 40 Hz) *structural data* consist of strain-gauge measurements from the 6 instrumented turbines (L1, L2, L3, M1, M2, K18) – cf. Figure 1. For each WT, the strain-gauge setup resolves two WT tower bottom bending moments and two WT tower top bending moments in mutual perpendicular directions as well as the tower top torsion (i.e. yaw) moment.

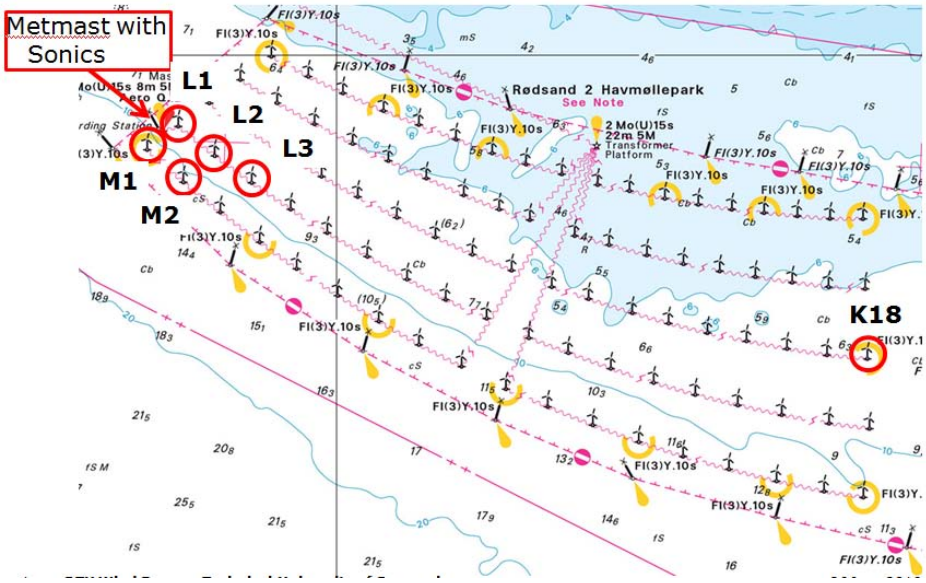

Figure 1: Site overview with instrumented WTs indicated.

Time series data from the WT *SCADA system* include yaw signals, mean wind speed signals, blade pitch signals for all blades, power signals from the 6 WT's instrumented with strain-gauges. The scan frequency varies from sensor to sensor and depends (probably) on whether or not variability in the particular sensor value is observed. For example the power signals are logged every 3-6 second, whereas the yaw signal is logged 3-300 second.

The statistical 10-minute data from the *meteorological mast* consists of wind speed measurements from cup-anemometers, wind direction measurements from wind vanes and absolute temperature measurements as well as temperature difference measurements. The cup-anemometers were installed at various heights: 68m above mean sea level (AMSL); 66m AMSL; 45m AMSL; and 22m AMSL. Except at the top of the meteorological mast (i.e. 68m AMSL) the mast was instrumented with two cup-anemometers at all heights to allow compensation for flow distortion caused by the meteorological mast at directions close to the boom direction. The wind vanes were located at 63m AMSL and 22m AMSL, respectively. Absolute temperature was measured at 63m AMSL, and two temperature differences were recorded between levels 63m/10m AMSL and 45m/10m AMSL, respectively. Finally, the above primary measuring channels was supplemented by recordings of relative humidity and pressure.

Referring to time spans of 10minutes the available statistical data from the WT *SCADA system* encompasses values of mean, standard deviation, maximum and minimum values of power production, wind speed and yaw position for all 85 WT's supplemented by mean of blade pitch signals for all blades at the 6 instrumented WT's.

2 .2 Data availability

The data availability varies from measurement system to measurement system and is summarized in Table 1 below ("→" without an end date means still ongoing).

Table 1: Data availability.

Sonic 17m AMSL	0205-2013 → 1306-2015
Sonic 40m AMSL	0902-2010 → 3010-2012
Sonic 57m AMSL	0902-2010 → 3010-2012; 2904-2013 → 0410-2013
WT loads; L1	1001-2013 →1306-2013; 1607-2013 →
WT loads; L2	1001-2013 →1306-2013; 1607-2013 →
WT loads; L3	1001-2013 →1306-2013; 1607-2013 →
WT loads; M1	0412-2012 → 0412-2012; 2102-2013 →1306-2013; 1607-2013 →
WT loads; M2	1001-2013 →1306-2013; 1607-2013 →
WT loads; K18	1001-2013 →1706-2013; 1607-2013 → 3108-2015
SCADA; time series: yaw	WT's L1-L3, M1, M2, K18: 1203-2014; 11:00 → 14.00
SCADA; time series: wind speed, power, yaw, pitch for all blades	WT L3: 3010-2014 →3110-2014
SCADA; time series: wind speed, power, yaw, pitch for all blades	WT's L1-L3, M1, M2, K18: 0101-2013 → 1512-2014
10-minute meteorological wind speed (WSP) data	68m, 66m and 22m AMSL: 1512-2009 → 0807-2010 45m AMSL: 1512-2009 →2007-2010
10-minute meteorological	63m AMSL: 1512-2009 → 0807-2010

wind direction (WD) data	22m AMSL: 1512-2009 → 3009-2010
10-minute meteorological temperature and pressure data	1512-2009 →
10-minute SCADA data (min., max., mean and std.): WSP, power, yaw	All 85 WT's: 0101-2013 →0509-2014
10-minute SCADA data (mean): WSP, power, yaw, pitch for all blades	WT's L1-L3, M1, M2, K18: 0101-2013 → 1012-2014

2 .3 Data processing

The meteorological sensors (i.e. wind speed, wind direction, temperature and pressure) are calibrated prior to mounting on the meteorological tower, and therefore the data processing is limited to computation of mean, standard deviation max. and min. values for the high frequency time series recordings.

Regarding the structural measurements the data processing is more involving. First of all, the measured tower moments has to be calibrated. For obvious reasons this is not possible prior to installation of the strain-gauges, and these consequently have to be calibrated in-situ. For the tower bending moments this is done by yawing the nacelle under conditions with negligible ambient wind speed, whereby the imposed tower bending moments, with good approximation, can be considered as resulting from the (known) nacelle gravity. Concerning tower torsion moments, it is not possible to impose a known external torsion load (at least under offshore conditions), and consequently advantage is taken of a simple analytical relation connection moment and stress for a circular symmetric cross section with known geometry and known material properties.

The elementary theory of twist of circular shafts states that the shear strain, γ_θ, (as measured by the torsion strain-gauges bridge at the tower inner radius $d/2$) at any point of the cross section is perpendicular to the radius and proportional to the applied external twist moment M_t

$$M_t = G\frac{I_t}{d/2}\gamma_\theta \tag{1}$$

with the area moment of inertia being determined from the tower top inner (d) and tower top outer (D) diameter as

$$I_t = \frac{\pi}{32}(D^4 - d^4) \tag{2}$$

and the modulus of rigidity determined from the material's Youngs modulus (E) and Poissons ratio (ν) as

$$G = \frac{E}{2(1+\nu)} \tag{3}$$

Coming back to the strain-gauge calibration it is readily seen from eq. (1) that the *gain* for the torsion moment is given by $2GI_t/d$. The bias depends on the particular strain-

gauge as well as its mounting and can consequently not be determined from theoretical considerations. Instead, the bias is determined from the calibration campaign with the nacelle yawed 4π (forth and back) under very calm wind conditions. Under such conditions the torsion moment is (close to) zero, and the recorded torsion signal therefore expected to be yaw angle independent and equal to the *bias*. At the same time this yaw exercise is also a test of the validity of the torsion signals, which potentially might be influenced by tower top non-linearities if mounted to close to the tower top thus resulting in yaw dependent calibration signals. Fortunately, this is not the case for the present setup as illustrated in Figure 2 showing the measured tower top torsion at all the instrumented WT's.

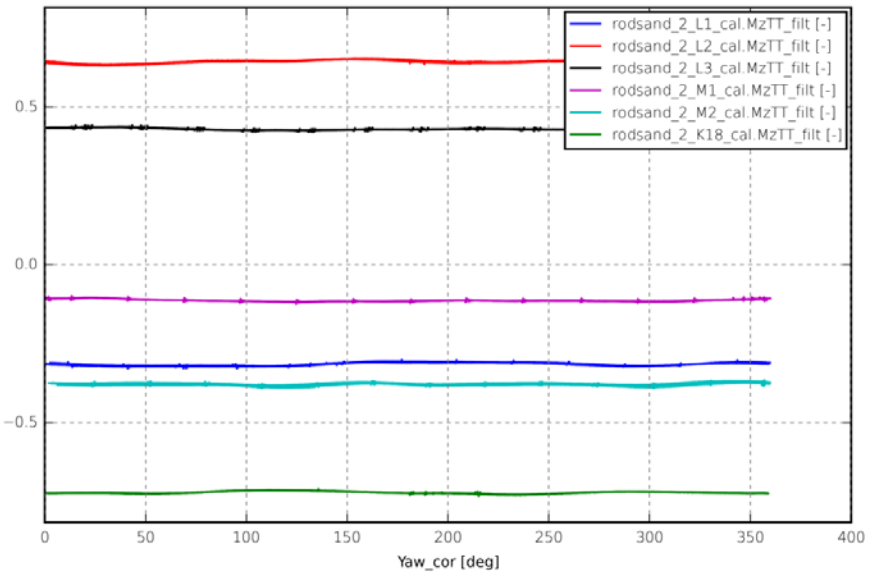

Figure 2: Tower top torsion signals as function of turbine yaw angle.

For the top bending signals, however, the situation is more critical. Under ideal conditions the calibration signal should be a pure sinusoid as function of yaw angle, because it results from a constant bending moment being rotated. This is unfortunately not the case with the present instrumentation as appears from Figure 3 below showing a representative tower top ending moment as function of yaw angle for WT L1.

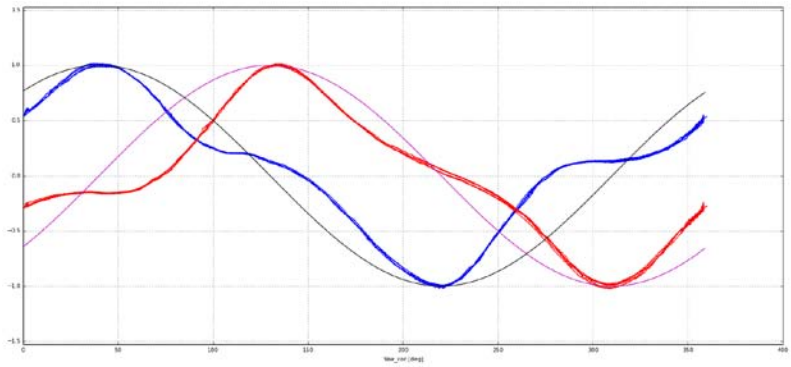

Figure 3: Representative tower top bending moment calibration signal, referring to two perpendicular directions, as function of turbine yaw angle (WT L1).

The reason is non-linear tower top boundary effects caused by the type of the nacelle mounting on the tower top, which is combining a slip bearing with a number of yaw claws that introduce significant local non-linearities caused by local bending of the circular tower top shell structure.

To circumvent this flaw, the tower top bending strain-gauges should have mounted with larger distance to the tower top (typically between 2D and 5D), which was unfortunately not possible due to lack of a mounting platform inside the turbine at relevant heights. Instead, a *yaw dependent calibration* approach has been developed in an attempt to circumvent the before mentioned boundary effects. The developed algorithm is described in detail in Appendix A.

Using the algorithm it is possible to obtain an approximate sinusoid calibration signal. However, when subsequently applying the derived yaw angle dependent calibration and investigating tower top bending response resulting from a free inflow sector referred to a particular mean wind speed bin, a constant total tower top bending moment should appear assuming direction independent inflow conditions. This is unfortunately not the case. However, a more detailed analysis is needed to finally validate or reject the developed yaw dependent approach, because the tower top rotor moments depend, besides mean wind speed, on other factors such as upstream roughness conditions and ABL stability conditions, which directly affect the mean wind shear profile and thus in turn the rotor moments. A more detailed analysis should also include normalization of the investigated mean wind speed bin velocities to a “collapsed” characteristic bin velocity to compensate for possible differences in the available mean wind speed bin “population”, and thus the mean wind speed shear, for different inflow directions.

Such a detailed analysis is outside the scope of the present project, and the tower top bending moments have therefore been disregarded in the analysis included in this report. Considering the fact that the focus of the project is on foundation loads this is considered acceptable.

As for the tower bottom bending moments the expected sinusoidal behaviour, as function of yaw angle, is observed – cf. Figure 4, which shows a representative calibration signal for WT L1.

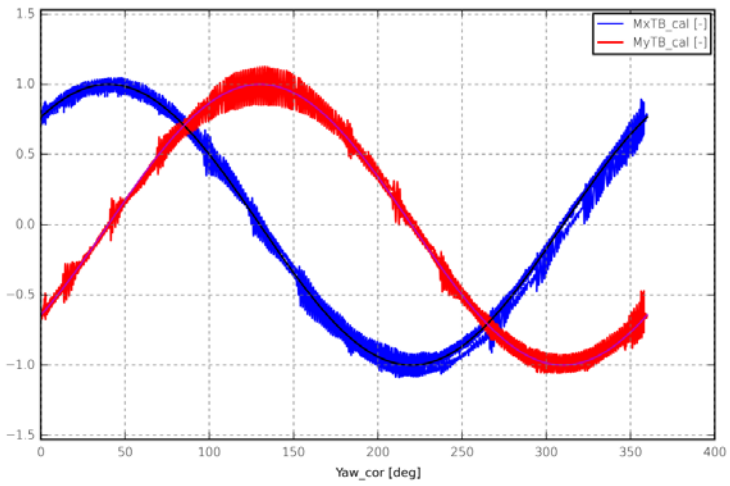

Figure 4: Representative tower bottom bending moment calibration signal, referring to two perpendicular directions, as function of turbine yaw angle (WT L1).

With known nacelle/rotor gravity both *gain* and *bias* is readily determined from such predominantly sinusoidal calibration signals.

Introducing the equivalent moment, M_{eq}, is a way to conveniently collapse the fatigue load spectrum into a single scalar. The fatigue equivalent moment, M_{eq}, is defined as

$$M_{eq} = \left(\frac{\sum_i n_i M_i^m}{n_{eq}} \right)^{1/m} \quad (4)$$

in which n_i is the number og fatigue cycles with magnitude M_i, n_{eq} is the equivalent total number of fatigue cycles (with magnitude M_{eq}) and m is the Wöhler exponent (i.e. the slope of the S-N curve) for the material in question. n_{eq} can be selected arbitrarily, and the particular choice will affect M_{eq} according to equation (1); i.e. a simple scaling, which for relative comparisons does not affect the results. We will make use of this property when analyzing the results in the result sections.

2 .4 Challenges

The experimental part of the project has faced some challenges which, except for the "misplacement" of the tower top strain-gauges resolving the tower top bending moments, have been overcome. The encountered challenges can be classified as related to:

- New strain-gauge monitoring system;
- Grounding of the strain-gauge monitoring system;
- Synchronization (i.e. time stamping) of recordings originating from different measuring systems;
- Degradation and re-calibration of Sonic anemometers.

Due to a budget cut resulting from the project negotiation phase, it was decided to use a new (and cheaper) *strain-gauge recording system* (i.e. National Inc. recording system). A drawback of this decision was less experience with the equipment, which concrete was manifested in challenges with low pass filtering of the directly measured signals before recording (to avoid aliasing) as well as in grounding issues. The sampling rate of the National system is significantly higher than that of the conventional HBM-system (i.e. AE301 Strain gauge Amplifier), and to compensate for this 20Hz low pass filters were added in the measuring chain.

As for the *grounding* issue, the National system was initially only grounded through the power supply. This turned out to be insufficient, thus resulting in very noisy signals. This was resolved by establishing a powerful grounding between the recording system and the WT.

Measured signals from all involved measuring systems are of cause synchronized. However, it turned out that the *time stamping* resulting from the Campell logger used for the met. mast recordings refer to the end of a given 10-minute period, whereas the time stamping for the strain-gauge recording system refer to the start of a given 10-minute period. This has been compensated for in the data analysis.

The *Sonic anemometers* mounted at the met. mast undergo continuous degradation. Starting with 3 Sonics in levels 17m, 40m and 57m AMSL, respectively, when the met. mast was erected, the last Sonic broke down 13-06-2015. In the intermediate period (i.e. from start of the measuring campaign and up to 13-06-2015), the Sonics were re-calibrated by Deutsche WindGuard to ensure optimal functionality. However, the

calibration of the Sonics resulted unfortunately in a down period of the Sonics extending from 30-10-2012 to 29-04-2013.

2 .5 Results

The high sampled *structural data* from the instrumented WT's are stored as 10-minute time series. Based on the recorded two WT tower bottom bending moments the total tower bottom bending moments are computed for each instantaneous recording, which in practice will approximately equal the tower bottom for-aft moment. The resulting time series are subsequently post processed to obtain the tower bottom bending fatigue equivalent moments using the recipe formulated in equation (4), with n_{eq} selected to obtain 1Hz equivalent fatigue moments. For the tower bottom bending moments a Wöhler exponent of 4 (typical for construction steel) is applied, whereas a Wöhler exponent of 7 (typical for the yaw mechanism construction material) is applied for the tower top yaw moments.

To facilitate load comparisons between different mean wind speed regimes, all results has finally been normalized with the fatigue loading corresponding to the 10m/s ambient case (i.e. without wake influence). Except, for the total moment computation, the same procedure has been applied for post processing of the WT tower top yaw moments. The tower top bending moments have in the first place been excluded from the analysis due to the previously described challenges with these measurements. This can be justified, as foundation loads are in focus in this project, and tower top bending moments therefore not of significant importance.

The above described data processing has been conducted for all instrumented WT's, and for each of these all computed fatigue equivalent moments has been plotted as function of ambient mean wind speed direction conditioned on the ambient mean wind speed as referring to on 2m/s bins. For the *10m/s case* the results are shown in Figure 5 - Figure 14, where each "dot" represents an equivalent moment associated with one 10-minute load time series. For each wind direction the mean is computed and in the plots represented as a solid line.

To facilitate interpretation of the results, wake generating upstream WT's are indicated in the "bottom" of the plots, where the size of these upstream WT's indicate the proximity of these – i.e. a "big" WT indicate a wake generating WT nearby, whereas a "small" WT indicate a wake generating WT far away.

It is characteristic that the fatigue loading is significantly enhanced, when the WT is exposed to wake affected inflow conditions. The fatigue load level is, as expected, most boosted in *single wake* situations associated with small WT interspacing as well as in *multi-wake* situations in general. In such cases the fatigue equivalent load level increased with a factor of the order 2.5 compared to the free wake fatigue equivalent load level.

The results for the entire available mean wind speed range [6m/s; 16m/s] are given in Appendix E. As can be seen, the amount of data (i.e. number of "dots" in the plots) diminishes with increasing ambient mean wind speed, as expected, and at 16m/s a somewhat limited number of data is available resulting in lack of data for some inflow directions.

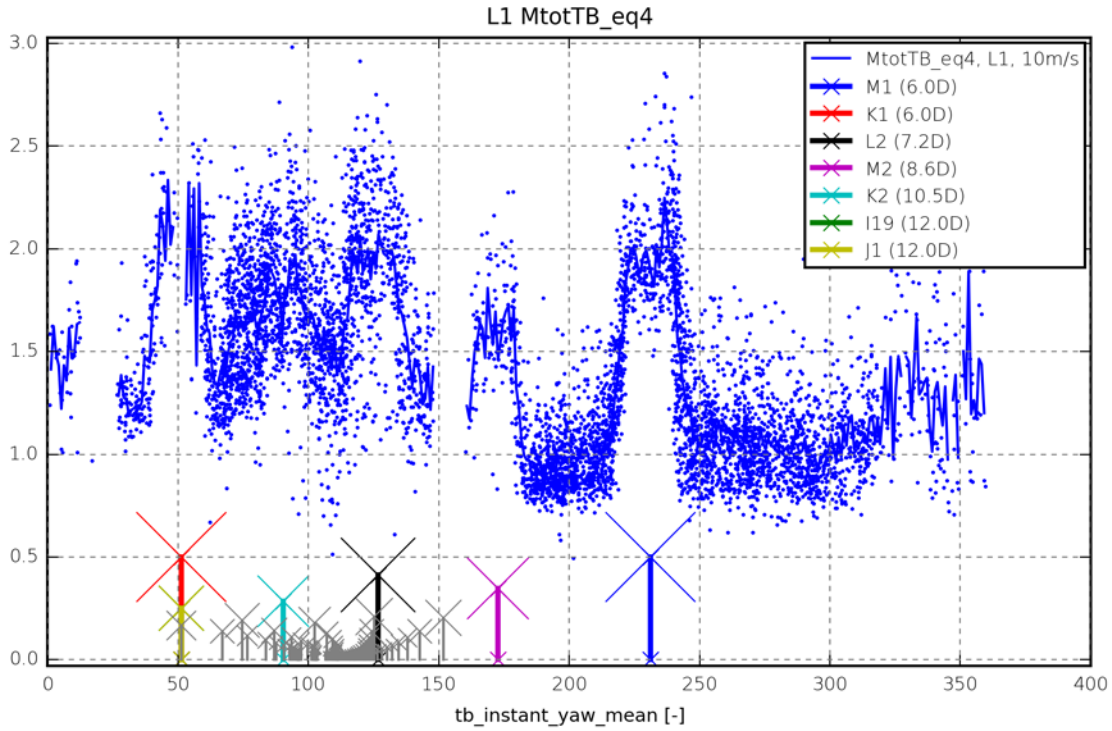

Figure 5: Tower bottom bending equivalent moment; turbine L1; m = 4; U = 10m/s.

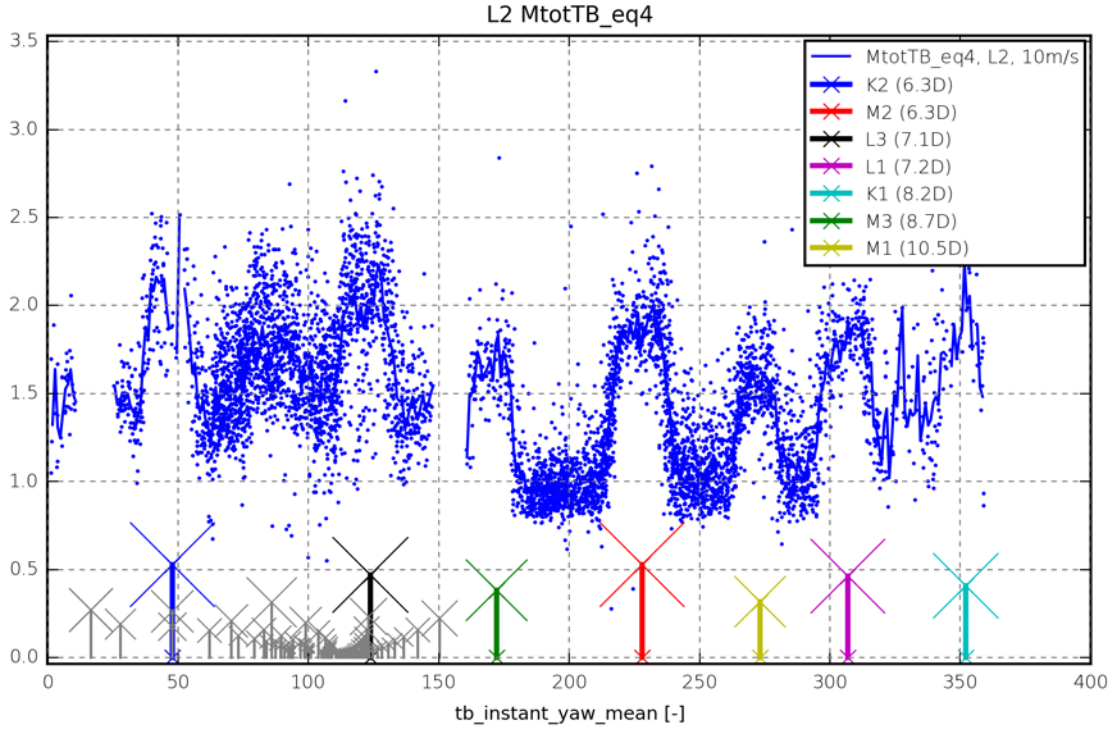

Figure 6: Tower bottom bending equivalent moment; turbine L2; m = 4; U = 10m/s.

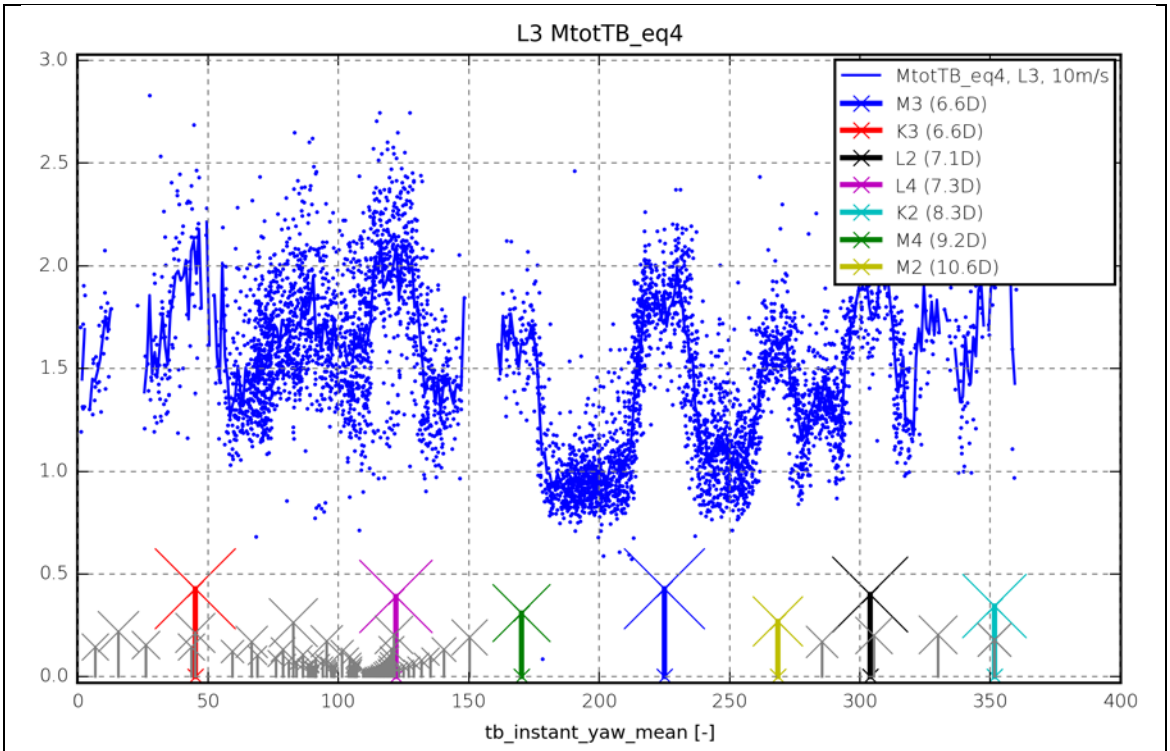

Figure 7: Tower bottom bending equivalent moment; turbine L3; m = 4; U = 10m/s.

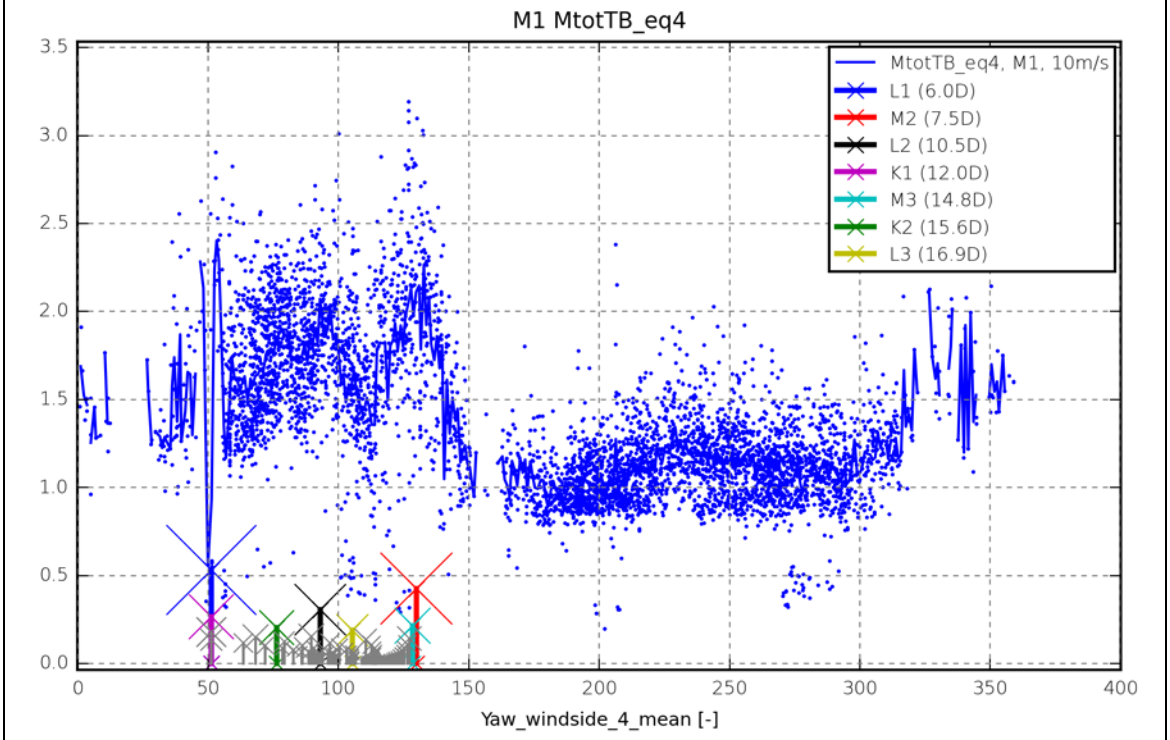

Figure 8: Tower bottom bending equivalent moment; turbine M1; m = 4; U = 10m/s.

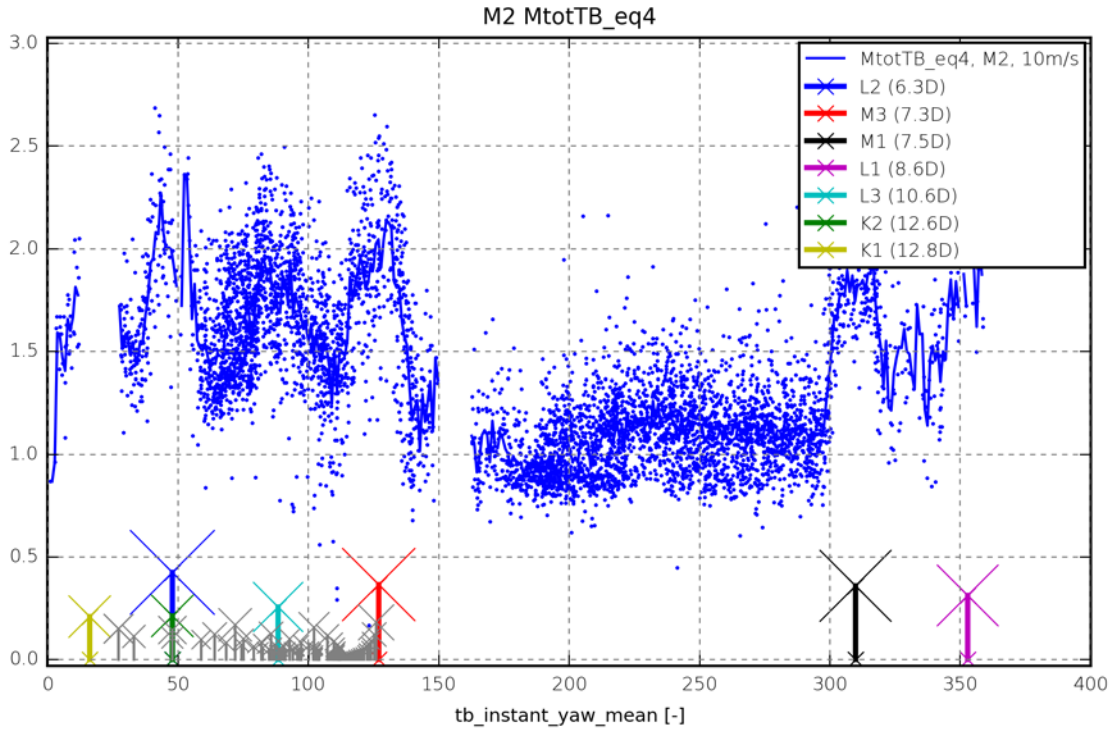

Figure 9: Tower bottom bending equivalent moment; turbine M2; m = 4; U = 10m/s.

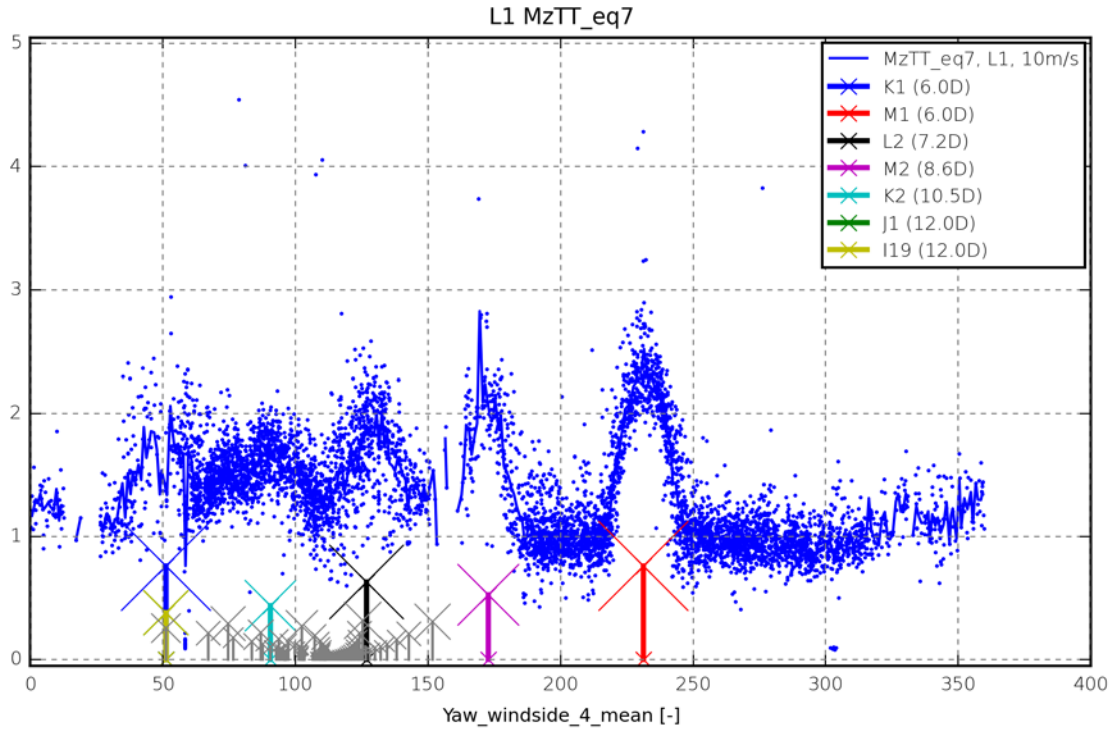

Figure 10:Tower top yaw equivalent moment; turbine L1; m = 7; U = 10m/s.

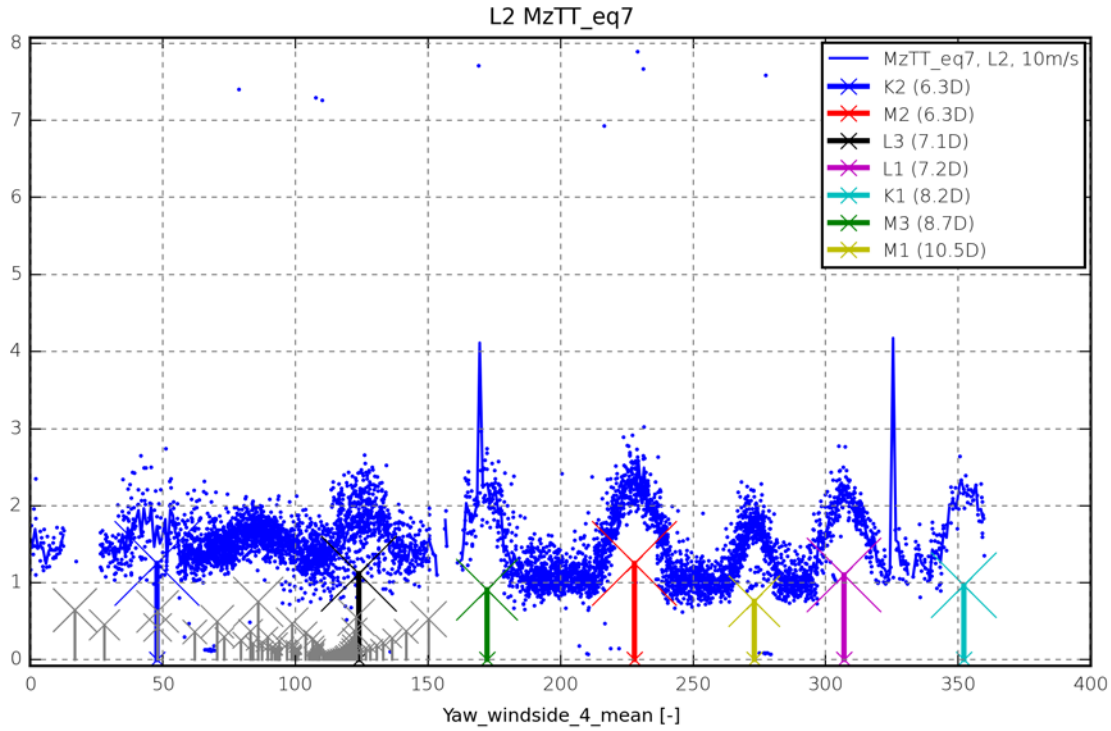

Figure 11: Tower top yaw equivalent moment; turbine L2; m = 7; U = 10m/s.

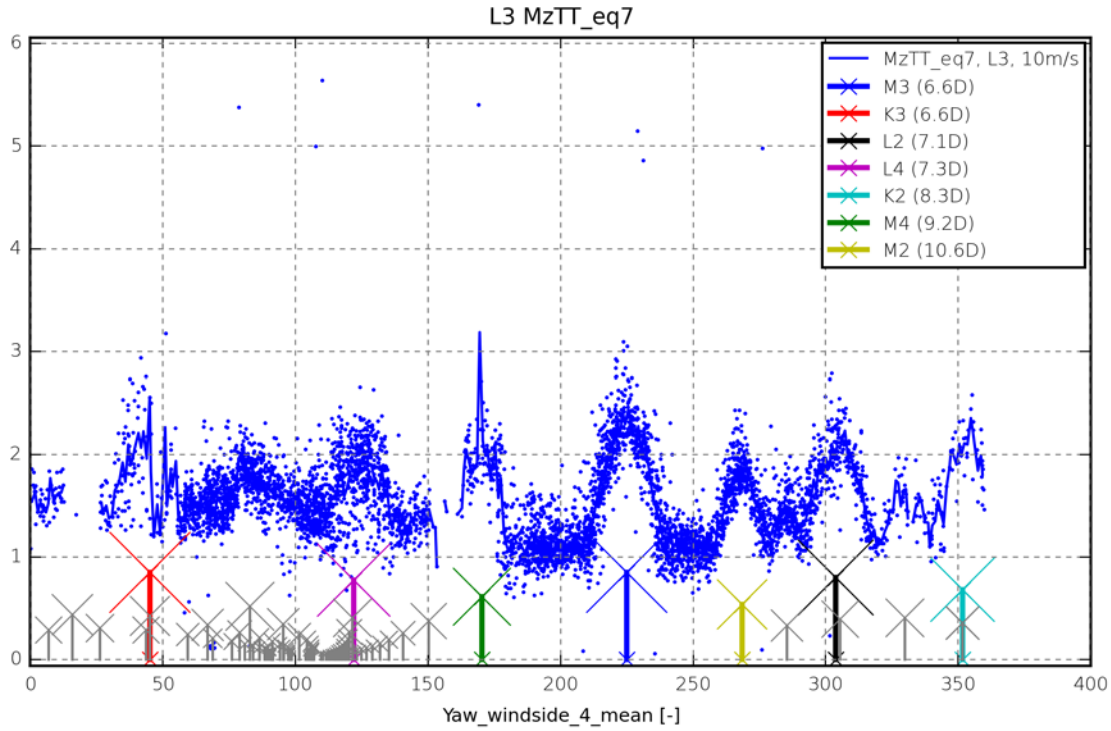

Figure 12: Tower top yaw equivalent moment; turbine L3; m = 7; U = 10m/s.

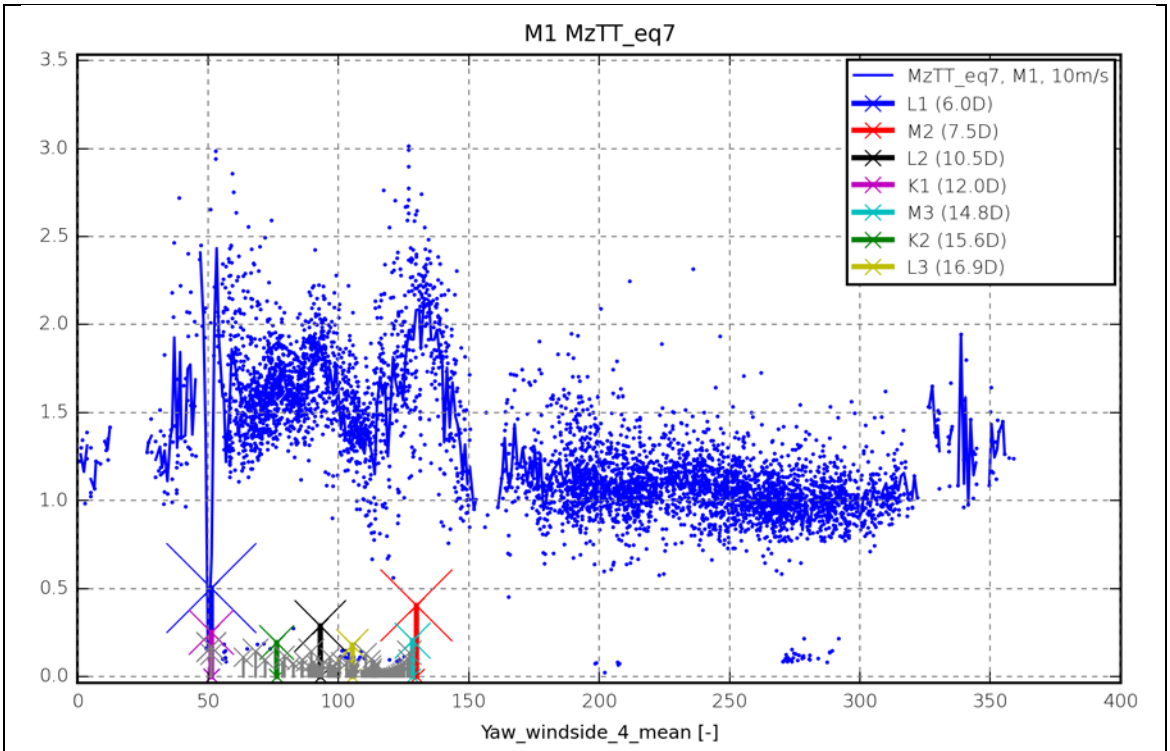

Figure 13: Tower top yaw equivalent moment; turbine M1; m = 7; U = 10m/s.

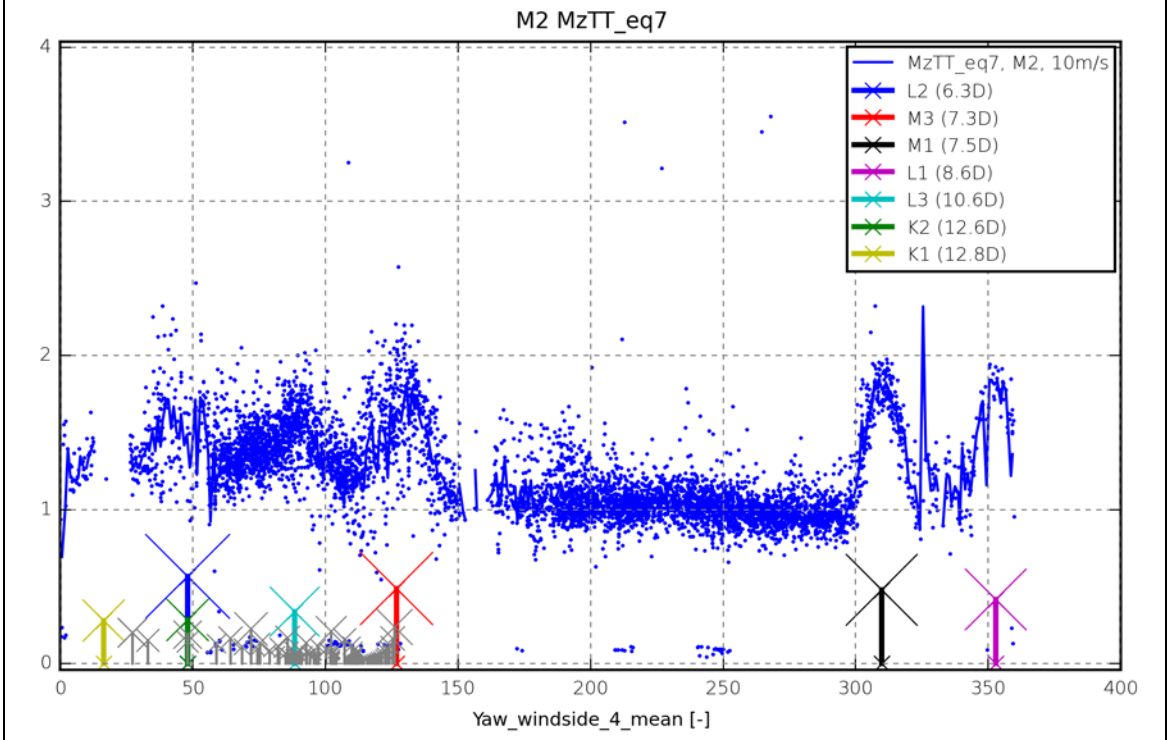

Figure 14: Tower top yaw equivalent moment; turbine M2; m = 7; U = 10m/s.

3 Simulations

3.1 Numerical setup

A popular approach for predicting the loads on WT's inside wind farms is to use the dynamic wake meandering (DWM) model [1] in combination with an aeroelastic code. The DWM model has recently been included in the IEC-code [2] as a recommended practice. The DWM approach uses the quasi-steady wind speed deficit of the upstream turbine together with a stochastic meandering process driven by large scale turbulence structures in the atmospheric boundary layer (ABL) in order to simulate the incoming flow field of a downstream WT. The combination of the resulting non-stationary inflow field with an aeroelastic code thus enables detailed analysis of both *production* and *loading* of arbitrary WT components.

3.1.1 The HAWC2 model

The HAWC2 code is an aeroelastic model for simulating WT response (i.e. load or power production) in time domain [3].

The *structural part* of the code is based on a multi-body formulation as described in Shabana [4] using the floating frame of reference method. In this formulation, the wind turbine main structures are subdivided into a number of bodies, where each body is an assembly of Timoshenko beam elements. Each body includes its own coordinate system with the calculation of internal inertia loads when this coordinate system is moved in space; hence, large rotation and translation of the body motion are accounted for. Inside a body, the formulation is linear, assuming small deflections and rotations. This means that a blade modeled as a single body will not include the same nonlinear geometric effects related to large deflections of a blade divided into several bodies. The bodies, representing the mechanical parts of the turbine, are connected by kinematic constraints. The constraints are formulated as algebraic equations, which impose limitations of the bodies' motion. Examples of such constraints are a fixed connection from a structural node to a global point (e.g. tower bottom clamping), a fixed coupling of the relative motion (e.g. fixed pitch, yaw), a frictionless bearing and a bearing where the rotation angle is controlled by the user. It may be worth to notice that also for the last constraint where the rotation is specified externally, inertial forces related to this movement are accounted for in the response. External forces are placed on the structure in the deformed state, which is especially important for pitch loads and twist of the blades, and since large rotations are handled by a proper subdivision of bodies, the code is suited for calculations on very flexible turbines subjected to, e.g. large blade deflections. The structural model is general, but in its simplest form, a WT is modeled using one body for the tower, one for the nacelle and one for each blade.

The *aerodynamic part* of the code is based on the blade element momentum (BEM) theory, but extended from the classic approach to handle dynamic inflow, dynamic stall, skew inflow, shear effects on the induction and effects from large deflections. One example is the effect of large flapwise blade deflections causing a change in the effective rotor diameter and that the blade forces are no longer perpendicular to the rotor plane. This reduces the thrust on the rotor and thereby changes the induced velocities and vice versa. The dynamic stall model [5] is a modified Beddoes–Leishmann [6] model that includes the effects of shed vorticity from the trailing edge (Theodorsen theory [7]), as well as the effects of stall separation lag caused by an instationary trailing

edge separation point. These effects are important in relation not only mainly to flutter analysis, but also generally to calculate loads and stability of blades with very low torsion stiffness. The induced velocities are calculated on the basis of the local inflow velocities causing different inductions in the upper and lower parts of the rotor, as in the case of a large wind shear [8].

The inflow *wind conditions* are divided into deterministic and stochastic contributions. The deterministic wind is mean wind velocity, wind steps, ramps, special gust events and special shears, including the possibility for fully user-defined shears. The stochastic turbulent wind is generated using the Mann model [9], which is an anisotropic full three-dimensional correlated kinematic turbulence flow field model. Tower shadow effects are included using a potential flow method.

Control of the WT is included through one or more dynamic link libraries and is conseqiuently not part of the HAWC2 core. The reason is that each WT usually is equipped with its own individual controller, which is normally kept confidential by the manufacturer. The calculation time, which is obtained using a Newmark-beta solution scheme together with Newton–Raphson iterations within each time step, is approximately a factor of 1–2 slower than real time on a 3 GHz CPU.

3.1.2 The DWM model

The DWM model complex [1] is based on the combination of three corner stones: (1) modeling of quasi-steady wake deficits; (2) a stochastic model of the downwind wake meandering; and (3) added or self-generated wake turbulence (cf. Figure 15).

The quasi-steady wake deficit is the wake deficit formulated in the moving (i.e. meandering) frame of reference and includes the wake expansion as a function of downstream transportation time caused partly by turbulence diffusion and partly by recovery of the rotor pressure field. The modeling of this deficit is based on a thin shear layer approximation of the Navier–Stokes equations in their rotational symmetric form combined with an eddy viscosity closure. The initial condition is constituted by the induced wind field in the rotor plane determined from a BEM approach. In the present formulation, the aerodynamic module of HAWC2 is used for this purpose. Further details on the implementation can be found in Madsen *et al.* [10].

The wake meandering part is based on a fundamental presumption stating that the transport of wakes in the atmospheric boundary layer can be modeled by considering the wakes to act as passive tracers driven by the large-scale turbulence structures in lateral and vertical directions [1]. Modeling of the meandering process consequently includes considerations of a suitable description of the ‘carrier’ stochastic transport media as well as a suitable definition of the cutoff frequency defining large-scale turbulence structures in this context. For the stochastic modeling of wake meandering, we imagine the wake as being constituted by a cascade of wake deficits, each ‘emitted’ at consecutive time instants in agreement with the passive tracer analogy [1], [10]. We then subsequently describe the propagation of each of the ‘emitted’ wake deficits,

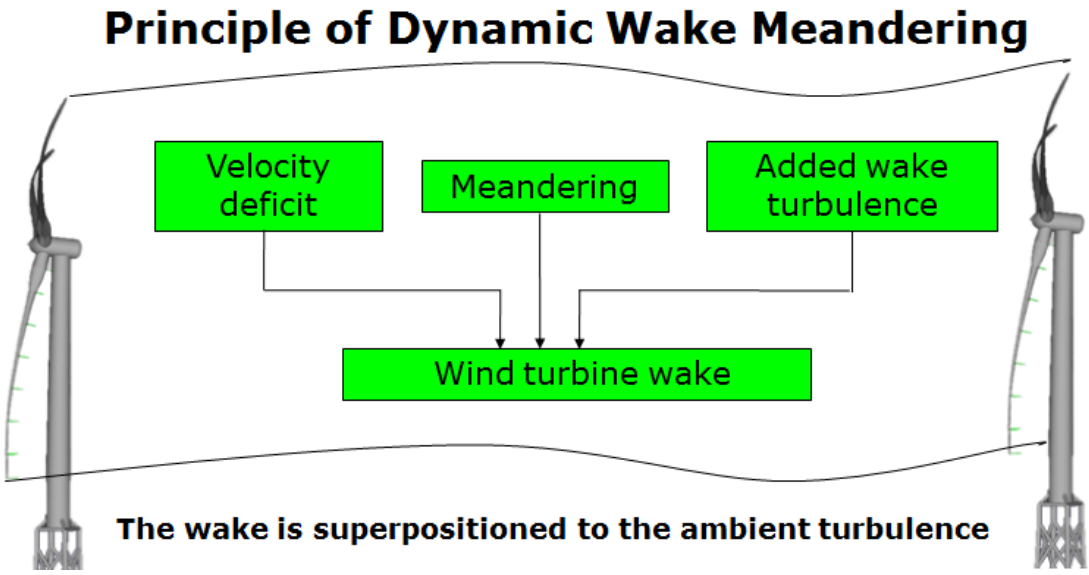

Figure 15: Overview of the three fundamental parts of the DWM model.

and the collective description of these thus constitutes the wake meandering model. Adopting Taylor's hypothesis [11], the downstream advection of these is assumed to be controlled by the mean wind speed of the ambient wind field. With this formulation, the wake momentum in the direction of the mean flow is invariant with respect to downstream displacement. This is a considerable simplification allowing for a straight forward decoupling of the wake along the wind deficit profile (and its expansion) and the wake transportation process. As for the dynamics in the lateral and vertical directions, each considered wake cascade element is displaced according to the large-scale lateral and vertical turbulence velocities at the position of the particular wake cascade element at each time instant. The choice of a suitable stochastic turbulence field, that in turn defines the stochastic wake transport process, is not mandatory, but may be guided by the characteristics of the atmospheric turbulence at the site of relevance. These characteristics encompass in principle not only turbulence standard parameters such as turbulence intensity, turbulence length scale and coherence properties, but also features such as degree of isotropy, homogeneity of the turbulence, Gaussianity of the turbulence, etc.

In this work, the turbulence box for the meandering process is generated using a transverse and vertical resolution of one rotor diameter, whereas the distance between the turbulence grid points in the time axis is 0.07s. Further on, a low pass filter on the transverse wake position is applied in order to exclude contributions from turbulence eddies with a characteristic scale smaller than two rotor diameters [1]. The physical reasoning behind this is that atmospheric vortex structures smaller than 2D tends to change the deficit mixing process rather than contribute to distinct meandering. The filter cutoff frequency, f_c, is defined in terms of the rotor diameter (D) and the ambient mean wind speed U as

$$f_c = \frac{U}{2D} \tag{5}$$

The added wake turbulence includes contributions from conventional mechanically generated turbulence, caused by the wake shear, as well as from the blade-bound vorticity, consisting mainly of tip and root vortices. In analogy with the description of the wake deficit, the added wake turbulence is formulated in the meandering frame of reference. In the present context, a simple scaling in the radial direction of a (small-scale) turbulence field originating from the Mann spectral tensor is adopted. The suggested scaling factor depends on the magnitude of the quasi-steady wake deficit as well as of the wake-deficit radial gradient. Further details can be found in Madsen *et al.* [10]. The required input to the DWM model in its present implementation is WF topology information and conventional aerodynamic wind turbine blade data supplemented by ambient wind field information such as mean wind speed and turbulence intensity.

3.1.3 Turbine and ambient inflow conditions

The baseline is a model of a 2.3MW pitch regulated turbine equipped with DTU controller in order to mimic as close as possible the Siemens 2.3MW WT's at the Nysted II site.

Simulations have been performed for mean wind speeds ranging between 6m/s and 24m/s with increments of 2m/s. The ambient turbulence level has been chosen to 6%, corresponding approximately to the mean turbulence level at different previously investigated offshore WF's (Egmond aan Zee, Lillgrund, Horns Rev I) as well as to the mean of the undisturbed ambient turbulence intensity level at the present Nysted II site – cf. Figure 16.

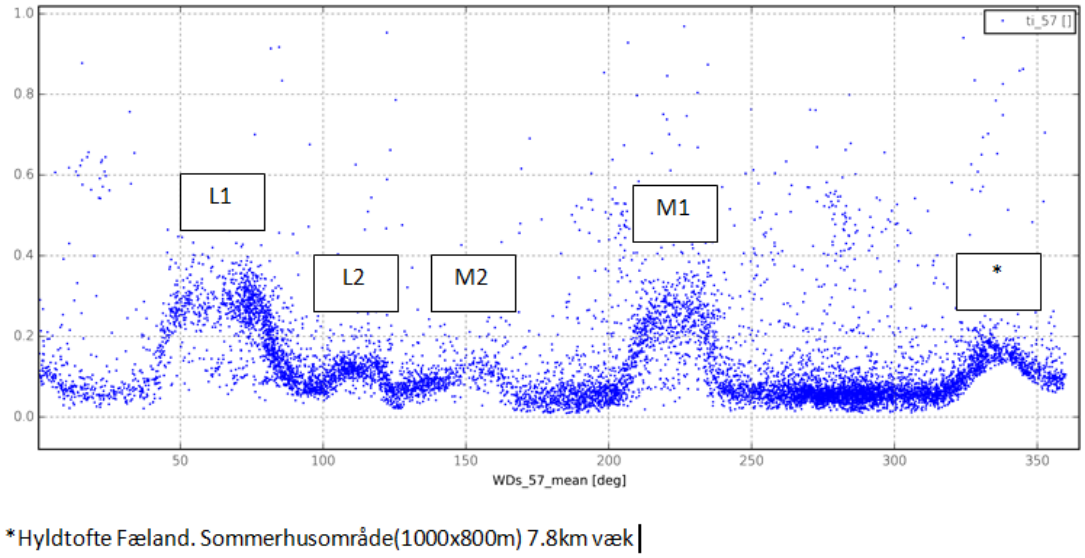

Figure 16: Measured turbulence intensity levels at the Nysted II site.

In Figure 16 the measured turbulence has been given for the full polar (i.e. [0^o; 360^o]), and as seen significant systematic variations are observed. These can be ascribed partly to upstream (turbulence generating) WT's (i.e. L1, L2, M1 and M2), partly to variations in the upstream fetch conditions as e.g. the upstream roughness element constituted by summer cottage area in direction 340^o. Binning in the mean wind speed, a notable

difference in the character of these upstream additional turbulence generators becomes apparent as illustrated in Figure 17.

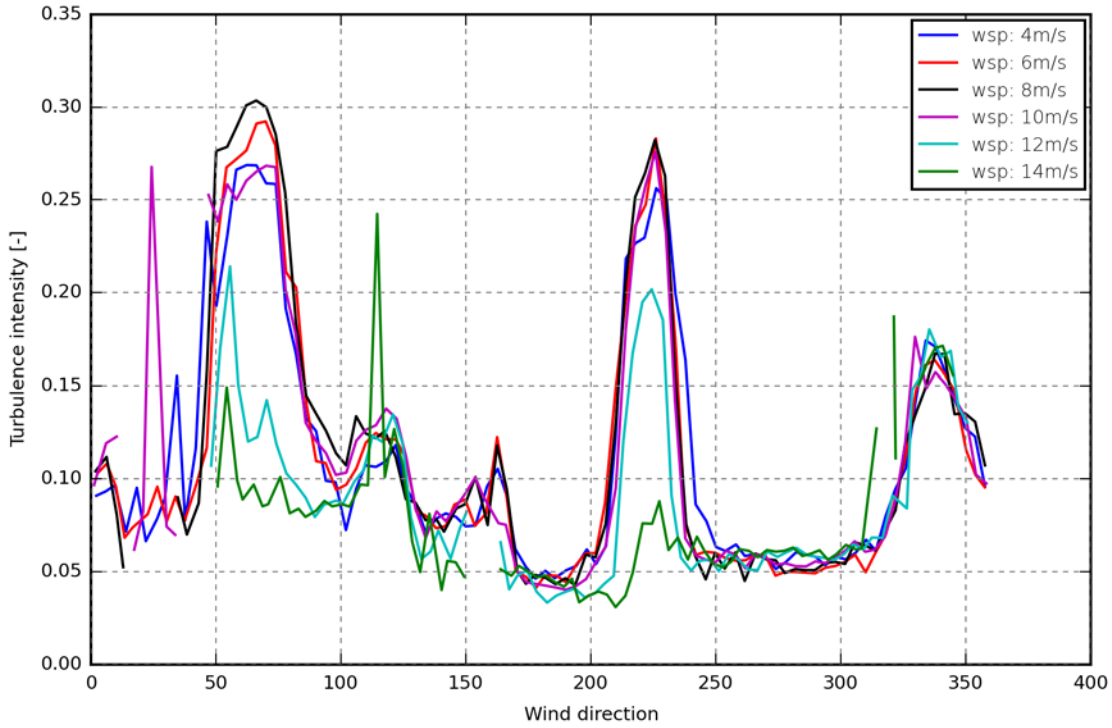

Figure 17: Mean of measured turbulence intensity levels at the Nysted II site for various mean wind speeds.

As expected the WT generated contribution to turbulence intensity diminishes with increasing mean wind speed, as the WT's become more "transparent" with increasing mean wind speed. This is particularly apparent for the turbines most significantly affecting the measured turbulence intensities (i.e. L1 and M1). Contrary to this behavior, the wind speed independent roughness element constituted by the onshore cottage area result in a wind speed independent turbulence increment as expected.
Based on the above analysis the free ambient turbulence intensity (in average) has been estimated to approximately 6% as based on the free inflow conditions observed in the [250^o; 310^o] sector. There is a slight tendency of increasing turbulence intensity with increasing mean wind speed – most pronounced for wind speeds 12m/s and 14m/s. This is expected due to increasing sea surface roughness with increasing mean wind speed. However, such details are not accounted for in the present study.

3 .2 Results

The simulation results focus on *single wake* situations and their dependence on both turbine interspacing and ambient turbulence intensity level as well as on *multi-wake* situations and their dependence on turbine interspacing. The wake characteristics depend on the turbine characteristics, which in turn depends on the mean wind speed regime. Consequently the analysis has been conducted for three different mean wind speeds – one below rated wind speed (8m/s); one at rated wind speed (12m/s); and one above rated wind speed (16m/s). The results from the full set of mean wind speeds can, for three different values of the ambient turbulence intensity (i.e. 3%, 6% and 9%), be found in appendices B, C and D, respectively.

3.2.1 Influence of turbine interspacing on single wake driven tower loads

The impact on wake affected loads originating from turbine interspacing is quantified by analyzing the comprehensive numerical result database conditioned on the three mean wind speeds each representing a typical WT operational regime – i.e. below rated wind speed (8m/s); at rated wind speed (12m/s); and above rated wind speed (16m/s). For each of these mean wind speed regimes the tower base bending equivalent moment and the tower top yaw equivalent moment have been analyzed as function of downstream distance and inflow wind direction. As the wake affected WT loads levels are highly sensitive to the exact inflow wind direction a wind direction range of +/-25 deg with a very high resolution (i.e. 1 deg.) has been adopted. All equivalent loads in this study have been normalized by the 1Hz equivalent fatigue load (cf. equation (4)) corresponding to the 10m/s case and with the ambient turbulence intensity level equal to 6%.

For the *8m/s case* the flapwise blade root load levels are shown in Figure 18. The load overview is presented as a surface plot including projections on the three planes spanning the 3D surface plot. The red-yellow colored surface shows the fatigue loads as function of distance and wind direction, whereas the back left projection shows the load level for selected distinct spacings with 1D interval and with the closest downstream distance being 4D. The back right projection shows the fatigue load level for selected wind directions within the regime -10 to +10 deg and with an interval of 5deg. All simulations are based on a time span of 1800s combined with a change in seed number when changing wind speed. However, when sweeping over the different wind directions the seed has been kept constant, as it would other wise create a significant amount of noise in the analysis.

Regarding the flapwise blade loads at 8m/s it can clearly be seen that significant half-wakes causes the highest load levels. Even at 11D downstream spacing it is still possible to see a ”double peak” in the loads. All load levels decrease for increased turbine spacing except for the full-wake case, where the maximum loading occur approximately 6D downstream. The fatigue load level ranges from 1.0 (same as free conditions at 10m/s) to 1.8 times larger in the half-wake situation 4D downstream.

A similar behaviour is seen for the tower bottom bending moment at 8m/s, cf. Figure 19. However, the wake dictated increase in load level is not as big as observed for the blade flapwise loading. In the worst half-wake situations at 4D spacing an increase of 30% is seen.

With respect to the tower top yaw moment, witch is important for the capacity of the nacelle yaw drive, a slightly different pattern is observed, see Figure 20. Especially for low spacings of 4D-5D three peak levels is clearly observed – one for each half-wake situation and in addition a smaller peak for the full wake situation. Further downstream, beyond 5D spacing, the full-wake situation creates the largest yaw load contributions. The load levels at 8D spacing are, however, very modest ranging from 0.9 to 1.1 times the reference levels.

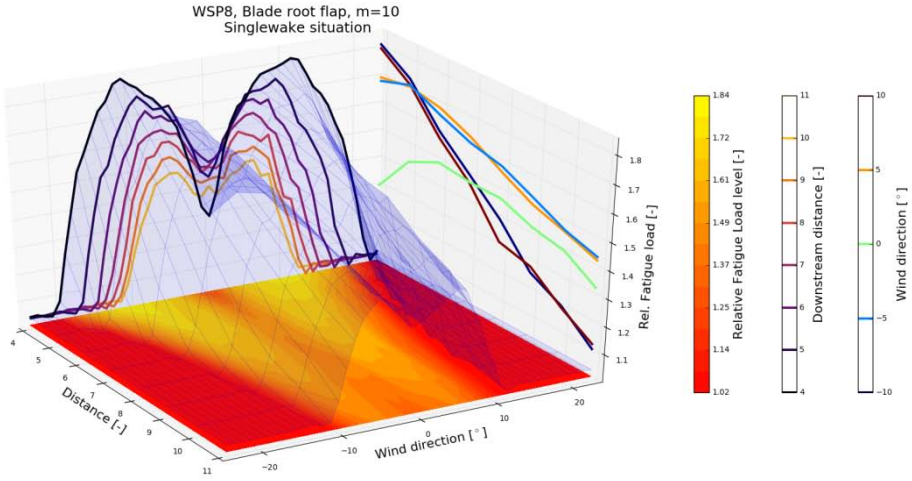

Figure 18**:** Blade flap root bending moments at 8m/s. Surface plot as well as projections on three planes are shown. Effects from half-wake operation are clearly visible.

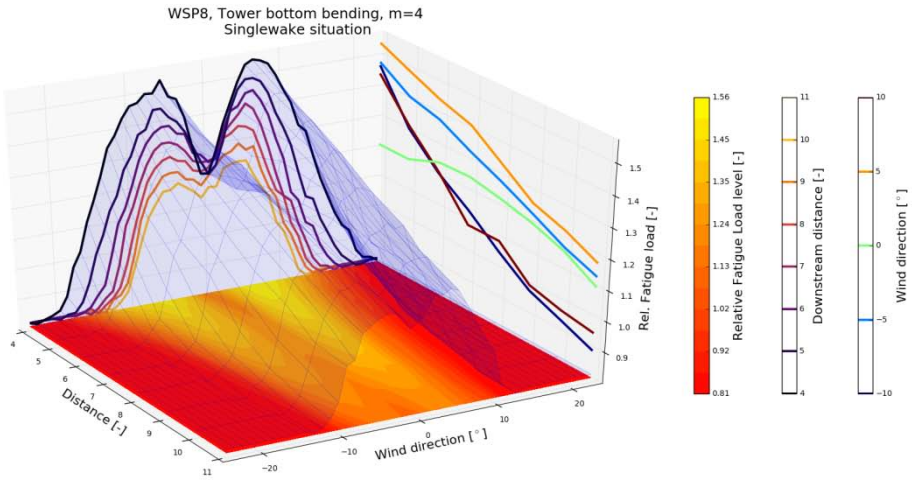

Figure 19: Tower bottom bending moments at 8m/s. Surface plot as well as projections on three planes are shown. Effects from half-wake operation are clearly seen in analogy with the blade flap loads.

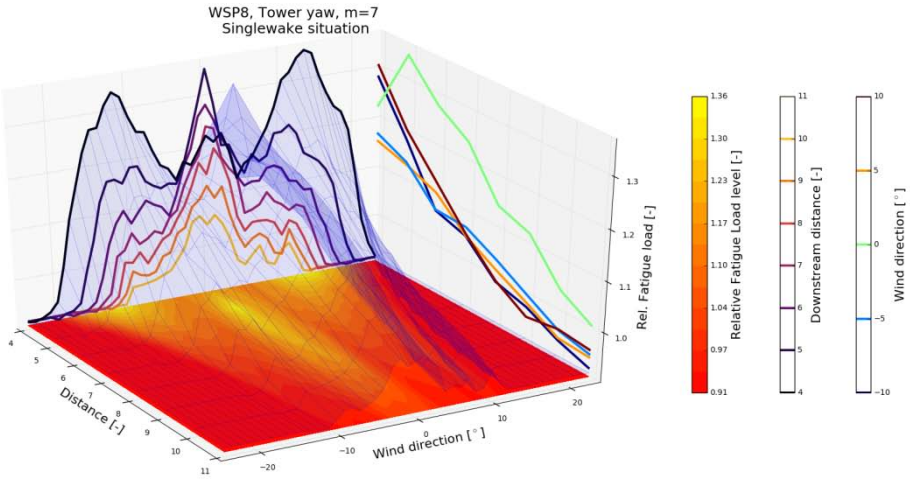

Figure 20: Tower top yaw moments at 8m/s. Surface plot as well as projections on three planes are shown. For small spacings (i.e. 4D-5D) three peak levels are seen, one for each half-wake situation and one for the full-wake situation. Further downstream the full-wake situation is the most important. However, the load level variations at 8D spacing are rather small.

In analogy with the 8m/s case, a similar set of results has been analyzed for the *12m/s case*. Starting with the blade flap root bending moment in Figure 21, a clear presence of half-wake load peaks are no longer visible as were the case for the 8m/s study. Instead the highest load levels occur for the full-wake situation. Compared to the 8m/s case, the magnitude of the loads are in general higher at 12m/s due to the higher wind speed. However, the increase in load lever as attributed to wake loading is relatively more modest (i.e. the wake loads increase the load level only from 1.4 to 1.9 times the reference loading). The load levels decrease in general for increasing turbine spacing.

For the tower loads, see Figure 22, it is clear that tower loads are slightly increasing for increased turbine distance, however, most pronounced in the full-wake situation. It appears that the maximum tower loads occur for turbine interspacings in the range 8D-10D. The physical explanation of this behavior is the meandering motion, where it takes some distance for the wake pattern to develop to a level where the load is varying across the entire rotor. When turbines are placed very close together the deficit from the closest WT will move only modestly, which may have a large impact on blade dynamics but only a limited impact on yaw- and tower loads. For longer downstream distances, the blade loading is less affected, but the yaw and tower loads may experience larger load variations. For very large spacings the strength of the wake velocity deficit is very reduced due to turbulent mixing, which in turn minimize the load impact on all WT components.

Yaw loads at 12m/s are shown in Figure 23. It can be seen that the maximum yaw loads occur in the full-wake situation and that loads decrease continuously for increased downstream turbine spacing. Compared to the wake free situation, the load level at 8D spacing increases from 1.1 to 1.5 times the reference loading due to the wake effects.

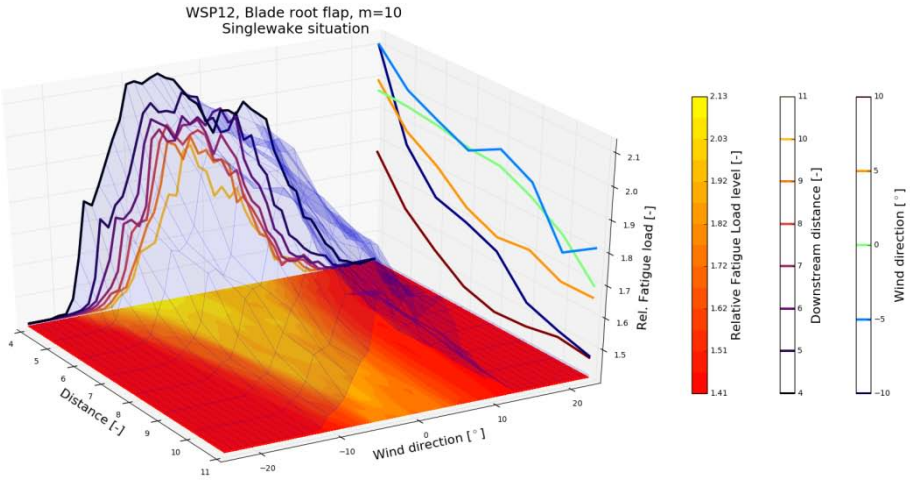

Figure 21: Blade flap root bending moments at 12m/s. Surface plot as well as projections on three planes are shown. The highest load levels occur in the full-wake situation.

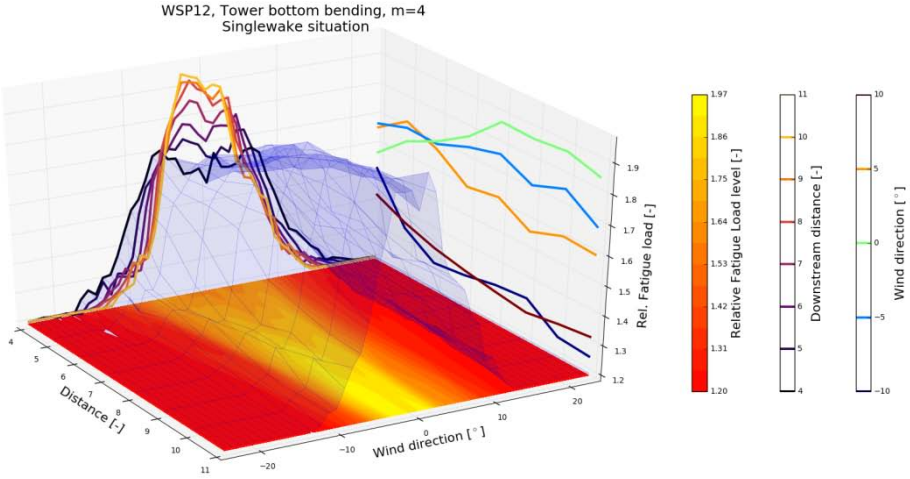

Figure 22: Tower bottom bending moments at 12m/s. Surface plot as well as projections on three planes are shown. Load levels are slightly increasing for increasing turbine distance. The highest fatigue load level occurs at spacings in the range 8D-10D.

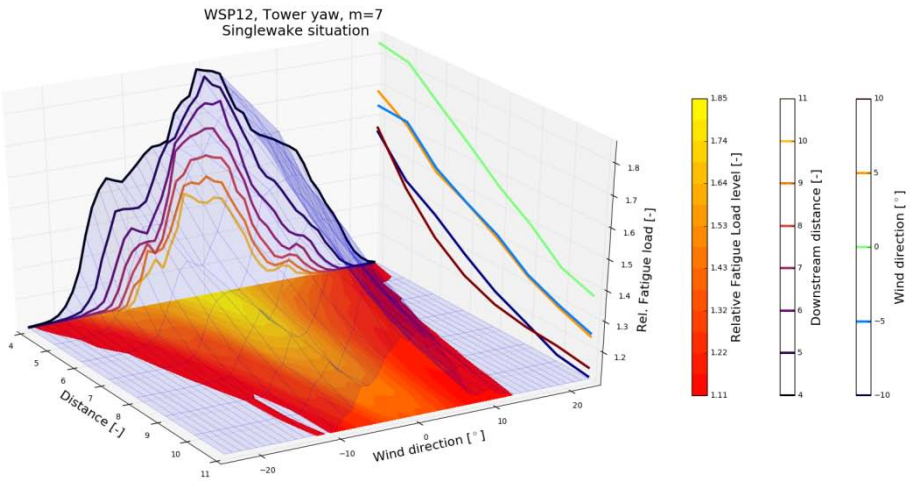

Figure 23: Tower top yaw moments at 12m/s. Surface plot as well as projections on three planes are shown. The highest load levels occur in the full-wake situation, and the load level decrease significant with the turbine spacing.

Above rated wind speed the turbine increase the blade pitch angles significantly and thereby decreases the load level. This means that the thrust coefficient of the upstream turbine decreases significantly and thus in turn the wake deficit. In other words, the upstream turbine becomes more aerodynamically transparent at high wind speeds and the impact on a downstream turbine thereby relatively less severe. However, at these high wind speeds the impact of turbulence has a rather high contribution to loads in general, and turbine fatigue loads are typically much higher above rated than below rated.

The impact on blade root flap-wise bending moments in the *16m/s case* can be seen in Figure 24. In general, the blade load decrease for increased spacings, but it is interesting to notice the significant asymmetry relative to the wind direction. The wake effects are most pronounced to one side. This may be caused by interaction with the load contribution from the tilt of the turbine (or the shear). Relative to the reference case, the load level varies between respectively 1.8 and 2.1 between the free and the wake affected situation for 8D spacing.

A significant impact from wake loading is seen on the tower loading, see Figure 25. Relative to the reference case the load levels increase slightly from 1.4 at 4D spacing to 1.9 at 7D spacing. As the wake-free load level is 1.26, the wake increased load effect is 50%. This load level is slowly decreasing for increased spacing beyond 7D.

The yaw loads decrease continuously for increased spacing, and the impact is rather modest at 8D spacing with load levels ranging from 1.45 in the free sector to 1.55 in the full-wake direction, see Figure 26.

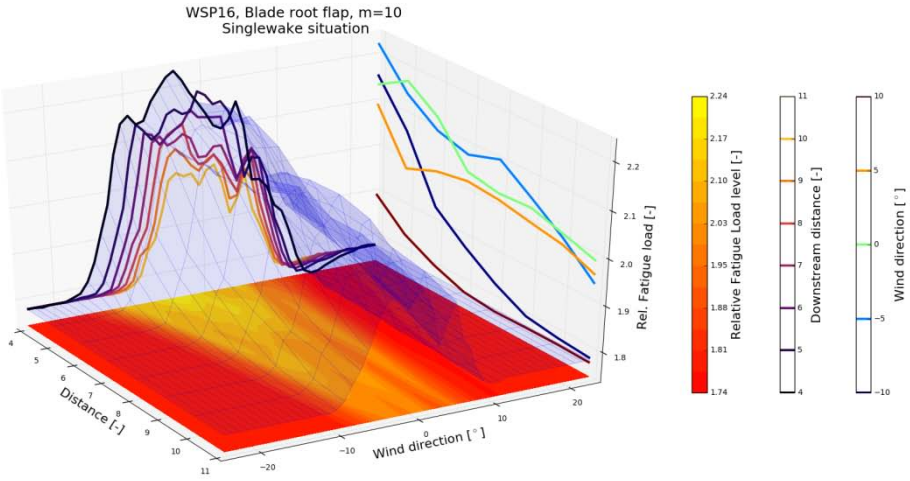

Figure 24: Blade flap root bending moments at 16m/s. Surface plot as well as projections on three planes are shown. The highest load levels occur in the full-wake situation.

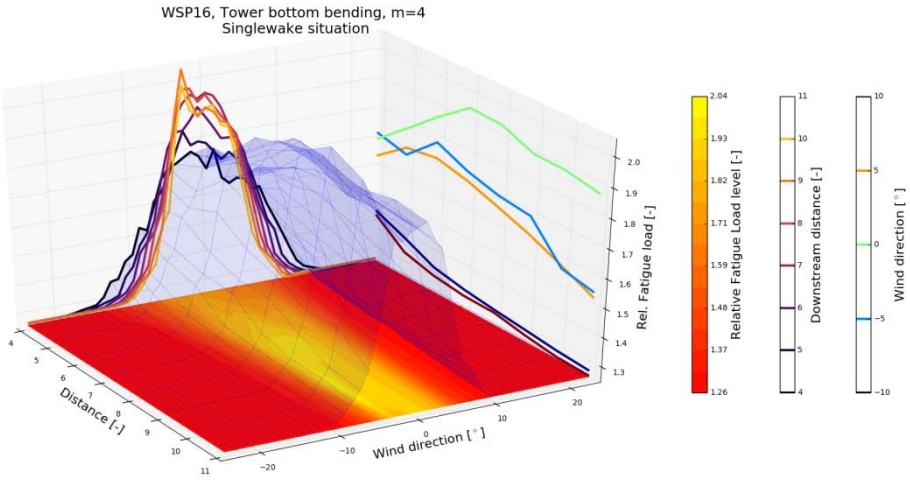

Figure 25: Tower bottom bending moments at 16m/s. Surface plot as well as projections on three planes are shown. Load levels are slightly increasing for increasing turbine distance up to a certain point, after which the load levels decreases again.

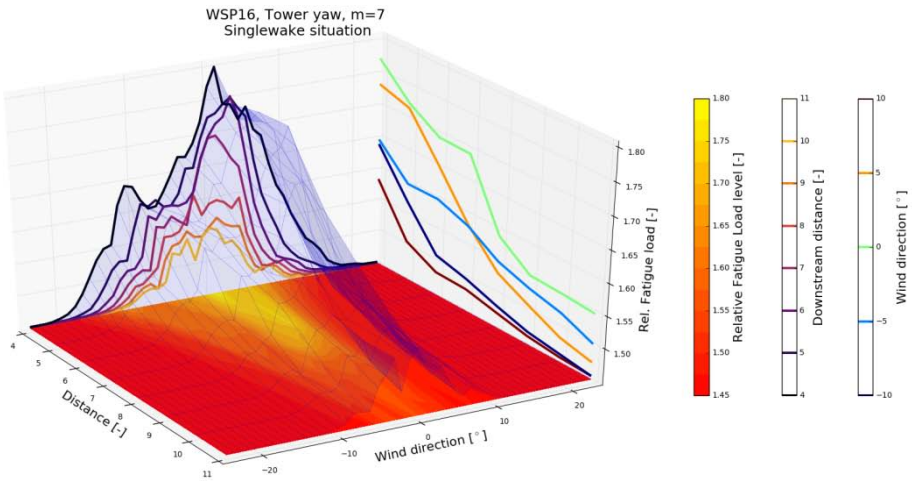

Figure 26: Tower top yaw moments at 16m/s. Surface plot as well as projections on three planes are shown. The highest load levels occur in the full-wake situation, and the load level decreases significant with the turbine.

3.2.2 Influence of ambient turbulence on single wake driven tower loads

A central element in the Dynamic Wake Meandering theory is the wake transport motion governed by the large scale turbulence structures in the ambient wind. The strength of these structures relates directly to the turbulence intensity level and thus in turn to buoyancy effects driven by vertical differences in the potential temperature (i.e. atmospheric stability) as well as to roughness effects originating from surface capillary waves or land roughness elements in the upstream direction. In order to evaluate the impact of such phenomena on the load levels, a separate study is conducted for turbulence intensity levels of 3%, 6% and 9%, respectively. In all cases neutral atmospheric conditions have been assumed to simplify matters. Consequently, this study mimic the change in turbulence intensity (although exaggerated) following from non-neutral stability conditions, but do not account for the accompanying change in turbulence length scale. As for the WT interspacing investigation, this investigation is performed for the mean wind speeds 8m/s, 12m/s and 16m/s.

In the *8m/s case*, Figure 27 shows the impact from turbulence intensity variability for blade root flap loads. As expected, low ambient turbulence result in less meandering and therefore also a more narrow wind direction interval in which wake effects are observed compared to higher ambient turbulence levels. Half-wake effects are clearly seen for all conditions. For low turbulence levels the relative impact of the wakes are higher than for higher ambient turbulence levels, however, the absolute fatigue load level is higher when the ambient turbulence level is increased. The reason is that the ambient turbulence has a direct impact on the fatigue loads driven by conventional turbulence, where an increased turbulence level causes increased fatigue loads. In addition an increased turbulence level enhances both the meandering dynamics as well as the wake deficit attenuation caused by turbulent mixing. The increased wake dynamics increases the blade fatigue loading, whereas the wake deficit attenuation diminish the wake impact on blade loads, and two counteracting effects are therefore in play. This creates a dilemma related to which turbulence level one should use for site specific load approvals, as a typical 90% quantile of the turbulence level distribution may not lead to a 90% load quantile of the fatigue load distribution.

Similar effects are also seen for the tower bottom bending moments (cf. Figure 28) and for the yaw loads (cf. Figure 29). Especially for the yaw loads related to low ambient turbulence conditions at small spacings the half-wake effects are very pronounced. However, the highest loads levels occur at high ambient turbulence conditions.

The same trends seen at 8m/s are also seen in the *12m/s case* (cf. Figure 30 - Figure 32). However, the load levels are in general higher at 12m/s than at 8m/s.

In the above rated wind speed *case of 16m/s* the behavior of the turbine changes as a consequence of the pitch control being active in this wind speed regime. As the upstream turbine thus operates with a reduced thrust coefficient, the deficit strength is also reduced relatively. However, as the downstream turbine also operates with pitched blades, the sensitivity to changes in the incoming wind is increased.

Regarding the blade loads, it is interesting to see that the wake loads are somewhat asymmetric with respect to wind direction, cf. Figure 33. The reason is probably related to the WT tilt angle, which creates load differences in the two sides of the rotor, depending on whether the blade is on the way “up” or “down”. In combination with an incoming wake deficit this leads to either an additional loading or a reduction. The wind shear may also have an impact on this. At 8D downstream distance the relative fatigue load induced by the wakes is 15% regardless of the turbulence level of the inflow field. The highest loads are seen for the highest ambient turbulence level.

The tower bottom bending moment fatigue loads increase with between 30% and 50% due to wake effects at 8D downstream distance, cf. Figure 34. It is, from a principal point, very interesting to notice that *the location of maximum fatigue loads on the downstream turbine depends directly on the ambient turbulence level*. At 3% turbulence level is can be clearly seen that the tower load levels increase for increasing distance until 10D-11D, whereas the distance of maximum tower loads is 7D-8D for 6% turbulence intensity case and 5D-6D spacing for 9% turbulence case. This is, as described earlier, directly related to the meandering motion of the wake. It takes time before the meandering has reached a magnitude, where the tower is significantly affected, and this directly related to ambient turbulence level, which can be realized as follows. Consider a given turbulence intensity (no matter what kind of roughness conditions that created it). Let’s assume that the horizontal wake “envelope” is proportional to the lateral standard deviation (associated with the large scales) times a transportation time from wake “emission” at the plane rotor to the downstream distance in focus. Adopting the Taylor hypothesis for downstream advection, the wake envelope will depend only on the (lateral) turbulence intensity, and not on the mean wind speed. This is because the transportation time is inversely proportional to the mean wind speed, whereas the lateral standard deviation, for a given turbulence intensity, is directly proportional to the mean wind speed. Consequently, the product of these depends only on the turbulence intensity.

Turning to the yaw fatigue loads, it is observed that the wake impact on these is in general rather modest for above rated wind speed operation, cf. Figure 35.

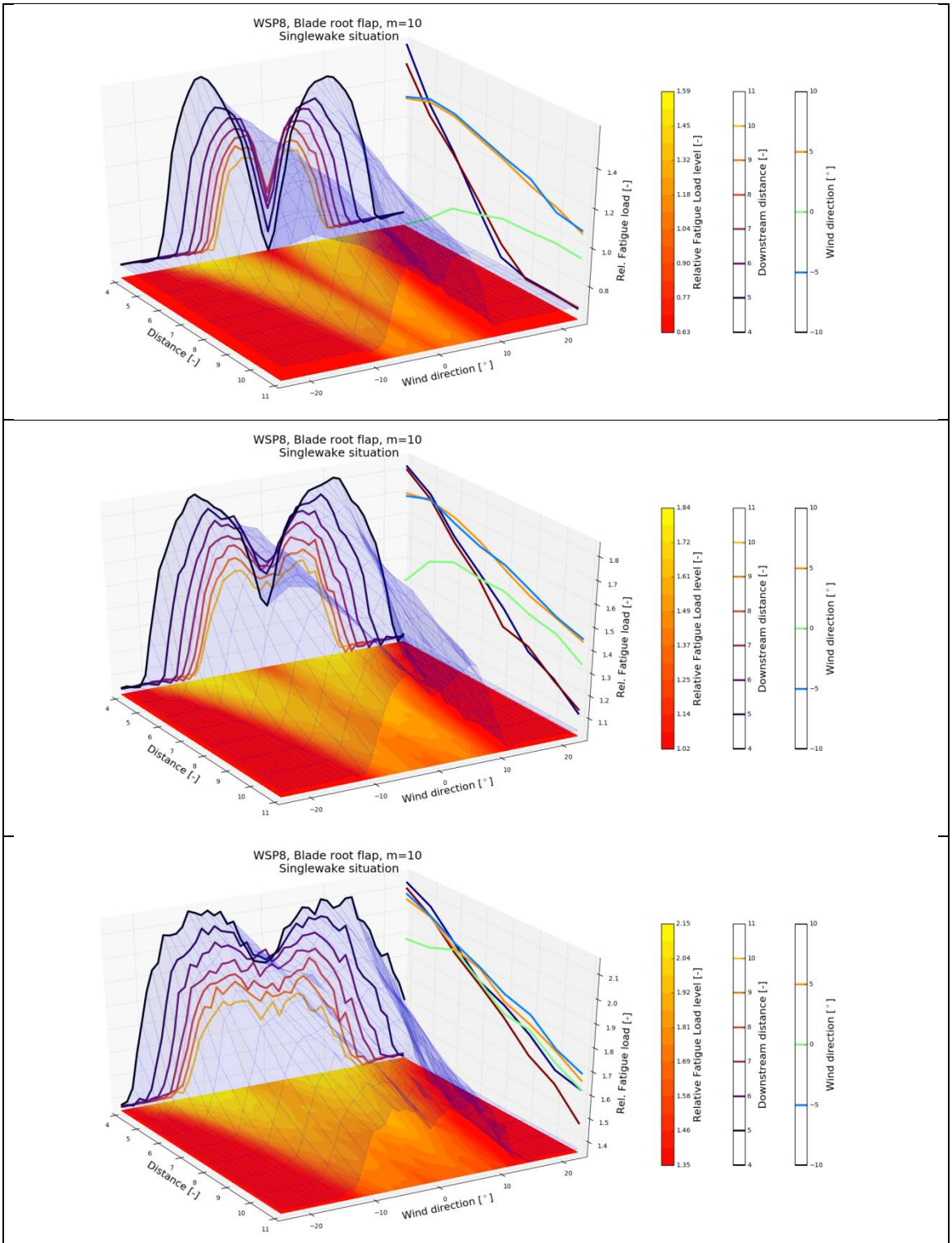

Figure 27: Blade root flap-wise bending moments at 8m/s. From top: 3%, 6% and 9% ambient turbulence intensity. Surface plot as well as projections on three planes are shown. Increased ambient turbulence causes a wider wake affected direction range, but lower relative load increase. Highest loads are seen with highest ambient turbulence levels.

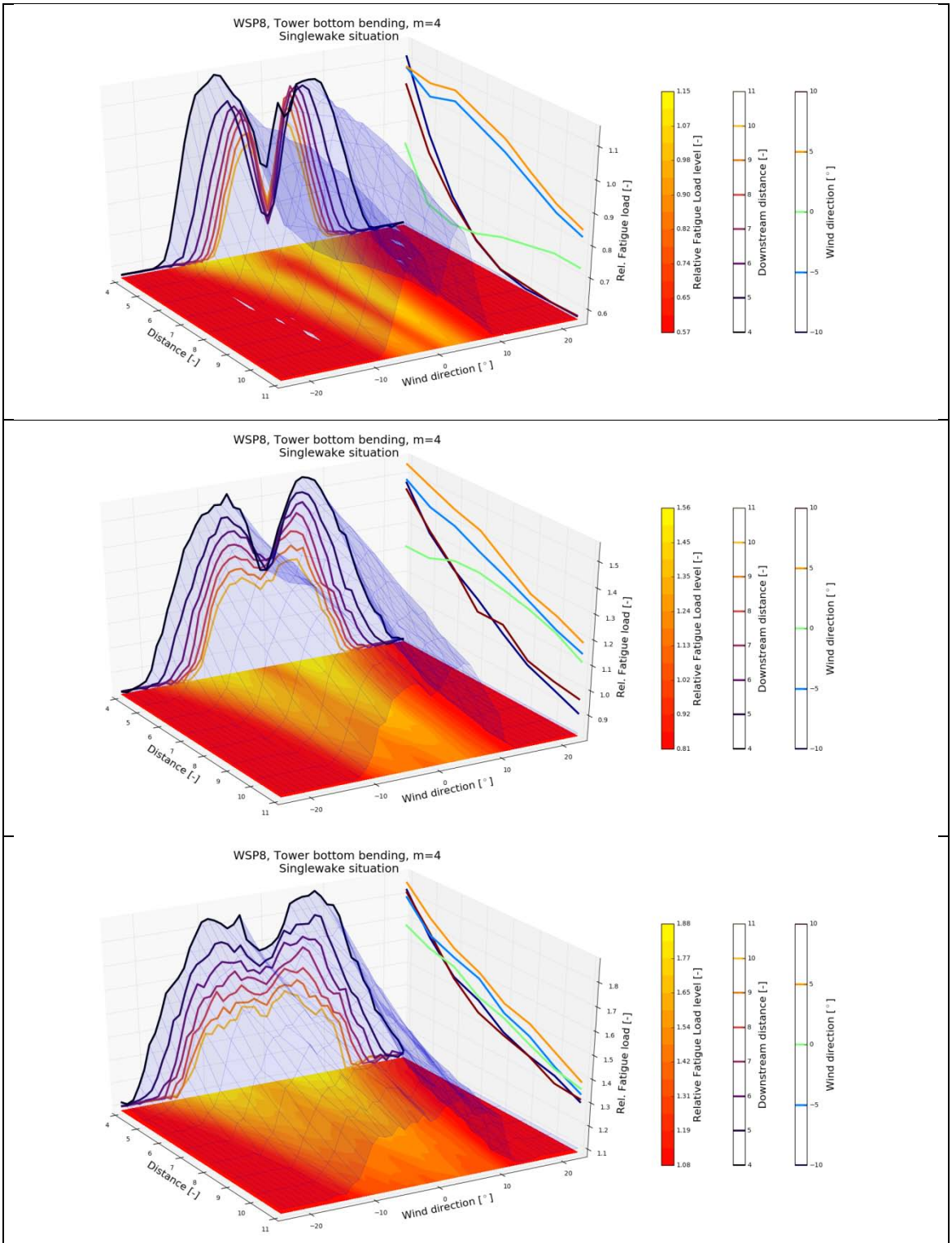

Figure 28: Tower bottom bending moments at 8m/s. From top: 3%, 6% and 9% ambient turbulence intensity. Surface plot and projections from all three sides are shown. Increased ambient turbulence causes a wider wake affected direction range, but lower relative load increase. Highest loads are seen with highest ambient turbulence levels.

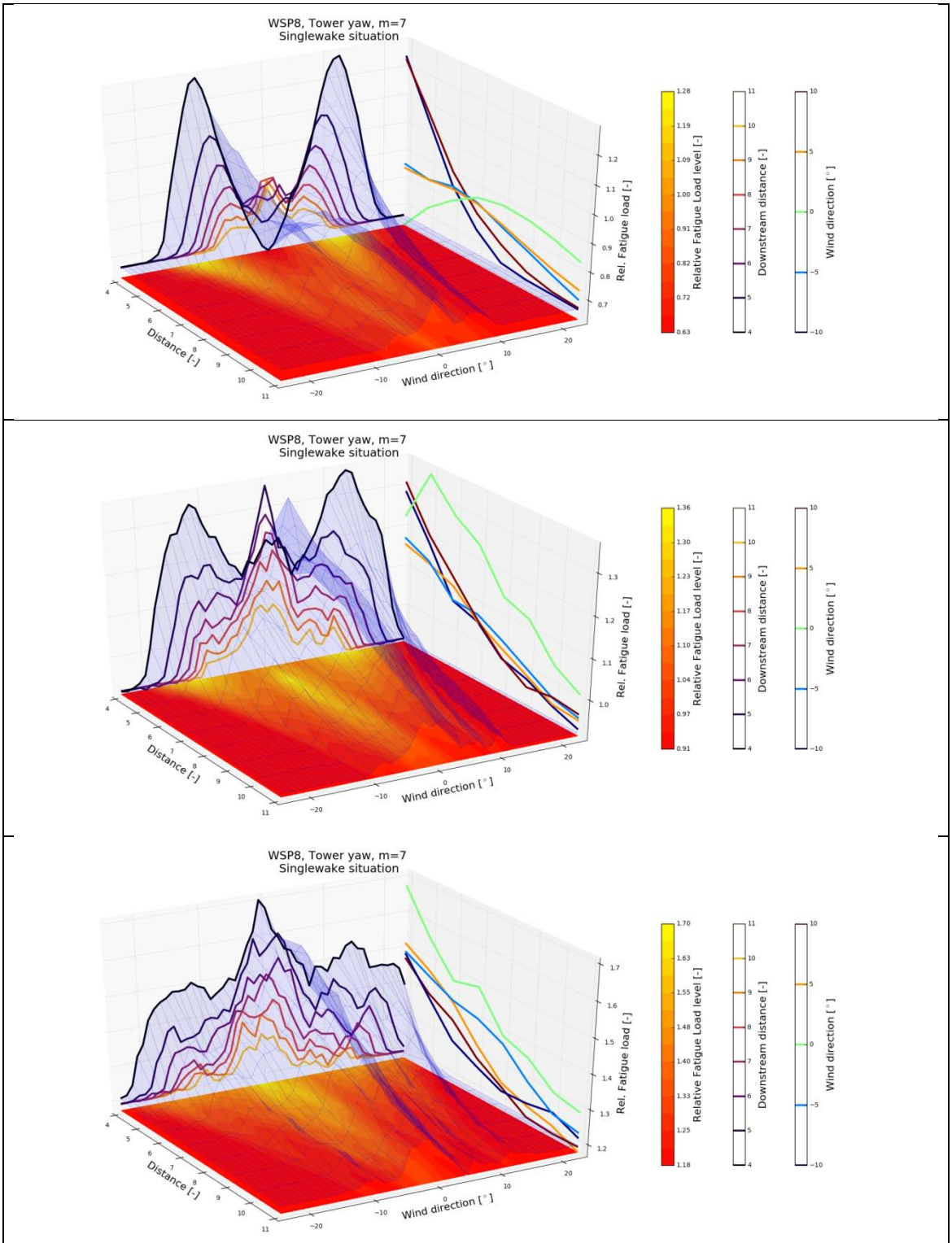

Figure 29: Tower top yaw moments at 8m/s. From top: 3%, 6% and 9% ambient turbulence intensity. Surface plot and projections from all three sides are shown. Increased ambient turbulence causes a wider wake affected direction range, but lower relative load increase. Highest loads are seen with highest ambient turbulence levels.

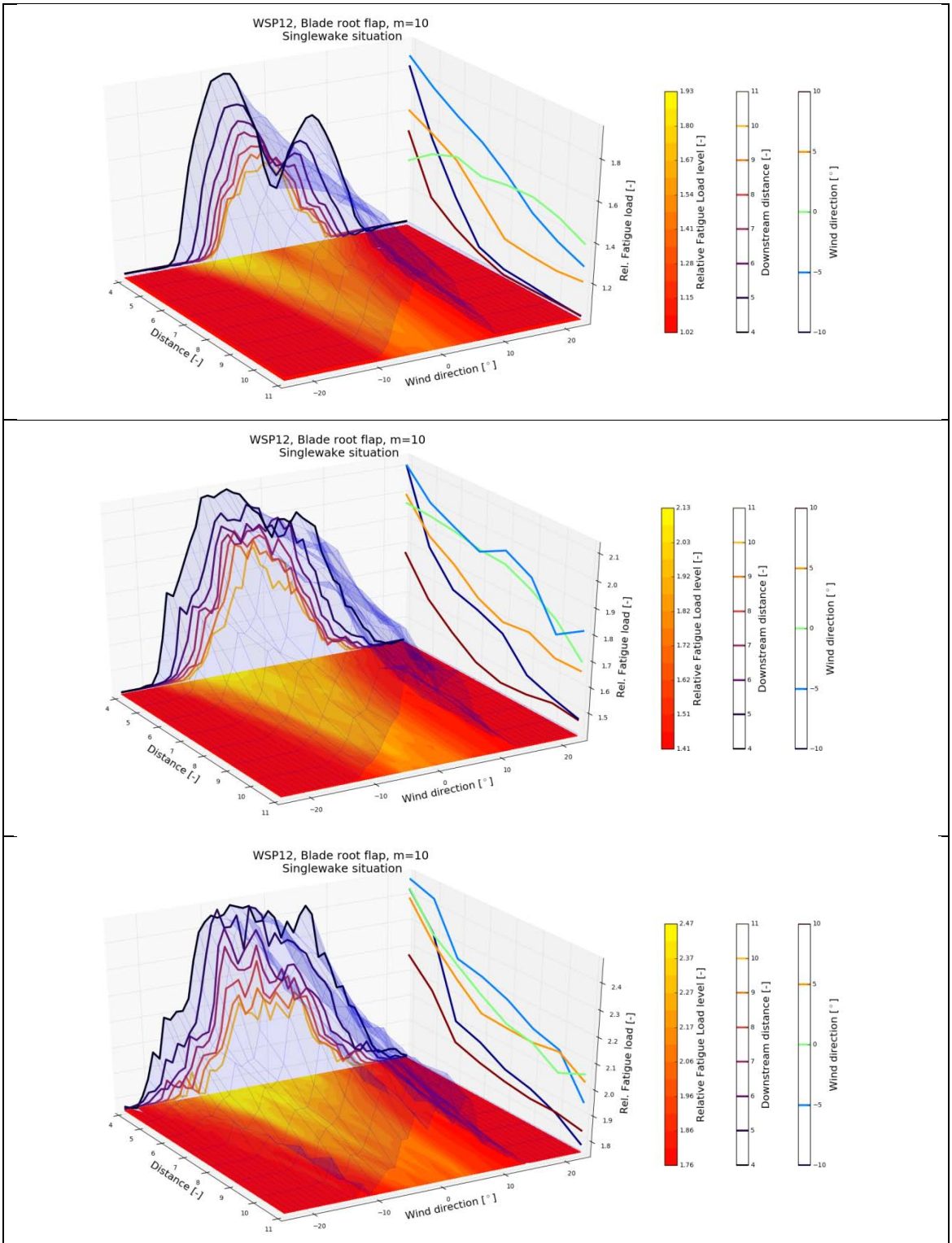

Figure 30: Blade root flap-wise bending moments at 12m/s. From top: 3%, 6% and 9% ambient turbulence intensity. Surface plot as well as projections on three planes are shown. Increased ambient turbulence causes a wider wake affected direction range, but lower relative load increase. Highest loads are seen with highest ambient turbulence levels.

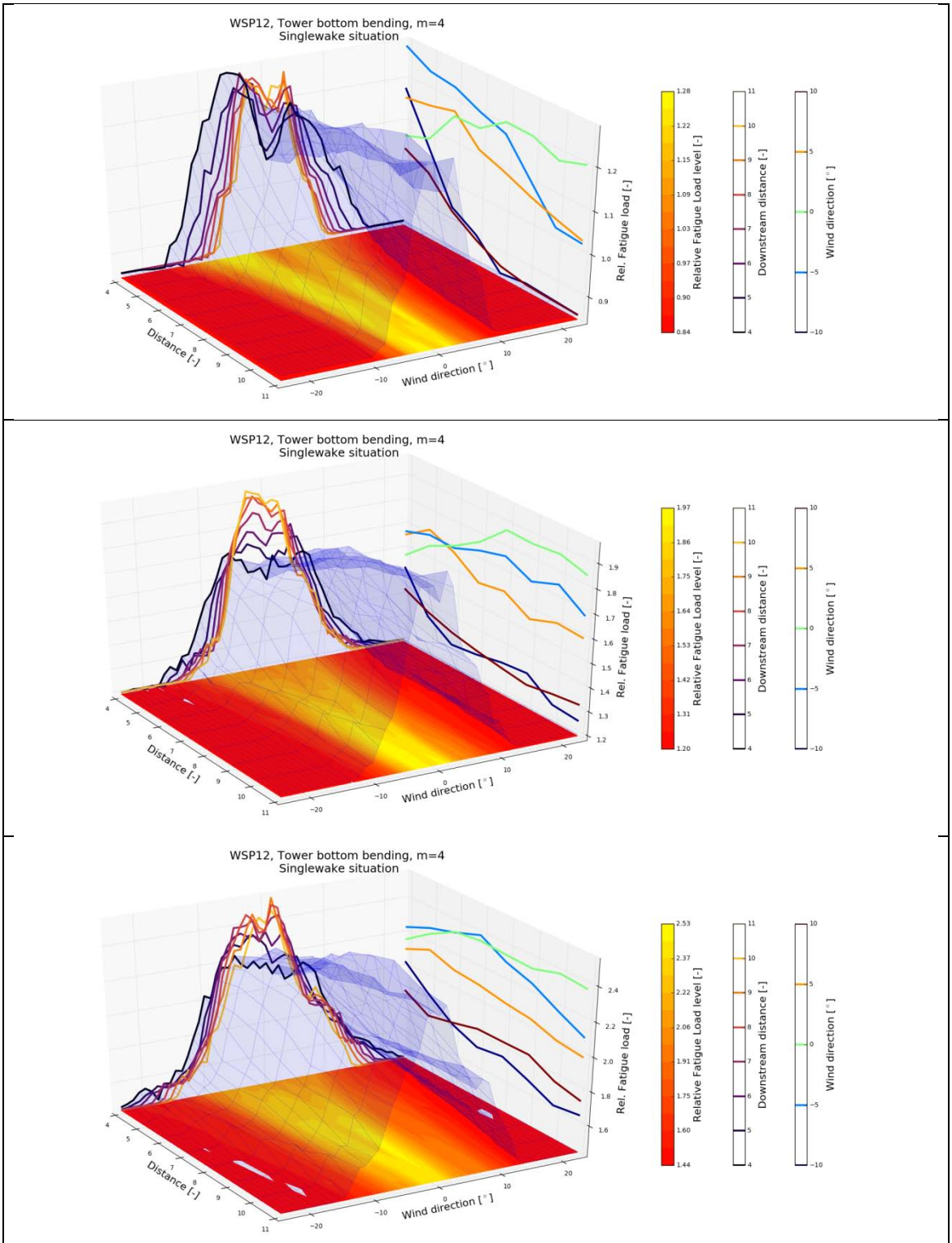

Figure 31: Tower bottom bending moments at 12m/s. From top: 3%, 6% and 9% ambient turbulence intensity. Surface plot and projections from all three sides are shown. Increased ambient turbulence causes a wider wake affected direction range, but lower relative load increase. Highest loads are seen with highest ambient turbulence levels.

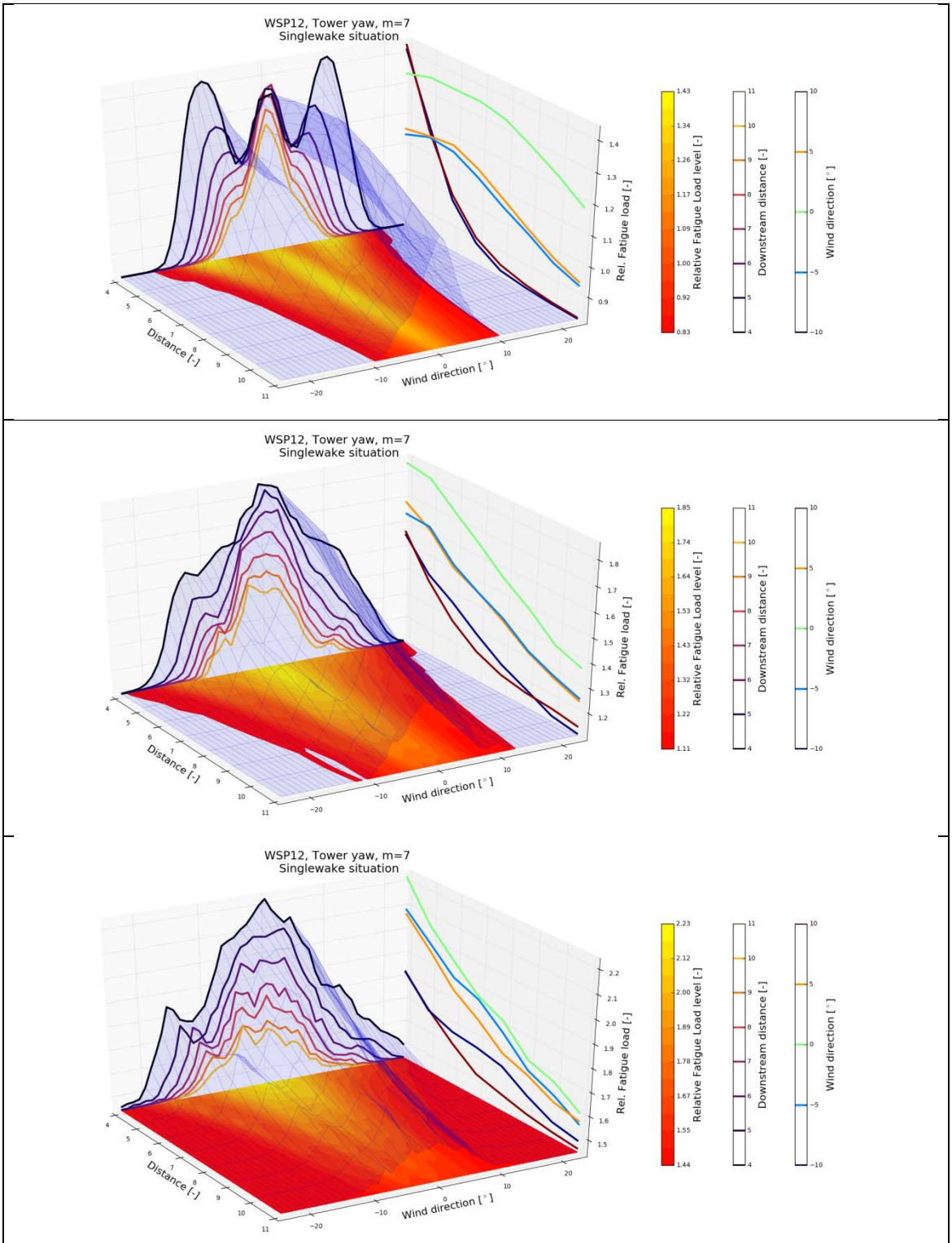

Figure 32: Tower top yaw moments at 12m/s. From top: 3%, 6% and 9% ambient turbulence intensity. Surface plot and projections from all three sides are shown. Increased ambient turbulence causes a wider wake affected direction range, but lower relative load increase. Highest loads are seen with highest ambient turbulence levels.

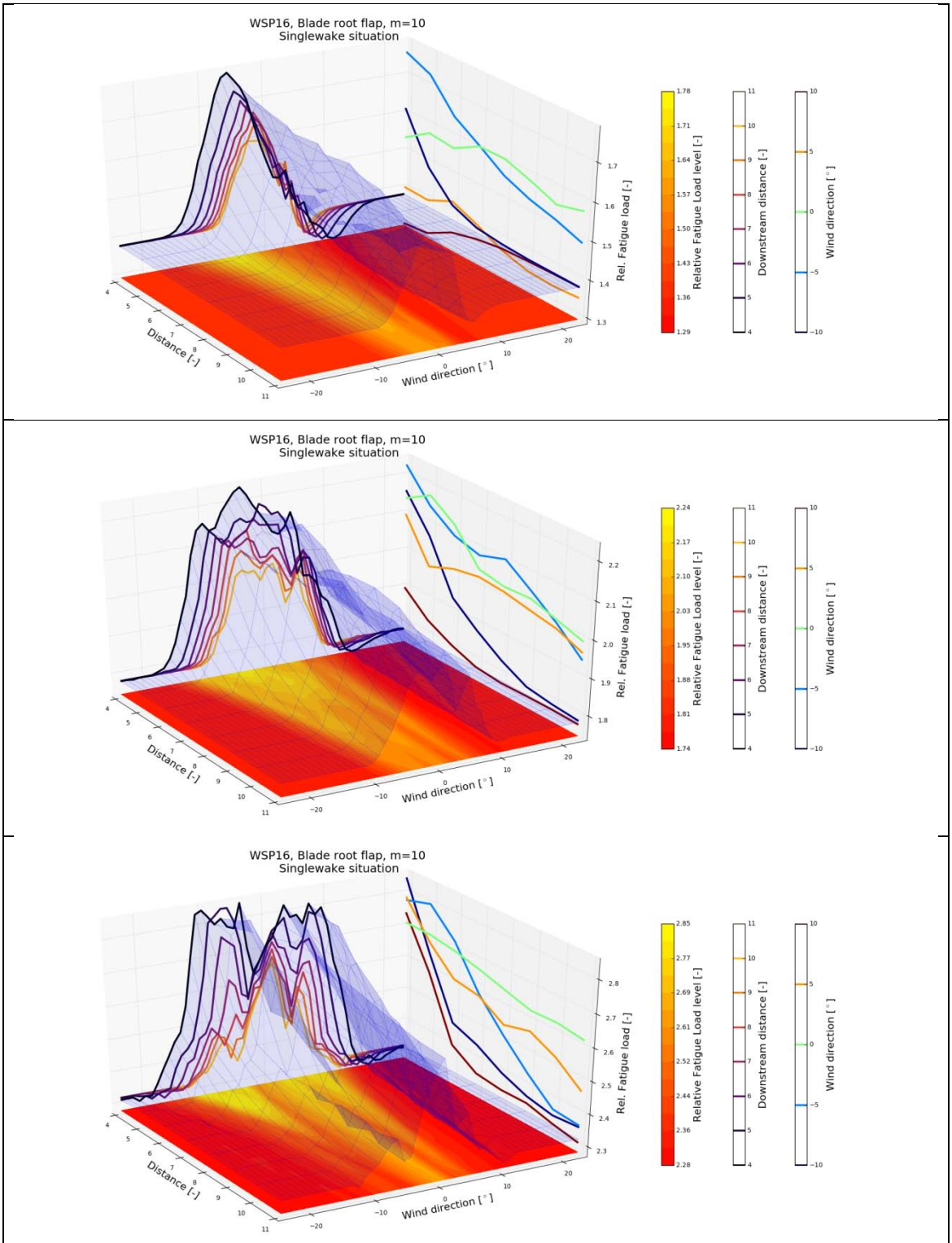

Figure 33: Blade root flap-wise bending moments at 16m/s. From top: 3%, 6% and 9% ambient turbulence intensity. Surface plot as well as projections on three planes are shown. Wake loads are asymmetric with respect to wind direction – especially for the 3% turbulence case. At 8D downstream distance the relative fatigue load induced by the wakes is 15% regardless of the turbulence level.

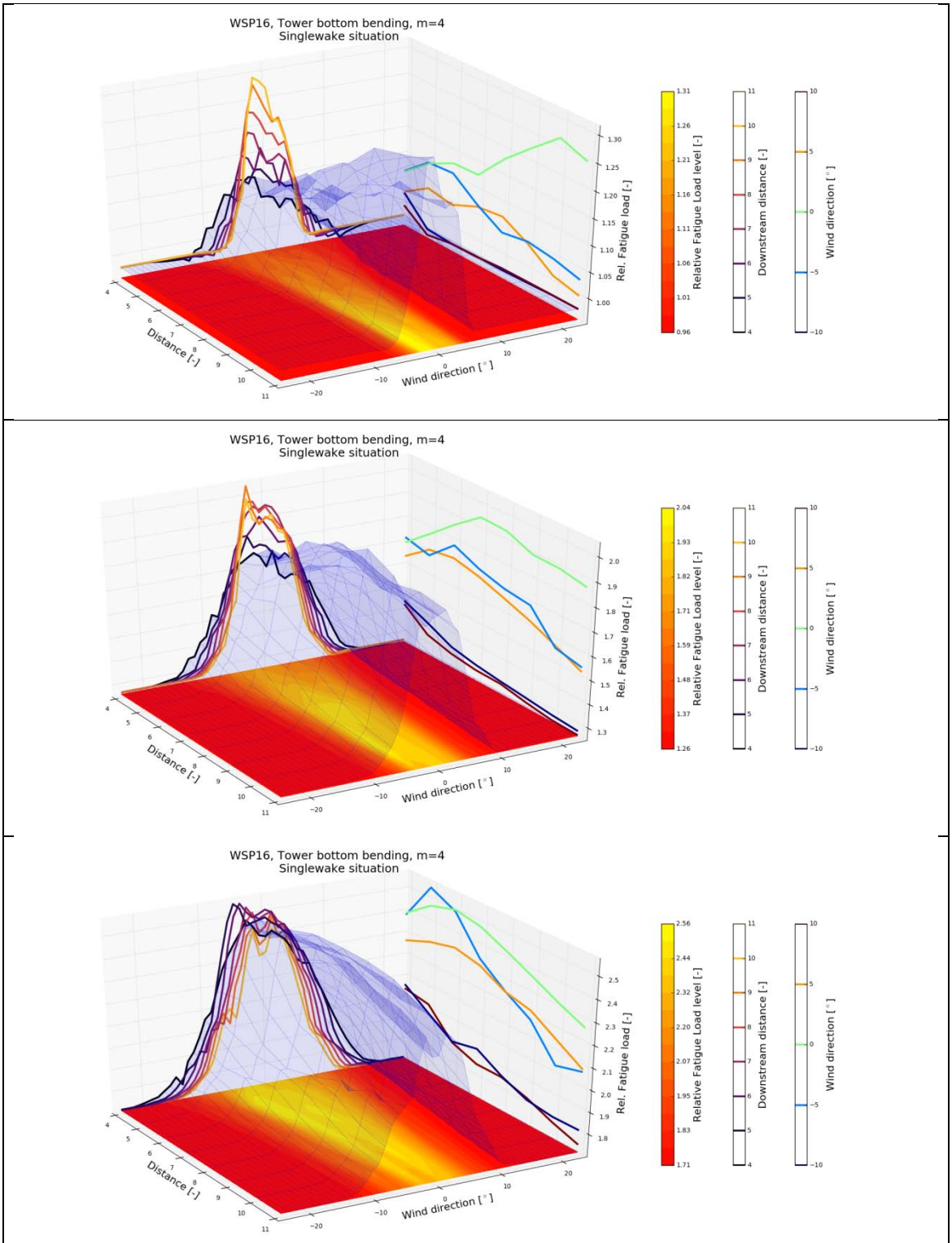

Figure 34: Tower bottom bending moments at 16m/s. From top: 3%, 6% and 9% ambient turbulence intensity. Surface plot and projections from all three sides are shown. Wake driven loading induce an increase between 30% and 50% in the fatigue loading at 8D. Note, that the *downstream location* of the peak fatigue loading depends directly on the ambient turbulence level.

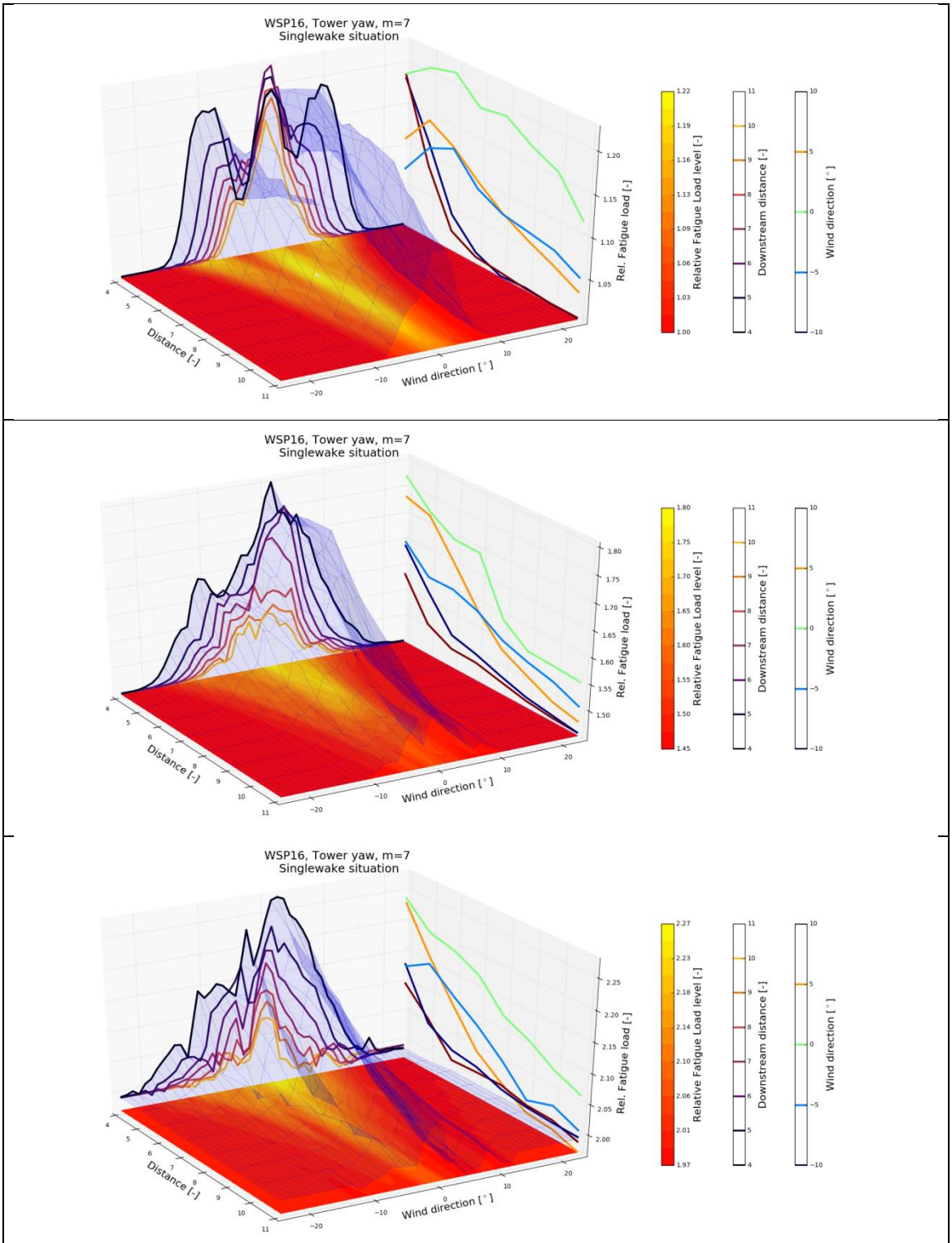

Figure 35: Tower top yaw moments at 16m/s. From top: 3%, 6% and 9% ambient turbulence intensity. Surface plot and projections from all three sides are shown. The impact from wakes on yaw fatigue loads is in general modest for above rated wind speed operation.

3.2.3 Influence of turbine interspacing in a multi-wake situation

A recent study [15] has revealed that *multi-wake* situations deviate crucially from single wake situations and contribute surprisingly significant to WT wind farm loading in the above rated wind speed regime, where such load cases may even have a design driven impact on the turbine load levels – at least for WF's with small WT interspacings. The reason is that even though each individual upstream WT has a small velocity deficit contribution, it add up for each turbine in a row and cause a large "efficient" wake velocity deficit, which in turn may lead to very large wind speed variations between the (aggregated) wake and the free regions.

To gain further insight into wake loading in multi-wake situations a generic numerical study has been undertaken primary in order to investigate the dependence of multi-wake loading with WT interspacing, which is obviously not an option for real full-scale WF's, where the WF layout is pre-defined. Thus, for this purpose a particularly simple WF has been modeled – namely a WF topology consisting of only one *straight line* and populated with 10 WT's. The WT's are the 2.3MW turbine used for the single wake Nysted II investigations presented in Sections 3.2.1-2, and the investigated WT interspacing ranges from 4D to 11D. The simulated loading refers to WT no. 10, which is consequently exposed to wake loading from 9 upstream WT's.

In addition to the generic study, the Nysted II WF topology has been modeled. Besides the fixed WT interspacing, a crucial difference between the real layout and the fictitious WF layout described above is, that the real layout consists of curved trace's populated with WF's (cf. Figure 1) contrary to the fictitious straight line topology. The consequence is that a given turbine – in the "direction" of the trace's will be exposed to wake contributions from a limited number of WT's only (say, of the order of 3 upstream turbines) contrary to the 9 upstream WT's in the generic case. The Nysted II WF model furthermore allow for a direct comparison with the measured full-scale tower data.

Finally, the Lillgrund study has been include partly because the Lillgrund data set is a unique data set, partly to shed light on the effect of WT interspacing in full-scale multiple-wake situations. The WT interspacing in the Lillgrund case is as small as 3.3D compared to between 7.1D and 7.5D along the curved trace's in the Nysted II case.

Generic WF case

At high wind speeds the load levels are in general high, and any additional increment has an important effect on the general turbine load level. Predicted loads are shown for the blades (Figure 36), for tower bottom bending (Figure 37) and for tower top yaw (Figure 38) for a case with an ambient wind speed being equal to 16m/s and with an ambient turbulence intensity equal to 6%. As mentioned this load case relates to a multi-wake configuration with 9 upstream turbines on a straight line.

For both blade and tower loads it is seen, that the fatigue load increase is very high within a narrow direction sector of +/-5deg. Within this sector and at 6D downstream the fatigue load level for the blades are increased by a factor of 4, whereas the fatigue load level for the tower top yaw moment are increased by a factor of 2.5. The tower bottom bending fatigue loads are increased by a factor as high as 6 due to the influence from the wakes. Such wake driven fatigue load increments are considerably higher than observed in the measurements (cf. Figure E18 and Figure E24), where both tower bottom bending loads and tower top yaw loads are increased by a factor of approximately 2 in multi-wake cases.

This is because the generic WF has a straight line topology, whereas the Nysted II WF has a curved line topology, essentially meaning that a given WT, for a wind direction aligned with the tangent of the curved trace, will be exposed to wake contributions from a limited number (i.e. significantly less than 9 as in the generic WF) of upstream WT's only. This will become clear from the succeeding analysis of the real Nysted II layout, and the conclusion is that one should avoid straight line topology layouts, at least if these lines is oriented along predominant wind directions. It should be noted, that the additional wake driven loading for the investigated case is on top of an already high initial load level.

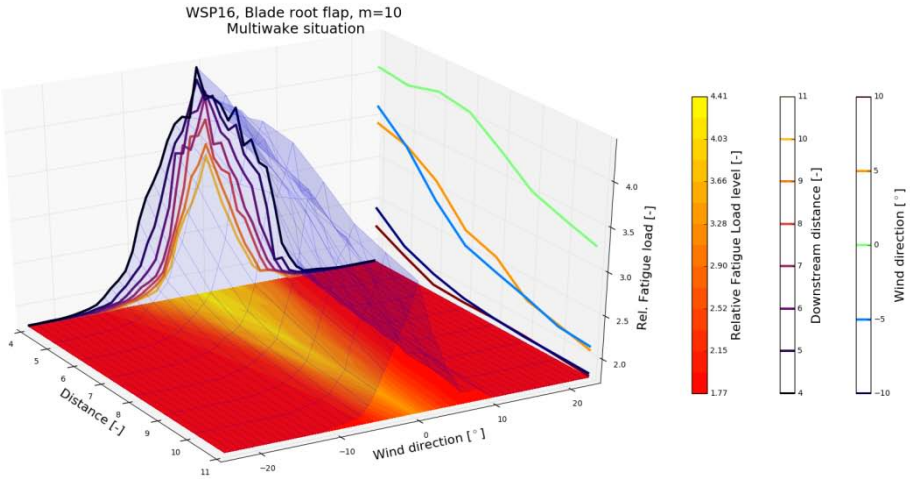

Figure 36: Blade root flap-wise bending moments at 16m/s. Surface plot as well as projections on three planes are shown. A significant load increase (i.e. a factor of approximately 4 at 6D) is observed within a narrow direction sector of +/-5deg.

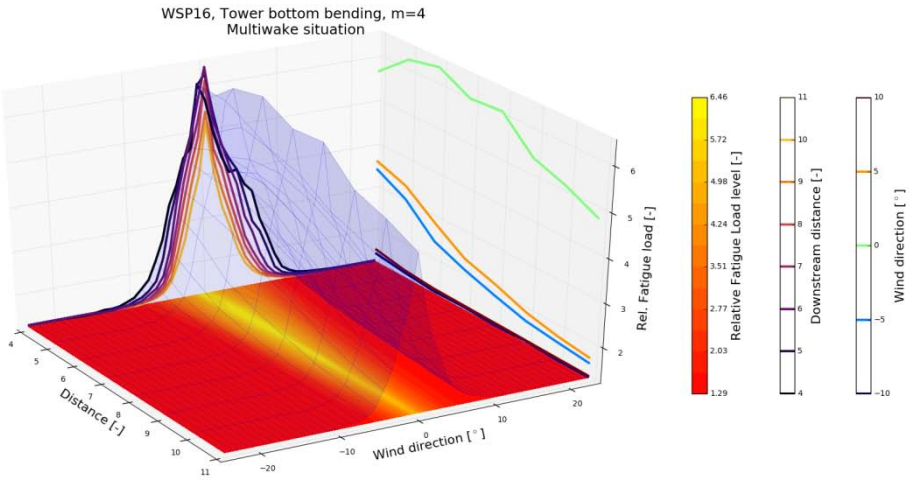

Figure 37: Tower bottom bending moments at 16m/s. Surface plot as well as projections on three planes are shown. A significant load increase (i.e. a factor of approximately 6 at 6D) is observed within a narrow direction sector of +/-5deg.

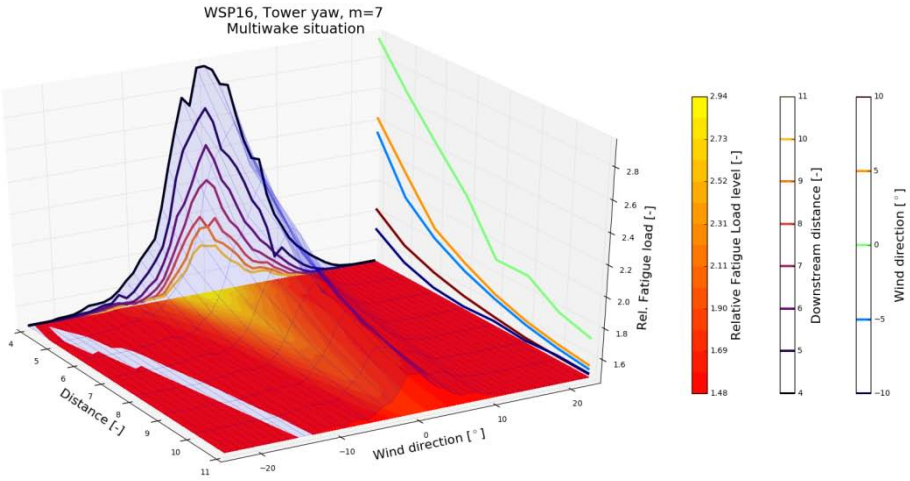

Figure 38: Tower top yaw moments at 16m/s. Surface plot as well as projections on three planes are shown. A significant load increase (i.e. a factor of approximately 2.5 at 6D) is observed within a narrow direction sector of +/-5deg.

Nysted II case

To investigate the effect of a *curved line topology* as well as to allow for comparisons with measured full-scale data, the Nysted II farm has also been modeled for the *16m/s case*, representing the above rated wind regime, as well as for the *10m/s case*, representing the below rated wind regime. Predicted normalized fatigue equivalent tower bottom bending moments are shown for turbines L1, L2, L3, M1 and M2 as function of inflow direction in Figure 39 and Figure 40, respectively.

For the 10m/s case it is interesting to compare Figure 39 with respectively Figure E3, Figure E15, Figure E27, Figure E39 and Figure E51 showing a convincing agreement between measurements and simulations on the wake dictated fatigue load increment level.

For the 16m/s case it is interesting to compare Figure 40 with respectively Figure E6, Figure E18, Figure E30, Figure E42 and Figure E54 showing a fair agreement between measurements and simulations on the wake dictated fatigue load increment level. The tower bottom bending fatigue loads are increased by a factor of up to 2.5, which is considerably less that the load increase predicted for the generic WF topology. Again, it should be underlined, that it consequently from a load perspective is recommended to avoid straight line topology layouts, at least if these lines is oriented along predominant wind directions.

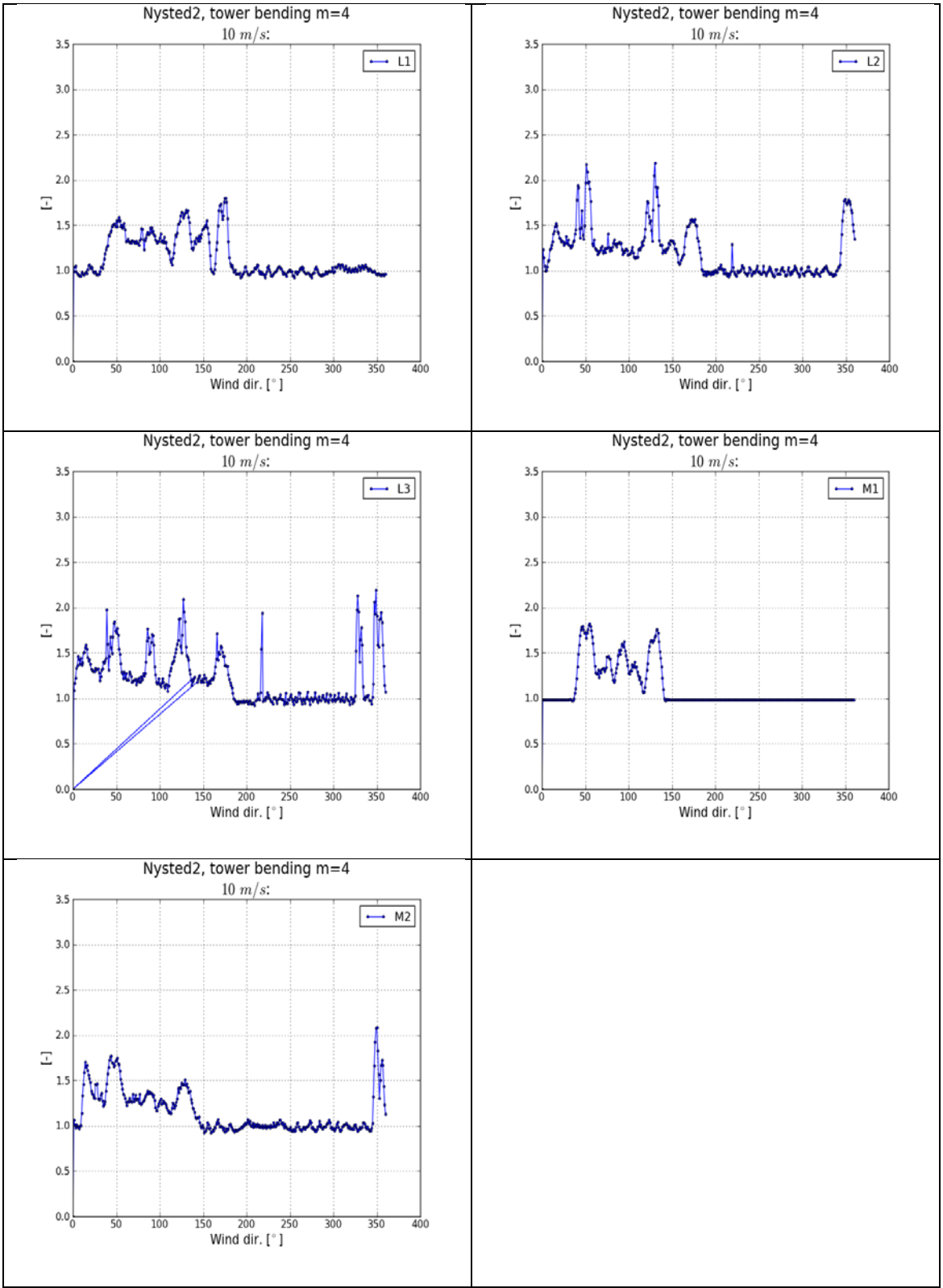

Figure 39: tower bottom bending moments for turbines L1, L2, L3, M1 and M2 as function of inflow direction for the 10m/s case.

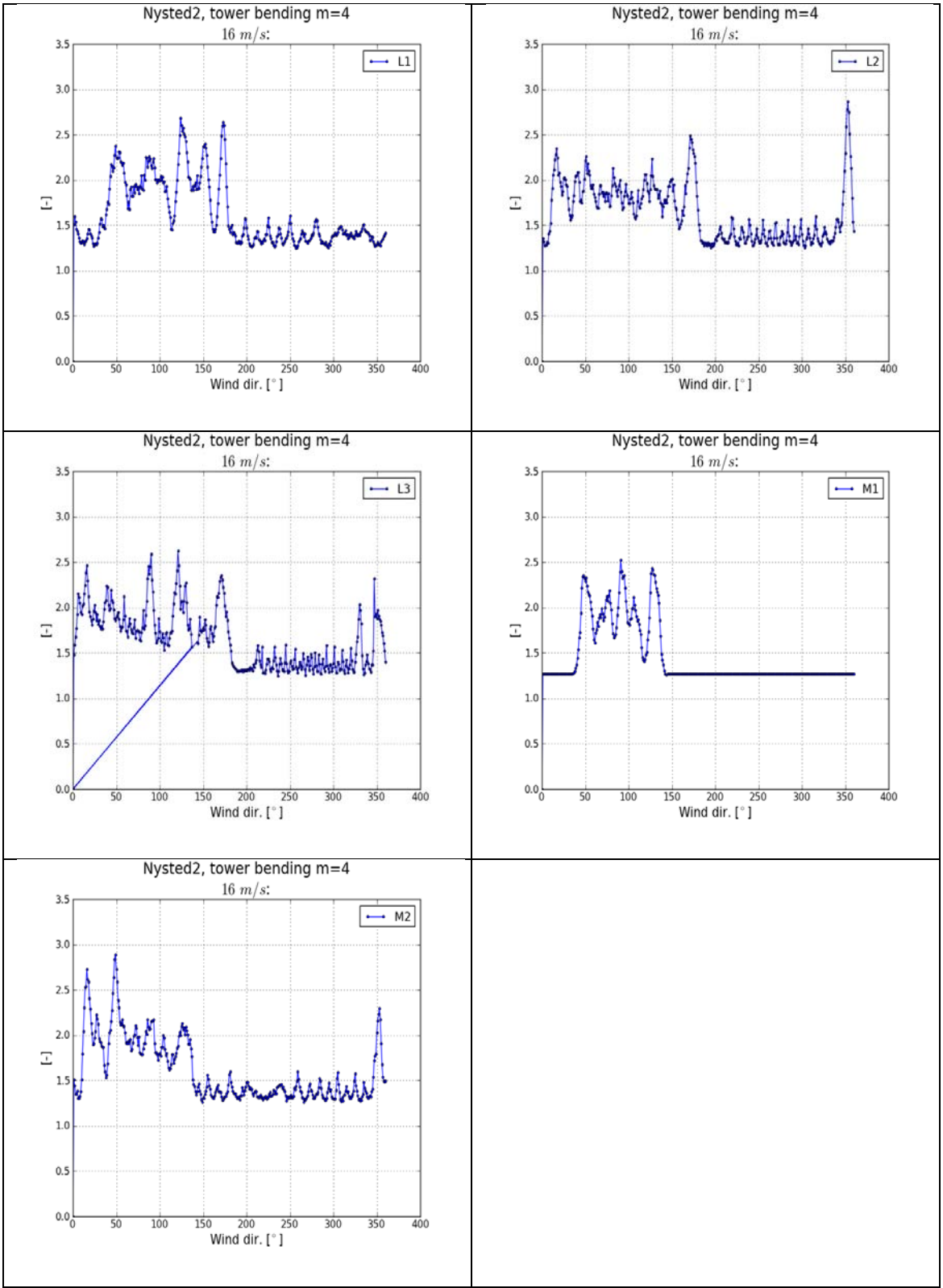

Figure 40: tower bottom bending moments for turbines L1, L2, L3, M1 and M2 as function of inflow direction for the 16m/s case.

Lillgrund case

Concerning validation of the Dynamic Wake Meander model, in terms of derived structural wind turbine loads, comprehensive comparisons were performed in the Egmond aan Zee study [12], where a very satisfactory agreement between model predictions and measurements was concluded for the ambient mean wind speed regime between 3m/s and 14m/s. This study was based on full-scale measurements from a Vestas V90 turbine located in the Dutch Egmond aan Zee WF for the *specific wind direction*, where the turbine in focus was located as the 6'th turbine in a row with uniform turbine interspacings equal to 7D.

In general only very limited load validation material from multi-wake WF conditions exist. This is particularly true for the mean wind speed regime above rated wind speed, because very long measurement campaign is in general required to ensure a sufficient amount of high wind speed data to facilitate such analyses.

The Swedish Lillgrund off-shore WF has a layout characterized by exceptionally small WT interspacings. Full-scale measurements from this WF have previously been presented with focus on power production [14], [16] as well as on wind turbine fatigue loading [13] effects in the *below rated* mean wind regime. In the load study predicted flapwise fatigue loads for a full polar were shown to agree very satisfactorily both for single turbine wake situations and for deep array wake operation up to about rated (ambient) mean wind speed. However, for higher than rated (ambient) mean wind speeds, significant deviations between predictions and full-scale measurements were observed for deep array wake cases; i.e. for wake situations characterized by multiple upstream turbines.

Initiated by this study the DWM model has been updated to facilitate correct predictions of WT loading caused by multi-wake exposure in the high ambient wind speed regime, and the performance of the updated model under such conditions is investigated in terms of both flapwise fatigue loads and tower fatigue loads with particular emphasis on deep array cases. The DWM update in the above rated wind speed regime is based on a linear perturbation approach, and a detailed description can be found in [15].

The Lillgrund WF consists of 48 Siemens SWT-2.3-93 turbines, and one of these (C-8) is instrumented with strain gauges resolving blade, main shaft and tower loads, cf. Figure 41. The present DWM model validation is based on recordings from this turbine.

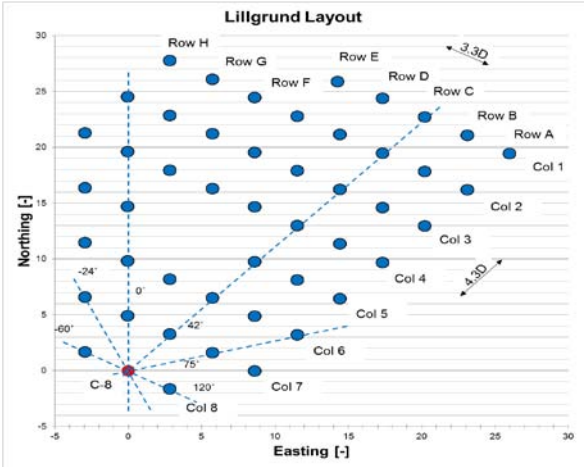

Figure 41: The Layout of the Lillgrund wind farm and location of WT C-8. Distances are non-dimensioned with the rotor diameter.

Whereas the Egmond aan Zee WF is characterized by a “conventional” turbine inter spacing, the layout of the Lillgrund WF is, as mentioned, characterized by very small turbine inter spacing's; i.e. down to 3.3 D. This makes the present Lillgrund load validation case a unique supplement to the former validation based on the Egmond ann Zee WF as well as to the present validation against the Nysted II data.

Measured and predicted fatigue loads are quantified as fatigue equivalent moments using the Palmgren-Miner approach; and Wöhler exponents of 5 and 10 were assumed for the tower and blade composite structures, respectively. The validation scenarios include load cases associated with normal turbine operation with mean wind speeds ranging from 8m/s to 16m/s. Measured wind speed dependent turbulence intensities (TI’s) are used, reflecting the offshore wind speed dependent “surface” roughness. However, no attempt is done to resolve TI as function of upstream fetch (i.e. direction). Thus, in the mean wind speed regime 6m/s-14m/s a TI of 5.8% is used - gradually increasing to 6.2% at 16m/s.

For a complete direction rose simulated and measured fatigue equivalent moments are compared (mean wind speed) bin wise for two WT main components – i.e. blade and tower. With the complete direction rose being represented, a multitude of load cases – ranging from ambient inflow conditions over single wake cases to various types of multiple wake inflow cases – are thus covered. All presented fatigue loads have been normalized with the fatigue load representing the respective sensors at 9m/s in the free sector.

The results for the blade load comparison can be seen in Figure 42. Results are presented as function of the wind direction for each wind speed bin covered. In the left column of the figure is shown the results from comparing the measurements, IEC class 1A and the Frandsen method [18] to results obtained with the original DWM approach. In the right column a similar comparison, but to the updated DWM approach, is shown. A similar comparison for the tower bottom bending moment is shown in Figure 43.

An excellent agreement between measurements and the DWM model results is evident. Note, that a WT exposed to multiple wakes in the high wind speed regime – with the Lillgrund interspacing – experience load levels that significantly exceed the corresponding single wake load levels despite the fact that a WT is more “aerodynamic transparent” above rated wind speed and therefore has a reduced wind speed deficit compared to below rated.

Further, as a supplement to the DWM validation, the investigation also includes comparative load simulations as based on the existing recommended practice in the IEC61400-1 ed. 4 standard [2]. Here it can be concluded that the Frandsen approach is highly conservative for *single wake* situations, especially above rated wind speed. This in turn means that adopting the DWM approach with site specific conditions allow for quantification of the build-in safety reserve in the existing IEC61400-1 recommended practice or, alternatively, opens for use of the DWM approach to reduce this safety reserve if appropriate. Even for a wind farm as the Lillgrund, with turbine spacings between 3D and 4D, it is seen that using a class 1A turbulence level still results in a conservative load estimate.

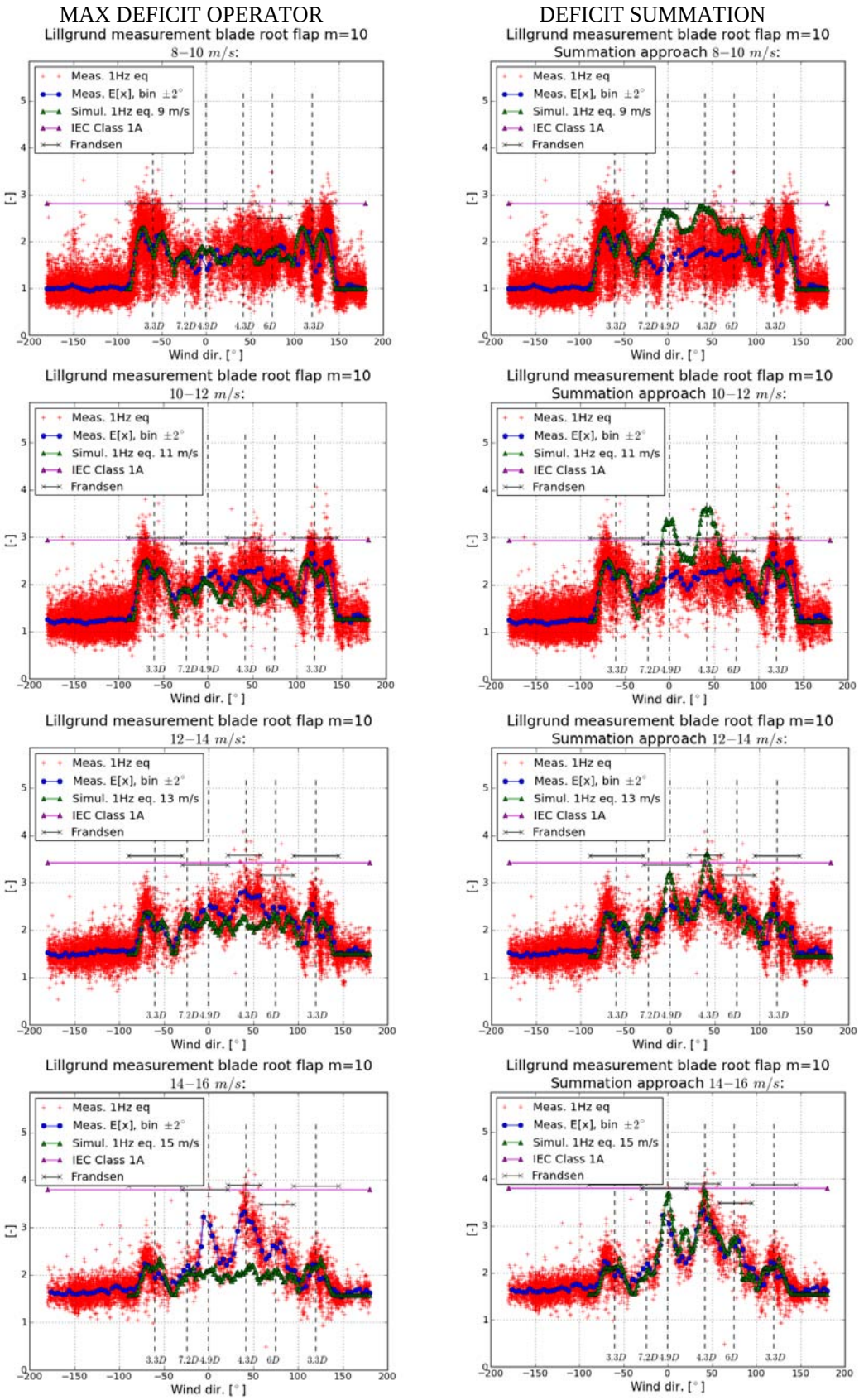

Figure 42: Comparison of blade root bending 1 Hz fatigue loads at wind speed from 8 to 16m/s. Left: DWM using max operator. Right: DWM using linear superposition.

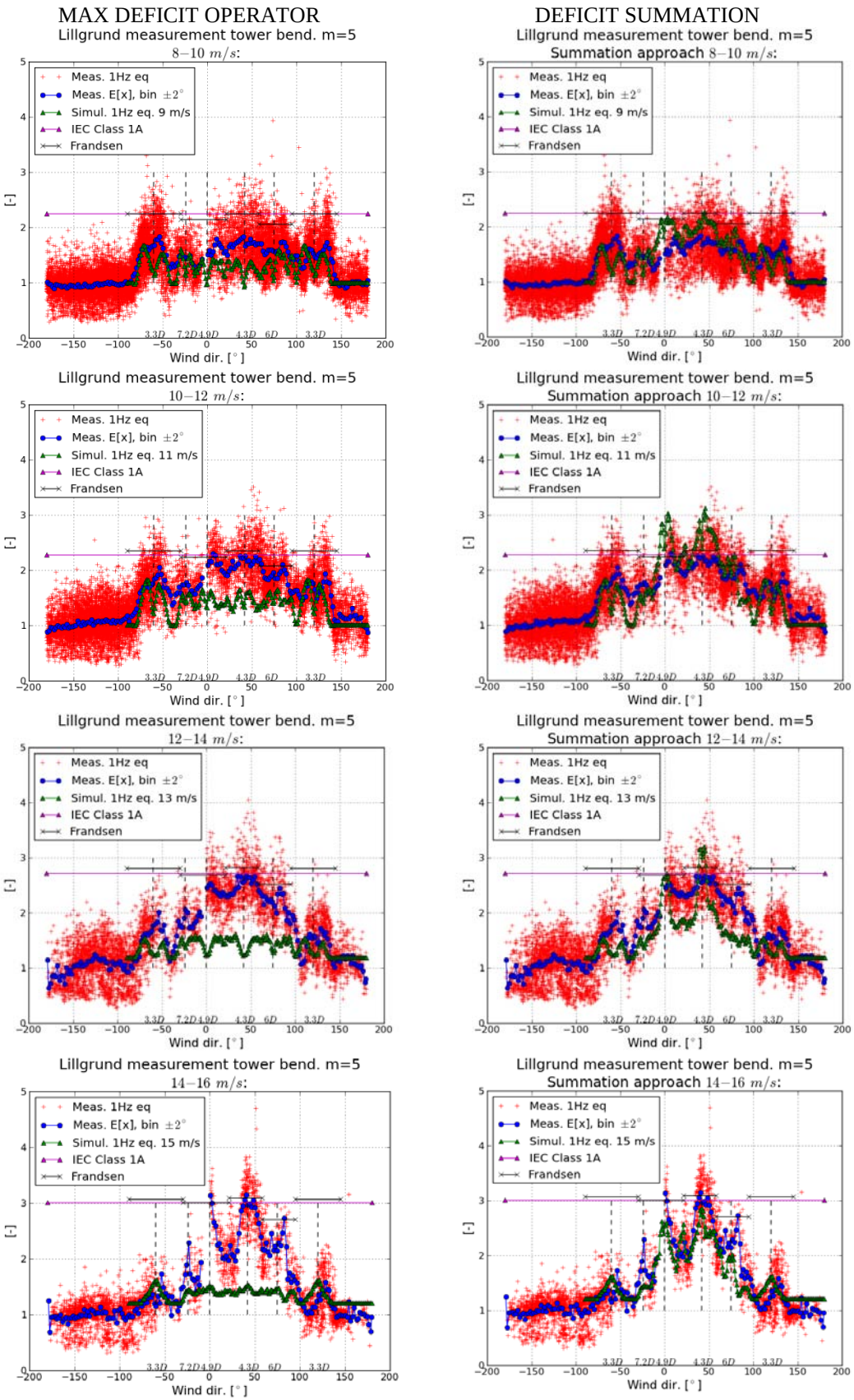

Figure 43: Comparison of tower bottom bending 1 Hz fatigue loads at wind speed from 8 to 16m/s. Left: DWM using max operator. Right: DWM using linear superposition.

4 Synthesis of measurements and simulations

For the distinct single wake situations facilitated by the instrumented WT's at specific inflow directions, the results of the full-scale measurements and the simulations are compared in this Chapter. For various mean wind speed conditions the data material allow for comparison of the tower bottom bending moment loading as well as tower top yaw moment loading. As in previous analyses the focus is on three selected mean wind speeds representing below rated operation conditions (8m/s), at rated operation conditions (12m/s), and above rated operation conditions (16m/s).

The analysis is split in two parts, with the first part dealing with the effect of WT interspacing, and the second part dealing with the character of peak loading in full-wake situations and its possible relationship to the level of the ambient turbulence intensity.

4.1 Tower loads as function of turbine interspacing

For single wake cases, representing different WT spacing, the tower loading is plotted as function of the inflow angle *relative* to the direction of the connection line between relevant sets of two WT's. For the measured data this is symbolized by stylized WT's (e.g. exemplified with the "crosses" at zero inflow direction in Figure 44) at zero inflow direction, where the colour of stylized upstream WT's relates to the specific interspacing between relevant sets of WT's as specified in the figure labels. Regarding WT sets the nomenclature is the following: WT_i-WT_j means measurements from WT_i associated with a wind direction sector, where WT_i operates in the wake of WT_j. It should be noted that the upstream fetch associated with the investigated single wake cases are comparable and dominated by free upstream sea conditions ensuring identical inflow turbulence conditions for comparable atmospheric boundary layer (ABL) stability conditions and thus comparable wake dynamics. No attempt has been done to add ABL stability conditions as a supplementing bin dimension.

The mean wind speed bin size used for the analysis of the measurements is 2m/s, and no attempt has been done to determine the "centre of gravity" of these bins to define the most descriptive mean wind speed for the simulations. Thus, the simulated mean wind speeds refer to the median of the respective wind speed bins.

For the analysis of both simulations and measurements a Wöhler exponent of 4 – typical for construction steel – is used for tower base bending moments, whereas a Wöhler exponent of 7 – typical for the type of steel used in the yaw mechanism structure – is used for tower top yaw moments.

For the *8m/s case* the *normalized tower bottom bending moment* load levels are shown in Figure 44 and Figure 45, respectively. The measured results offer single wake cases corresponding to WT interspacings ranging between 6D and 10.6D, as the L3-M1 case (16.9D), with M1 being the wake generating WT, seems to be influenced by wakes from other nearby WT's too and as such not can be considered as a pure single wake case. In an atempt to quantify the uncertainty on the measured data error bars, indicating the standard deviation of the measurements on which the measured graphs are based, have been added. However, comparing the L1-M1 and the L2-M2 cases, which a priory should be expected to give very similar results as both spacing and inflow direction (i.e. upstream fetch) is very similar, indicate an uncertainty larger than what is quantified by the error bars. An alternative uncertainty indicator is the spread among the single wakes cases "outside" the wake influence regime, where "identical" free wake inflow

conditions prevail – e.g. in the inflow direction interval [-25^0; -20^0]. With this uncertainty in mind, there is a fair agreement between measured and simulated results both quantitatively and qualitatively, although the double peak character (reflecting half-wake situations with a substantial load generating potential) of the load response is much more pronounced in the simulated results. Both measurements and simulations display a week asymmetry in the inflow direction, which may be associated with tilt of the rotor.

For the 12*m/s case* the normalized tower bottom bending moment load levels are shown in Figure 46 and Figure 47, respectively. As for the 8m/s case a fair qualitative and quantitative agreement between measured and simulated results are observed. Contrary to the 8m/s case, the half-wake induced double peak character of the load response is almost diminished in both measurements and simulations roughly speaking resulting in a single peak response curve extending between inflow directions -10^0 and 10^0. Notable is the very large scatter among the measured results beyond $+10^0$, which might be attributed to "secondary" wake effects.

For the 16*m/s case* the normalized tower bottom bending moment load levels are shown in Figure 48 and Figure 49, respectively. The load levels of measured and simulated results are of comparable magnitude, but very large scaller is observed among the measured single wake cases, which preventing more detailed comparisons between measured and simulated results. Part of the explanation may be that the number of measured records at these high mean wind speeds are significanly smaller that the the number of available records at mean wind speeds 8m/s and 12m/s, respectively.

Turning to the *tower top yaw equivalent moments*, the normalized results are shown in Figure 50 and Figure 51, respectively, for the *8m/s case*. Again discharging the L3-M1 case (16.9D) it characteristic for both measured and simulated results, that the interspacing dependence is significantly more pronounced for the tower top yaw moments than for the tower bottom bending moments. The simulations seems to underestimate the yaw equivalent moment with a factor of the order of 2, however, with the width of the response peak being of the same order of magnitude. The tripple peak character of the simulated response relates primary to WT interspacings in the range [4D; 5D]. For larger downstrean distances the 3 peaks merge into only one dominating peak. As the measurememts do not offer WT interspacings smaller than 6D, the one peak character of the measured response is consistent with the simulated results.

For the 12*m/s case* the normalized tower top yaw equivalent moments are shown in Figure 52 and Figure 53, respectively. Compared to the 8m/s case it is notable that the triple peak character of the (simulated) results for very small WT spacings (i.e. 4D and 5D) diminish significantly – in fact it almost dissapears. Again the interspacing dependence is significantly more pronounced for the tower top yaw moments than observed for the tower bottom bending moments and, as observed in 8m/s case, the simulations seems to underestimate the yaw equivalent moment with a factor of approximately 2. Qualitatively, the width of the response peak is of the same order of magnitude for measurements and simulations, respectively.

For the 16*m/s case* the normalized tower top yaw equivalent moments are shown in Figure 54 and Figure 55, respectively. The load levels of measured and simulated results still differs by a factor of approximately 2. In analogy with the tower bottom bending high wind case, very large scaller is observed among the measured single wake cases, which preventing more detailed comparisons between measured and simulated

results, and again part of the explanation may be that the relatively small number of available measured records at high mean wind speeds.

As the measured and simulated results seems consistently (i.e. independent of the mean wind speed) to differ by a factor of approximately 2, a possible explation might be the indirect (i.e. analytical – cf. equation 1)) used for the tower yaw moments, which is contrary to the direct calibration applied for the tower bottom bending moments.

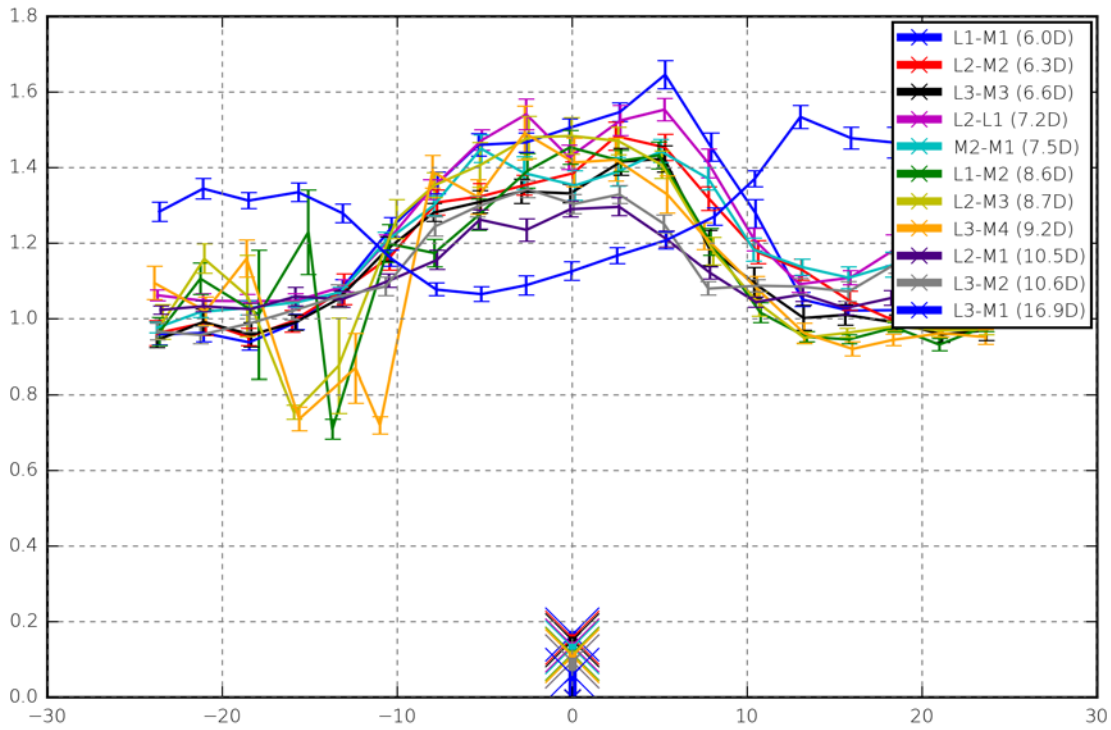

Figure 44: Measured tower bottom bending equivalent moment as function of inflow angle; m = 4; U = 8m/s.

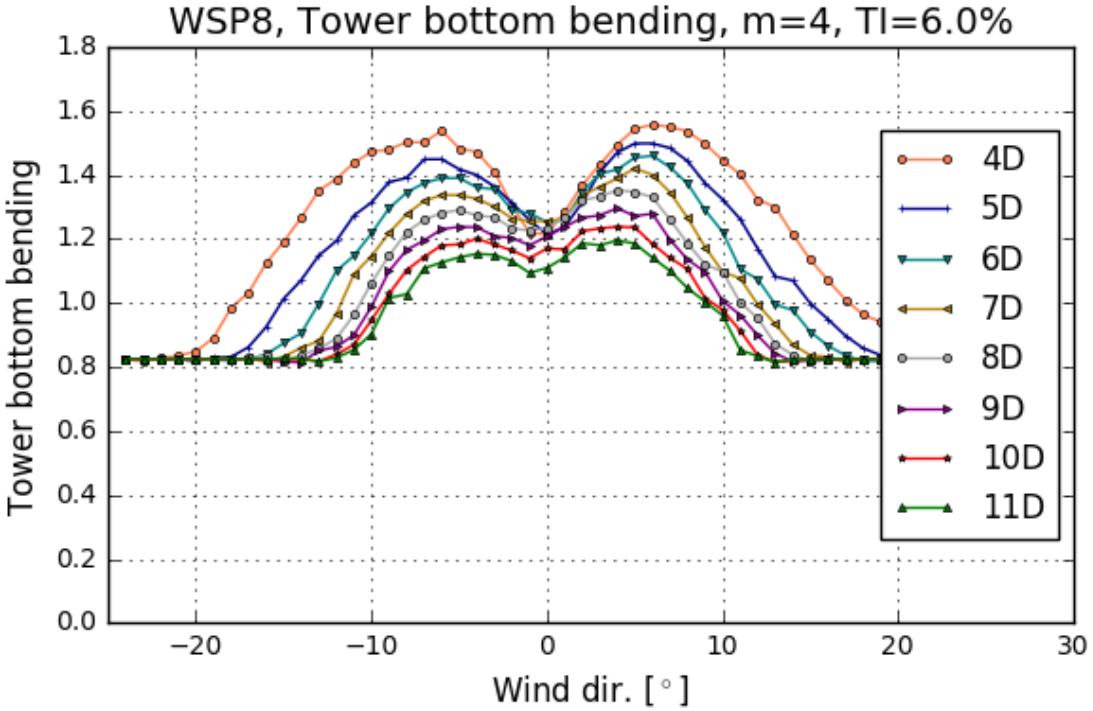

Figure 45: Simulated tower bottom bending equivalent moment as function of inflow angle; m = 4; U = 8m/s.

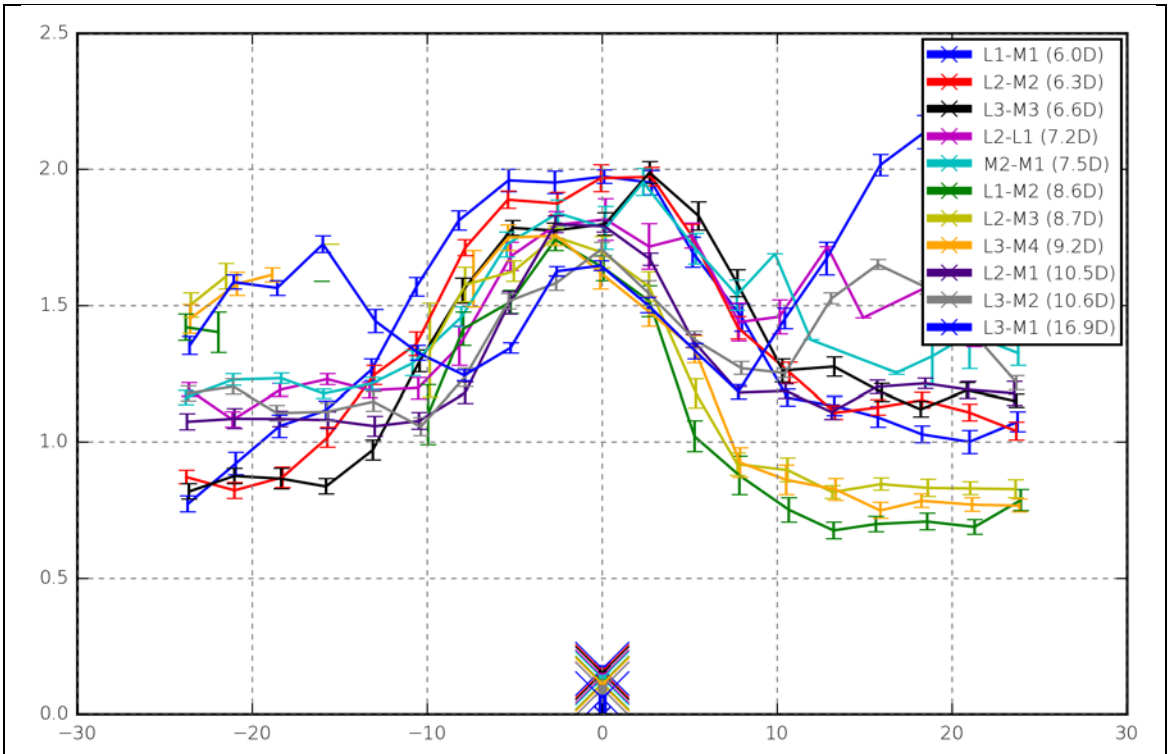

Figure 46: Measured tower bottom bending equivalent moment as function of inflow angle; m = 4; U = 12m/s.

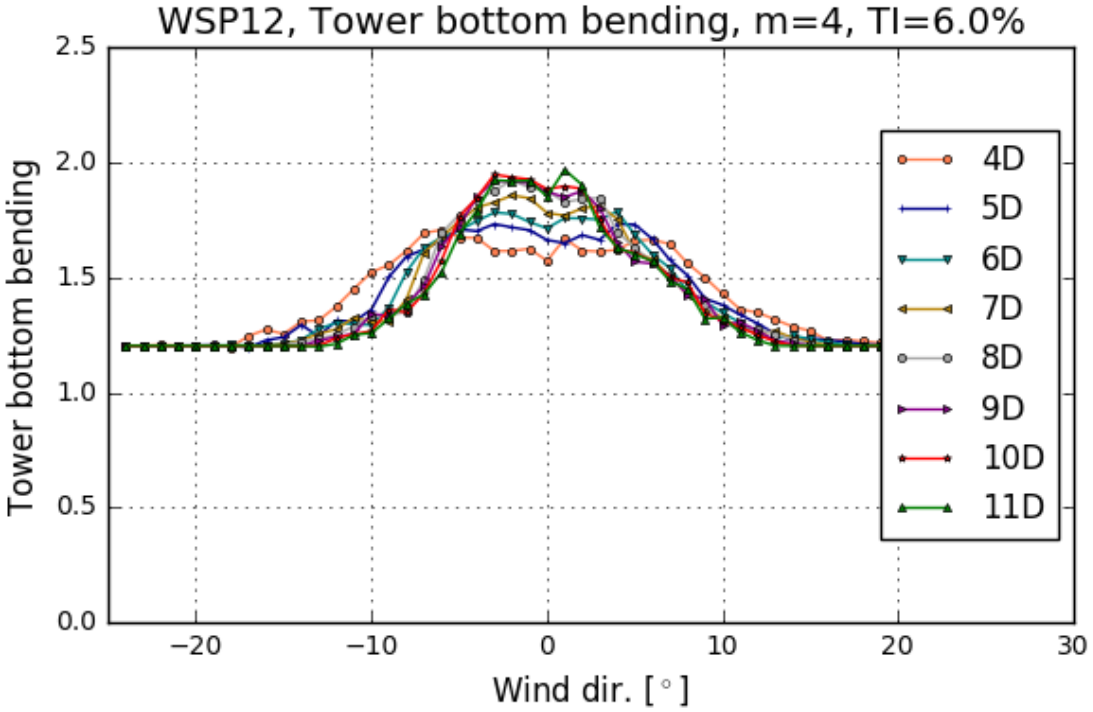

Figure 47: Simulated tower bottom bending equivalent moment as function of inflow angle; m = 4; U = 12m/s.

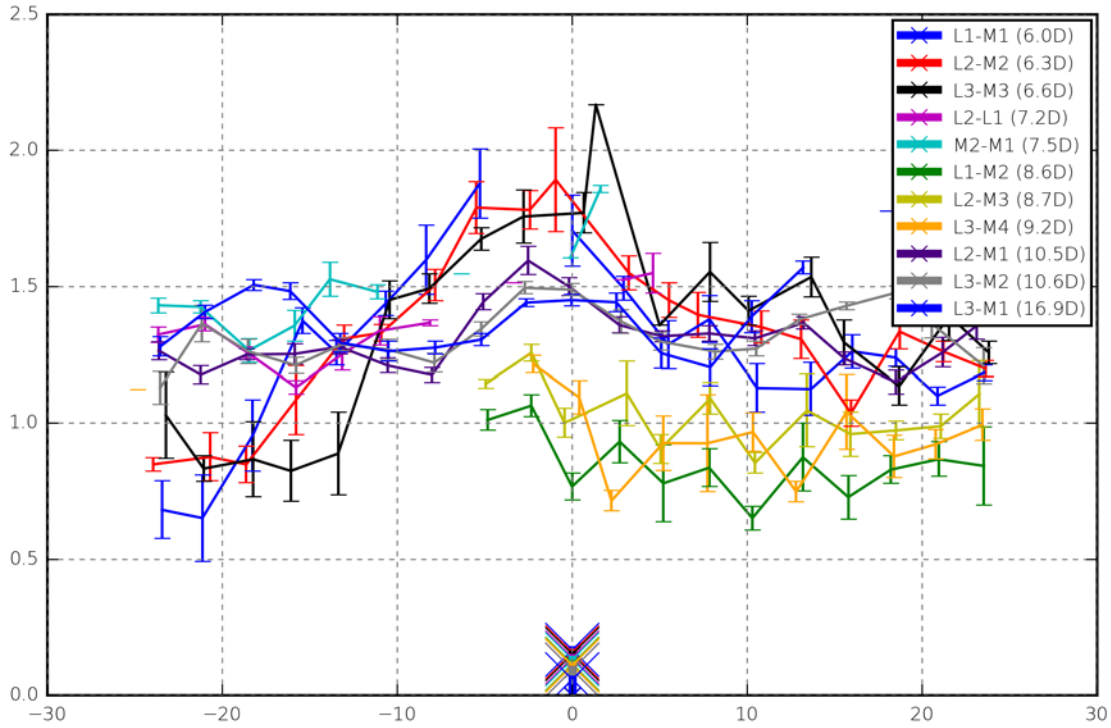

Figure 48: Measured tower bottom bending equivalent moment as function of inflow angle; m = 4; U = 16m/s.

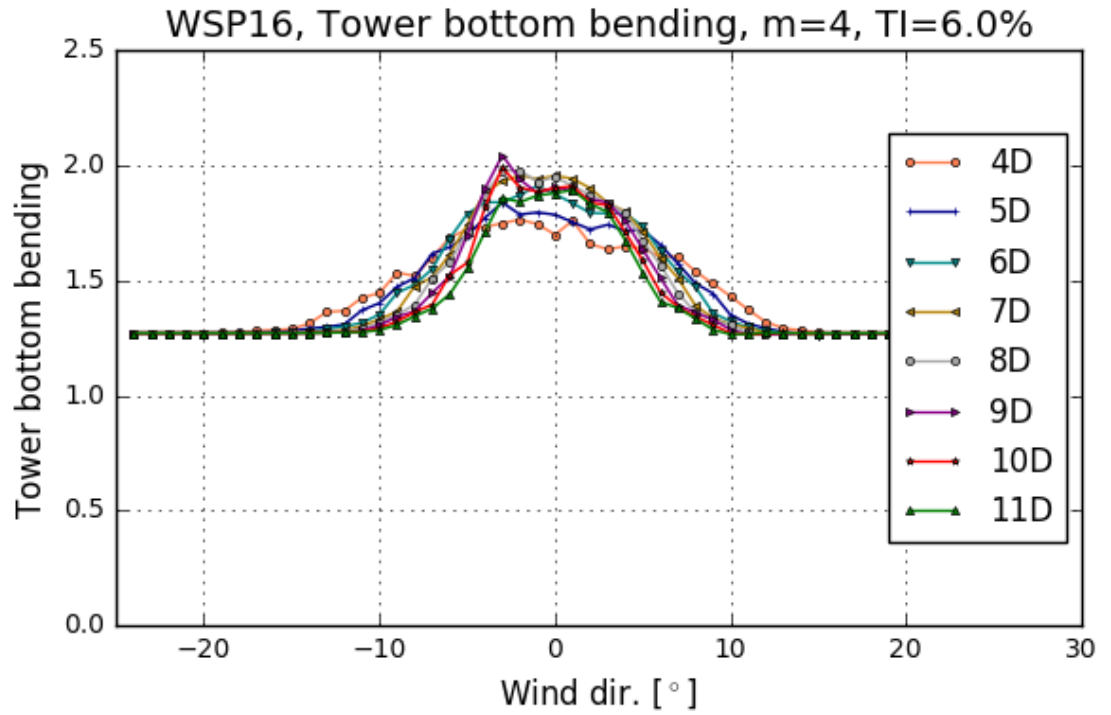

Figure 49: Simulated tower bottom bending equivalent moment as function of inflow angle; m = 4; U = 16m/s.

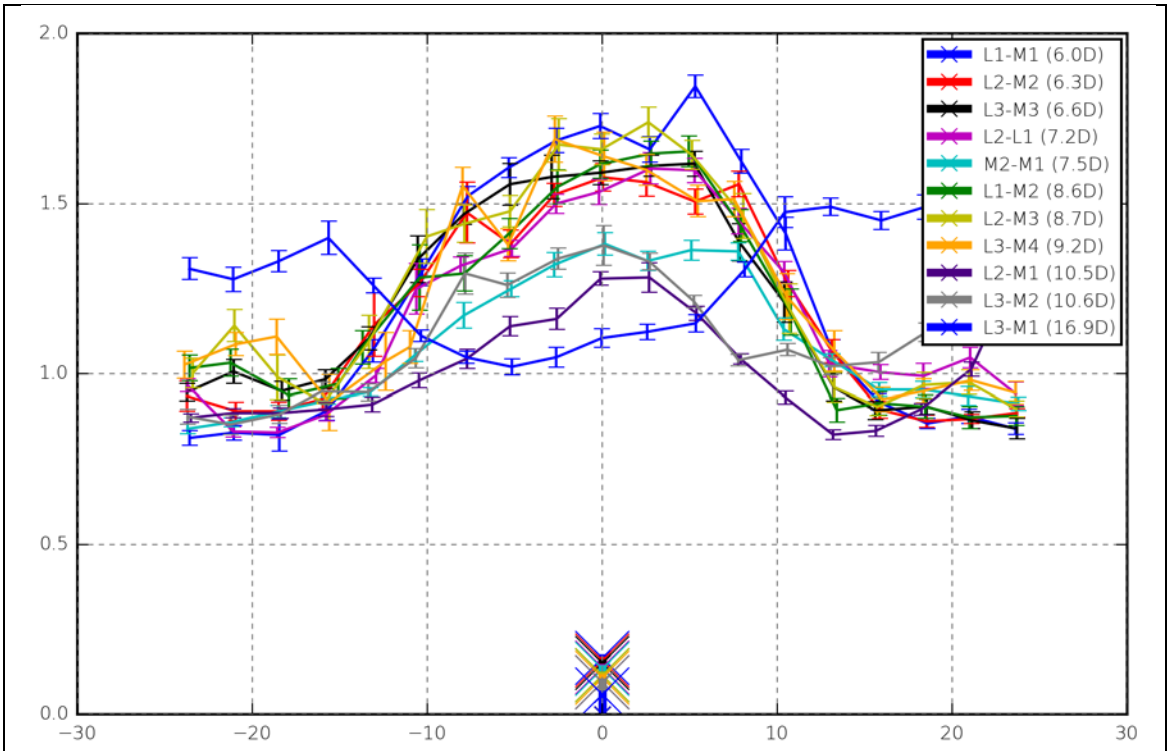

Figure 50: Measured tower top yaw equivalent moment as function of inflow angle; m = 7; U = 8m/s.

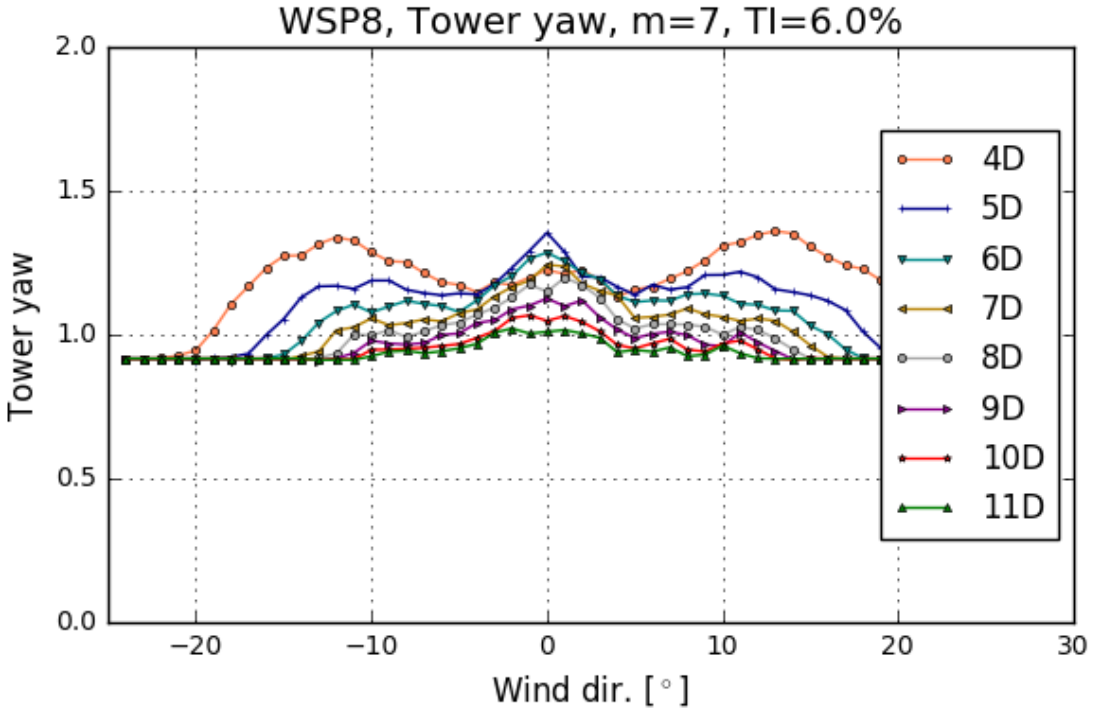

Figure 51: Simulated tower top yaw equivalent moment as function of inflow angle; m = 7; U = 8m/s.

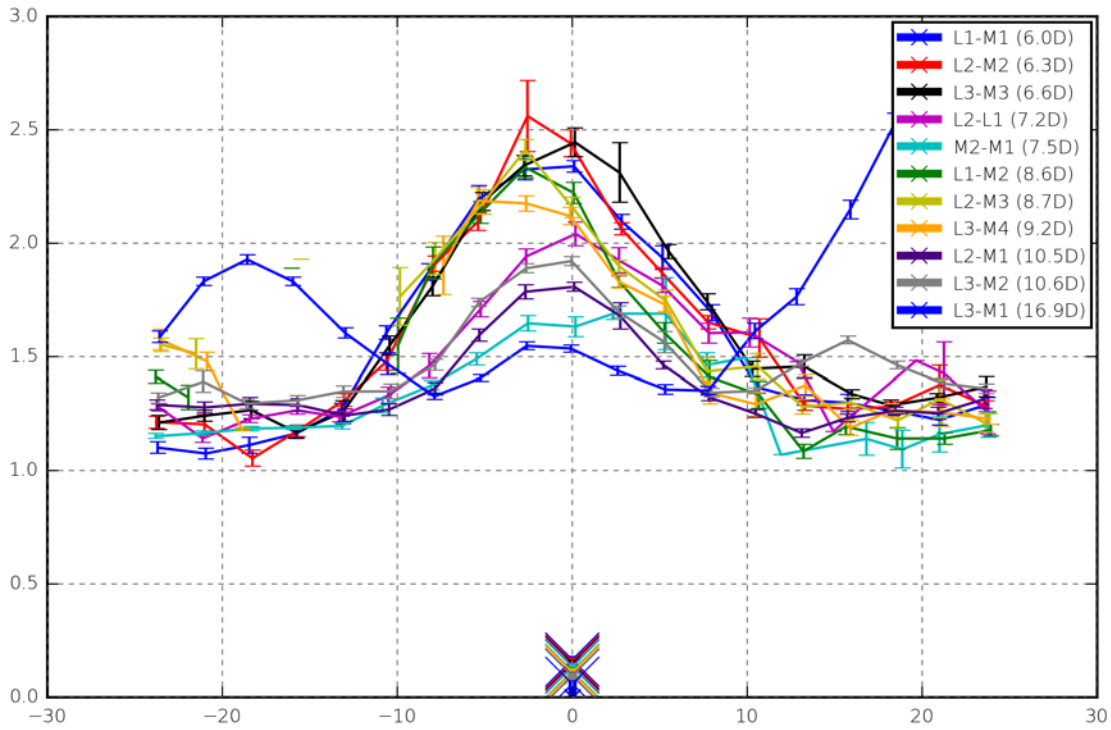

Figure 52: Measured tower top yaw equivalent moment as function of inflow angle; m = 7; U = 12m/s.

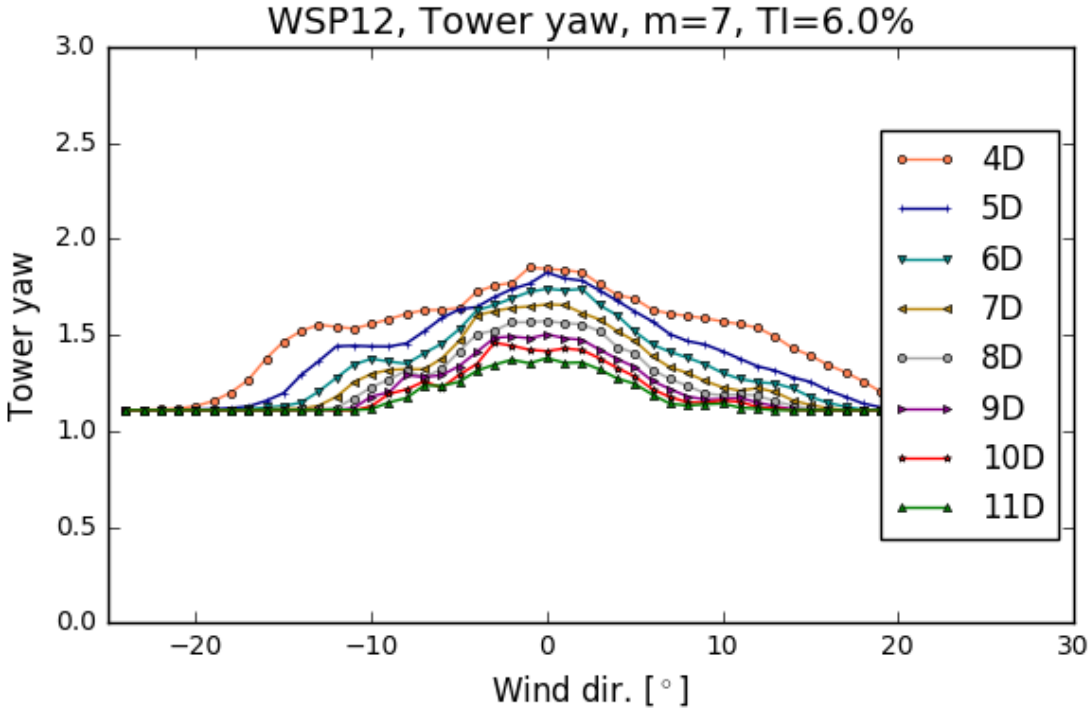

Figure 53: Simulated tower top yaw equivalent moment as function of inflow angle; m = 7; U = 12m/s.

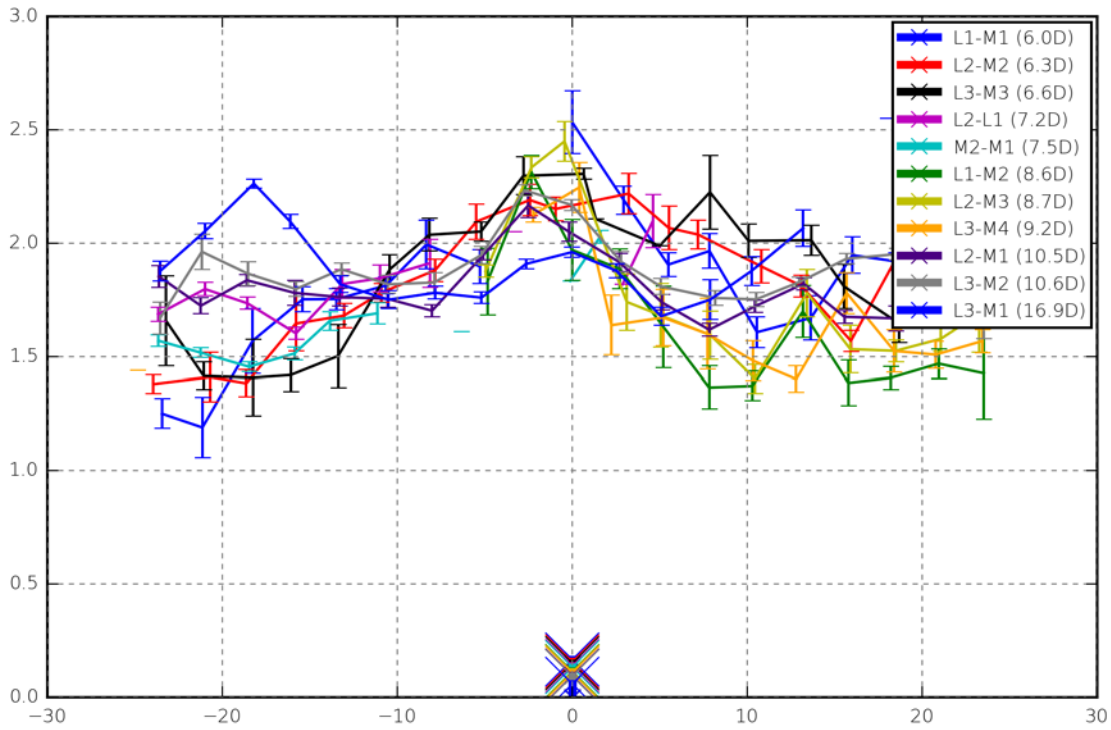

Figure 54: Measured tower top yaw equivalent moment as function of inflow angle; m = 7; U = 16m/s.

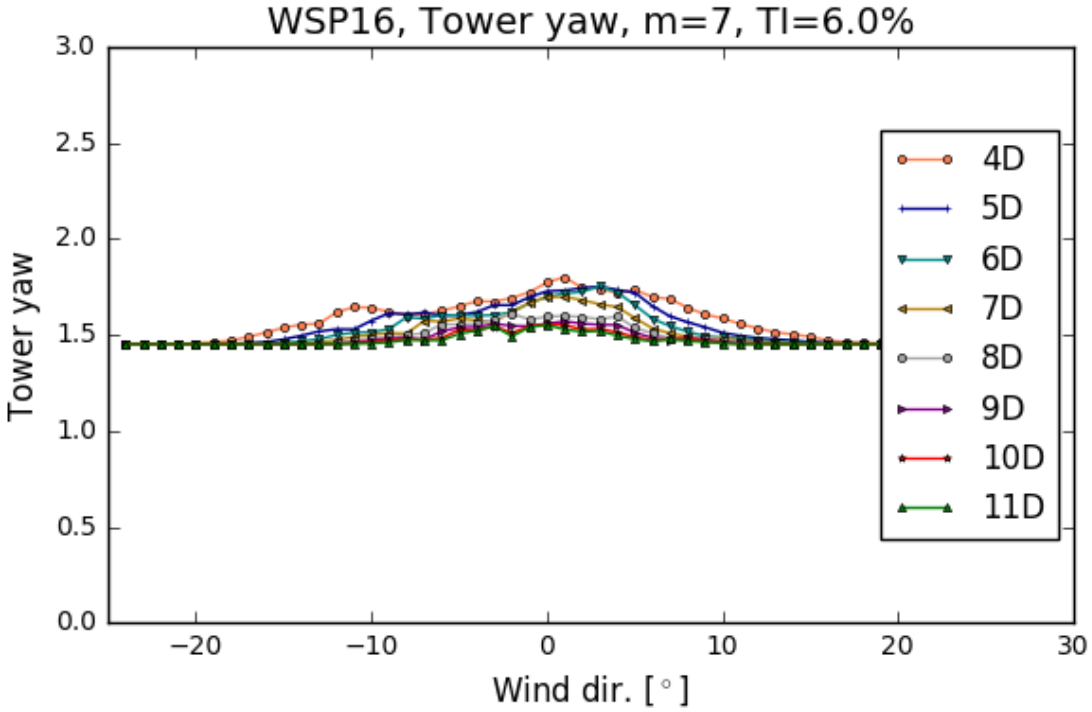

Figure 55: Simulated tower top yaw equivalent moment as function of inflow angle; m = 7; U = 16m/s.

4 .2 Tower full-wake peak loads

In the *full wake* situation a fatigue load peak was conjectured already in the project formulation phase. This section focuses on this phenomenon as well as the influence from ambient turbulence intensity on the downstream location of this possible full wake induced load peak.

As for the simulation results it was observed in Section 3.2, that the *tower bottom fatigue bending* equivalent moments, for the three investigated mean wind speed regimes, attain a maximum in the range of 7D – 8D downstream for the full wake case. This is illustrated for the 12m/s case in Figure 56 (cf. the green projection curve in the distance-load plane).

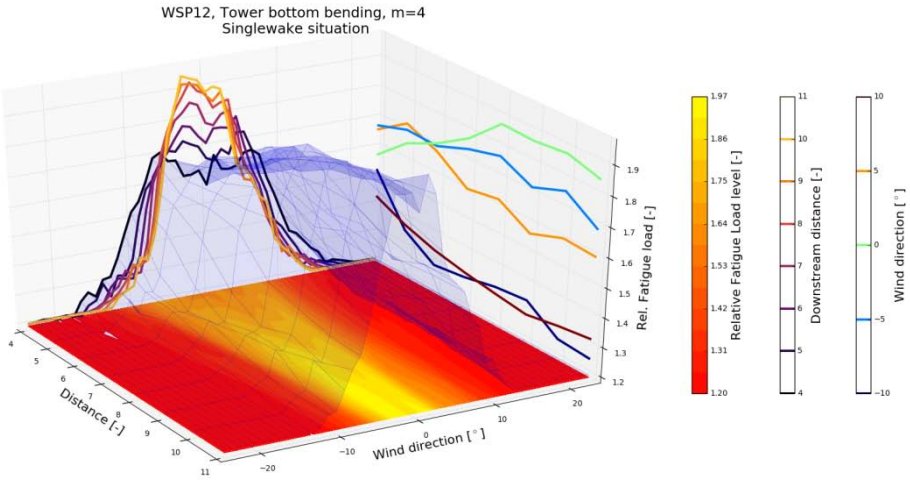

Figure 56: Tower bottom bending moments at 12m/s and 6% turbulence intensity. In the full wake situation the load level takes its maximum approximately 8D downstream.

In an attempt to capture the same phenomenon in the measured data these has been binned and subsequently averaged in a very narrow sector (i.e. +/- 1 deg.) around the full wake direction. The result is shown in Figure 57.

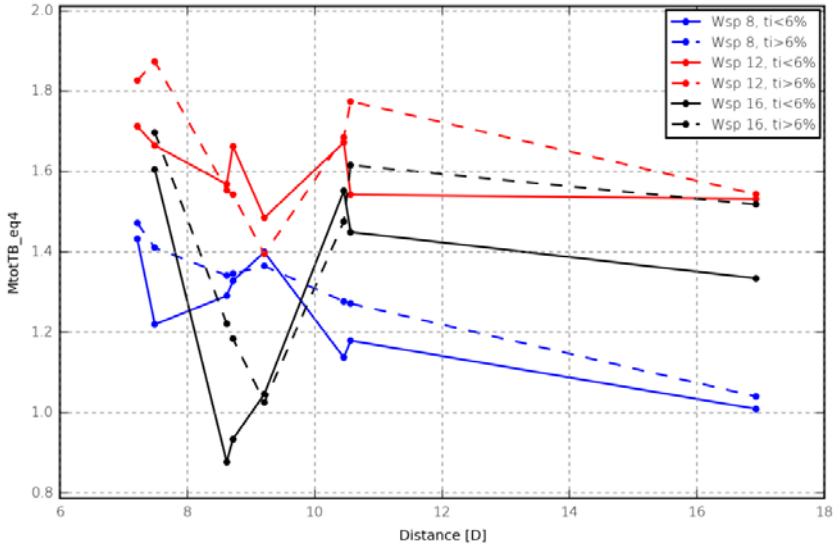

Figure 57: Full wake tower bottom bending moments for mean wind speed bins 8m/s, 12m/s and 16m/s. Results are split on turbulence intensity levels below and above 6%.

The load seems to peak around 7.75D downstream, but as the results are very scattered and as no results are available at smaller downstream distances than 7.5D, it is difficult to judge whether the peak identified at 7.75D is in fact really a peak.

Turning to the *tower top yaw* fatigue equivalent moment the sought peak can only be identified in the 8m/s case for ambient turbulence intensity equal to 6%. However, for less ambient turbulence intensity (i.e. 3%), the peak become visible for all investigated mean wind speed regimes – cf. Figure 29, Figure 32, and Figure 35, respectively. The peak identified for the 8m/s case (6% turbulence intensity) at 5D downstream is shown in Figure 58 (cf. the green projection curve in the distance-load plane).

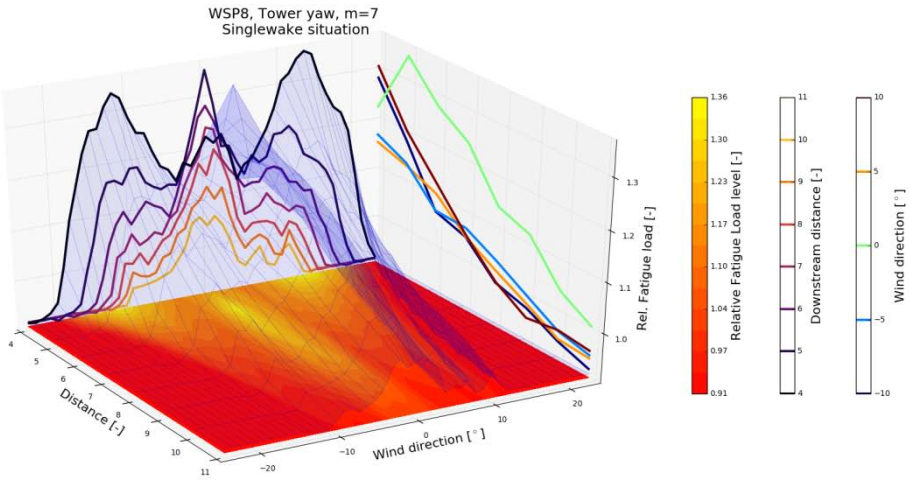

Figure 58: Tower top yaw moments at 8m/s and 6% turbulence intensity. In the full wake situation the load level takes its maximum at approximately 5D downstream.

The analog full-scale experimental results are shown in Figure 59.

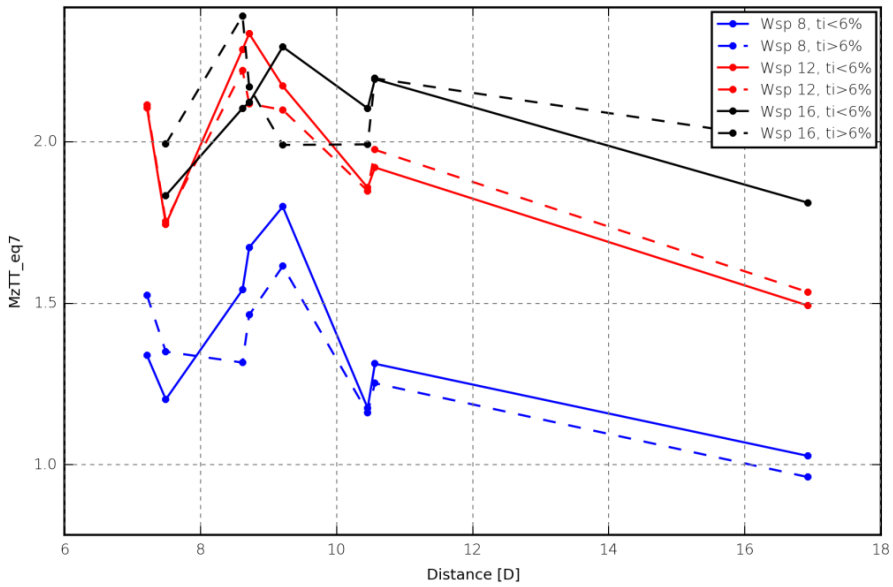

Figure 59: Full wake tower top yaw moments for mean wind speed bins 8m/s, 12m/s and 16m/s. Results are split on turbulence intensity levels below and above 6%.

Peaks in the *tower top yaw* fatigue equivalent moment can be identified in Figure 59 at downstream locations in the range 8D – 9D, and for the 16m/s case the location of the fatigue load peaks is seen to depend on the ambient turbulence level, with the peak associated with high turbulence intensity conditions (> 6%) being closer to the wake generating WT than the peak associated with low turbulence intensity conditions (< 6%) as expected. Despite this qualitative agreement with the simulated results, it should be noticed that the identified peaks in the measured data are located further downstream than predicted by the simulations – in fact closer to the downstream location predicted for the tower bottom fatigue equivalent bending moment, cf. Figure 56. The reason why turbulence intensity dependence of the peak location is only manifesting itself in the 16m/s case might be, that the difference between "< 6%" and "> 6%" turbulence intensities is particularly pronounced in this wind regime, but this is so far only speculations which will require a more detailed analysis to be validated.

5 Summary of project achievements

The project achievements can be summarized as follows:

- Six WT's located in the Nysted II WF have been instrumented with strain-gauge based measuring systems to resolve tower top and tower bottom moments;
- All recorded structural data have been organized in a database, which in addition contains relevant WT SCADA data as well as relevant meteorological data – as e.g. wind speed and wind direction – from an offshore mast located in the immediate vicinity of the wind farm. The database contains data from a period extending over a time span of more than 3 years;
- Based on the recorded data material basic mechanisms driving the increased loading experienced by WT's operating in offshore wind farm conditions has been identified, characterized and modeled. The modeling is based on the Dynamic Wake Meandering approach in combination with the state-of-the-art aeroelastic model HAWC2, and shown good agreement with the measurements. The a priory conjectured downstream peak in full wake WT loading cases has been indentified in both simulations and measurements. Further, generic WF studies combined with analyses of the Nysted II layout has revealed that (from a load perspective) it is recommended to avoid straight line topology layouts, at least if these lines is oriented along predominant wind directions. Finally, comparative load simulations based on the existing recommended practice in the IEC61400-1 ed. 4 standard [2] has been conducted, and it can be concluded that this approach is highly conservative for *single wake* situations, especially above rated wind speed.
- In a *separate report* the present design criteria for tower foundation loads has been reviewed. Based on analysis of the measurements as well as supporting aero-elastic Flex5 calculations this study indicates, that the wave conditions in the Nysted II area are moderate, and thus that the wave effect on the tower load is low. The conventional design criteria for the wave impact have consequently been too conservative in the Nysted II case.

6 List of publications, presentations and reports

[1] Larsen, G.C.; Larsen, T.J. and Madsen, H.Aa. (2013). Proceedings of the 2013 International Conference on aerodynamics of Offshore Wind Energy Systems and wakes (ICOWES2013). Technical University of Denmark, p. 450-459.

[2] Larsen, T.J.; Madsen, H.Aa.; Larsen, G.C. and Hansen, K.S. (2013). Validation of the dynamic wake meander model for loads and power production in the Egmond aan Zee wind farm. Wind Energy, Vol. 16, No. 4, p. 605-624.

[3] Larsen, T.J.; Larsen, G.C.; Madsen, H.Aa.; Thomsen, K. and Pedersen, S.M. (2015). Comparison of measured and simulated loads for the Siemens swt2.3 operating in wake conditions at the Lillgrund Wind Farm using HAWC2 and the dynamic wake meander model. Poster session presented at EWEA Offshore 2015 Conference, Copenhagen, Denmark.

[4] Larsen, T.J.; Larsen, G.C.; Madsen, H.Aa.; Petersen and Pedersen, S.M. 82015). Wake effects above rated wind speed. An overlooked contributor to high loads in wind farms. Scientific Proceedings. EWEA Annual Conference and Exhibition 2015. European Wind Energy Association (EWEA), p. 95-99.

[5] Larsen, G.C. (2013). Challenges in wind farm optimization. Invited presentation. International Conference on Future Technologies for Wind Energy, Laramie, Wyoming, United States.

[6] Jørgensen, L.B. and Helkjær, A. (2015). Tower loads affected by foundation loads. Technical Note, Grontmij A/S.

[7] Larsen, G.C.; Larsen, T.J.; Pedersen, M.M.; Enevoldsen, K. and Madsen, h.Aa. (2016). Wake affected offshore tower and foundation loads – project final report. Technical University of Denmark.

7 References

[1] Larsen, G.C.; Madsen, H.Aa.; Thomsen, K. and Larsen, T.J. (2008). Wake meandering - a pragmatic approach. Wind Energy, 11, pp. 377–395.

[2] IEC 61400-1 ed. 4. Wind turbines - part 1: design requirements.

[3] Larsen, T.J. and Hansen, A.M. (2007). How to HAWC2, the Users Manual, Risø-R-1597(EN), Risø National Laboratory - Technical University of Denmark.

[4] Shabana, A. (1998). *Dynamics of Multibody Systems*. Cambridge University Press: New York.

[5] Hansen, M.H.; Gaunaa, M. and Madsen H.Aa. (2004). A Beddoes-Leishman type dynamic stall model in state-space and indicial formulations. Risø-R-1354(EN), Risø National Laboratory.

[6] Leishman J. and Beddoes T. (1986). A generalized model for airfoil unsteady aerodynamic behavior and dynamic stall using the indicial method, Proceeding of the 42nd Annual Forum of the American Helicopter Society, Washington D.C., 243–265.

[7] Theodorsen T. (1935). General theory of aerodynamic instability and the mechanism of flutter. *NACA Report 435*, 413–433.

[8] Madsen, H.Aa.; Riziotis, V.; Zahle, F.; Hansen, M.; Snel, H.; Grasso. L.T.F.; Politis, E. and Rasmussen, F. (2011). BEM Blade element momentum modeling of inflow with shear in comparison with advanced model results. *Wind Energy*; **15**(1): 63–81.

[9] Mann, J. (1994). The spatial structure of neutral atmospheric surface-layer turbulence. J. Fluid Mech., vol. 273, p 141-168.

[10] Madsen, H.Aa.; Larsen, G.C.; Larsen, T.J.; and Troldborg, N. (2010). Calibration and Validation of the Dynamic Wake Meandering Model for Implementation in an Aeroelastic Code. J. Sol. Energy Eng., 132(4).

[11] Kaimal, J.C. and Finnigan, J.J. (1994). *Atmospheric Boundary layer Flows—Their Structure and measurement*. Oxford University Press.

[12] Larsen, T.J.; Madsen, H.Aa.; Larsen, G.C. and Hansen, K.S. (2013). Validation of the Dynamic Wake Meander Model for Loads and Power Production in the Egmond aan Zee Wind Farm. Wind Energy, Volume 16, pp. 605–624.

[13] Larsen, T.J.; Larsen, G.C.; Madsen, H.Aa.; Thomsen, K. and Petersen, S.M. (2015). Comparison of measured and simulated loads for the Siemens SWT 2.3 operating in wake conditions at the Lillgrund wind farm using HAWC2 and the Dynamic Wake Meander model. EWEA offshore 2015, Copenhagen 10 – 12 March 2015.

[14] Nilsson, K.; Ivanell S.; Hansen K.S.; Mikkelsen R.; Sørensen J.N.; Breton S.-P. and Henningson D. (2015). Large-eddy simulations of the Lillgrund wind farm, Wind Energy. 18, pages 449–467. doi: 10.1002/we.1707.

[15] Larsen, T.J.; Larsen, G.C.; Madsen, H.Aa.; Petersen and Pedersen, S.M. (2015). Wake effects above rated wind speed. An overlooked contributor to high loads in wind farms. Scientific Proceedings. EWEA Annual Conference and Exhibition 2015. European Wind Energy Association (EWEA), p. 95-99.

[16] Keck, R.-E. (2014). Validation of the standalone implementation of the dynamic wake meandering model for power production. Wind Energy. doi: 10.1002/we.1777.

[17] Love, A.E.H. (1927). *A treatise on the mathematical theory of elasticity*, Cambridge University Press. (Dover reprint ISBN 0-486-60174-9).

[18] Frandsen, S.T. (2005). Turbulence and turbulence-generated structural loading in wind turbine clusters. Technical Report Risø-R-1188(EN).

Appendix A – Yaw dependent calibration of wind turbine mounted strain-gauges

Statement of the problem

Depending on the particular design of a wind turbine (WT) yaw system, the stress conditions in a tower cross section close to the top may be very complex and inhomogeneous in the azimuthal direction. Therefore, strain gauges measuring tower top moments are, as a rule of thumb, advised *not* to be mounted closer to the tower top than one tower (top) diameter, which basically is a pragmatic application of Saint-Venant's Principle [17], stating that "*the difference between the effects of two different but statically equivalent loads becomes very small at sufficiently large distances from load*".

However, for practical reasons it is not always possible to mount tower top strain gauges at a sufficient distance from the tower top, and consequently strongly non-ideal calibration signals may result from the standard procedure, where the nacelle is slowly yawing under mean wind conditions close to zero and thus ideally resulting in a cosine variation in the strain gauge calibration signal. This calls for procedure to treat such calibration signals, and the present Appendix addresses this challenge.

Assumptions

We will assume that the strain gauge sensor is *linear*; i.e. that the physical signal, S_P, relates to the measured signal, S_M, as

$$S_P = GS_M + B \equiv G\left(S_M + B_G\right), \tag{1}$$

where G is the gain factor, whereas B and B_G denote bias terms.
In the case of azimuthal stress inhomogeneities of the character described above, we will allow gain as well as bias to be *azimuth dependent*, whereby eq. (1) degenerate to

$$S_P(\theta) = G(\theta)\left[S_M(\theta) + B_G(\theta)\right], \tag{2}$$

where Θ denotes the yaw angle. Based on the calibration layout we infer that the following symmetry relation holds

$$G(\theta) = G(\theta + \pi). \tag{3}$$

This relation is a direct consequence of requiring the gain to be independent of the sign of the externally imposed loading. Argued in terms of tower bending moment signals this is because the gravity loading applied at the yaw angle Θ equals minus the gravity loading applied at the yaw angle $\Theta+\pi$, assuming that the yaw system is approximately π-symmetric. From eq. (3) it particularly follows, that the two gain values corresponding to zero external moment loading are azimuthally displaced by π. The same is true for the two gain values corresponding to maximum and minimum external moment loading, respectively.

Approach

As mentioned the standard procedure for (offshore) tower bending moment calibration is to take advantage of the nacelle/rotor gravity loading imposed at the corresponding centre of gravity, which has an offset to the tower elastic axis. Let us assume that, due

to the centre of gravity offset, the resulting physical tower bending moment has the magnitude M_{max}. The yaw dependent *external loading*, $S_P(\Theta)$, is therefore given as

$$S_P(\theta) = M_{\max} Cos(\theta) + M_W(\theta), \tag{4}$$

where $M_W(\Theta)$ denotes the wind field driven part of the external loading. Assuming zero – or close to zero – wind speed conditions, the known external moment loading is expressed by

$$S_P(\theta) = M_{\max} Cos(\theta), \tag{5}$$

where the yaw angle, for simplicity and without restrictions, is assumed to have zero-point at the nacelle yaw-location imposing maximum moment at the moment sensor location.

The *measured* signal may, due to the "end effects", deviate significantly from the generic shape of the external loading expressed in eq. (5). However, the measured signal is at least 2π-periodic, which allow for a Fourier expansion of this signal as

$$S_M(\theta) = \sum_{i=0}^{N} a_i Cos(i\theta) + \sum_{i=1}^{N} b_i Sin(i\theta), \tag{6}$$

with the Fourier series truncated after $(2N+1)$ terms.

Introducing eqs. (5) and (6) in eq. (2) we obtain

$$M_{\max} Cos(\theta) = G(\theta)\left[\sum_{i=0}^{N} a_i Cos(i\theta) + \sum_{i=1}^{N} b_i Sin(i\theta) + B_G(\theta)\right]. \tag{7}$$

Noting the following symmetries and anti-symmetries

$$Cos(i\theta) = \begin{cases} Cos(i[\theta+\pi]) & \text{for } i \text{ even} \\ -Cos(i[\theta+\pi]) & \text{for } i \text{ odd} \end{cases} \tag{8}$$

and

$$Sin(i\theta) = \begin{cases} Sin(i[\theta+\pi]) & \text{for } i \text{ even} \\ -Sin(i[\theta+\pi]) & \text{for } i \text{ odd} \end{cases} \tag{9}$$

we split the Fourier expansion in symmetric and anti-symmetric terms, and rewrite eq. (7) as

$$M_{\max} Cos(\theta) = G(\theta)\left[\left(\sum_{\substack{i=1,\\ i\,\text{odd}}}^{N} a_i Cos(i\theta) + \sum_{\substack{i=1,\\ i\,\text{odd}}}^{N} b_i Sin(i\theta)\right) + \left(B_G(\theta) + a_0 + \sum_{\substack{i=2,\\ i\,\text{even}}}^{N} a_i Cos(i\theta) + \sum_{\substack{i=2,\\ i\,\text{even}}}^{N} b_i Sin(i\theta)\right)\right]. \tag{10}$$

To arrive at the requested symmetry condition for the gain factor expressed in eq. (3), the multiplication factor on $G(\Theta)$ on the right hand side of eq. (10) must possess the same type of symmetry as the left hand side of this equation. This can be achieved only by defining the bias as

$$B_G(\theta) = f(\theta) - a_0 - \sum_{\substack{i=2,\\ i\,\text{even}}}^{N} a_i Cos(i\theta) - \sum_{\substack{i=2,\\ i\,\text{even}}}^{N} b_i Sin(i\theta), \tag{11}$$

where $f(\Theta)$ is an arbitrary 2π-periodic function satisfying the symmetry condition $f(\Theta) = -f(\Theta+\pi)$.

For the present purpose it seems reasonable to choose the *smoothest possible* bias function; i.e. the bias function with the least possible gradient variability defined in terms of the following metric

$$\Pi = \int_0^{2\pi} \left[\frac{dB_G(\theta)}{d\theta} \right]^2 d\theta. \tag{12}$$

With this approach the bias will explain the *least possible part* of the deviation between measured (normalized) signal and the (normalized) physical signal. In case of no constraints, the bias function will be identical zero. Contrary to this approach, one could chose to let the bias function explain the *largest possible part* of the deviation between measured (normalized) signal and the (normalized) physical signal. Using eq.'s (5) and (6), the deviation between the (normalized) measured and the (normalized) physical signal is given by

$$\Delta(\theta) = Cos(\theta) - \sum_{i=0}^{N} a_i Cos(i\theta) - \sum_{i=1}^{N} b_i Sin(i\theta). \tag{13}$$

Requiring the bias function to approach Δ as close as possible is obtained by finding the stationary points of the functional

$$\begin{aligned}
\Pi &= \int_0^{2\pi} \left[\Delta(\theta) - B_G(\theta) \right]^2 d\theta \\
&= \int_0^{2\pi} \left[Cos(\theta) - \sum_{i=0}^{N} a_i Cos(i\theta) - \sum_{i=1}^{N} b_i Sin(i\theta) - f(\theta) + a_0 + \sum_{\substack{i=2, \\ i\,\text{even}}}^{N} a_i Cos(i\theta) + \sum_{\substack{i=2, \\ i\,\text{even}}}^{N} b_i Sin(i\theta) \right]^2 d\theta \\
&= \int_0^{2\pi} \left[Cos(\theta) - \sum_{i=1}^{N} a_i Cos(i\theta) - \sum_{i=1}^{N} b_i Sin(i\theta) - f(\theta) + \sum_{\substack{i=2, \\ i\,\text{even}}}^{N} a_i Cos(i\theta) + \sum_{\substack{i=2, \\ i\,\text{even}}}^{N} b_i Sin(i\theta) \right]^2 d\theta \\
&= \int_0^{2\pi} \left[(1-a_1) Cos(\theta) - \sum_{\substack{i=3 \\ i\,odd}}^{N} a_i Cos(i\theta) - \sum_{\substack{i=1 \\ i\,odd}}^{N} b_i Sin(i\theta) - f(\theta) \right]^2 d\theta \\
&= \int_0^{2\pi} \left[(1-a_1) Cos(\theta) - \sum_{\substack{i=3 \\ i\,odd}}^{N} a_i Cos(i\theta) - \sum_{\substack{i=1 \\ i\,odd}}^{N} b_i Sin(i\theta) - \sum_{\substack{i=1, \\ i\,\text{odd}}}^{\tilde{N}} \tilde{a}_i Cos(i\theta) - \sum_{\substack{i=1, \\ i\,\text{odd}}}^{\tilde{N}} \tilde{b}_i Sin(i\theta) \right]^2 d\theta \\
&= \pi \left[(1-a_1)^2 + \sum_{\substack{i=3 \\ i\,odd}}^{N} a_i^2 + \sum_{\substack{i=1 \\ i\,odd}}^{N} b_i^2 + \sum_{\substack{i=1, \\ i\,\text{odd}}}^{\tilde{N}} \tilde{a}_i^2 + \sum_{\substack{i=1, \\ i\,\text{odd}}}^{\tilde{N}} \tilde{b}_i^2 - 2(1-a_1)\tilde{a}_1 + 2 \sum_{\substack{i=3, \\ i\,\text{odd}}}^{N_{\min}} a_i \tilde{a}_i + 2 \sum_{\substack{i=1, \\ i\,\text{odd}}}^{N_{\min}} b_i \tilde{b}_i \right],
\end{aligned} \tag{14}$$

with $N_{\min}$ denoting $min(N, \tilde{N})$, and $min(\bullet)$ being the minimum operator.

However, basically we do *not* know a priori how much of the "generic" deviation from the ideal signal is attributed to gain and how much is due to bias! In the following analysis we will (arbitrarily) adopt the approach expressed in eq. (12).

To proceed, we will require that the zero-crossings[1] of ($S_M(\Theta) + B_G(\Theta)$) is phase shifted $\pi/2$ to the extremes of ($S_M(\Theta) + B_G(\Theta)$) to ensure that the sign (and thus in turn also the magnitudes) of the measured moment is correct for *arbitrary* physical moment amplitudes. In mathematical terms, this condition can be formulated as

$$S_M\left(\theta_e + \frac{\pi}{2}\right) + B_G\left(\theta_e + \frac{\pi}{2}\right) = 0 \tag{15}$$

and

$$\frac{d}{d\theta}\left[S_M(\theta) + B_G(\theta)\right]_{\theta=\theta_e} = 0, \tag{16}$$

where Θ_e, as seen from eq. (16), is a point where ($S_M(\Theta) + B_G(\Theta)$) takes an extreme value. It follows from the mathematical structure of the problem (i.e. the imposed symmetry condition on $G(\Theta)$), that Θ_e can be any point, where ($S_M(\Theta) + B_G(\Theta)$) takes an extreme value.

Now, from eq. (11) it is clear that determination of Θ_e requires knowledge to $f(\Theta)$, which is to be based on the constraints defined by eq.'s (12 and 15-16). Therefore the determination of $f(\Theta)$ in principle calls for an iterative procedure. However, from studies of measured signals, $S_M(\varphi)$ with φ being the yaw coordinate expressed in a sensor specific frame of reference, it has been observed that the extremes of such are with good approximation phase shifted with π. This is illustrated in Figure A1.

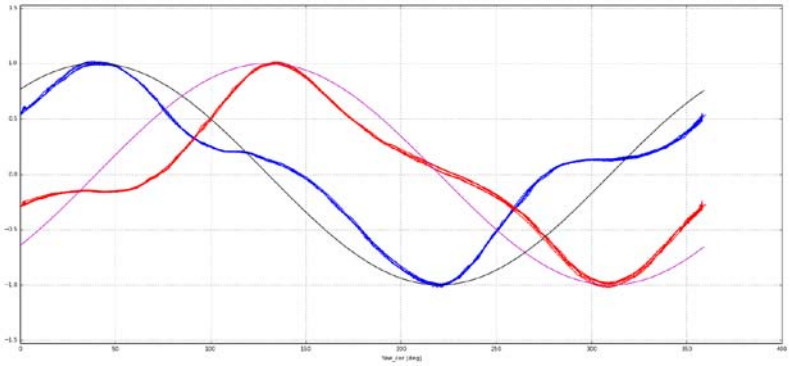

Figure A1: Measured bending moments along two perpendicular directions.

Therefore, we will attempt a first order approximation, in which Θ_e upfront is approximated based on the extremes of the measured signals $S_M(\varphi)$. To reduce uncertainty in this approximation we will define φ_e as

$$\varphi_e = \frac{\varphi_{e1} + \varphi_{e2} - \pi}{2}, \tag{17}$$

[1] Note, that we here, without consequences for the generality of the approach, implicitly assume that the measured calibration signal has been pre-scaled to range between -x and x, which is consistent with eq. 3 and its motivation. In practice x is chosen as x = 1. Denoting the yaw independent gain and bias scaling factors as G_S and B_S, respectively, the total yaw-dependent calibration of the sensor output, $S_M(\Theta)$, is thus given by
$S_P = [G_S G(\Theta)]S_M(\Theta) - [G(\Theta)B_G(\Theta) + G_S B_S G(\Theta)]$.

where φ_{e1} and φ_{e2} denote φ-values where respectively the maximum and the minimum of $S_M(\varphi)$ is taken. It should be noted, that the conditions expressed in eq.'s (15-16) in principle also could be formulated based on a zero point, Θ_0, of $(S_M(\Theta) + B_G(\Theta))$ where $S_M(\Theta_0) + B_G(\Theta_0) = 0$. However, this choice would prohibit the simple approximation introduced above, as measured zero crossings are experienced to be far from phase shifted by π. With φ_e determined from eq. (17), we are now able to relate respectively the *sensor specific* frame of reference and the *model* frame of reference by the following transformation

$$\theta = \varphi - \varphi_e \,, \tag{18}$$

from which it follows that Θ_e conveniently may be chosen as $\Theta_e = 0$, which is consistent with the remark following eq. (5).

To proceed we note that, considering the imposed symmetry condition on $f(\Theta)$, the Fourier expansion of $f(\Theta)$ can be written as

$$f(\theta) = \sum_{\substack{i=1,\\ i\,\mathrm{odd}}}^{\infty} \tilde{a}_i Cos(i\theta) + \sum_{\substack{i=1,\\ i\,\mathrm{odd}}}^{\infty} \tilde{b}_i Sin(i\theta). \tag{19}$$

Introducing eq. (19) into eq. (11), we obtain

$$B_G(\theta) = \sum_{\substack{i=1,\\ i\,\mathrm{odd}}}^{\infty} \tilde{a}_i Cos(i\theta) + \sum_{\substack{i=1,\\ i\,\mathrm{odd}}}^{\infty} \tilde{b}_i Sin(i\theta) - a_0 - \sum_{\substack{i=2,\\ i\,\mathrm{even}}}^{N} a_i Cos(i\theta) - \sum_{\substack{i=2,\\ i\,\mathrm{even}}}^{N} b_i Sin(i\theta), \tag{20}$$

whereby the gradient is given by

$$\frac{dB_G(\theta)}{d\theta} = -\sum_{\substack{i=1,\\ i\,\mathrm{odd}}}^{\infty} i\tilde{a}_i Sin(i\theta) + \sum_{\substack{i=1,\\ i\,\mathrm{odd}}}^{\infty} i\tilde{b}_i Cos(i\theta) + \sum_{\substack{i=2,\\ i\,\mathrm{even}}}^{N} i a_i Sin(i\theta) - \sum_{\substack{i=2,\\ i\,\mathrm{even}}}^{N} i b_i Cos(i\theta). \tag{21}$$

and the (selected) metric Π in turn given by

$$\Pi = \pi \left[\sum_{\substack{i=1,\\ i\,\mathrm{odd}}}^{\infty} i^2 \tilde{a}_i^2 + \sum_{\substack{i=1,\\ i\,\mathrm{odd}}}^{\infty} i^2 \tilde{b}_i^2 + \sum_{\substack{i=2,\\ i\,\mathrm{even}}}^{N} i^2 a_i^2 + \sum_{\substack{i=2,\\ i\,\mathrm{even}}}^{N} i^2 b_i^2 \right], \tag{22}$$

where it has been utilized that the Fourier expansion basis forms a complete orthogonal system. By truncating the Fourier expansion of $f(\Theta)$, eq. (22) is reduced to

$$\Pi = \pi \left[\sum_{\substack{i=1,\\ i\,\mathrm{odd}}}^{\tilde{N}} i^2 \tilde{a}_i^2 + \sum_{\substack{i=1,\\ i\,\mathrm{odd}}}^{\tilde{N}} i^2 \tilde{b}_i^2 + \sum_{\substack{i=2,\\ i\,\mathrm{even}}}^{N} i^2 a_i^2 + \sum_{\substack{i=2,\\ i\,\mathrm{even}}}^{N} i^2 b_i^2 \right], \tag{23}$$

and the sought Fourier coefficients, defining the requested $f(\Theta)$, is then in turn determined from minimizing the metric Π under the constraints expressed in eq.'s (15) and (16). The constraints are accounted for by introducing two Lagrange multipliers, λ_1 and λ_2, which results in the following modified metric

$$\tilde{\Pi} = \pi\left[\sum_{\substack{i=1,\\ i\,\mathrm{odd}}}^{\tilde{N}} i^2\tilde{a}_i^2 + \sum_{\substack{i=1,\\ i\,\mathrm{odd}}}^{\tilde{N}} i^2\tilde{b}_i^2 + \sum_{\substack{i=2,\\ i\,\mathrm{even}}}^{N} i^2 a_i^2 + \sum_{\substack{i=2,\\ i\,\mathrm{even}}}^{N} i b_i^2\right] +$$
$$\lambda_1\left[\sum_{\substack{i=1,\\ i\,\mathrm{odd}}}^{N} a_i Cos\left(i\theta_e + \frac{i\pi}{2}\right) + \sum_{\substack{i=1,\\ i\,\mathrm{odd}}}^{N} b_i Sin\left(i\theta_e + \frac{i\pi}{2}\right) + \sum_{\substack{i=1,\\ i\,\mathrm{odd}}}^{\tilde{N}} \tilde{a}_i Cos\left(i\theta_e + \frac{i\pi}{2}\right) + \sum_{\substack{i=1,\\ i\,\mathrm{odd}}}^{\tilde{N}} \tilde{b}_i Sin\left(i\theta_e + \frac{i\pi}{2}\right)\right] +$$
$$\lambda_2\left[-\sum_{\substack{i=1,\\ i\,\mathrm{odd}}}^{N} i a_i Sin(i\theta_e) + \sum_{\substack{i=1,\\ i\,\mathrm{odd}}}^{N} i b_i Cos(i\theta_e) - \sum_{\substack{i=1,\\ i\,\mathrm{odd}}}^{\tilde{N}} i\tilde{a}_i Sin(i\theta_e) + \sum_{\substack{i=1,\\ i\,\mathrm{odd}}}^{\tilde{N}} i\tilde{b}_i Cos(i\theta_e)\right]. \tag{24}$$

Minimizing this metric with respect to the unknown parameters (i.e. Lagrange multipliers and the Fourier expansion coefficients of $f(\Theta)$) results in the following linear system of equations

$$\begin{cases} \dfrac{\partial\tilde{\Pi}}{\partial\tilde{a}_{2i+1}} = 0\ ;\ i = 0,\ldots,\dfrac{\tilde{N}-1}{2} \\ \dfrac{\partial\tilde{\Pi}}{\partial\tilde{b}_{2i+1}} = 0\ ;\ i = 0,\ldots,\dfrac{\tilde{N}-1}{2} \\ \dfrac{\partial\tilde{\Pi}}{\partial\lambda_1} = 0 \\ \dfrac{\partial\tilde{\Pi}}{\partial\lambda_2} = 0 \end{cases} \tag{25}$$

the solution of which, through eq.'s (11) and (19), uniquely defines the yaw dependent bias $B_G(\Theta)$.

The sought gain factor is thus finally defined by

$$G(\theta) = M_{\max} Cos(\theta)\left(\sum_{\substack{i=1,\\ i\,\mathrm{odd}}}^{N} a_i Cos(i\theta) + \sum_{\substack{i=1,\\ i\,\mathrm{odd}}}^{N} b_i Sin(i\theta) + f(\theta)\right)^{-1}$$
$$= M_{\max} Cos(\theta)\left(\sum_{\substack{i=1,\\ i\,\mathrm{odd}}}^{N} a_i Cos(i\theta) + \sum_{\substack{i=1,\\ i\,\mathrm{odd}}}^{N} b_i Sin(i\theta) + \sum_{\substack{i=1,\\ i\,\mathrm{odd}}}^{\tilde{N}} \tilde{a}_i Cos(i\theta) + \sum_{\substack{i=1,\\ i\,\mathrm{odd}}}^{\tilde{N}} \tilde{b}_i Sin(i\theta)\right)^{-1}. \tag{26}$$

We note that the denominator in eq. (26) is zero where the physical moment is zero, and the gain factor thus in principle undetermined, where the imposed physical moment is zero. For the particular such two moment directions, that cannot be resolved by a channel sensor setup, we will, without any restrictions, define the gain as equal to zero.

Some calibration signals may suffer from being very "flat" (i.e. close to zero derivative with respect to the yaw angle) around zero crossings, basically meaning that there is very little information in the signal in such regimes. To understand this, imagine the zero-information case defined by a completely flat calibration signal over the entire yaw-domain. We will attempt to compensate this by letting the bias function "destroy"/"distort" this flatness by requiring that the *absolute value* of the yaw gradient

at zero crossings of ($S_M(\Theta)$ + $B_G(\Theta)$) to equal 1× ($S_M(\Theta_e)$ + $B_G(\Theta_e)$) – i.e. to force the signal to have the same gradient at such zero points as the ideal harmonic cosine signal with an identical amplitude. This can be accomplished by introducing an additional Lagrange multiplier, λ_3, in the functional defined by eq. (24). Knowing that Θ_e is associated with a positive extreme value, the condition to be fulfilled is

$$\frac{d}{d\theta}\left[S_M(\theta)+B_G(\theta)\right]_{\theta=\theta_e-\pi/2}=S_M(\theta_e)+B_G(\theta_e). \tag{27}$$

Due to the anti-symmetry properties of $B_G(\Theta)$ it is clear that not only the zero-crossing at $\Theta_{e-\pi/2}$ but also the zero-crossing at $\Theta_{e+\pi/2}$ will be affected by imposing the constraint defined in eq. (27).

Introducing eq.'s (6) and (20) in to eq. (27) we obtain

$$\begin{aligned}&-\sum_{\substack{i=1,\\ i\,\mathrm{odd}}}^{N} i a_i Sin\left(i\theta_e-\frac{i\pi}{2}\right)+\sum_{\substack{i=1,\\ i\,\mathrm{odd}}}^{N} i b_i Cos\left(i\theta_e-\frac{i\pi}{2}\right)-\sum_{\substack{i=1,\\ i\,\mathrm{odd}}}^{\tilde{N}} i\tilde{a}_i Sin\left(i\theta_e-\frac{i\pi}{2}\right)+\sum_{\substack{i=1,\\ i\,\mathrm{odd}}}^{\tilde{N}} i\tilde{b}_i Cos\left(i\theta_e-\frac{i\pi}{2}\right)=\\ &\sum_{\substack{i=1,\\ i\,\mathrm{odd}}}^{N} a_i Cos(i\theta_e)+\sum_{\substack{i=1,\\ i\,\mathrm{odd}}}^{N} b_i Sin(i\theta_e)+\sum_{\substack{i=1,\\ i\,\mathrm{odd}}}^{\tilde{N}} \tilde{a}_i Cos(i\theta_e)+\sum_{\substack{i=1,\\ i\,\mathrm{odd}}}^{\tilde{N}} \tilde{b}_i Sin(i\theta_e)\end{aligned} \tag{28}$$

or

$$\begin{aligned}&-\sum_{\substack{i=1,\\ i\,\mathrm{odd}}}^{N} i a_i Sin\left(i\theta_e-\frac{i\pi}{2}\right)+\sum_{\substack{i=1,\\ i\,\mathrm{odd}}}^{N} i b_i Cos\left(i\theta_e-\frac{i\pi}{2}\right)-\sum_{\substack{i=1,\\ i\,\mathrm{odd}}}^{\tilde{N}} i\tilde{a}_i Sin\left(i\theta_e-\frac{i\pi}{2}\right)+\sum_{\substack{i=1,\\ i\,\mathrm{odd}}}^{\tilde{N}} i\tilde{b}_i Cos\left(i\theta_e-\frac{i\pi}{2}\right)\\ &-\sum_{\substack{i=1,\\ i\,\mathrm{odd}}}^{N} a_i Cos(i\theta_e)-\sum_{\substack{i=1,\\ i\,\mathrm{odd}}}^{N} b_i Sin(i\theta_e)-\sum_{\substack{i=1,\\ i\,\mathrm{odd}}}^{\tilde{N}} \tilde{a}_i Cos(i\theta_e)-\sum_{\substack{i=1,\\ i\,\mathrm{odd}}}^{\tilde{N}} \tilde{b}_i Sin(i\theta_e)=0.\end{aligned} \tag{29}$$

whereby the following generalized metric results

$$\begin{aligned}\hat{\Pi}=&\frac{1}{2}\left[\sum_{\substack{i=1,\\ i\,\mathrm{odd}}}^{\tilde{N}} i^2\tilde{a}_i^2+\sum_{\substack{i=1,\\ i\,\mathrm{odd}}}^{\tilde{N}} i^2\tilde{b}_i^2+\sum_{\substack{i=2,\\ i\,\mathrm{even}}}^{N} i^2 a_i^2+\sum_{\substack{i=2,\\ i\,\mathrm{even}}}^{N} i b_i^2\right]+\\ &\lambda_1\left[\sum_{\substack{i=1,\\ i\,\mathrm{odd}}}^{N} a_i Cos\left(i\theta_e+\frac{i\pi}{2}\right)+\sum_{\substack{i=1,\\ i\,\mathrm{odd}}}^{N} b_i Sin\left(i\theta_e+\frac{i\pi}{2}\right)+\sum_{\substack{i=1,\\ i\,\mathrm{odd}}}^{\tilde{N}} \tilde{a}_i Cos\left(i\theta_e+\frac{i\pi}{2}\right)+\sum_{\substack{i=1,\\ i\,\mathrm{odd}}}^{\tilde{N}} \tilde{b}_i Sin\left(i\theta_e+\frac{i\pi}{2}\right)\right]+\\ &\lambda_2\left[-\sum_{\substack{i=1,\\ i\,\mathrm{odd}}}^{N} i a_i Sin(i\theta_e)+\sum_{\substack{i=1,\\ i\,\mathrm{odd}}}^{N} i b_i Cos(i\theta_e)-\sum_{\substack{i=1,\\ i\,\mathrm{odd}}}^{\tilde{N}} i\tilde{a}_i Sin(i\theta_e)+\sum_{\substack{i=1,\\ i\,\mathrm{odd}}}^{\tilde{N}} i\tilde{b}_i Cos(i\theta_e)\right]+\\ &\lambda_3\left[\begin{array}{l}-\sum_{\substack{i=1,\\ i\,\mathrm{odd}}}^{N} i a_i Sin\left(i\theta_e-\frac{i\pi}{2}\right)+\sum_{\substack{i=1,\\ i\,\mathrm{odd}}}^{N} i b_i Cos\left(i\theta_e-\frac{i\pi}{2}\right)-\sum_{\substack{i=1,\\ i\,\mathrm{odd}}}^{\tilde{N}} i\tilde{a}_i Sin\left(i\theta_e-\frac{i\pi}{2}\right)+\sum_{\substack{i=1,\\ i\,\mathrm{odd}}}^{\tilde{N}} i\tilde{b}_i Cos\left(i\theta_e-\frac{i\pi}{2}\right)\\ -\sum_{\substack{i=1,\\ i\,\mathrm{odd}}}^{N} a_i Cos(i\theta_e)-\sum_{\substack{i=1,\\ i\,\mathrm{odd}}}^{N} b_i Sin(i\theta_e)-\sum_{\substack{i=1,\\ i\,\mathrm{odd}}}^{\tilde{N}} \tilde{a}_i Cos(i\theta_e)-\sum_{\substack{i=1,\\ i\,\mathrm{odd}}}^{\tilde{N}} \tilde{b}_i Sin(i\theta_e)\end{array}\right].\end{aligned} \tag{30}$$

Minimizing this metric with respect to the unknown parameters (i.e. the three Lagrange multipliers and the Fourier expansion coefficients of $f(\Theta)$) results, again, in a linear system of equations

$$\begin{cases} \dfrac{\partial \hat{\Pi}}{\partial \tilde{a}_{2i+1}} = 0 \; ; \; i = 0,\ldots, \dfrac{\tilde{N}-1}{2} \\ \dfrac{\partial \hat{\Pi}}{\partial \tilde{b}_{2i+1}} = 0 \; ; \; i = 0,\ldots, \dfrac{\tilde{N}-1}{2} \\ \dfrac{\partial \hat{\Pi}}{\partial \lambda_1} = 0 \\ \dfrac{\partial \hat{\Pi}}{\partial \lambda_2} = 0 \\ \dfrac{\partial \hat{\Pi}}{\partial \lambda_3} = 0 \end{cases} \tag{31}$$

which solution in turn uniquely defines a new yaw dependent bias $\hat{B}_G(\theta_e)$.

The constraint expressed in eq. (27) has proven to work fine in the sense that the previous "spiky" signal behaviour of measured *total* calibration moments, at yaw values around zero crossings, are now virtually removed, meaning that the derived calibration results in close-to-constant *total* calibration moments for arbitrary WT yaw positions.

However, this is unfortunately(?) not the case for WT load cases, where wind loading adds to the gravity dictated calibration loading, as observed from WT M1 measurements in the wake-free sector. This could be caused by a non-linear relationship between measured signals and the analogue physical signal, in which case a classical linear calibration based on gain and bias is not possible but, as mentioned in Chapter 2, it could also be an artefact of yaw dependent inflow (i.e. mean wind shear) conditions, in which case a yaw independent total moment should not be expected. Further analysis of this issue is left for future investigations, but preliminary analysis based on HAWC2 simulations indicate that the present model might under-predict the gain, which in turn means that the difference between the measured signal and the bias is over-estimated – i.e. that the bias should explain a bigger part of the measured signal than is presently the case, implying that a mix of the metrics defined in eq. 12) and eq. (14) might be advantageous.

Appendix B

Simulated single wake cases; ambient turbulence intensity 3%

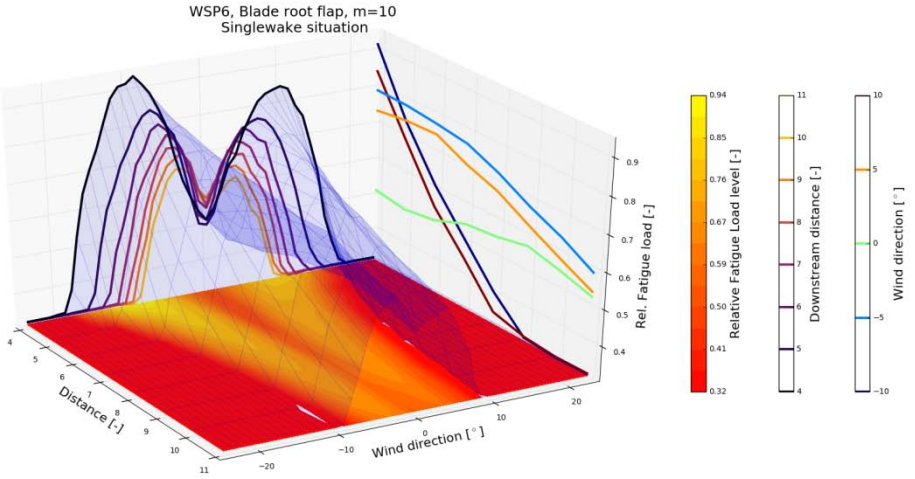

Figure B1: Blade root flap equivalent moment; U = 6m/s; TI = 3%.

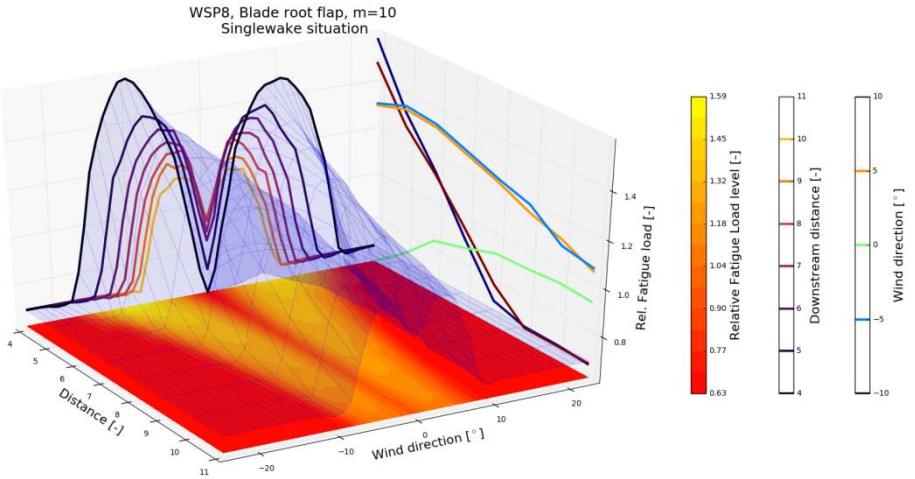

Figure B2: Blade root flap equivalent moment; U = 8m/s; TI = 3%.

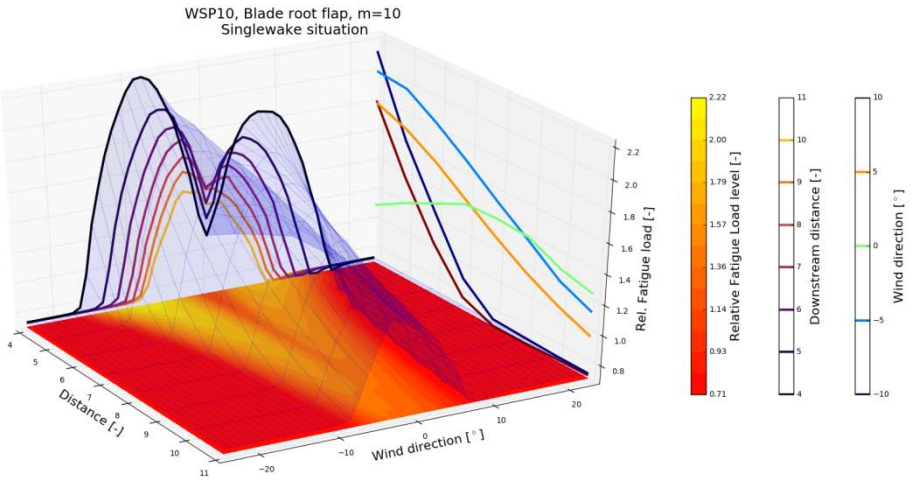

Figure B3: Blade root flap equivalent moment; U = 10m/s; TI = 3%.

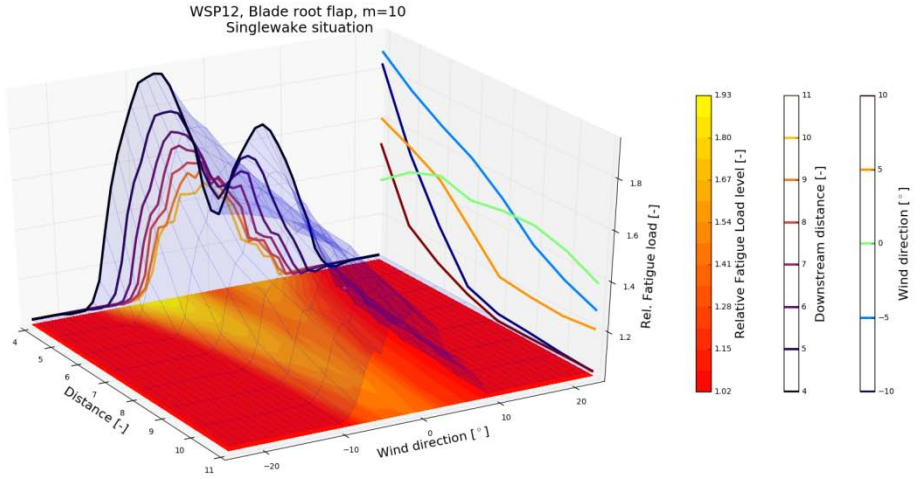

Figure B4: Blade root flap equivalent moment; U = 12m/s; TI = 3%.

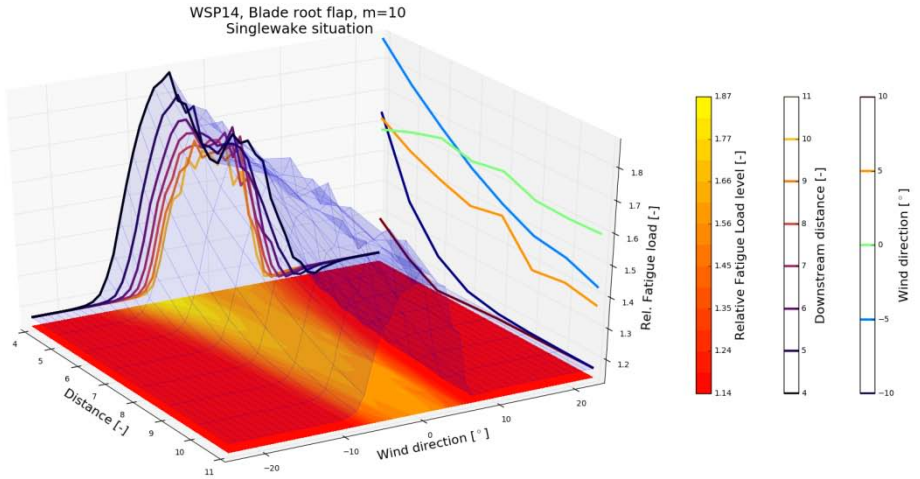

Figure B5: Blade root flap equivalent moment; U = 14m/s; TI = 3%.

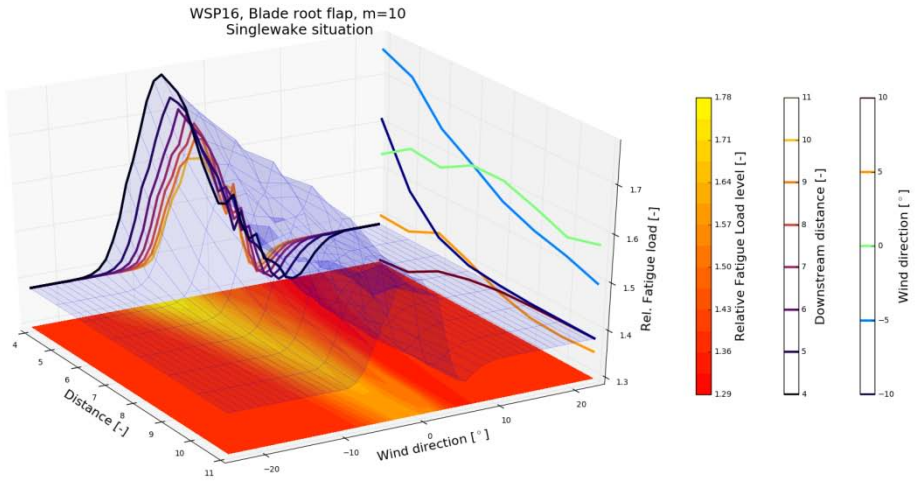

Figure B6: Blade root flap equivalent moment; U = 16m/s; TI = 3%.

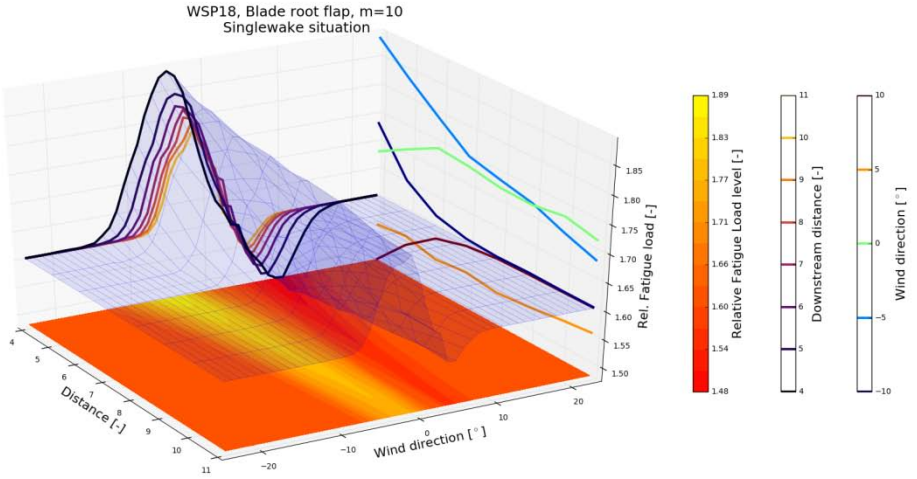

Figure B7: Blade root flap equivalent moment; U = 18m/s; TI = 3%.

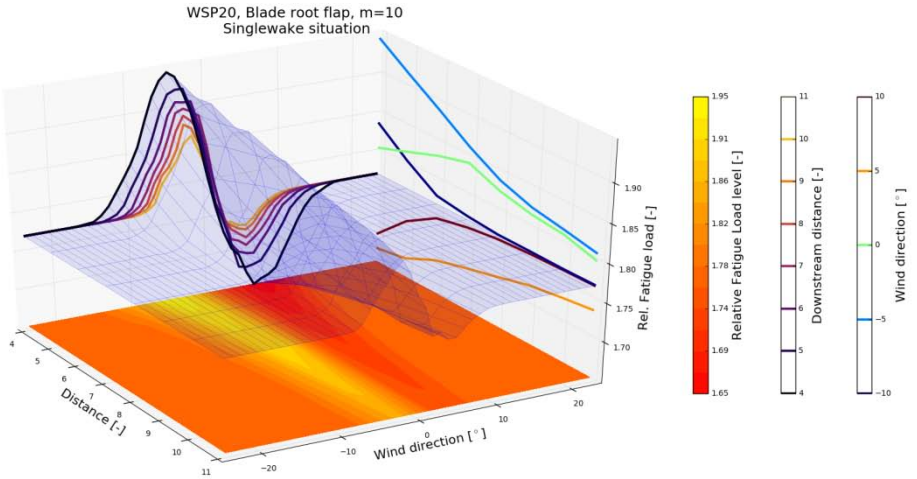

Figure B8: Blade root flap equivalent moment; U = 20m/s; TI = 3%.

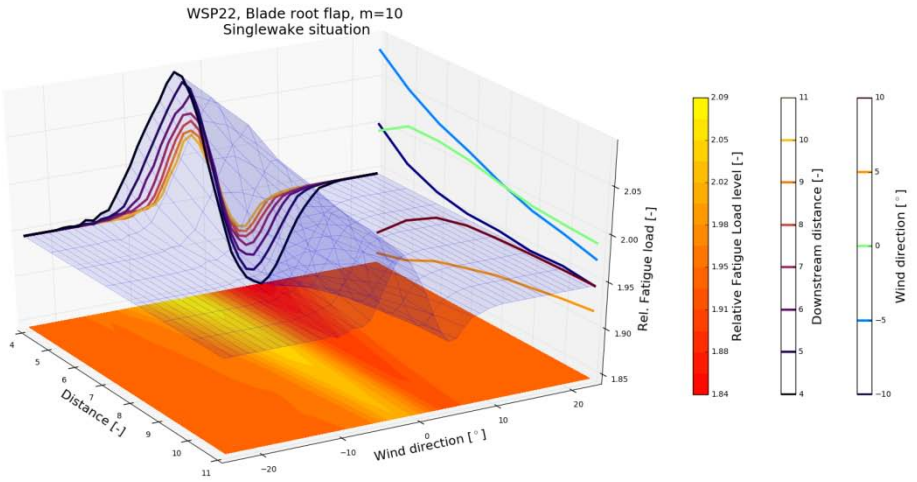

Figure B9: Blade root flap equivalent moment; U = 22m/s; TI = 3%.

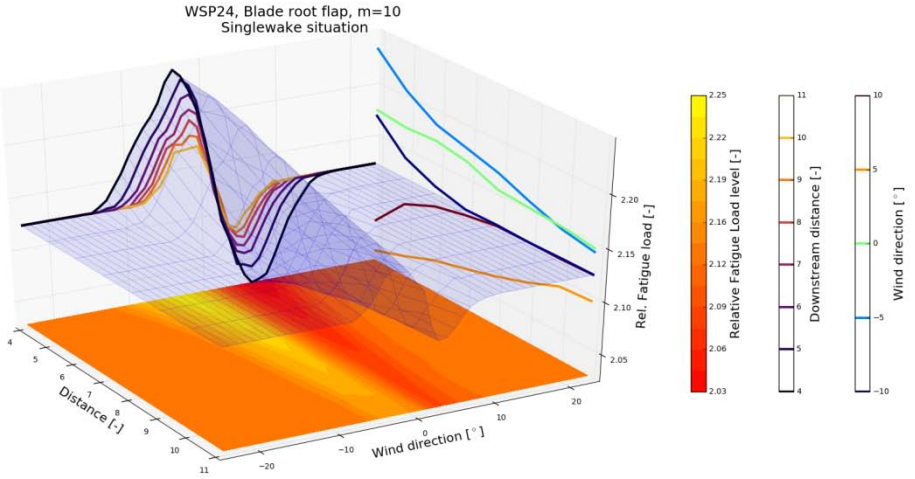

Figure B10: Blade root flap equivalent moment; U = 24m/s; TI = 3%.

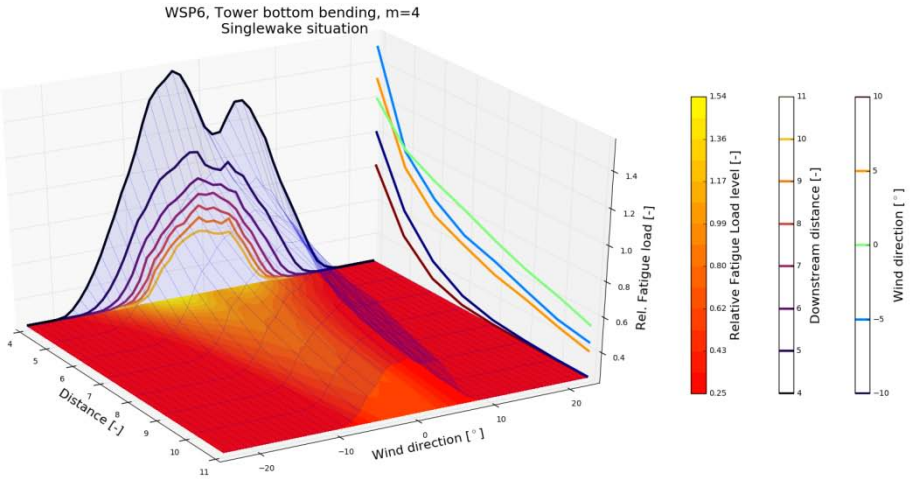

Figure B11: Tower bottom bending equivalent moment; U = 6m/s; TI = 3%.

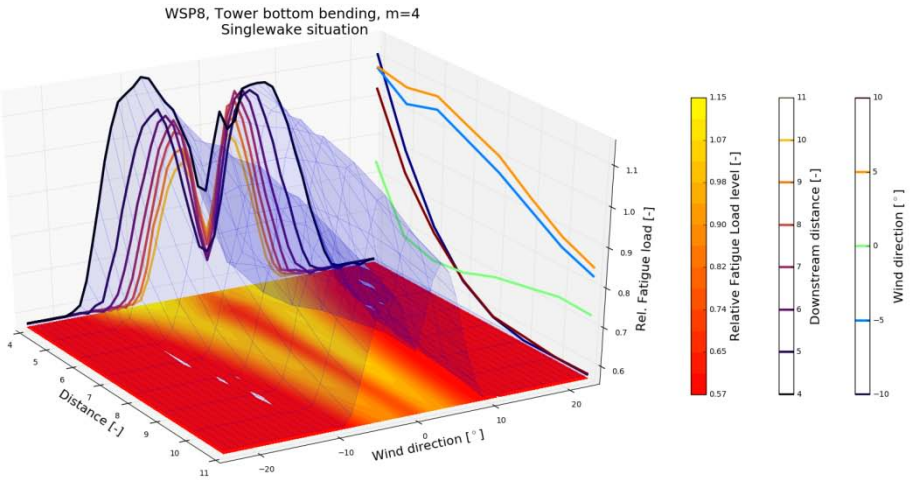

Figure B12: Tower bottom bending equivalent moment; U = 8m/s; TI = 3%.

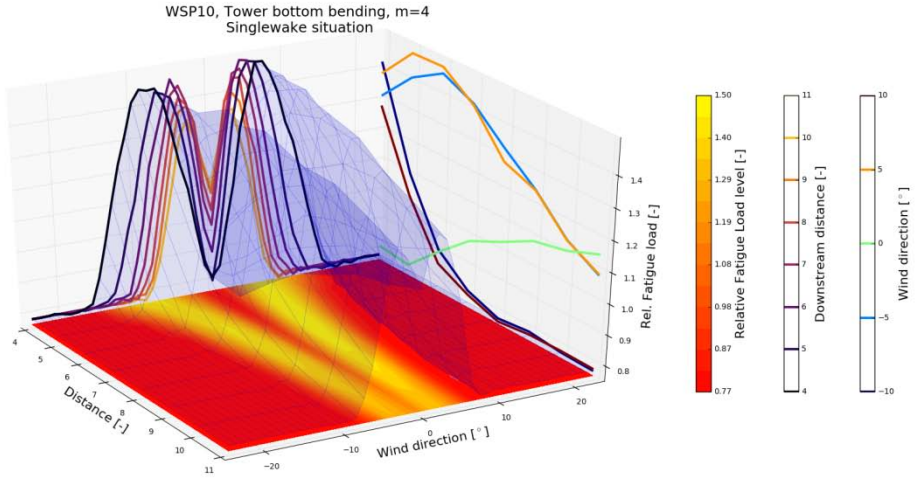

Figure B13: Tower bottom bending equivalent moment; U = 10m/s; TI = 3%.

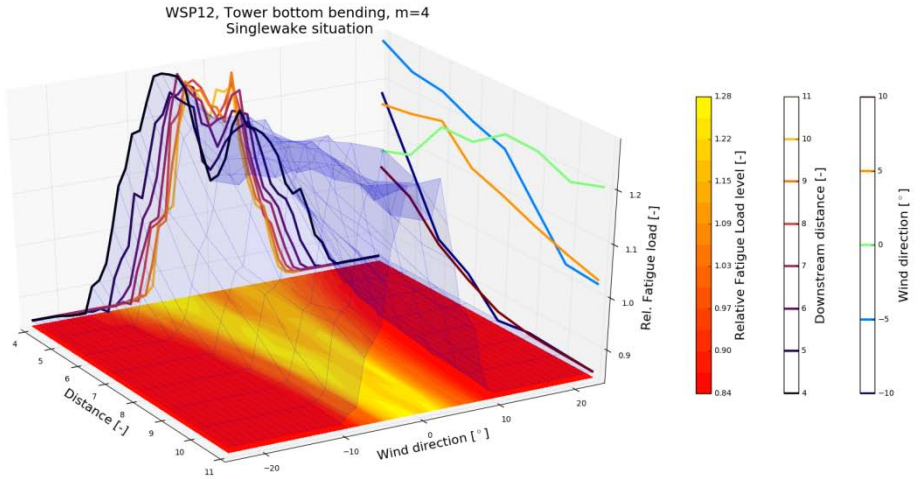

Figure B14: Tower bottom bending equivalent moment; U = 12m/s; TI = 3%.

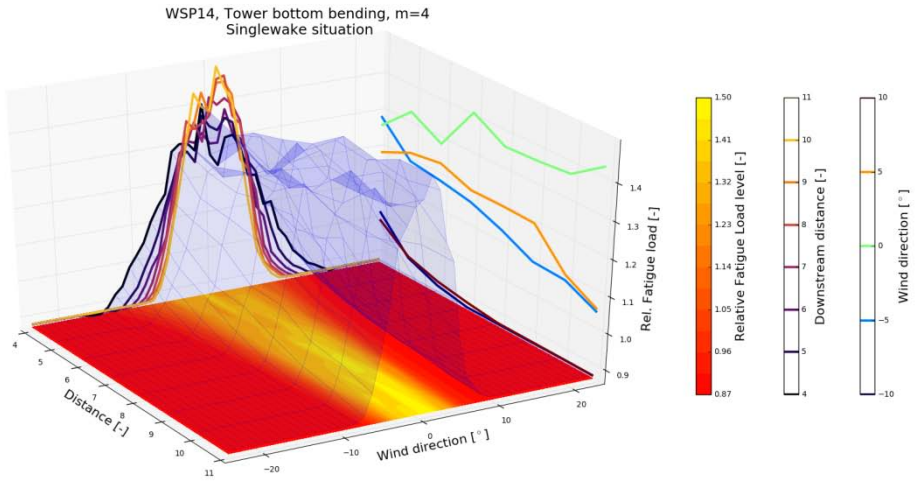

Figure B15: Tower bottom bending equivalent moment; U = 14m/s; TI = 3%.

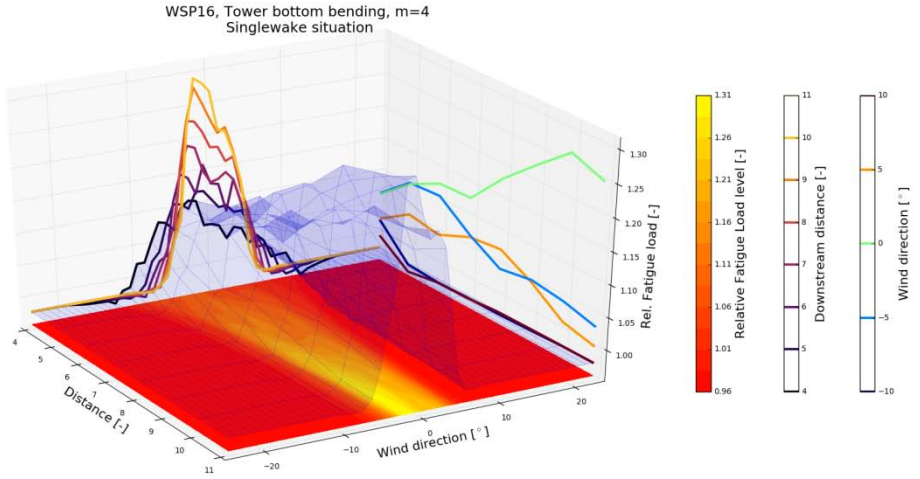

Figure B16: Tower bottom bending equivalent moment; U = 16m/s; TI = 3%.

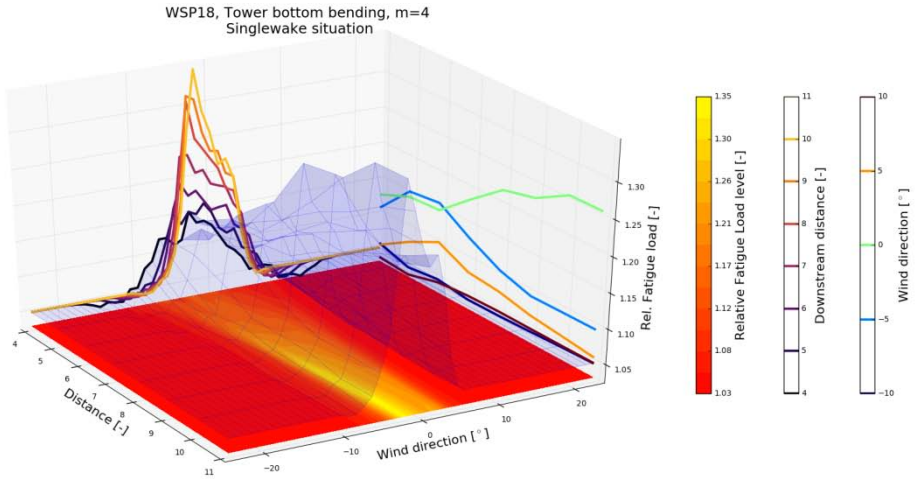

Figure B17: Tower bottom bending equivalent moment; U = 18m/s; TI = 3%.

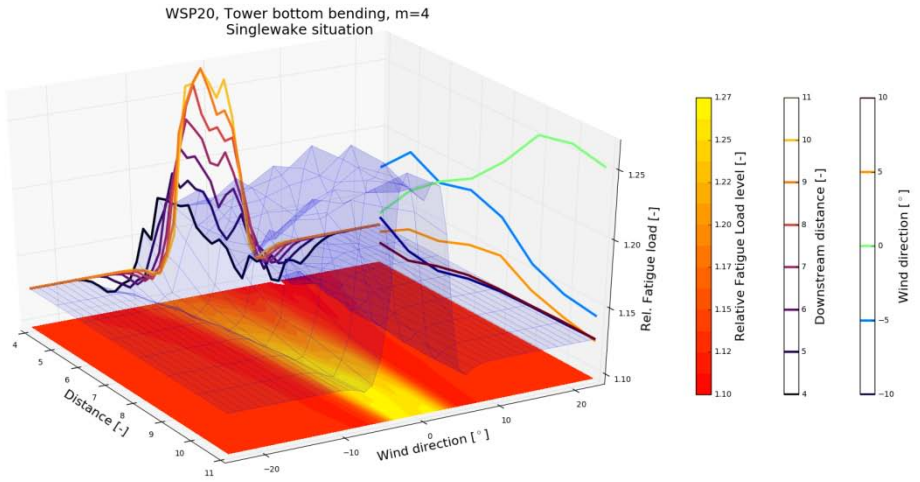

Figure B18: Tower bottom bending equivalent moment; U = 20m/s; TI = 3%.

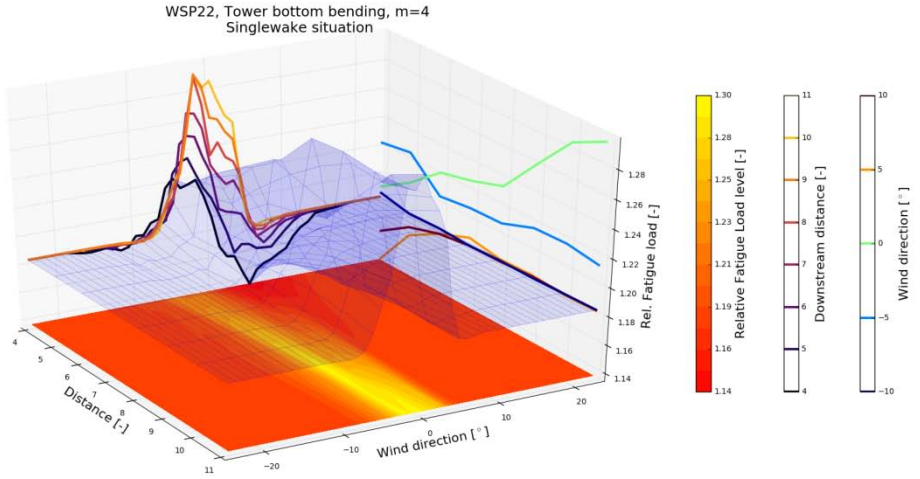

Figure B19: Tower bottom bending equivalent moment; U = 22m/s; TI = 3%.

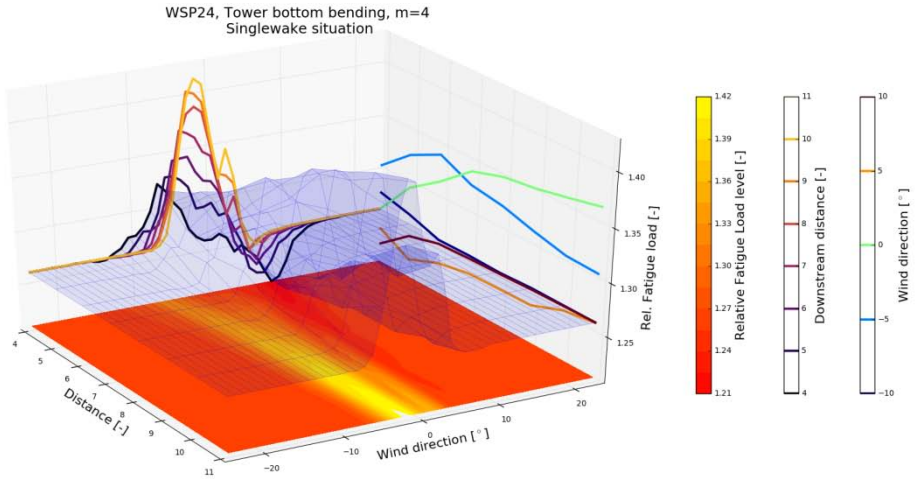

Figure B20: Tower bottom bending equivalent moment; U = 24m/s; TI = 3%.

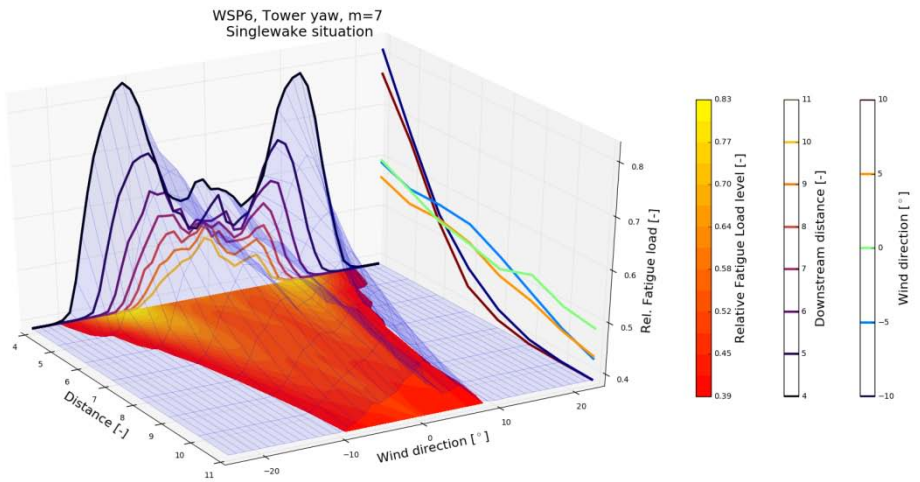

Figure B21: Tower top torsion equivalent moment; U = 6m/s; TI = 3%.

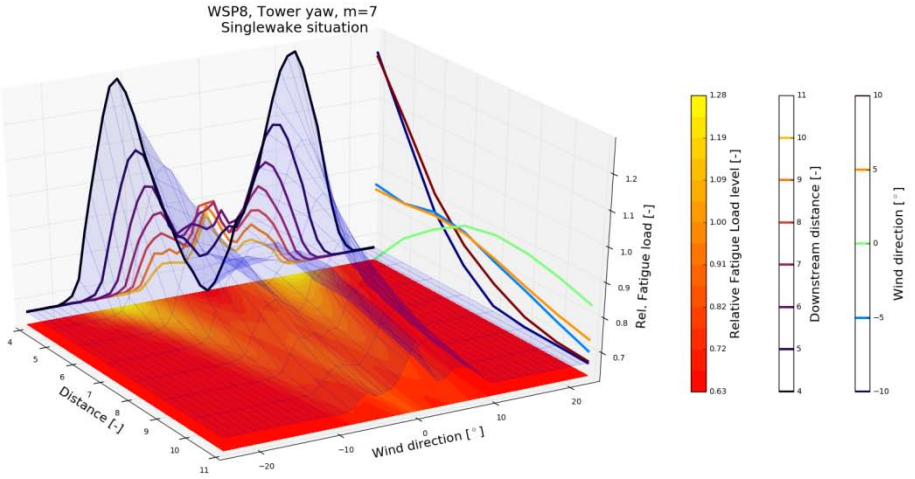

Figure B22: Tower top torsion equivalent moment; U = 8m/s; TI = 3%.

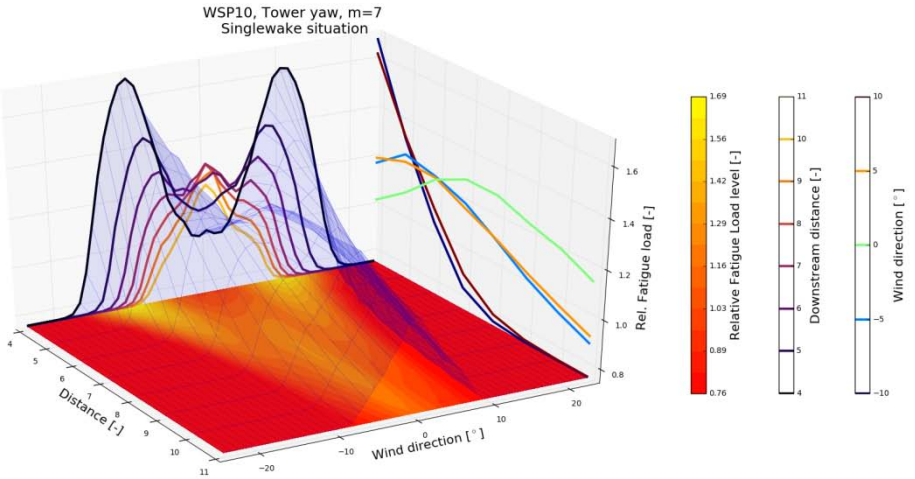

Figure B23: Tower top torsion equivalent moment; U = 10m/s; TI = 3%.

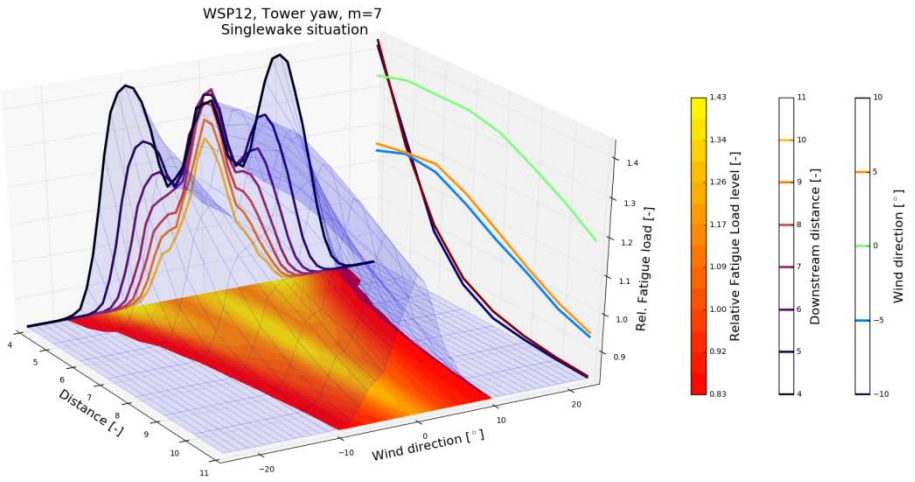

Figure B24: Tower top torsion equivalent moment; U = 12m/s; TI = 3%.

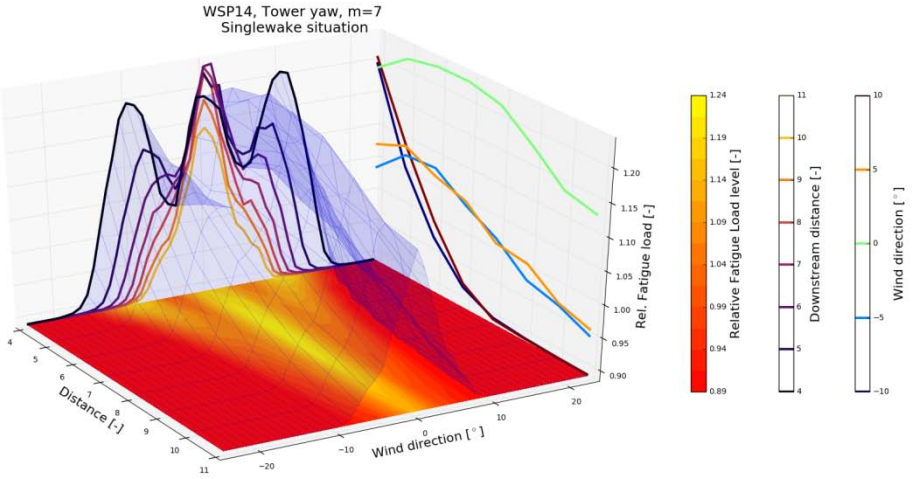

Figure B25: Tower top torsion equivalent moment; U = 14m/s; TI = 3%.

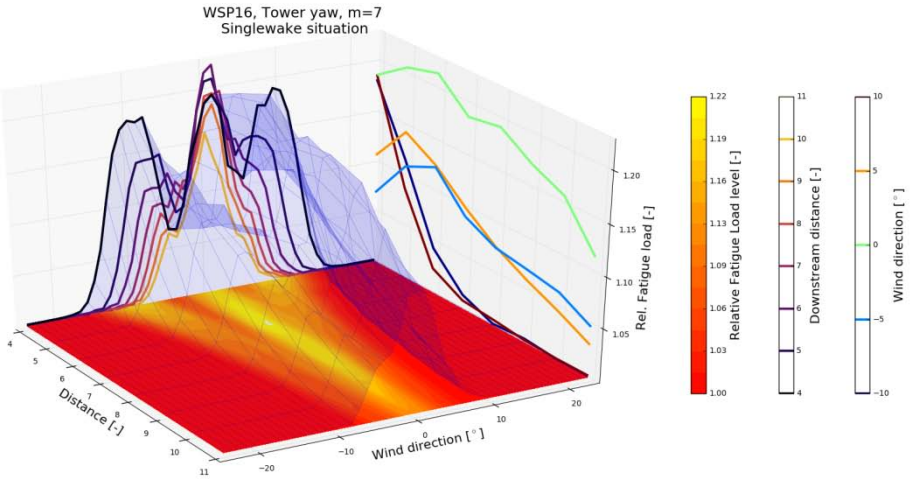

Figure B26: Tower top torsion equivalent moment; U = 16m/s; TI = 3%.

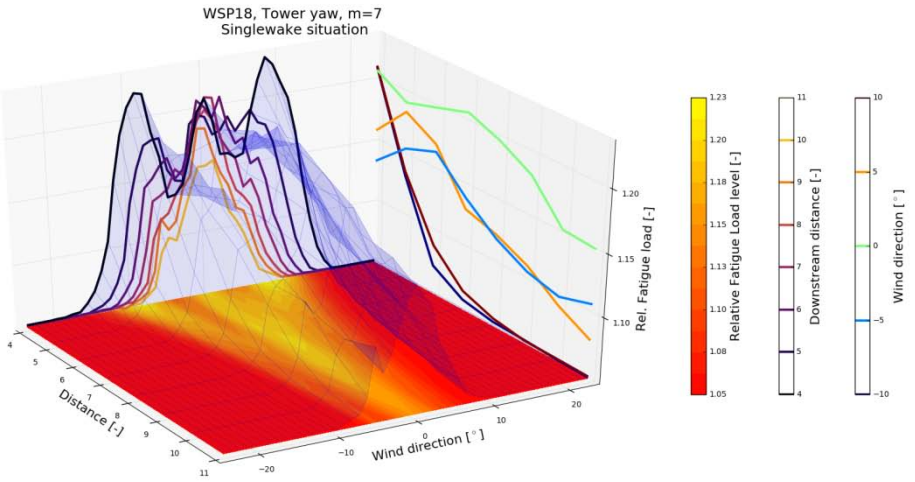

Figure B27: Tower top torsion equivalent moment; U = 18m/s; TI = 3%.

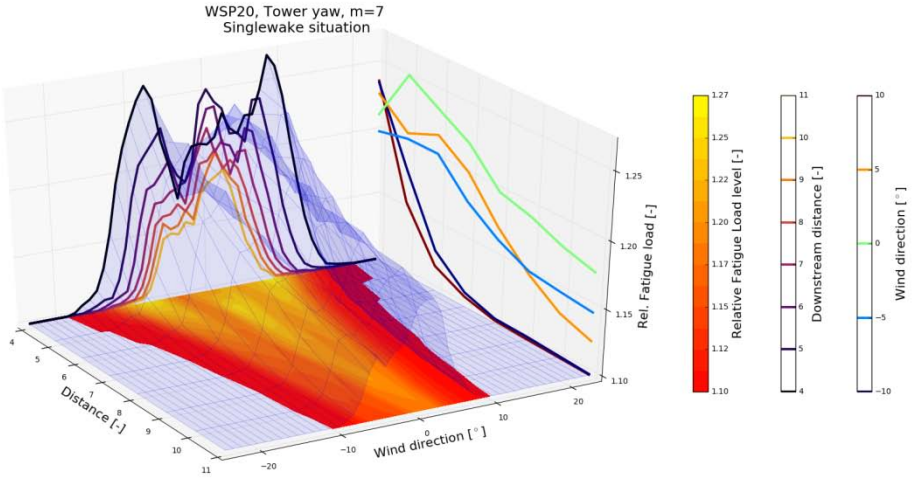

Figure B28: Tower top torsion equivalent moment; U = 20m/s; TI = 3%.

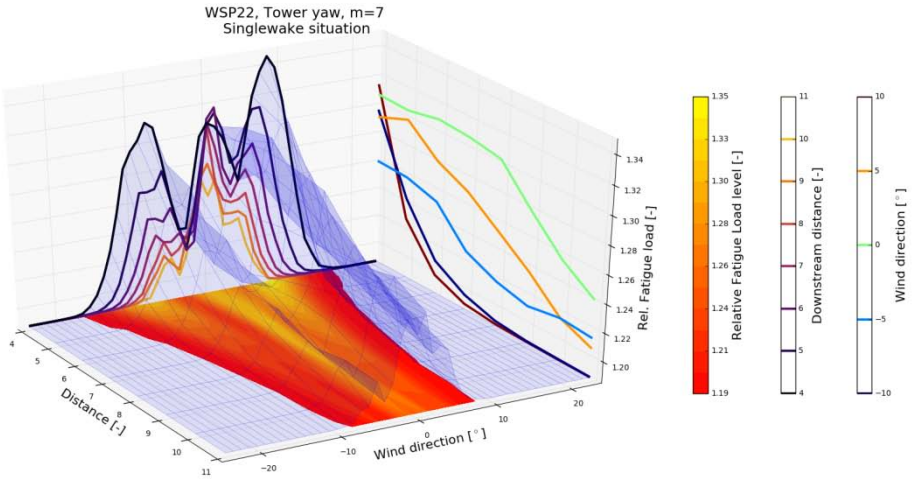

Figure B29: Tower top torsion equivalent moment; U = 22m/s; TI = 3%.

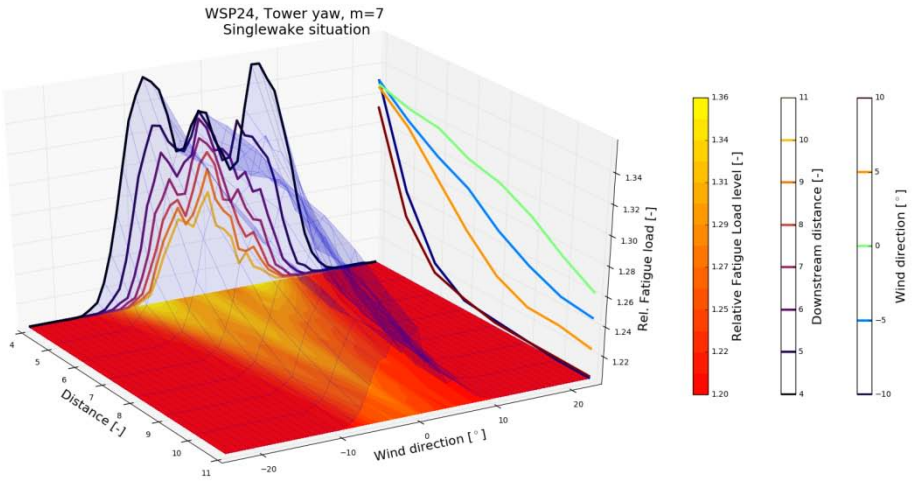

Figure B30: Tower top torsion equivalent moment; U = 24m/s; TI = 3%.

Appendix C

Simulated single wake cases; ambient turbulence intensity 6%

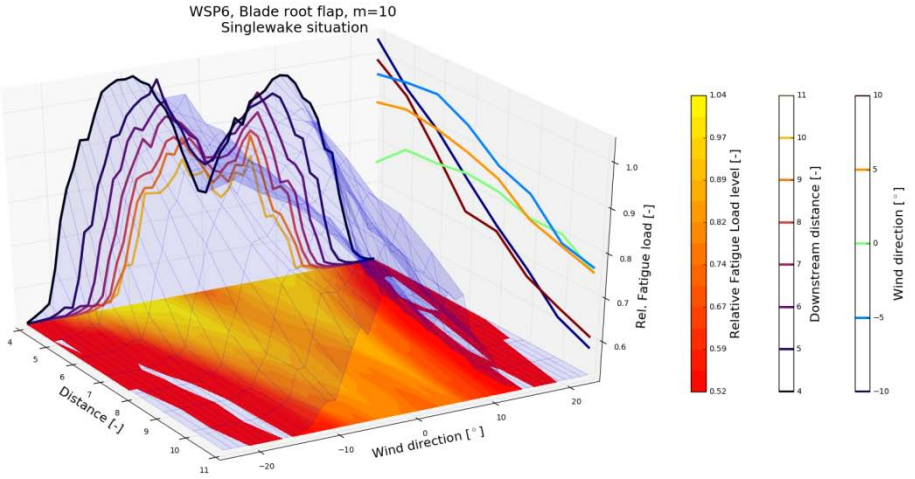

Figure C1: Blade root flap equivalent moment; U = 6m/s; TI = 6%.

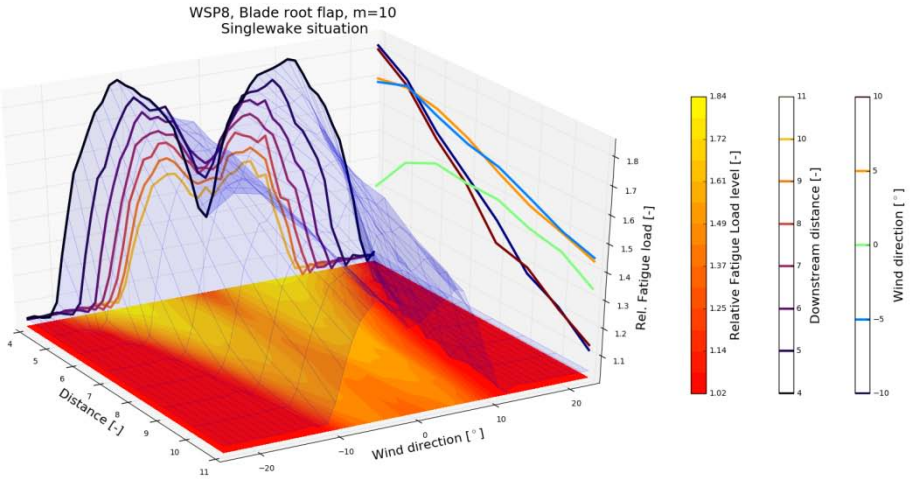

Figure C2: Blade root flap equivalent moment; U = 8m/s; TI = 6%.

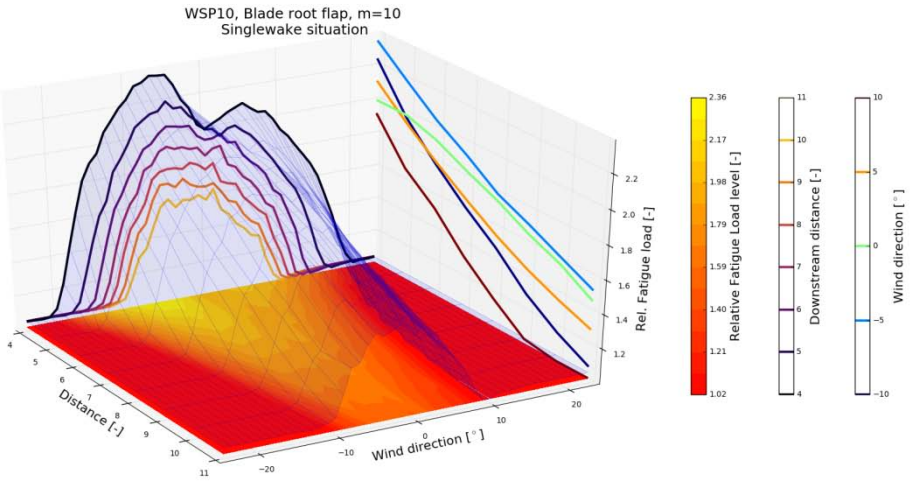

Figure C3: Blade root flap equivalent moment; U = 10m/s; TI = 6%.

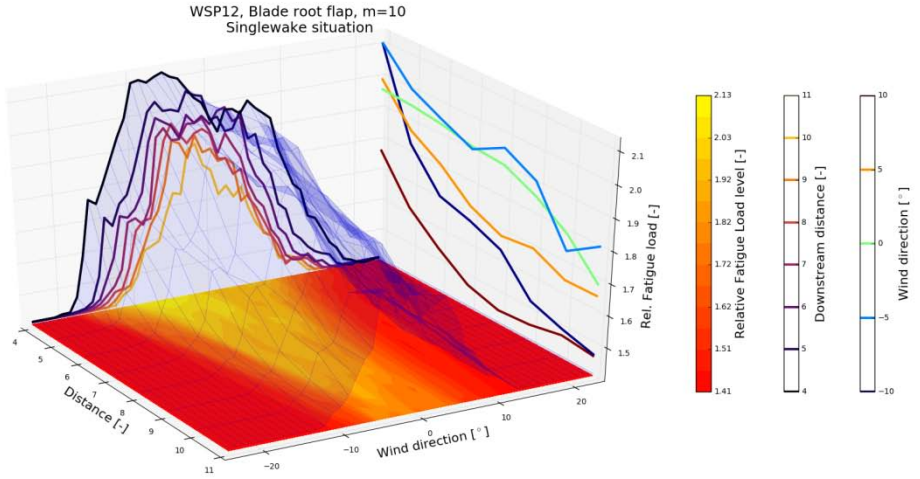

Figure C4: Blade root flap equivalent moment; U = 12m/s; TI = 6%.

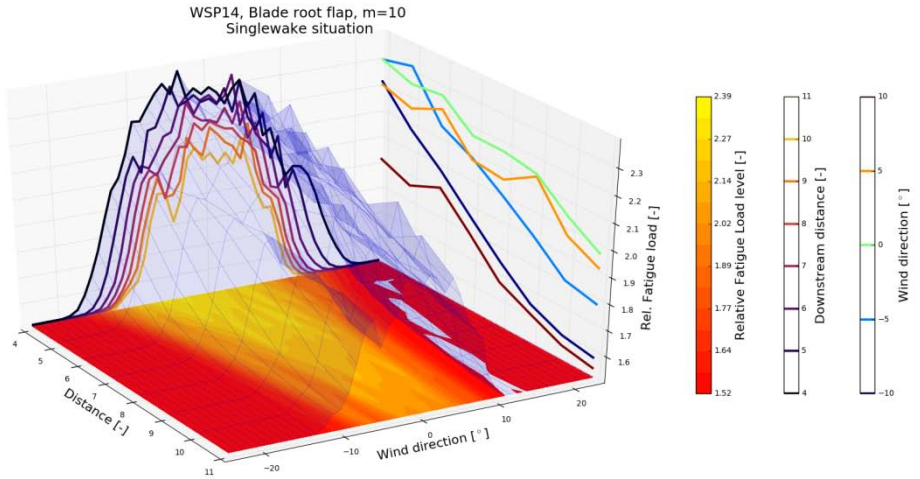

Figure C5: Blade root flap equivalent moment; U = 14m/s; TI = 6%.

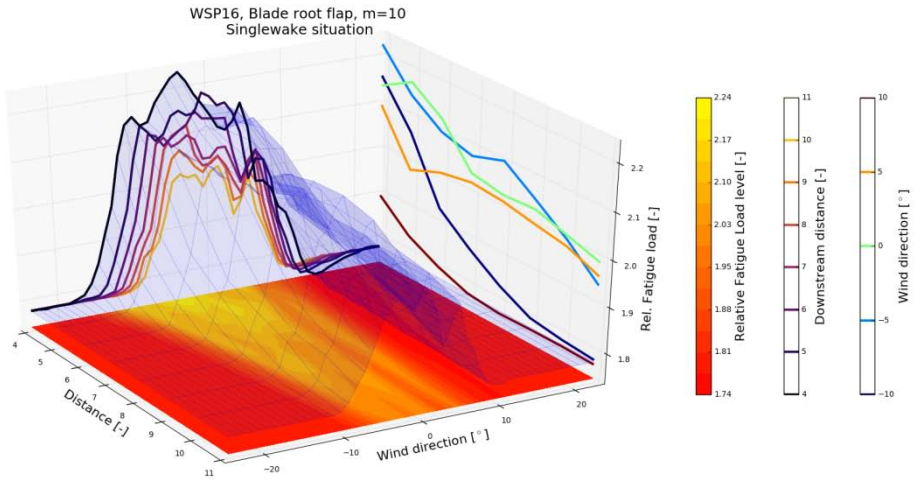

Figure C6: Blade root flap equivalent moment; U = 16m/s; TI = 6%.

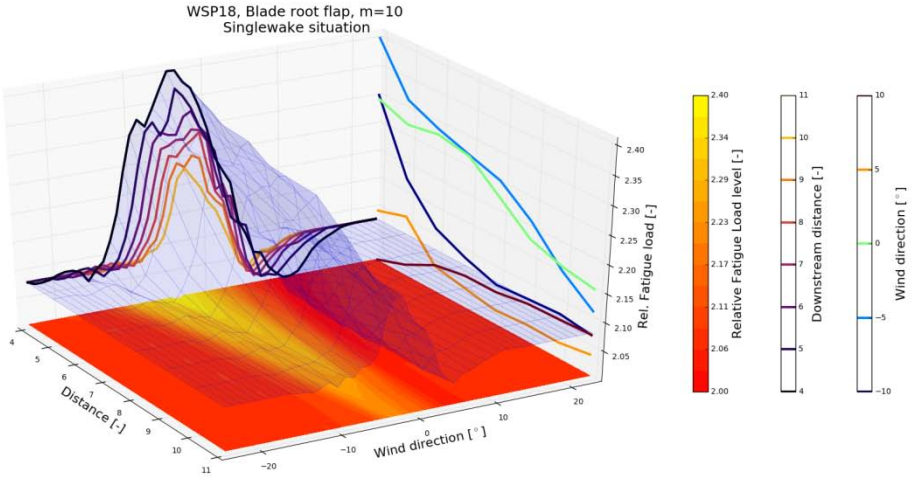

Figure C7: Blade root flap equivalent moment; U = 18m/s; TI = 6%.

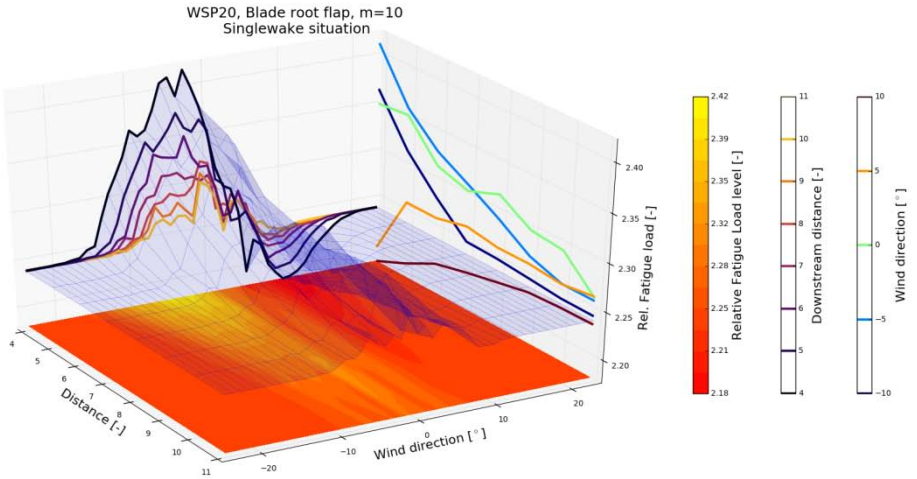

Figure C8: Blade root flap equivalent moment; U = 20m/s; TI = 6%.

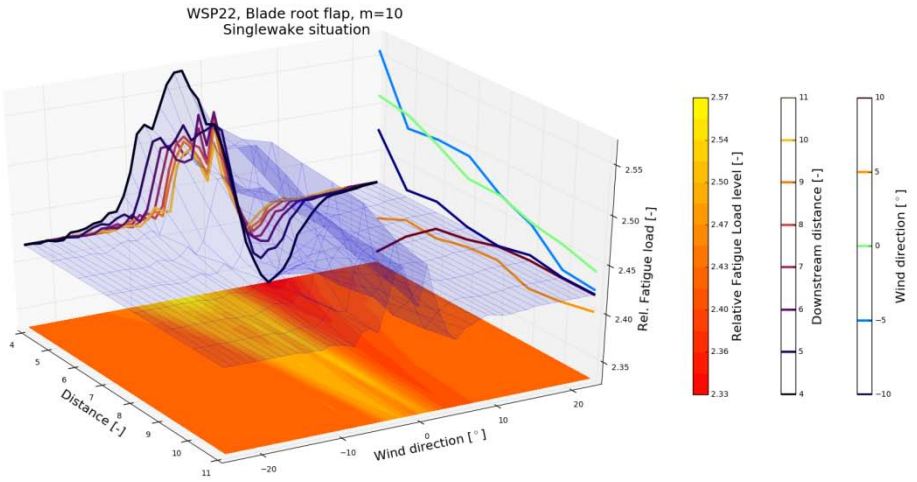

Figure C9: Blade root flap equivalent moment; U = 22m/s; TI = 6%.

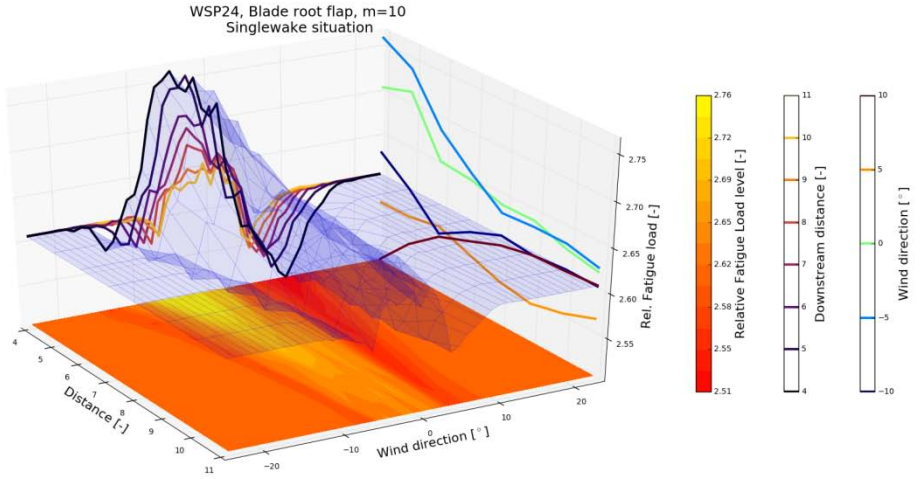

Figure C10: Blade root flap equivalent moment; U = 24m/s; TI = 6%.

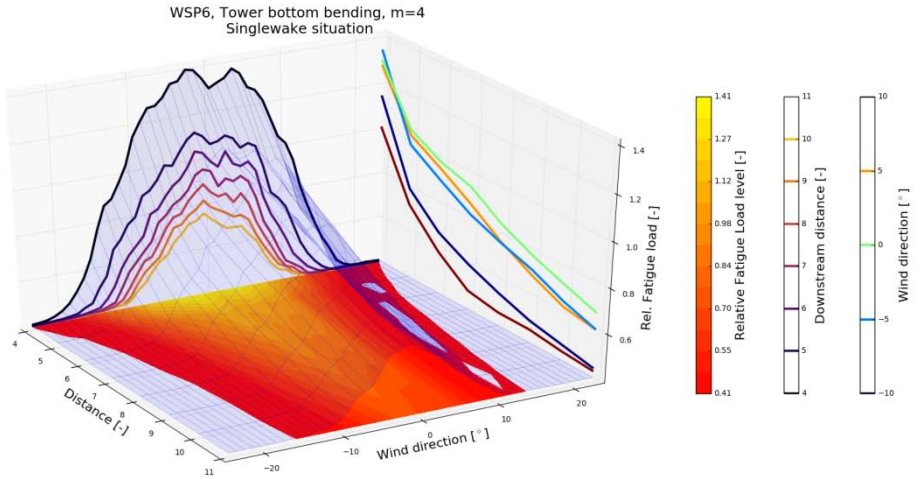

Figure C11: Tower bottom bending equivalent moment; U = 6m/s; TI = 6%.

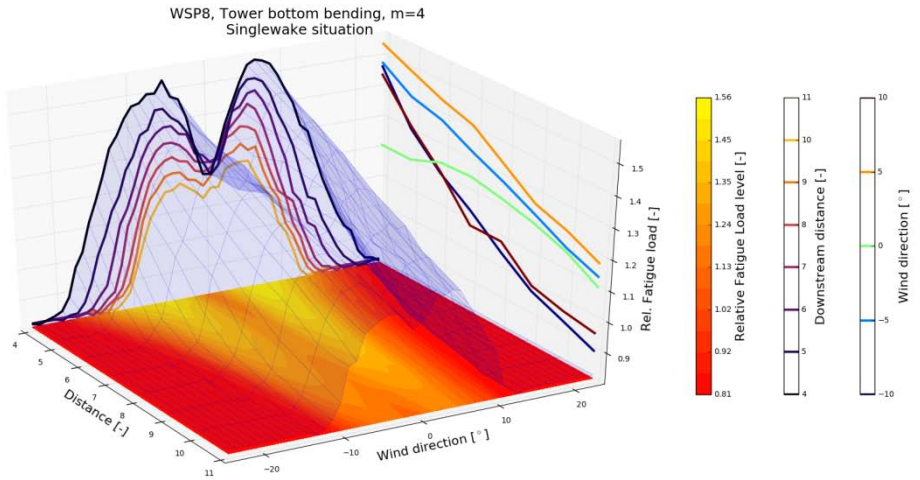

Figure C12: Tower bottom bending equivalent moment; U = 8m/s; TI = 6%.

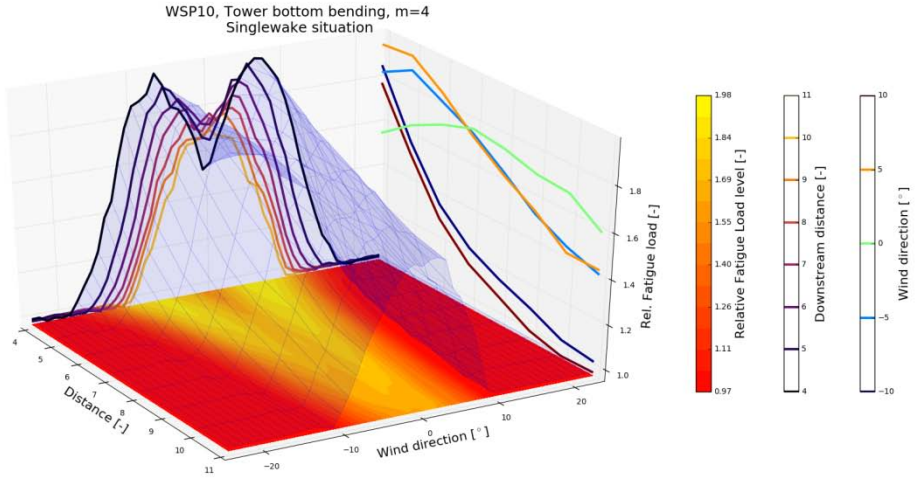

Figure C13: Tower bottom bending equivalent moment; U = 10m/s; TI = 6%.

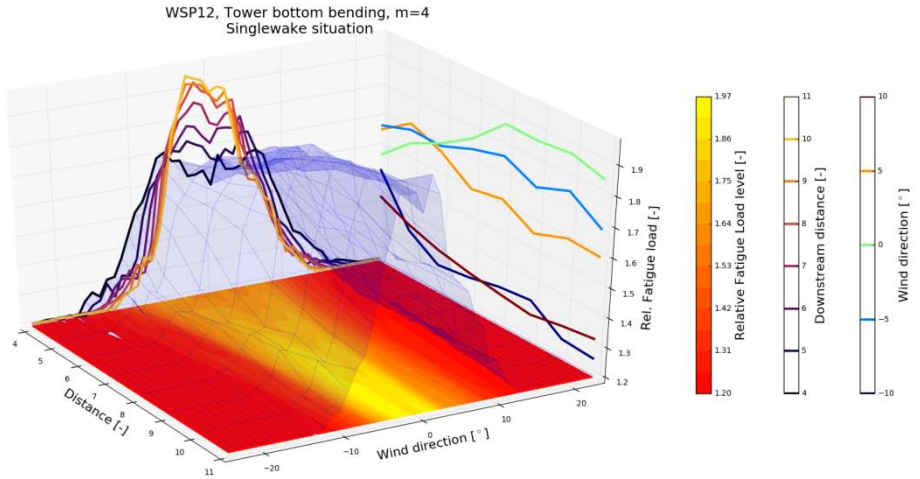

Figure C14: Tower bottom bending equivalent moment; U = 12m/s; TI = 6%.

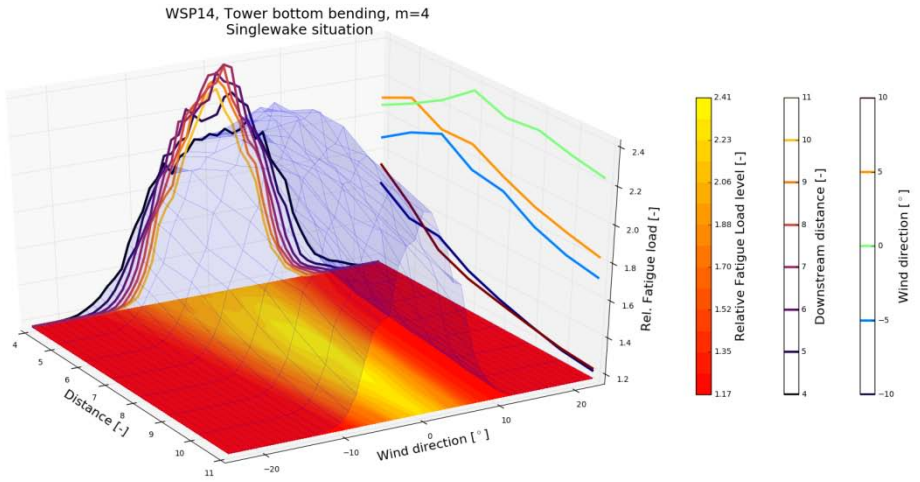

Figure C15: Tower bottom bending equivalent moment; U = 14m/s; TI = 6%.

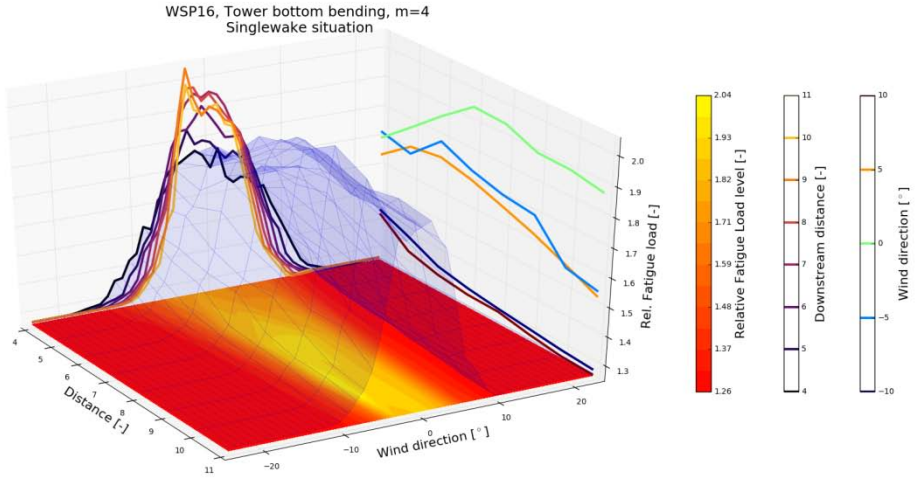

Figure C16: Tower bottom bending equivalent moment; U = 16m/s; TI = 6%.

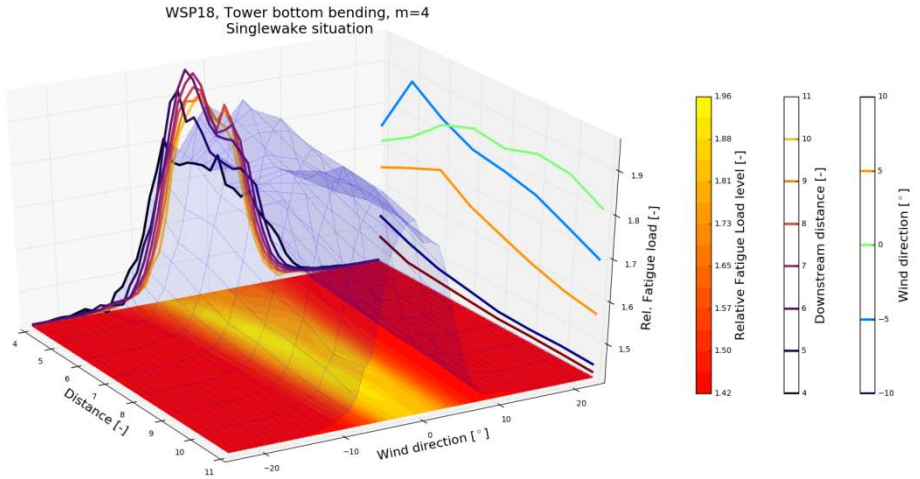

Figure C17: Tower bottom bending equivalent moment; U = 18m/s; TI = 6%.

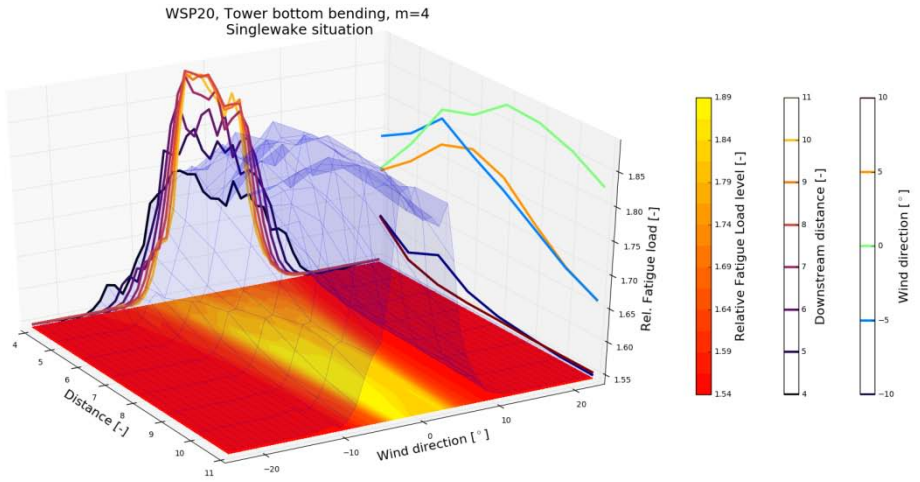

Figure C18: Tower bottom bending equivalent moment; U = 20m/s; TI = 6%.

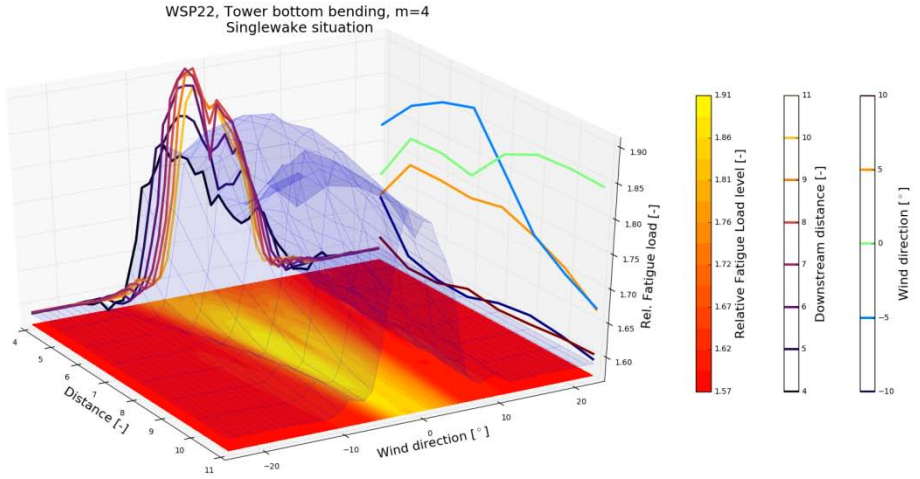

Figure C19: Tower bottom bending equivalent moment; U = 22m/s; TI = 6%.

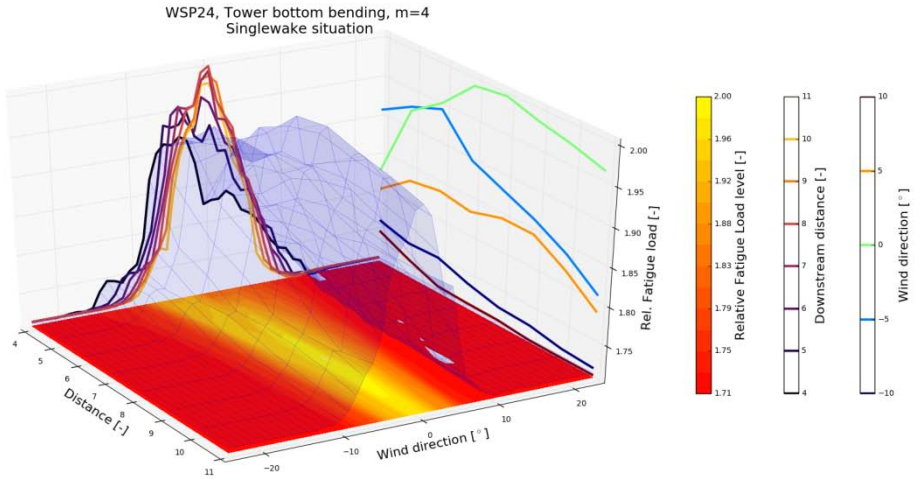

Figure C20: Tower bottom bending equivalent moment; U = 24m/s; TI = 6%.

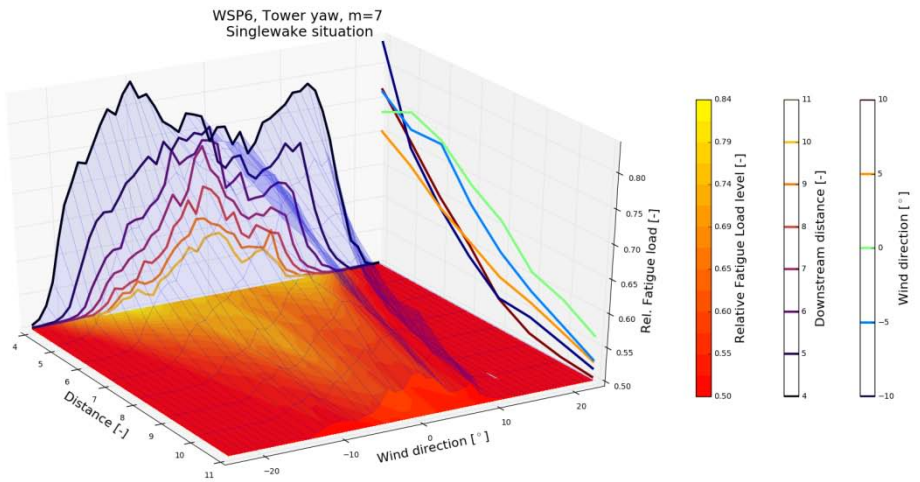

Figure C21: Tower top torsion equivalent moment; U = 6m/s; TI = 6%.

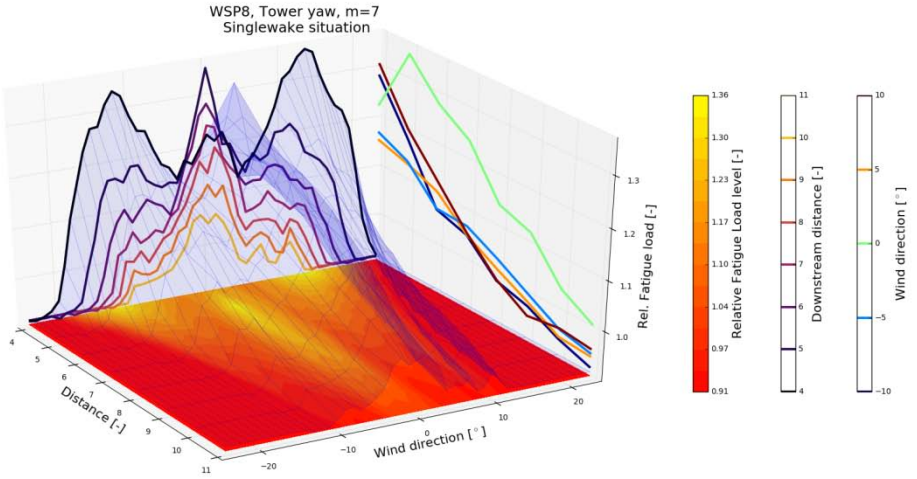

Figure C22: Tower top torsion equivalent moment; U = 8m/s; TI = 6%.

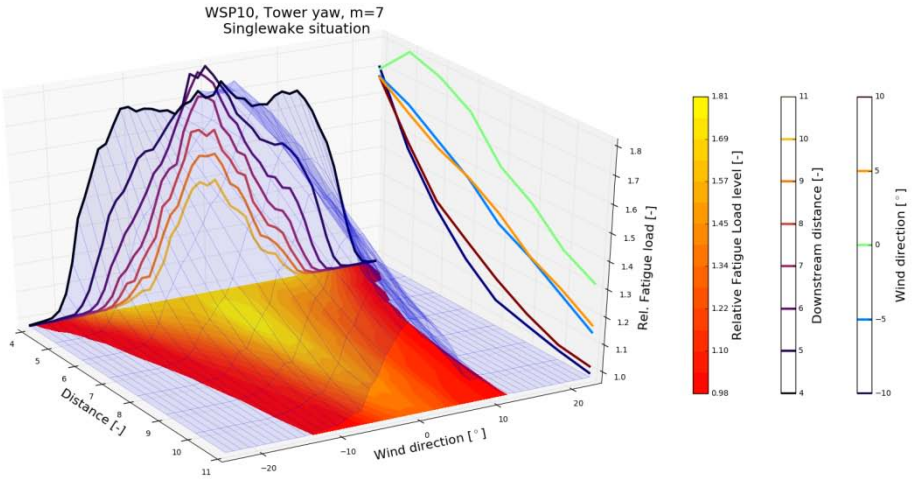

Figure C23: Tower top torsion equivalent moment; U = 10m/s; TI = 6%.

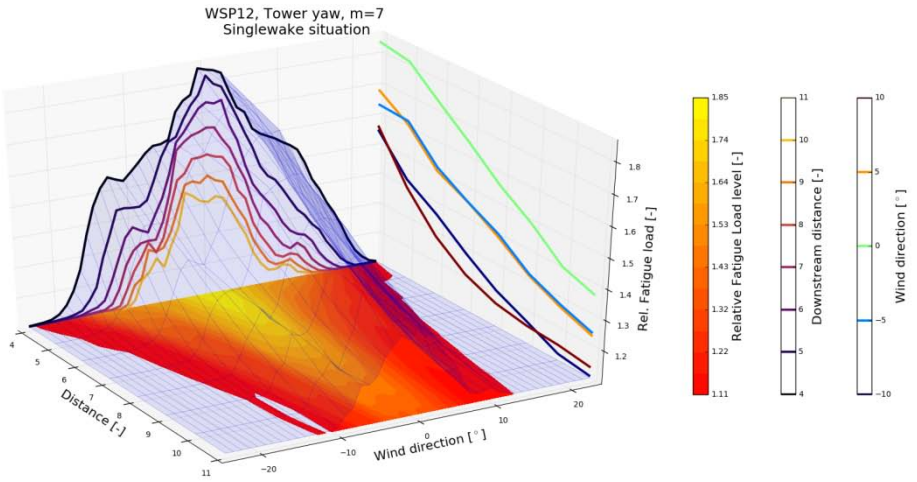

Figure C24: Tower top torsion equivalent moment; U = 12m/s; TI = 6%.

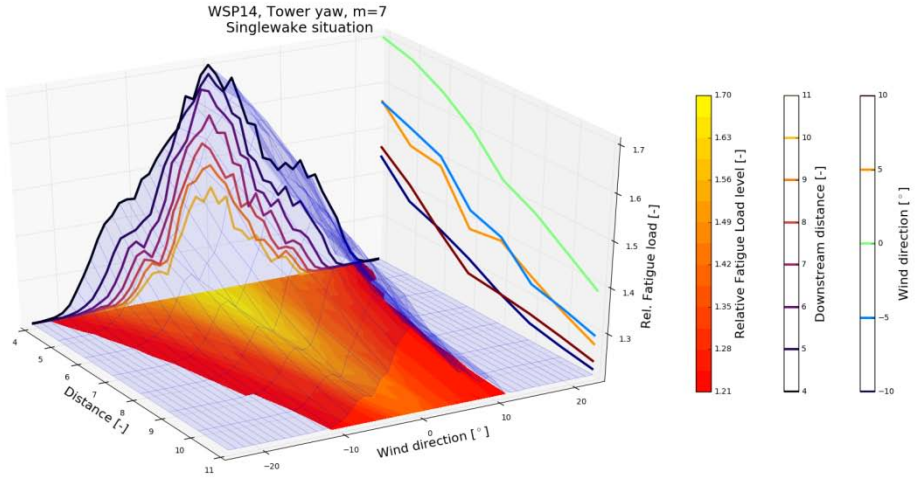

Figure C25: Tower top torsion equivalent moment; U = 14m/s; TI = 6%.

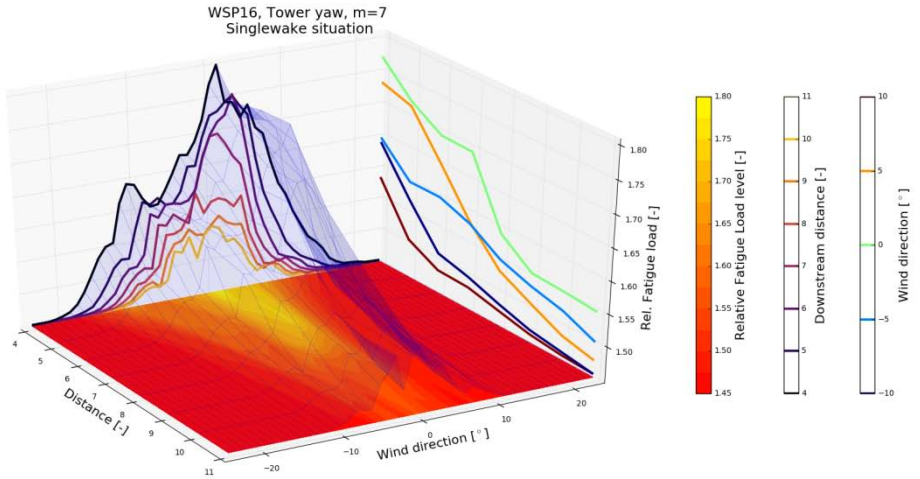

Figure C26: Tower top torsion equivalent moment; U = 16m/s; TI = 6%.

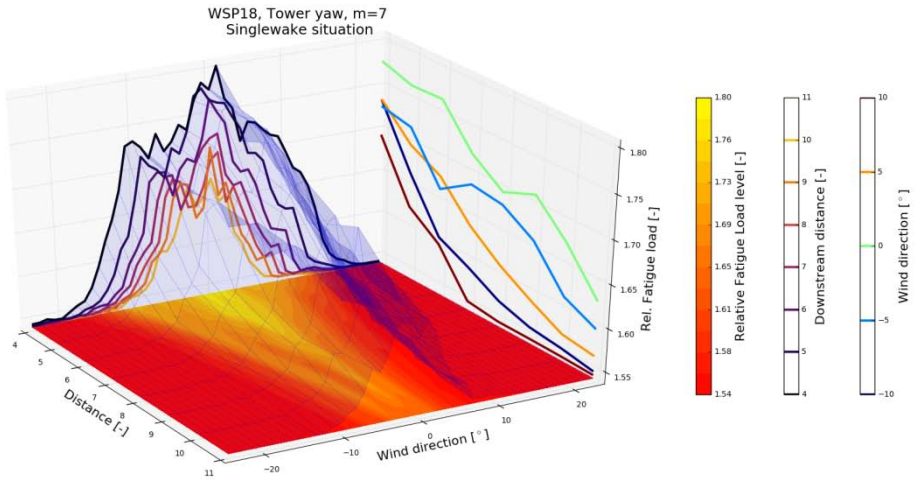

Figure C27: Tower top torsion equivalent moment; U = 18m/s; TI = 6%.

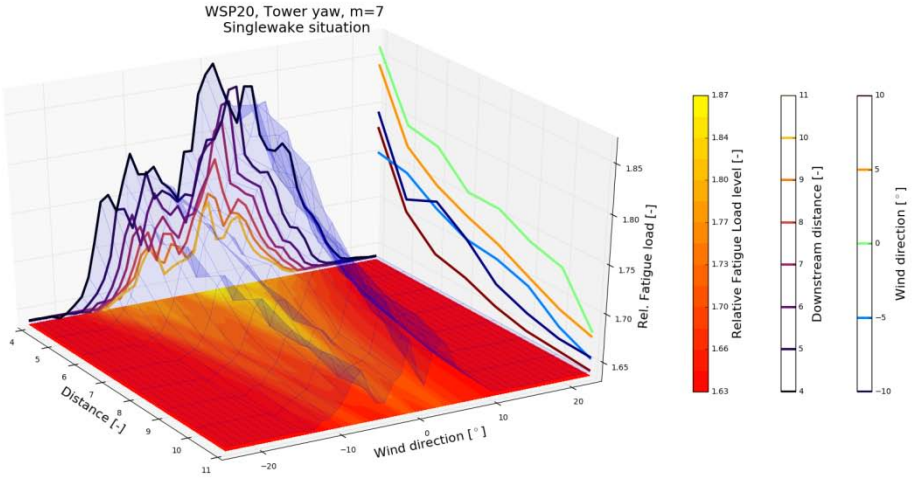

Figure C28: Tower top torsion equivalent moment; U = 20m/s; TI = 6%.

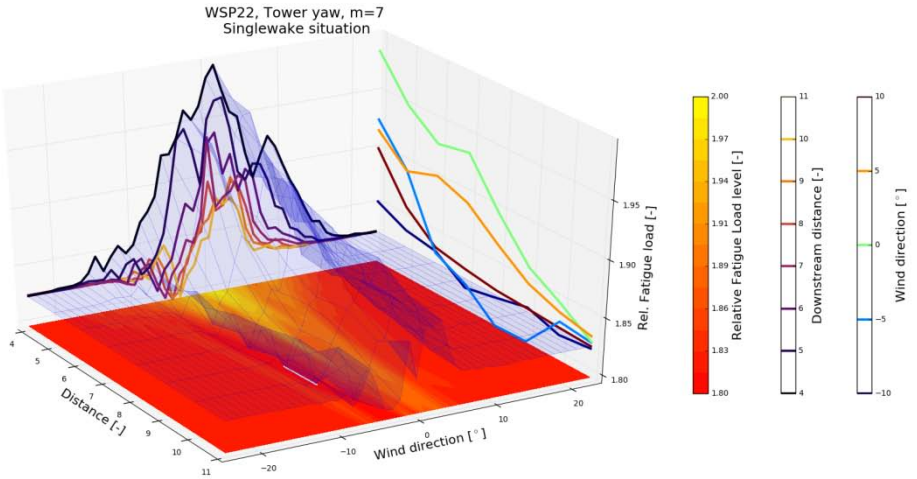

Figure C29: Tower top torsion equivalent moment; U = 22m/s; TI = 6%.

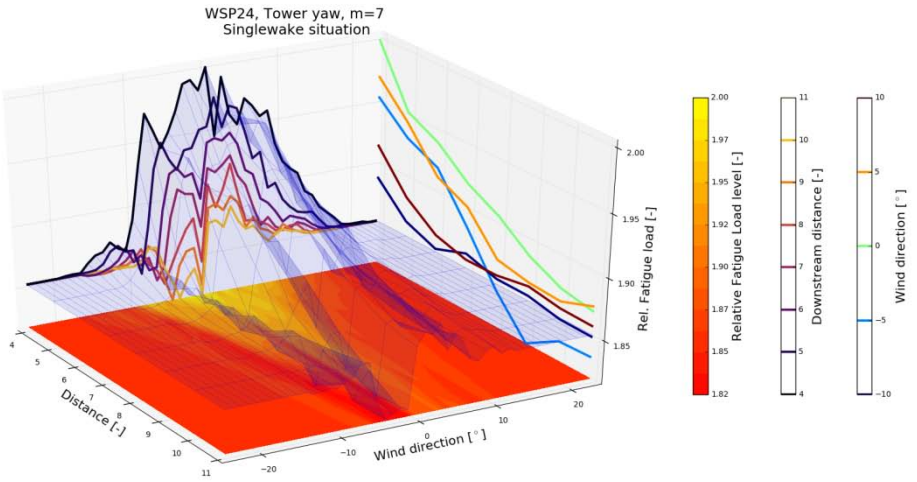

Figure C30: Tower top torsion equivalent moment; U = 24m/s; TI = 6%.

Appendix D

Simulated single wake cases; ambient turbulence intensity 9%

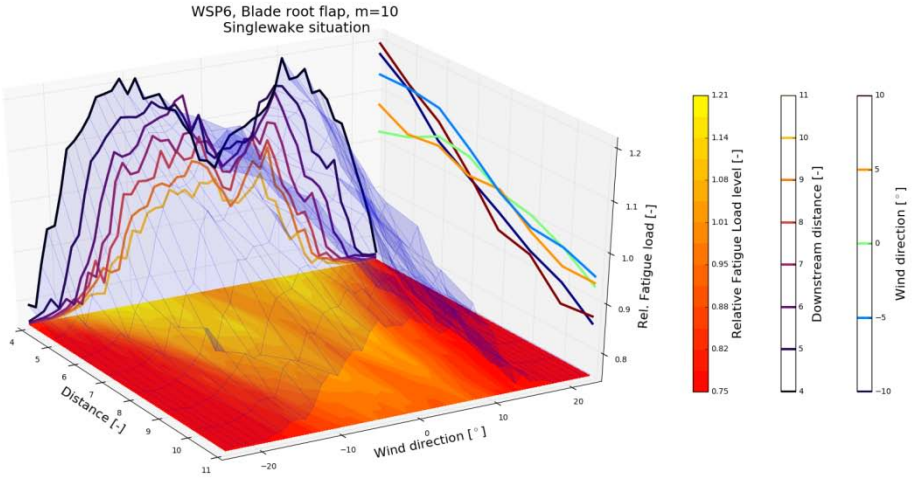

Figure D1: Blade root flap equivalent moment; U = 6m/s; TI = 9%.

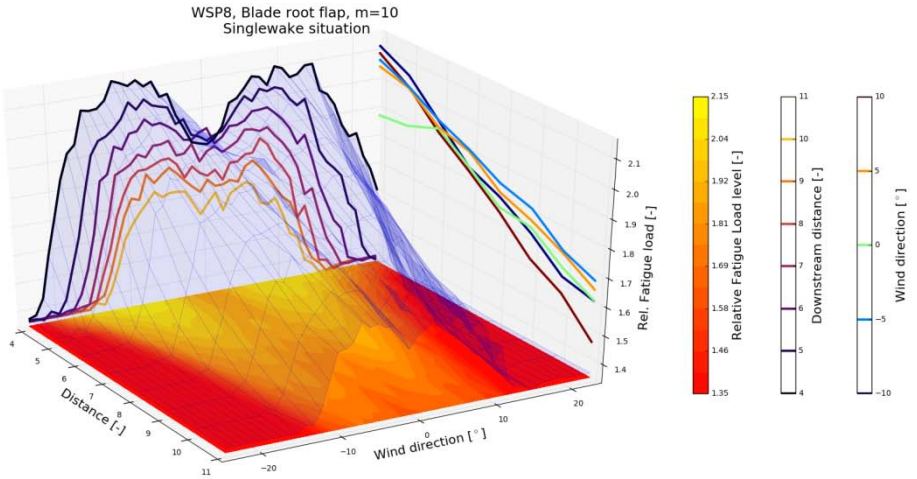

Figure D2: Blade root flap equivalent moment; U = 8m/s; TI = 9%.

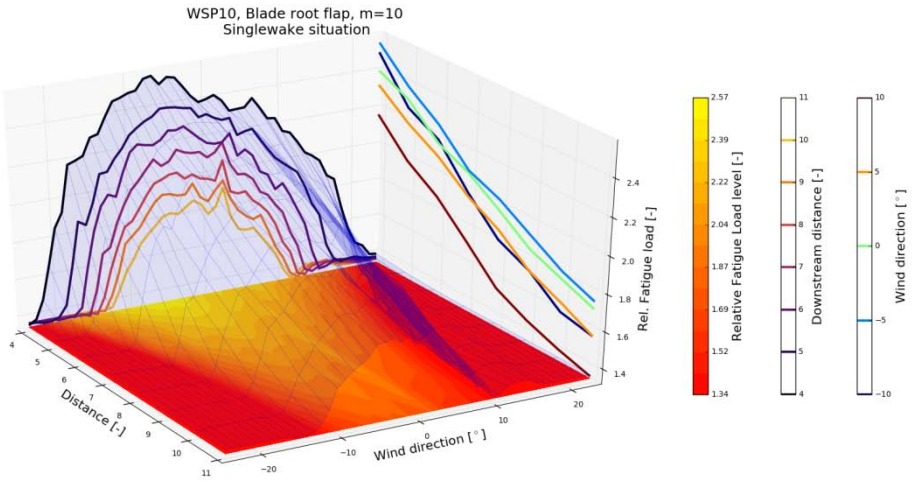

Figure D3: Blade root flap equivalent moment; U = 10m/s; TI = 9%.

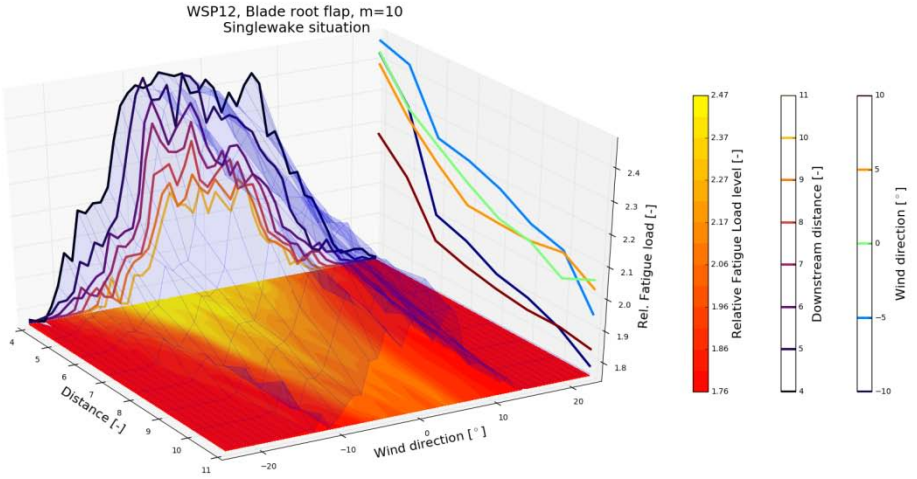

Figure D4: Blade root flap equivalent moment; U = 12m/s; TI = 9%.

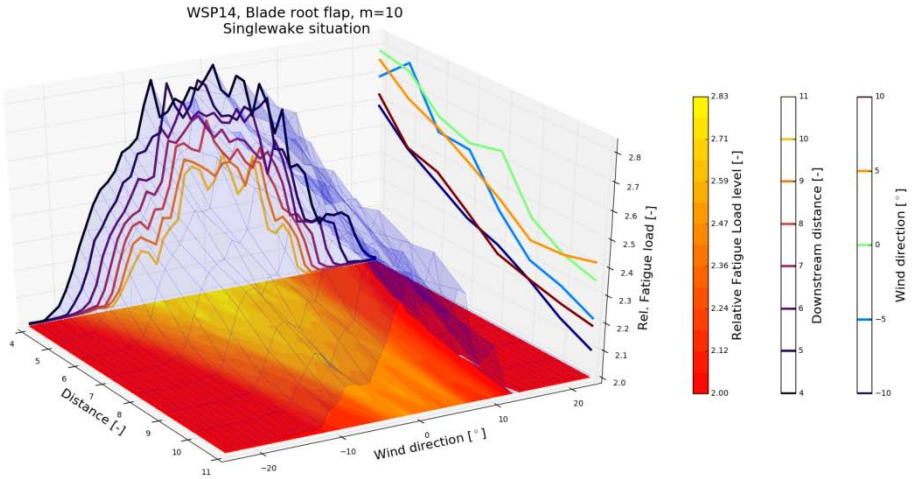

Figure D5: Blade root flap equivalent moment; U = 14m/s; TI = 9%.

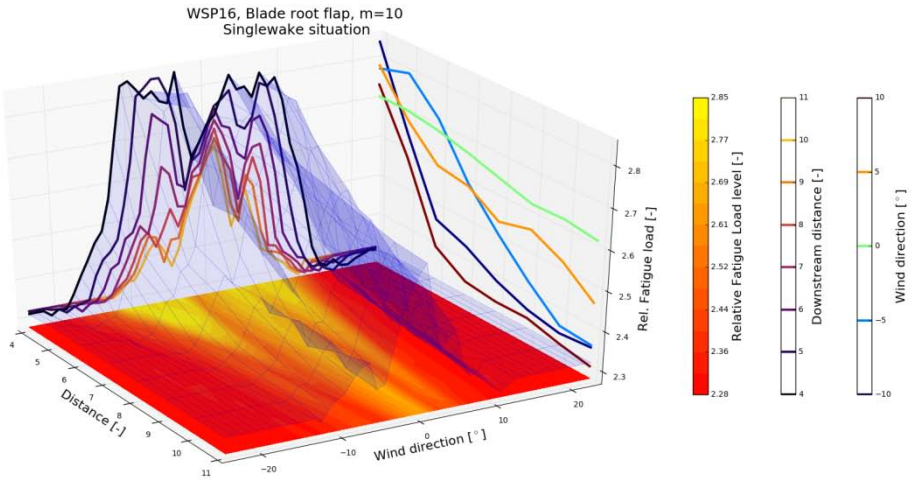

Figure D6: Blade root flap equivalent moment; U = 16m/s; TI = 9%.

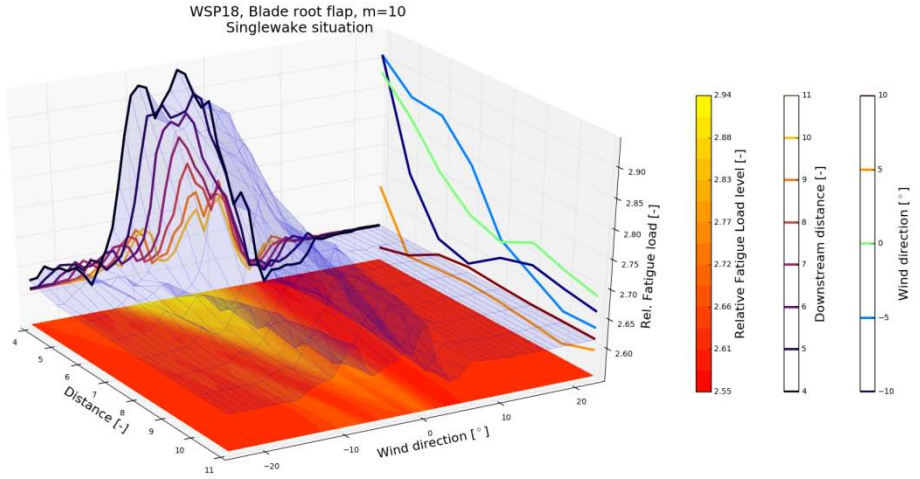

Figure D7: Blade root flap equivalent moment; U = 18m/s; TI = 9%.

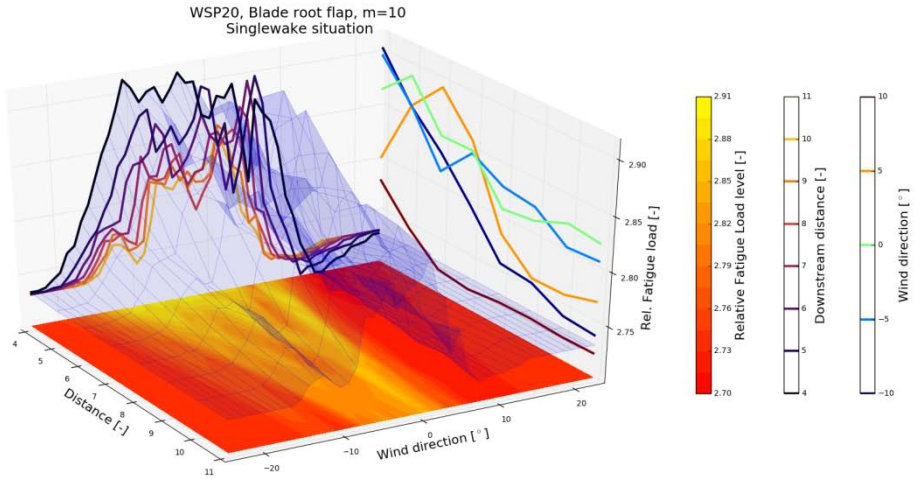

Figure D8: Blade root flap equivalent moment; U = 20m/s; TI = 9%.

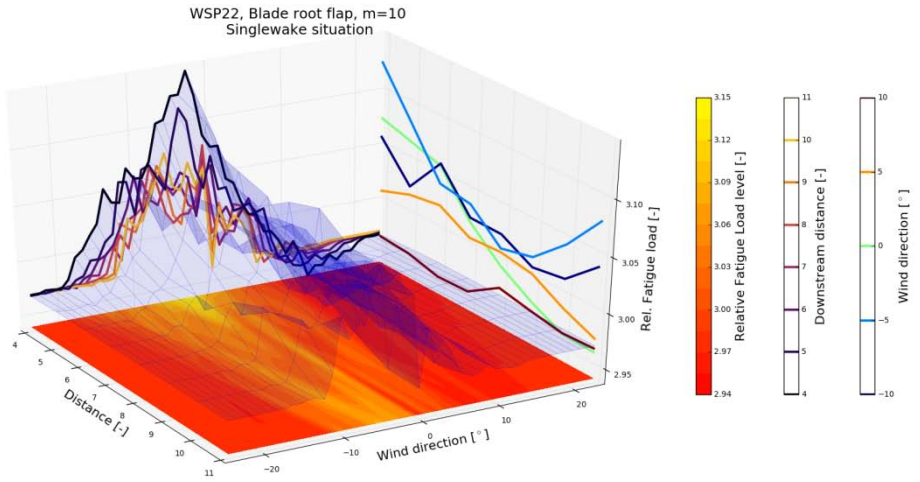

Figure D9: Blade root flap equivalent moment; U = 22m/s; TI = 9%.

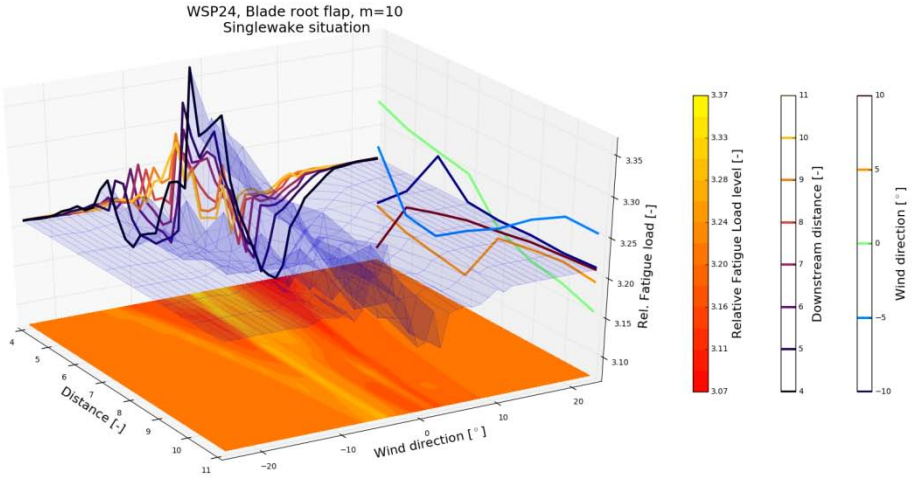

Figure D10: Blade root flap equivalent moment; U = 24m/s; TI = 9%.

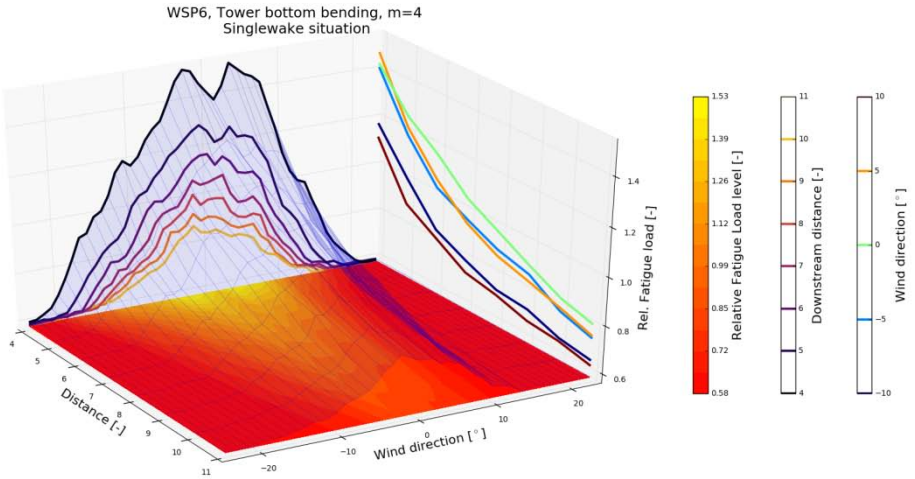

Figure D11: Tower bottom bending equivalent moment; U = 6m/s; TI = 9%.

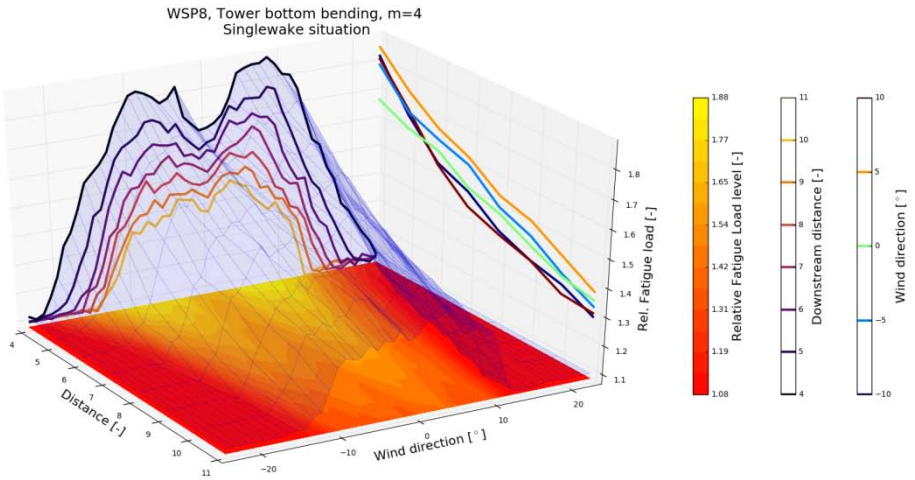

Figure D12: Tower bottom bending equivalent moment; U = 8m/s; TI = 9%.

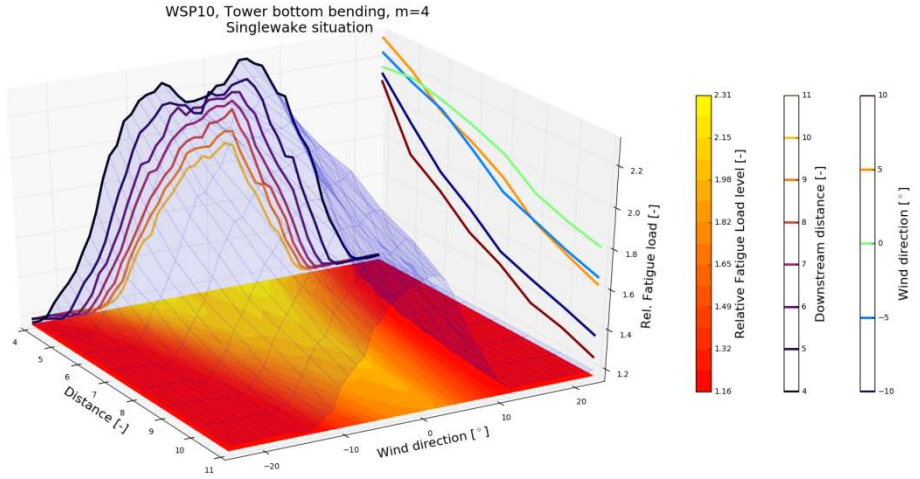

Figure D13: Tower bottom bending equivalent moment; U = 10m/s; TI = 9%.

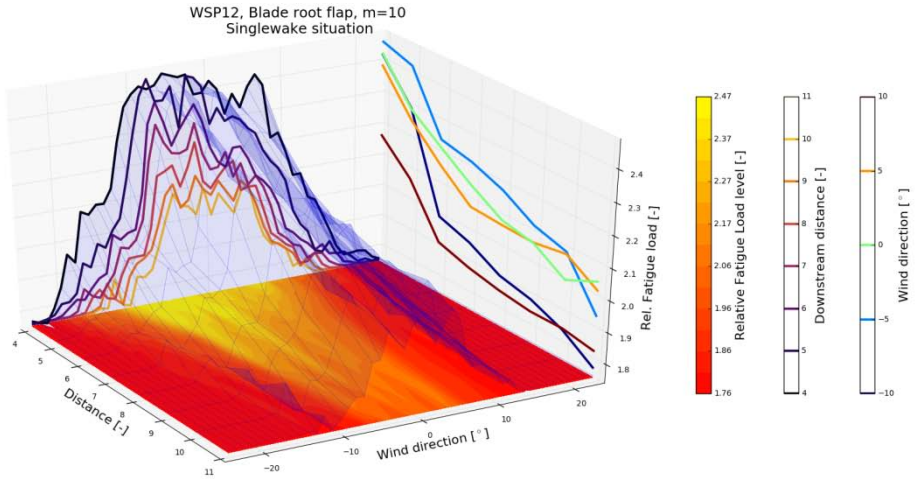

Figure D14: Tower bottom bending equivalent moment; U = 12m/s; TI = 9%.

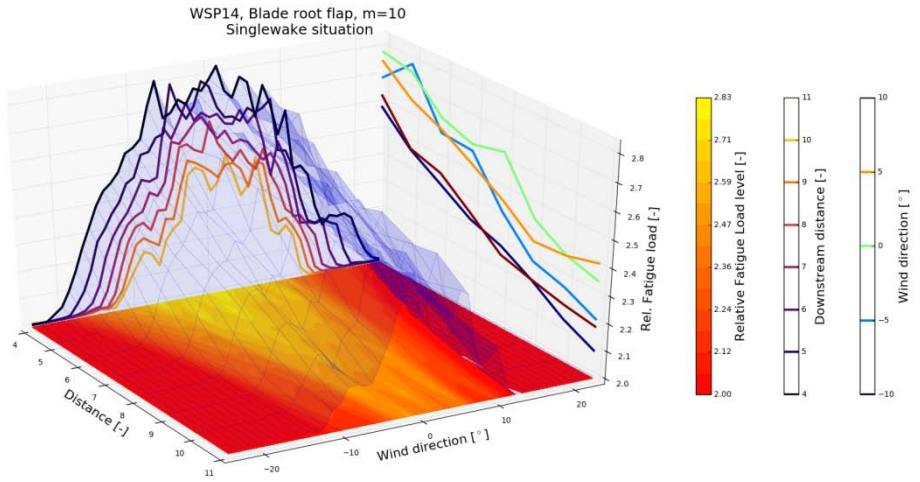

Figure D15: Tower bottom bending equivalent moment; U = 14m/s; TI = 9%.

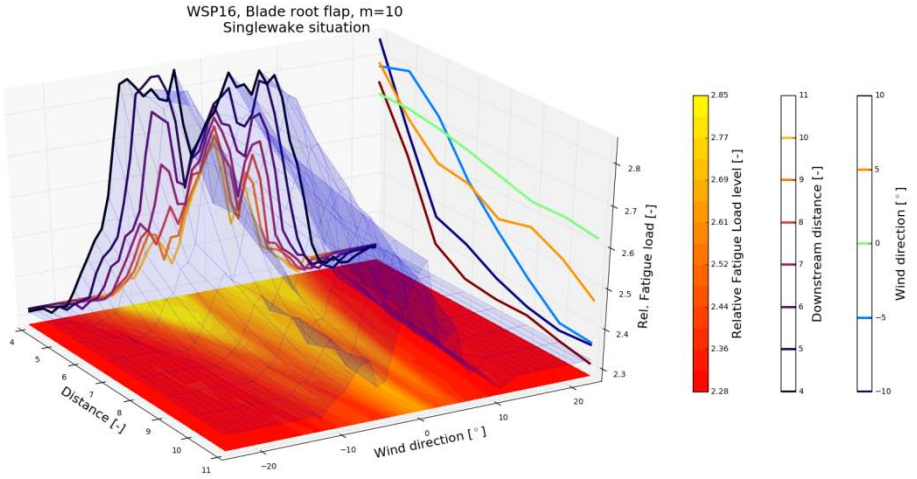

Figure D16: Tower bottom bending equivalent moment; U = 16m/s; TI = 9%.

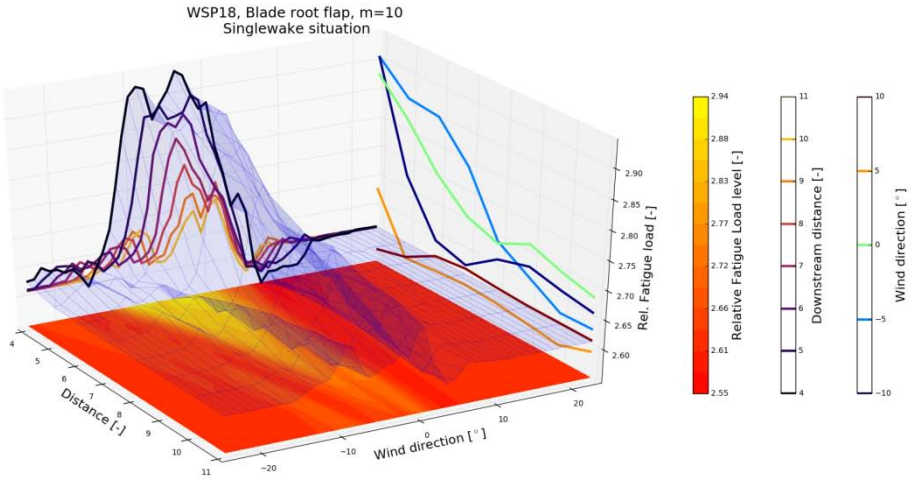

Figure D17: Tower bottom bending equivalent moment; U = 18m/s; TI = 9%.

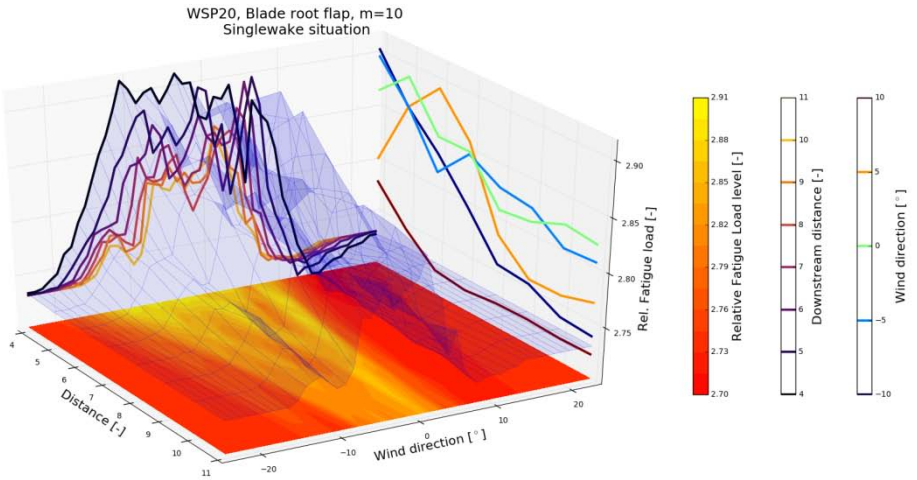

Figure D18: Tower bottom bending equivalent moment; U = 20m/s; TI = 9%.

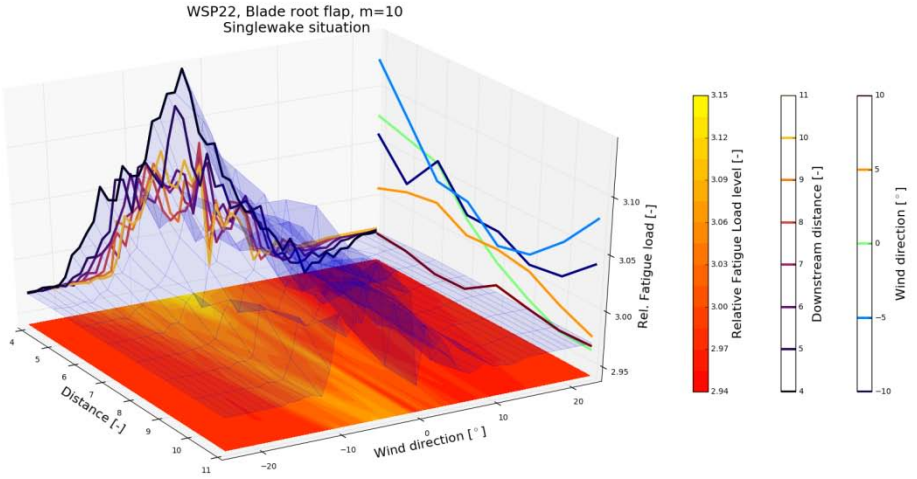

Figure D19: Tower bottom bending equivalent moment; U = 22m/s; TI = 9%.

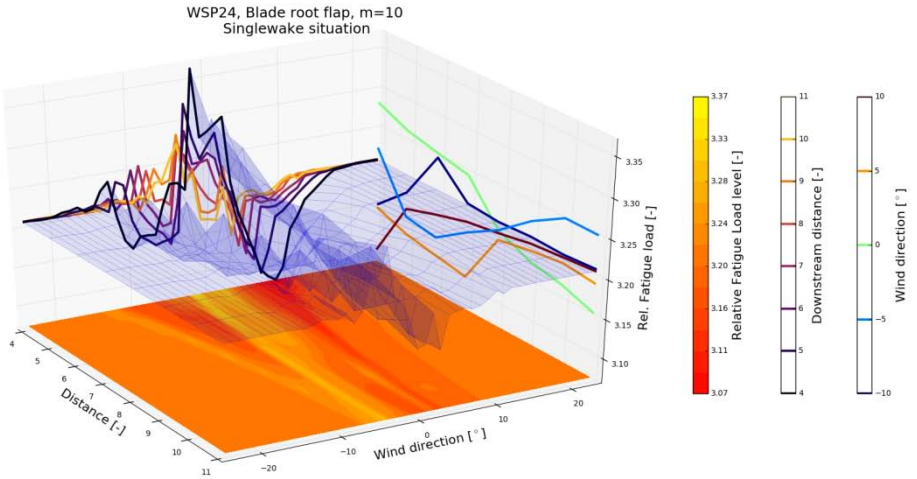

Figure D20: Tower bottom bending equivalent moment; U = 24m/s; TI = 9%.

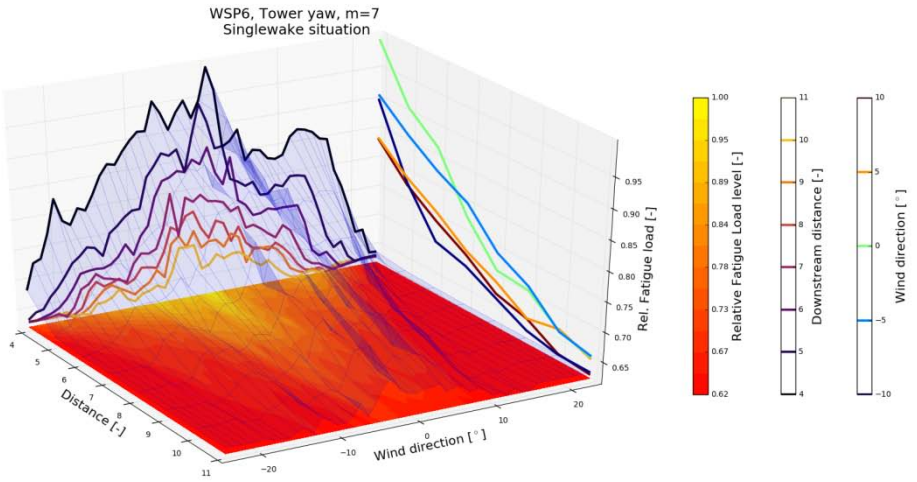

Figure D21: Tower top torsion equivalent moment; U = 6m/s; TI = 9%.

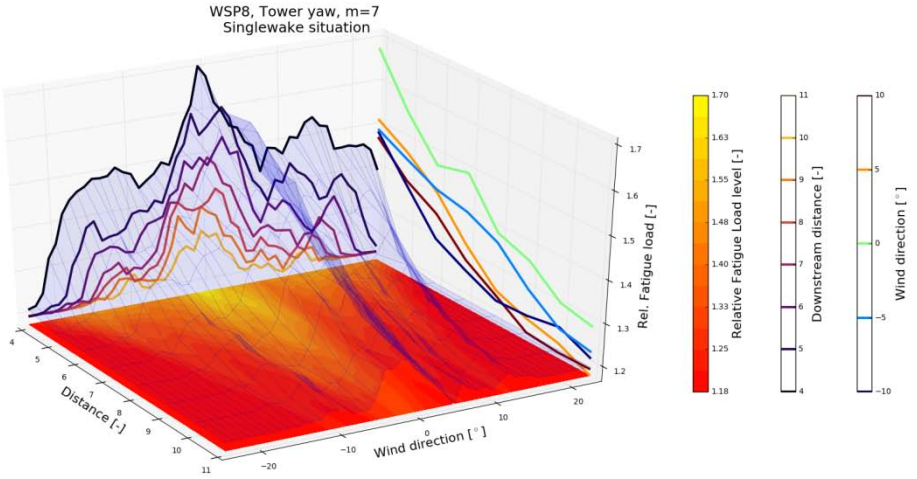

Figure D22: Tower top torsion equivalent moment; U = 8m/s; TI = 9%.

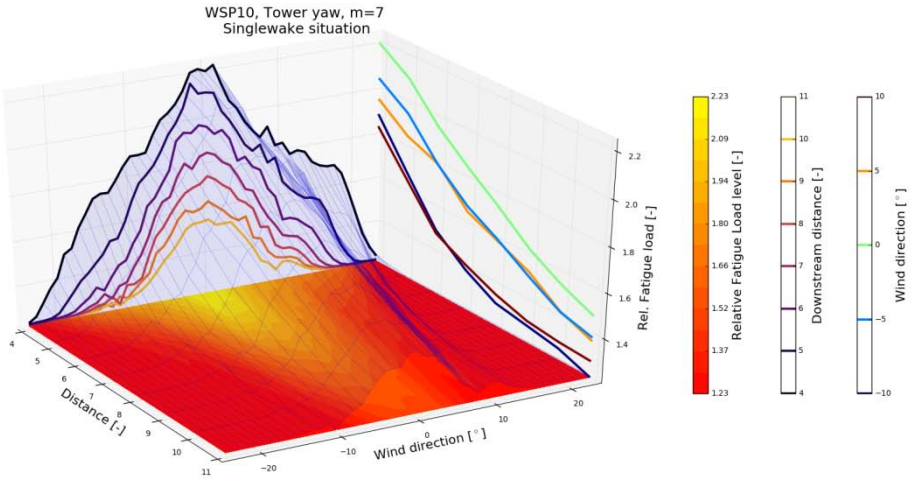

Figure D23: Tower top torsion equivalent moment; U = 10m/s; TI = 9%.

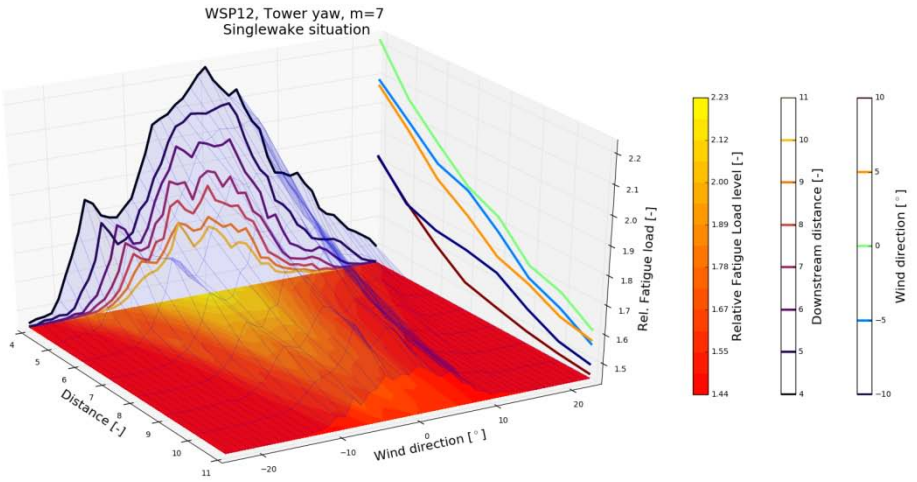

Figure D24: Tower top torsion equivalent moment; U = 12m/s; TI = 9%.

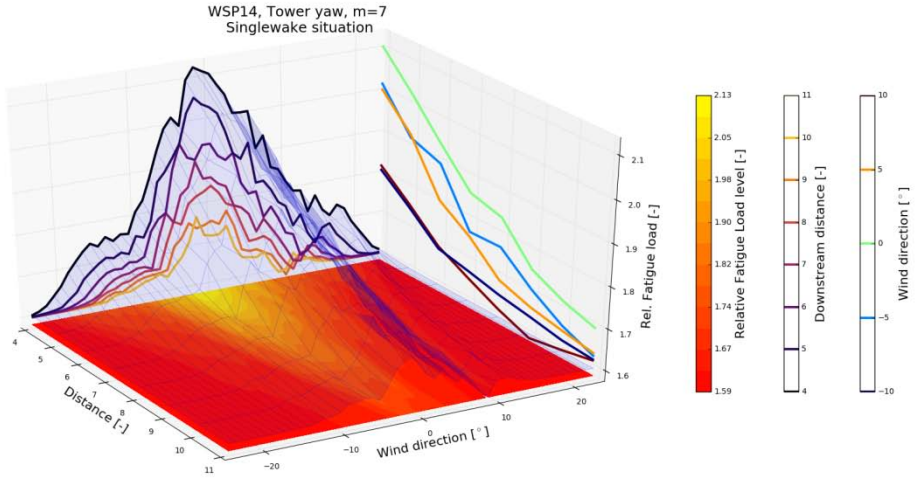

Figure D25: Tower top torsion equivalent moment; U = 14m/s; TI = 9%.

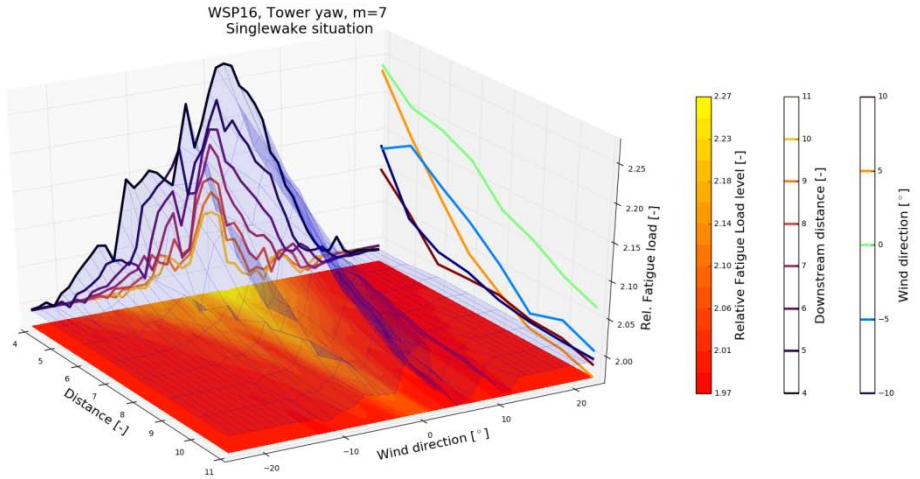

Figure D26: Tower top torsion equivalent moment; U = 16m/s; TI = 9%.

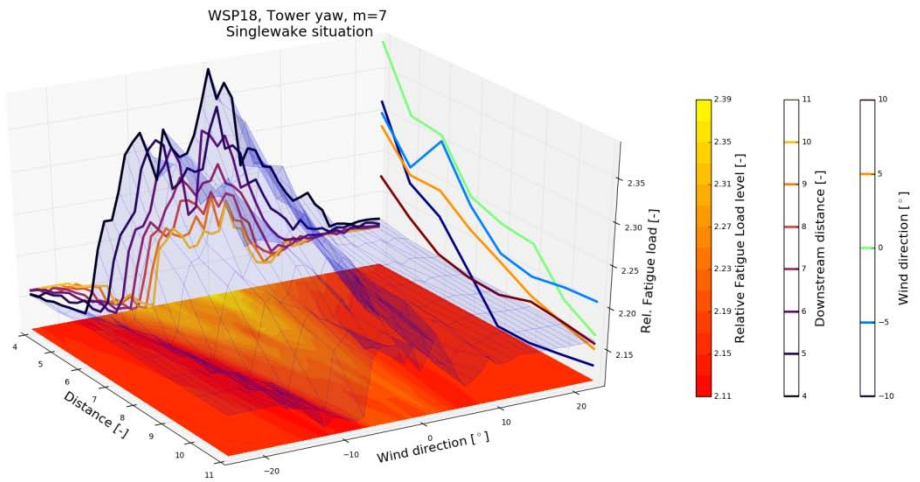

Figure D27: Tower top torsion equivalent moment; U = 18m/s; TI = 9%.

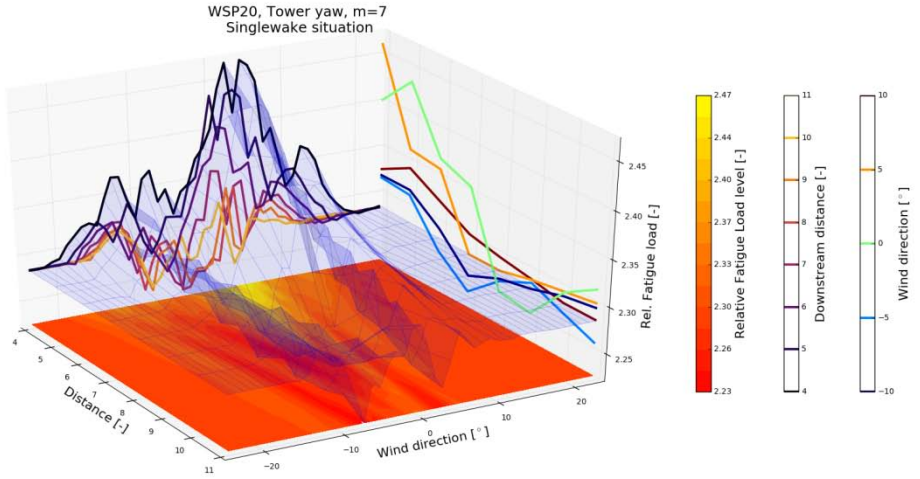

Figure D28: Tower top torsion equivalent moment; U = 20m/s; TI = 9%.

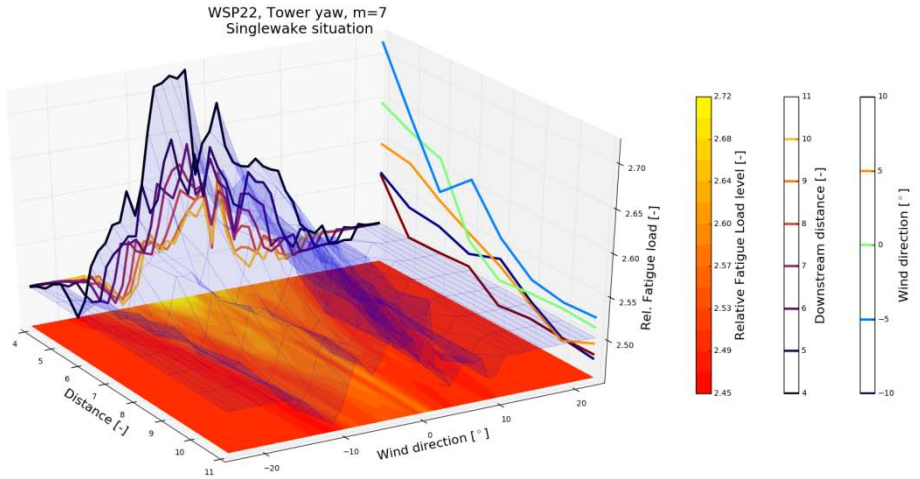

Figure D29: Tower top torsion equivalent moment; U = 22m/s; TI = 9%.

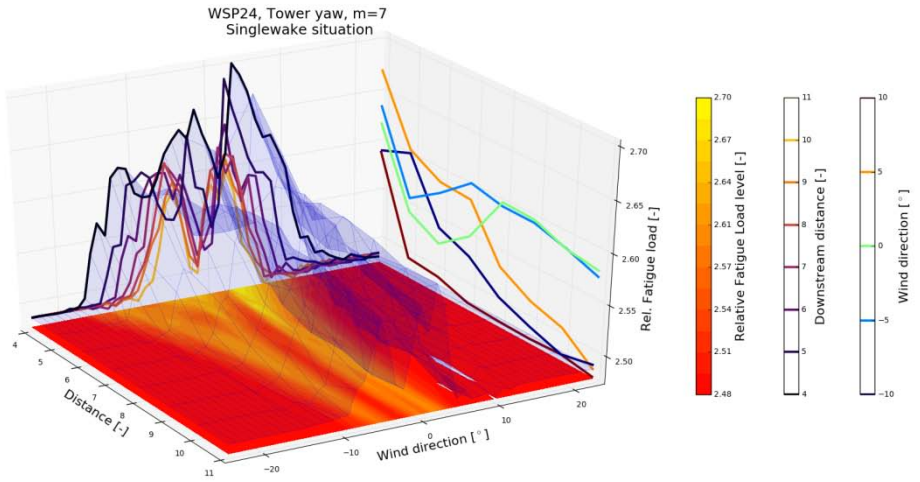

Figure D30: Tower top torsion equivalent moment; U = 24m/s; TI = 9%.

Appendix E

Measured wake cases

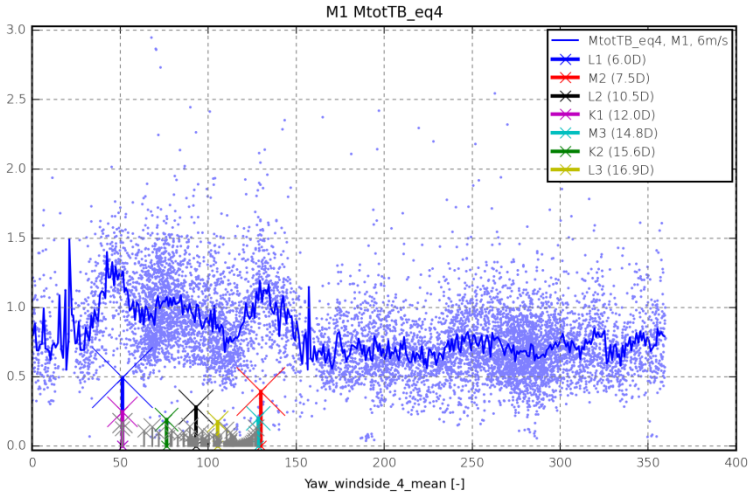

Figure E1: Tower bottom bending equivalent moment; WT M1; m = 4; U = 6m/s.

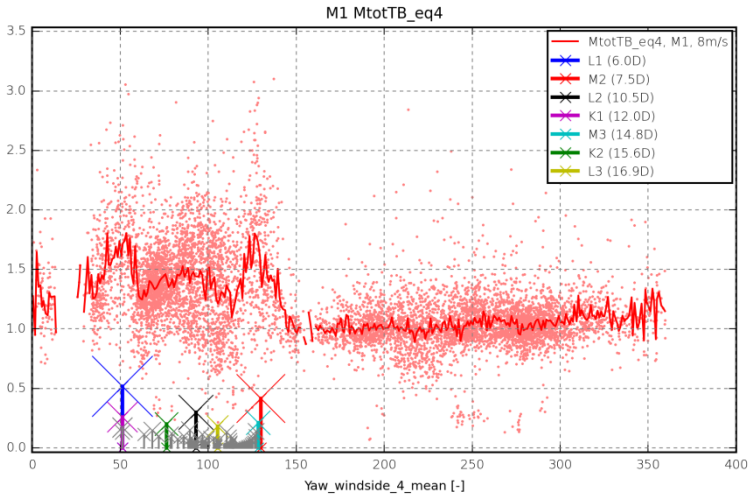

Figure E2: Tower bottom bending equivalent moment; WT M1; m = 4; U = 8m/s.

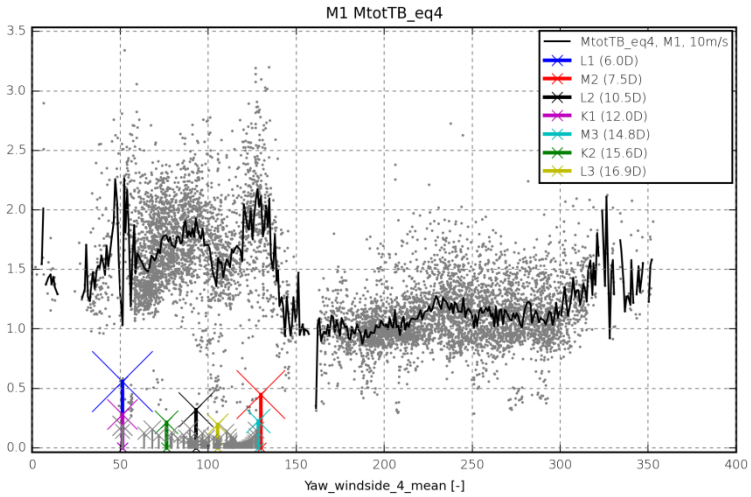

Figure E3: Tower bottom bending equivalent moment; WT M1; m = 4; U = 10m/s.

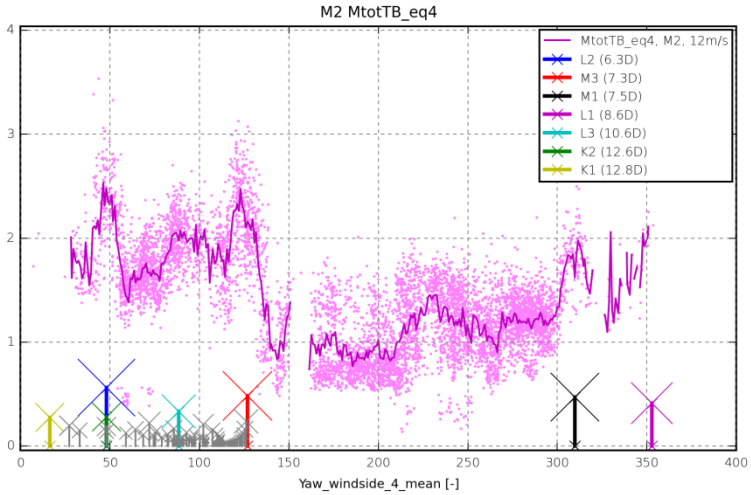

Figure E4: Tower bottom bending equivalent moment; WT M1; m = 4; U = 12m/s.

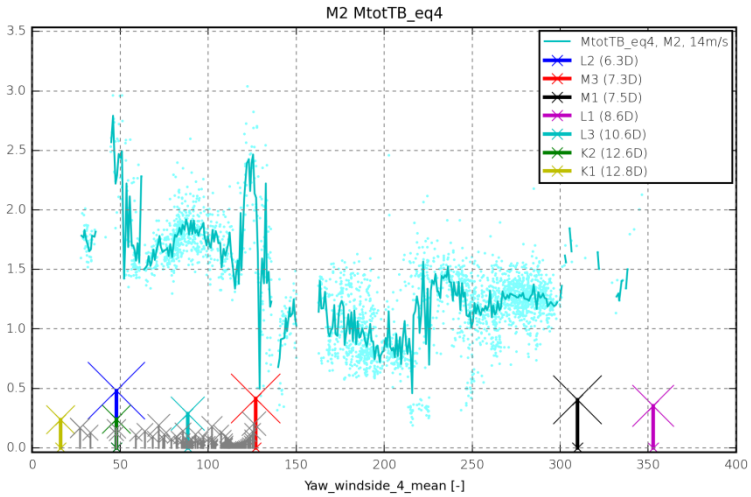

Figure E5: Tower bottom bending equivalent moment; WT M1; m = 4; U = 14m/s.

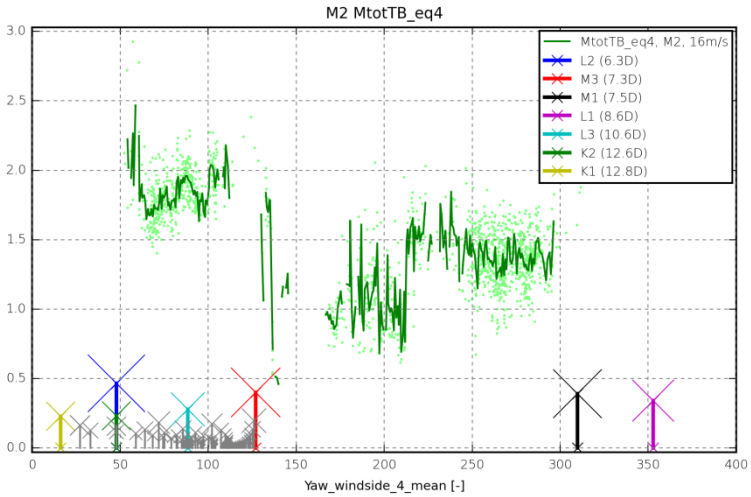

Figure E6: Tower bottom bending equivalent moment; WT M1; m = 4; U = 16m/s.

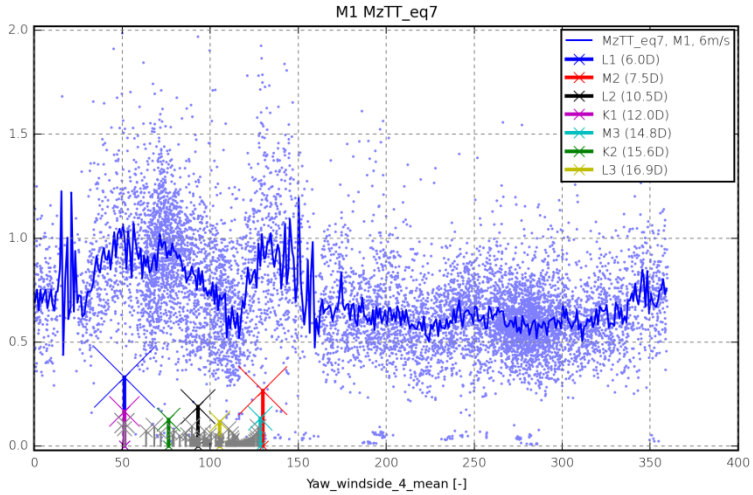

Figure E7: Tower top yaw equivalent moment; WT M1; m = 7; U = 6m/s.

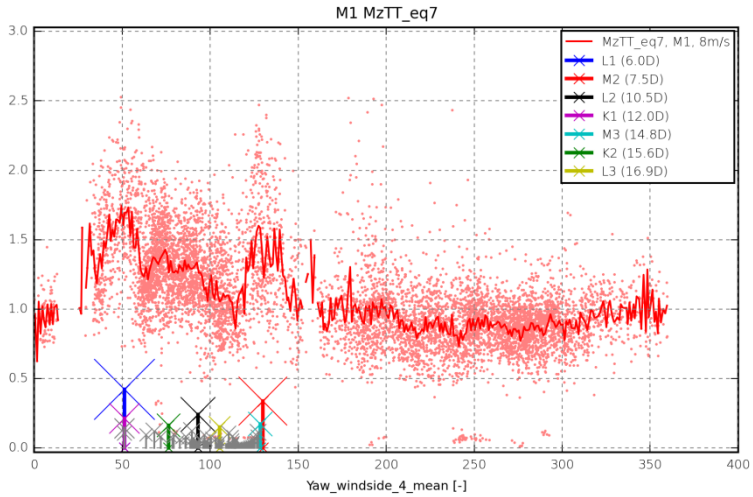

Figure E8: Tower top yaw equivalent moment; WT M1; m = 7; U = 8m/s.

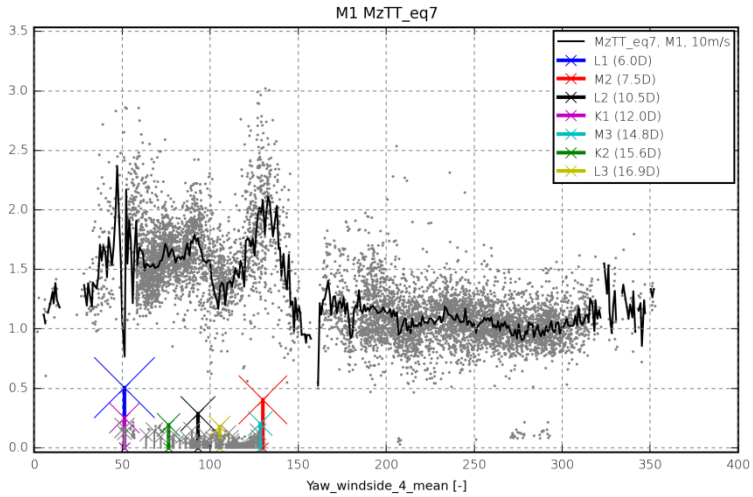

Figure E9: Tower top yaw equivalent moment; WT M1; m = 7; U = 10m/s.

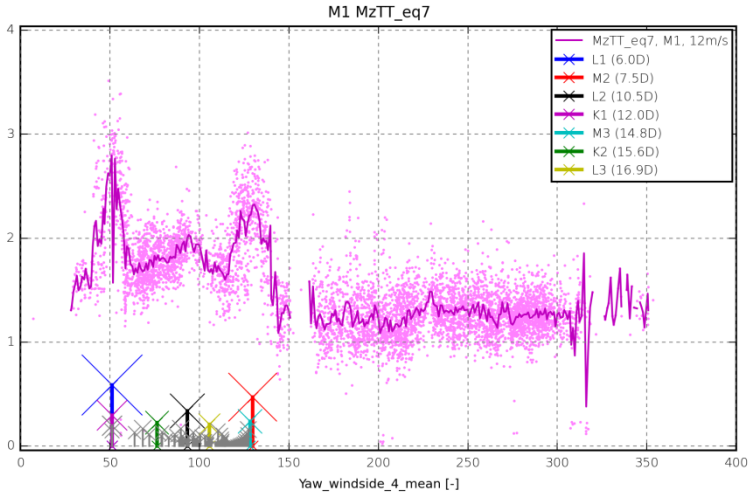

Figure E10: Tower top yaw equivalent moment; WT M1; m = 7; U = 12m/s.

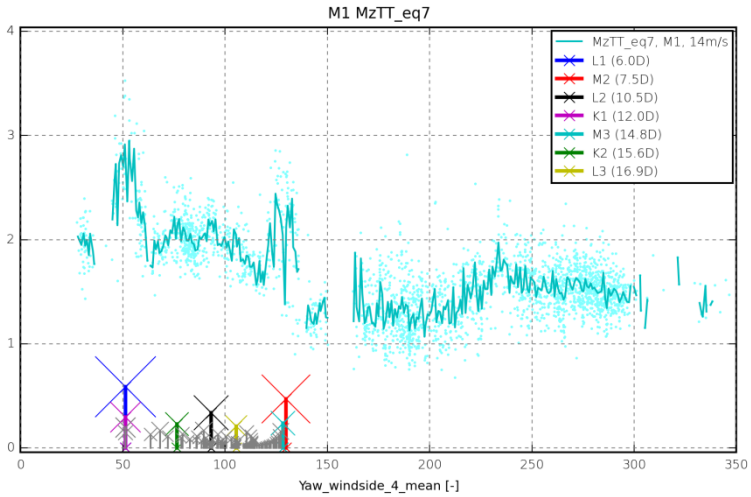

Figure E11: Tower top yaw equivalent moment; WT M1; m = 7; U = 14m/s.

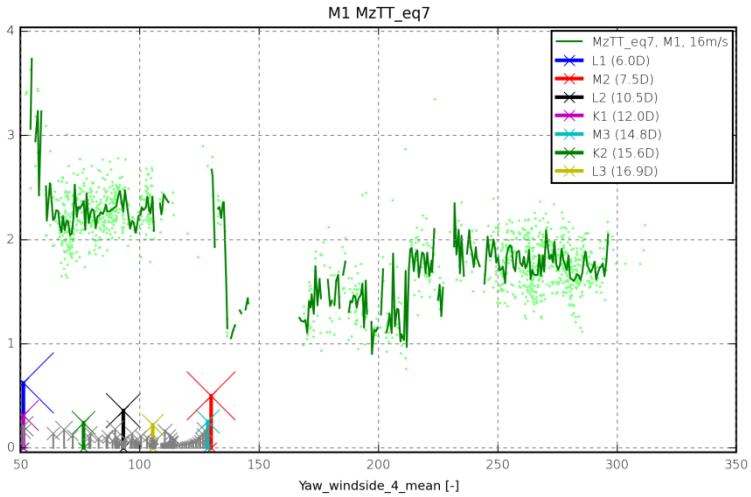

Figure E12: Tower top yaw equivalent moment; WT M1; m = 7; U = 16m/s.

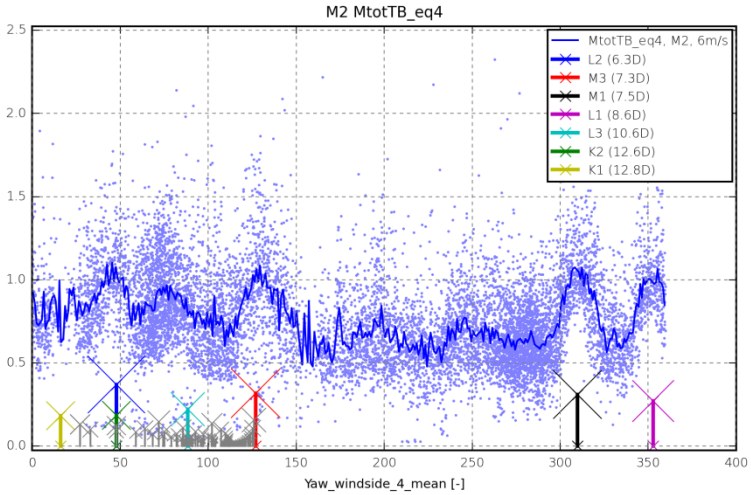

Figure E13: Tower bottom bending equivalent moment; WT M2; m = 4; U = 6m/s.

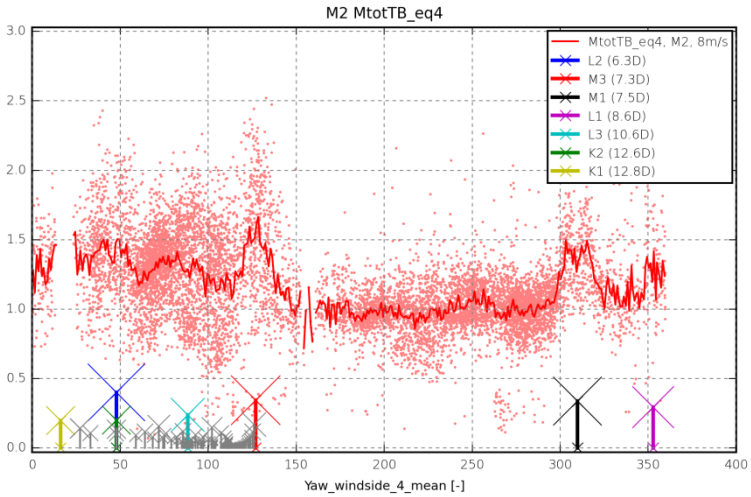

Figure E14: Tower bottom bending equivalent moment; WT M2; m = 4; U = 8m/s.

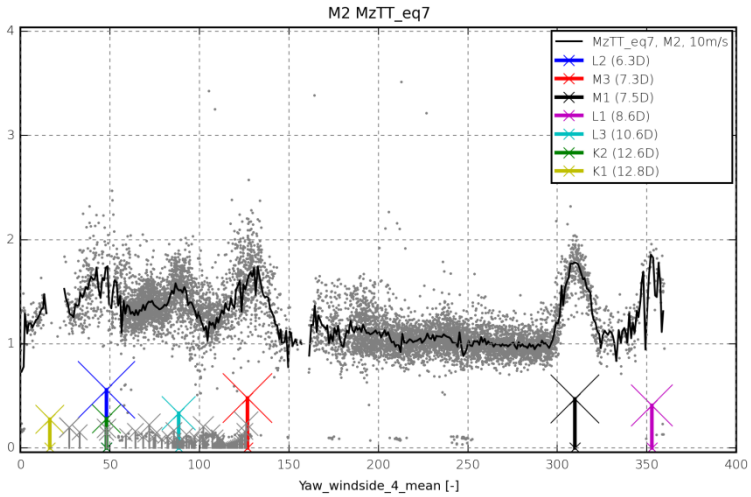

Figure E15: Tower bottom bending equivalent moment; WT M2; m = 4; U = 10m/s.

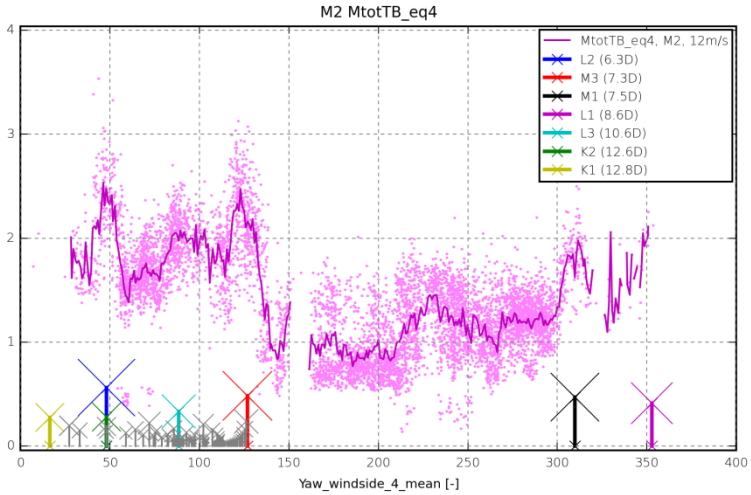

Figure E16: Tower bottom bending equivalent moment; WT M2; m = 4; U = 12m/s.

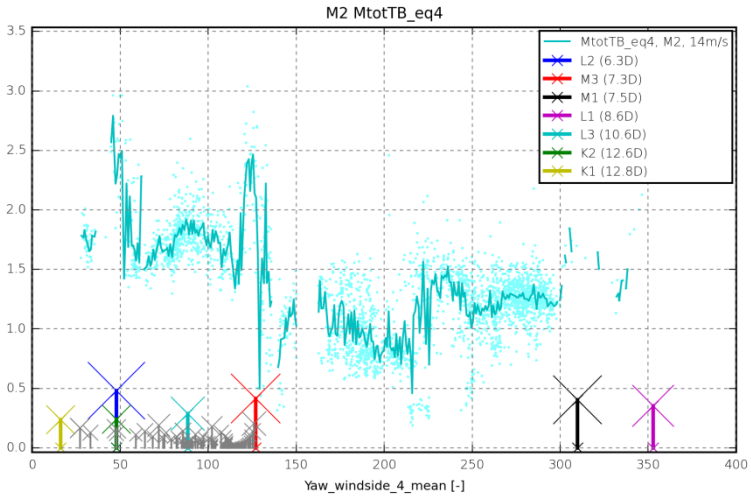

Figure E17: Tower bottom bending equivalent moment; WT M2; m = 4; U = 14m/s.

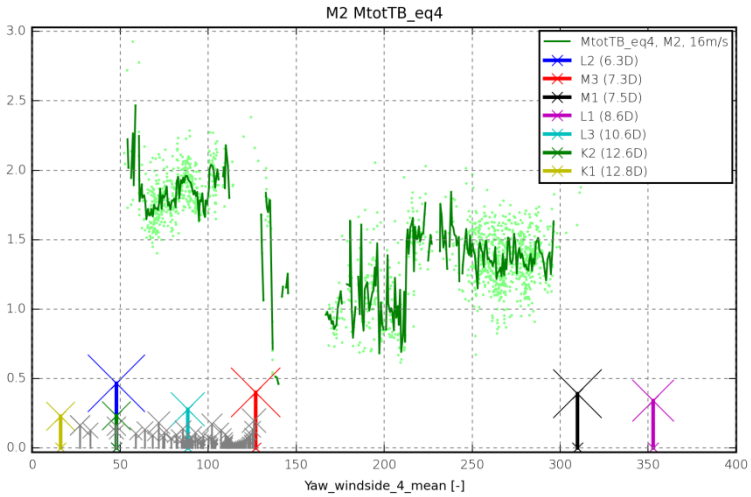

Figure E18: Tower bottom bending equivalent moment; WT M2; m = 4; U = 16m/s.

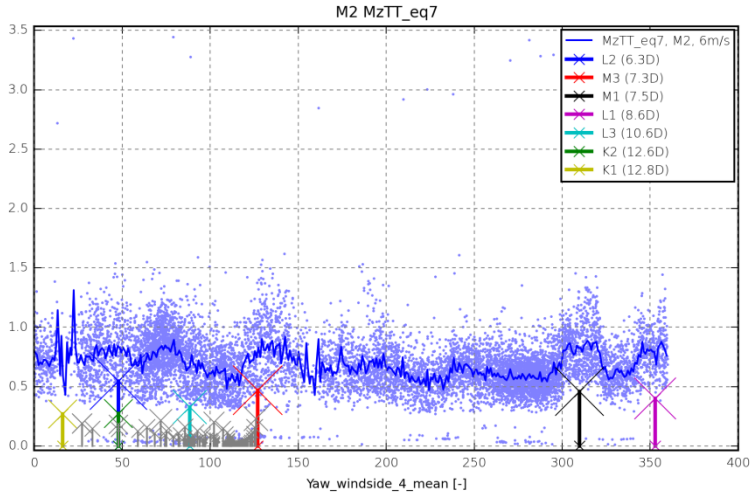

Figure E19: Tower top yaw equivalent moment; WT M2; m = 7; U = 6m/s.

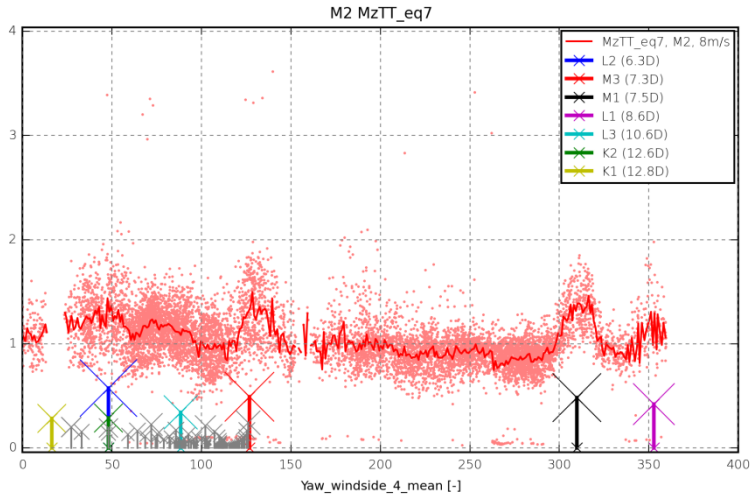

Figure E20: Tower top yaw equivalent moment; WT M2; m = 7; U = 8m/s.

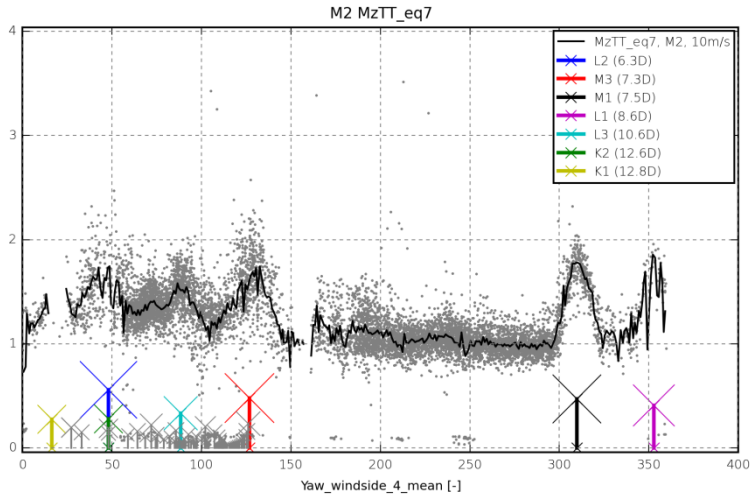

Figure E21: Tower top yaw equivalent moment; WT M2; m = 7; U = 10m/s.

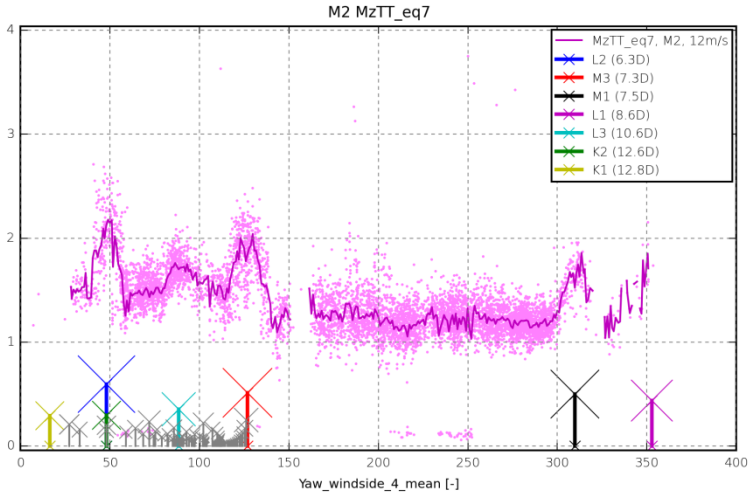

Figure E22: Tower top yaw equivalent moment; WT M2; m = 7; U = 12m/s.

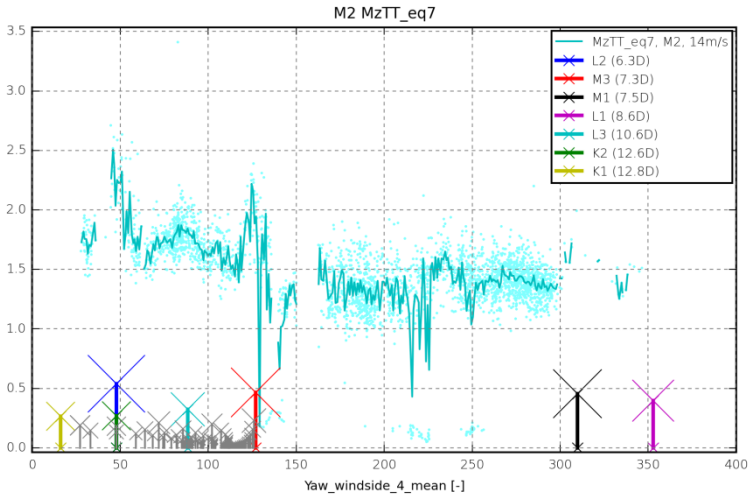

Figure E23: Tower top yaw equivalent moment; WT M2; m = 7; U = 14m/s.

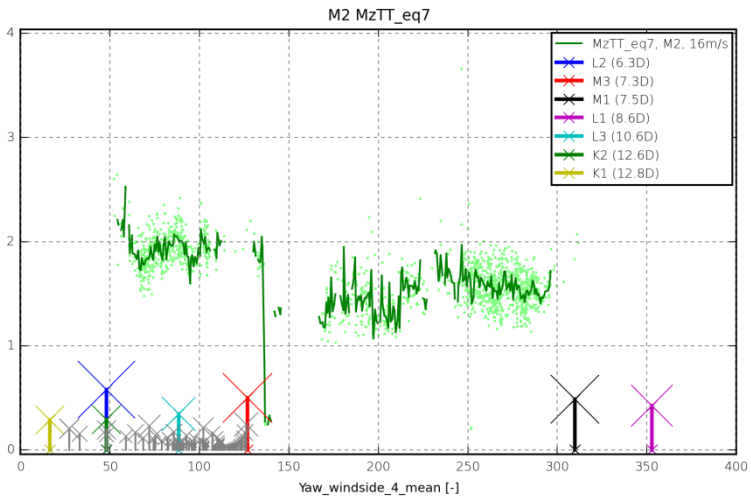

Figure E24: Tower top yaw equivalent moment; WT M2; m = 7; U = 16m/s.

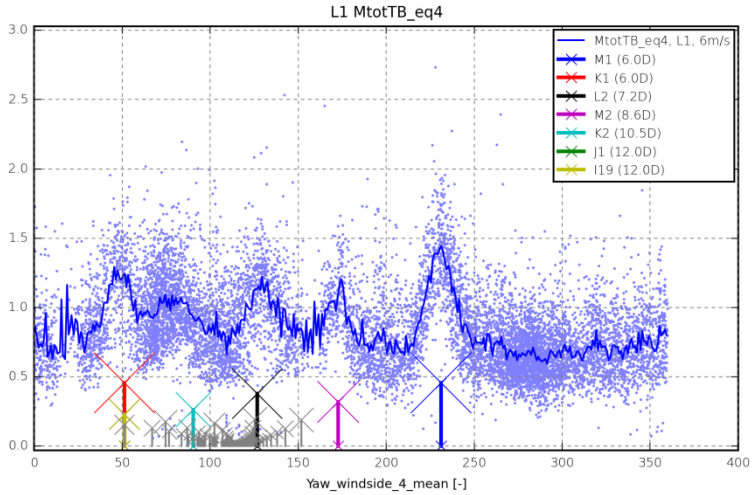

Figure E25: Tower bottom bending equivalent moment; WT L1; m = 4; U = 6m/s.

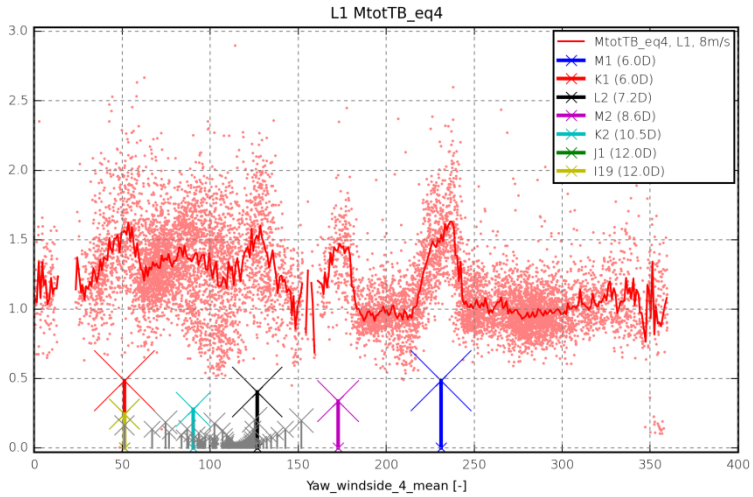

Figure E26: Tower bottom bending equivalent moment; WT L1; m = 4; U = 8m/s.

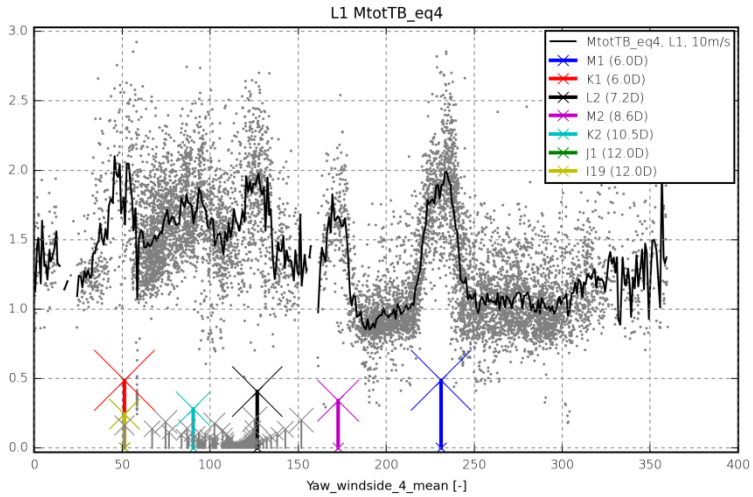

Figure E27: Tower bottom bending equivalent moment; WT L1; m = 4; U = 10m/s.

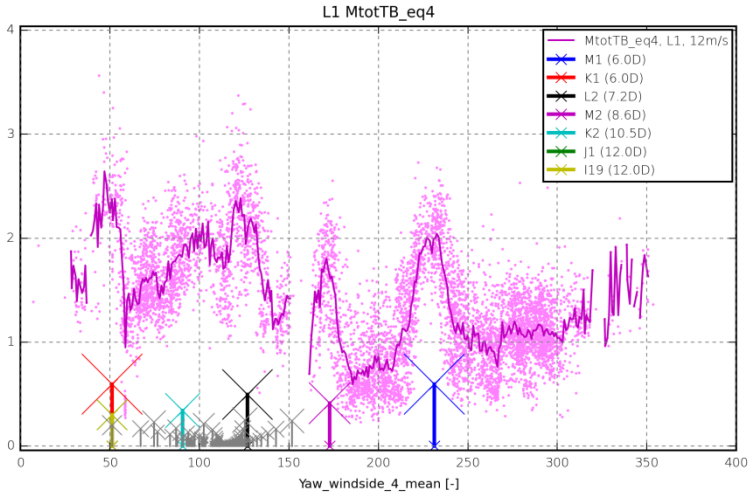

Figure E28: Tower bottom bending equivalent moment; WT L1; m = 4; U = 12m/s.

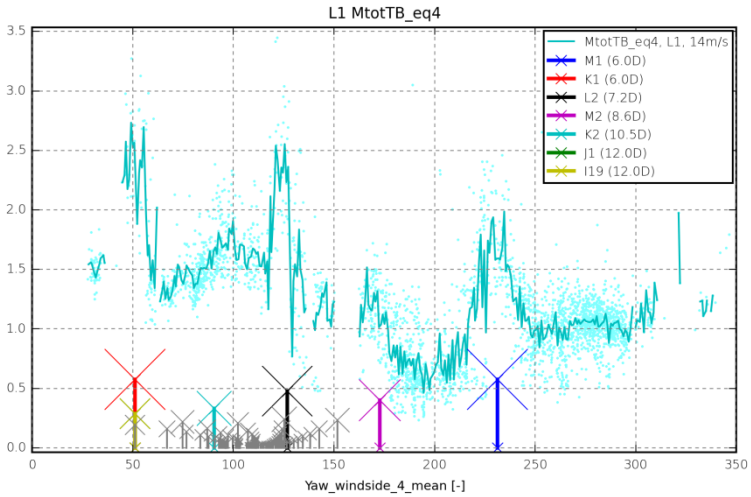

Figure E29: Tower bottom bending equivalent moment; WT L1; m = 4; U = 14m/s.

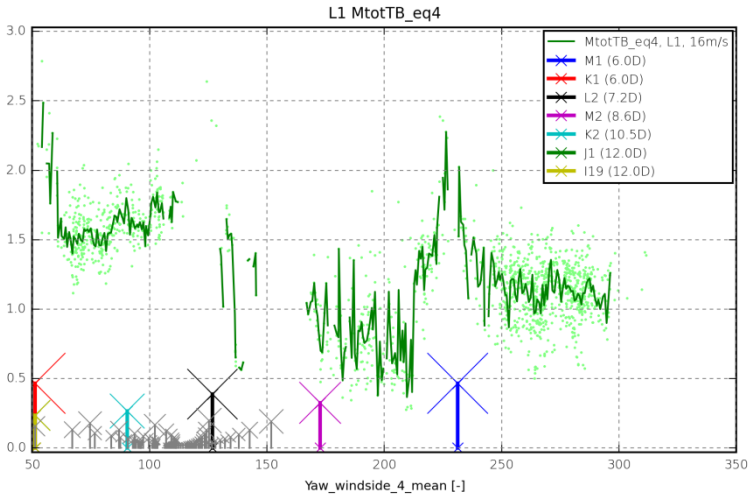

Figure E30: Tower bottom bending equivalent moment; WT L1; m = 4; U = 16m/s.

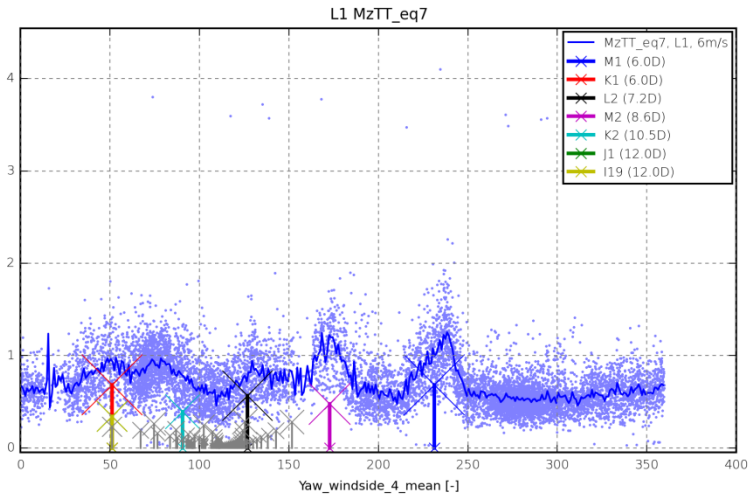

Figure E31: Tower top yaw equivalent moment; WT L1; m = 7; U = 6m/s.

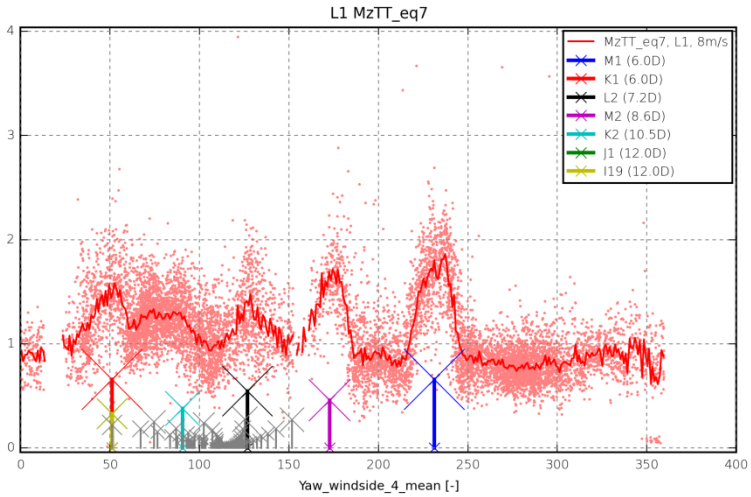

Figure E32: Tower top yaw equivalent moment; WT L1; m = 7; U = 8m/s.

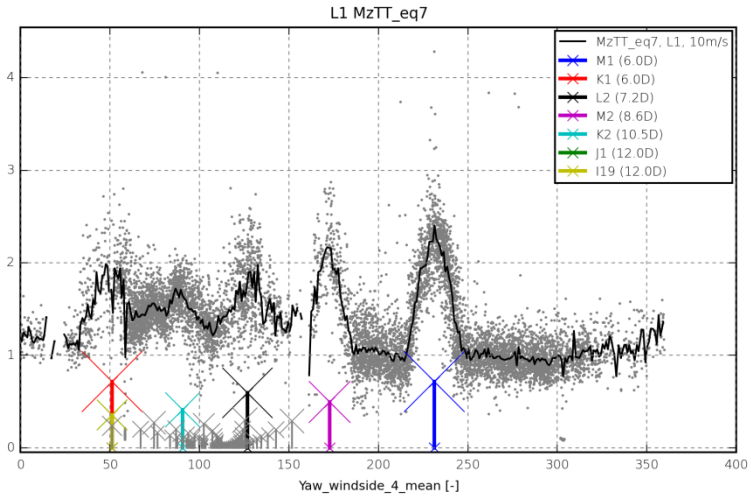

Figure E33: Tower top yaw equivalent moment; WT L1; m = 7; U = 10m/s.

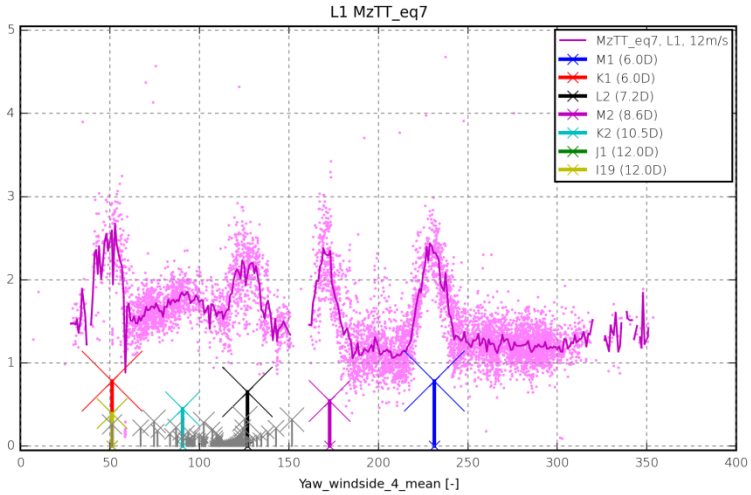

Figure E34: Tower top yaw equivalent moment; WT L1; m = 7; U = 12m/s.

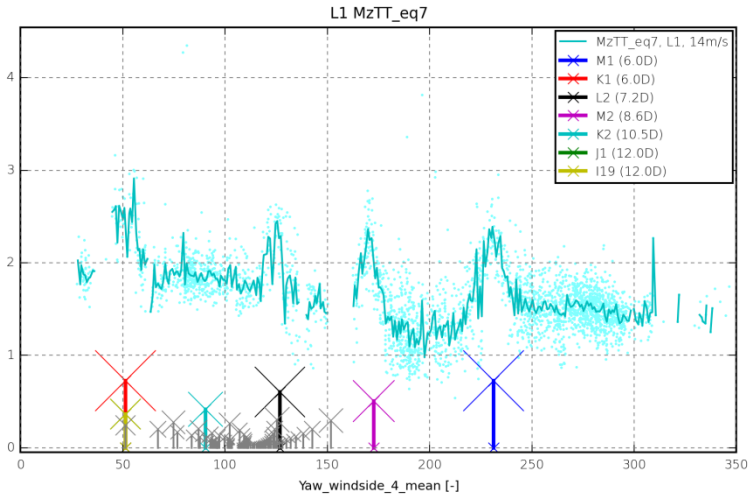

Figure E35: Tower top yaw equivalent moment; WT L1; m = 7; U = 14m/s.

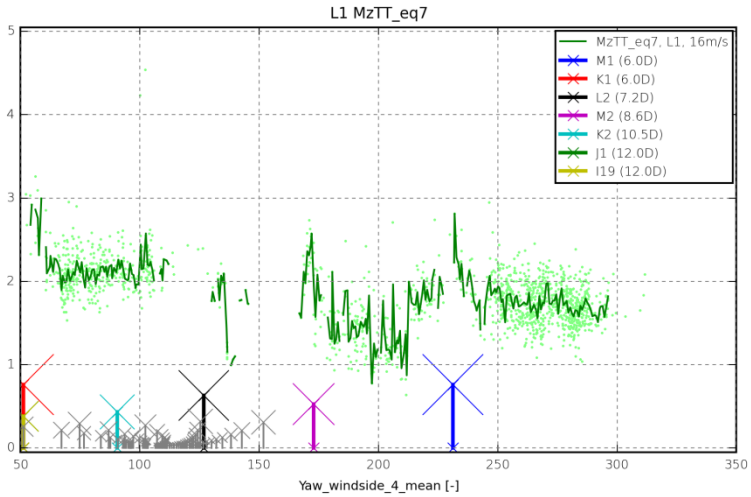

Figure E36: Tower top yaw equivalent moment; WT L1; m = 7; U = 16m/s.

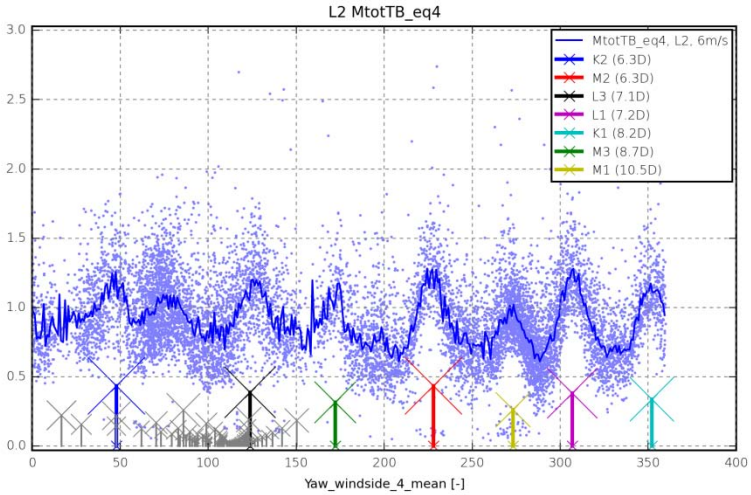

Figure E37: Tower bottom bending equivalent moment; WT L2; m = 4; U = 6m/s.

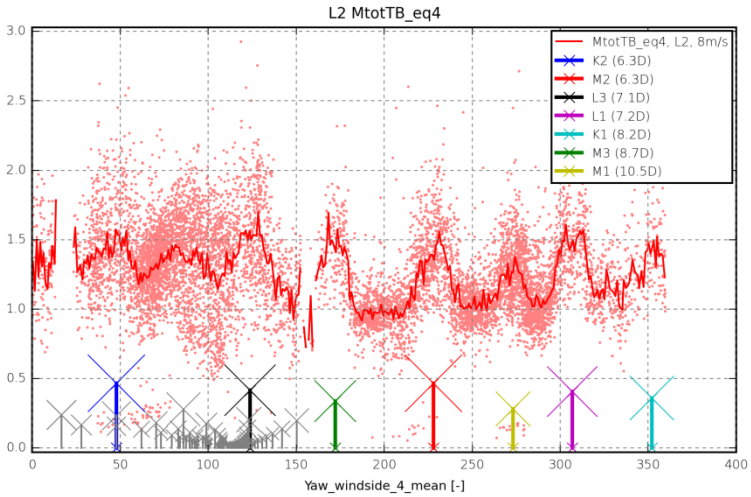

Figure E38: Tower bottom bending equivalent moment; WT L2; m = 4; U = 8m/s.

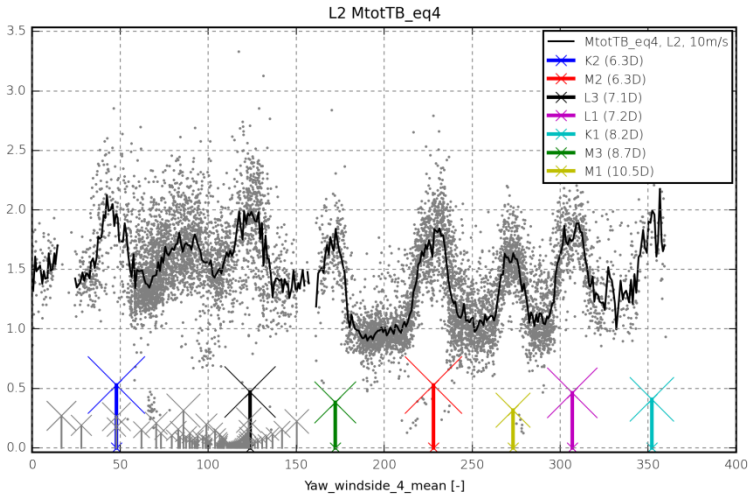

Figure E39: Tower bottom bending equivalent moment; WT L2; m = 4; U = 10m/s.

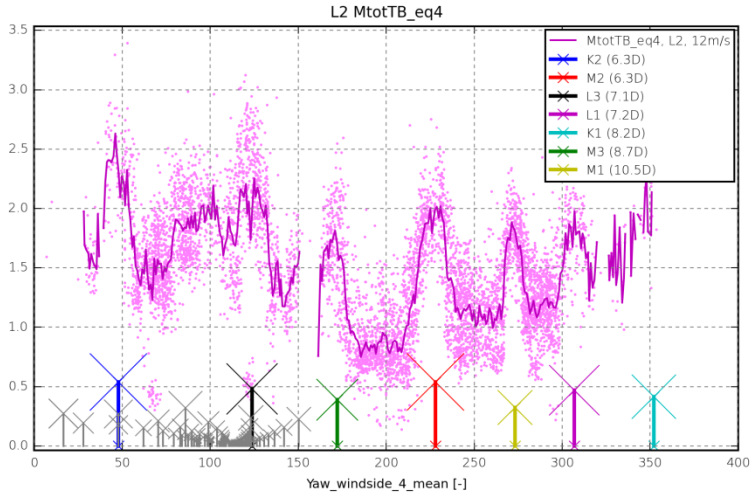

Figure E40: Tower bottom bending equivalent moment; WT L2; m = 4; U = 12m/s.

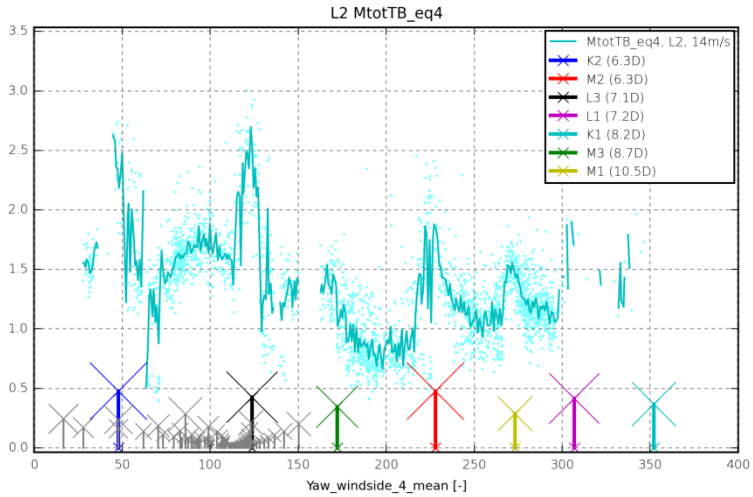

Figure E41: Tower bottom bending equivalent moment; WT L2; m = 4; U = 14m/s.

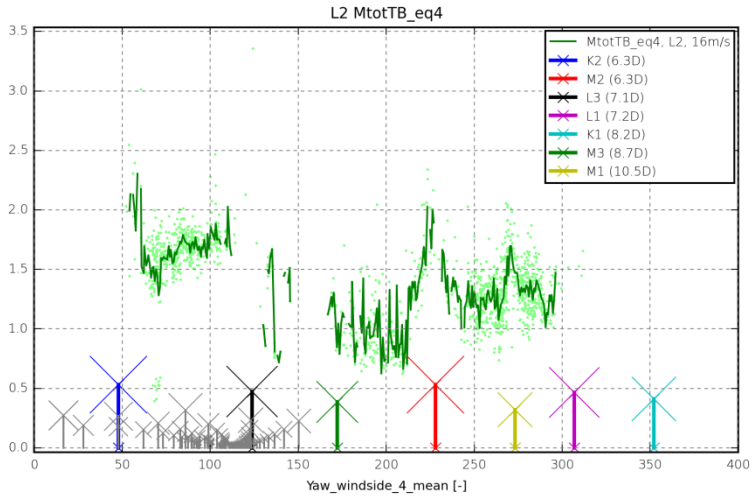

Figure E42: Tower bottom bending equivalent moment; WT L2; m = 4; U = 16m/s.

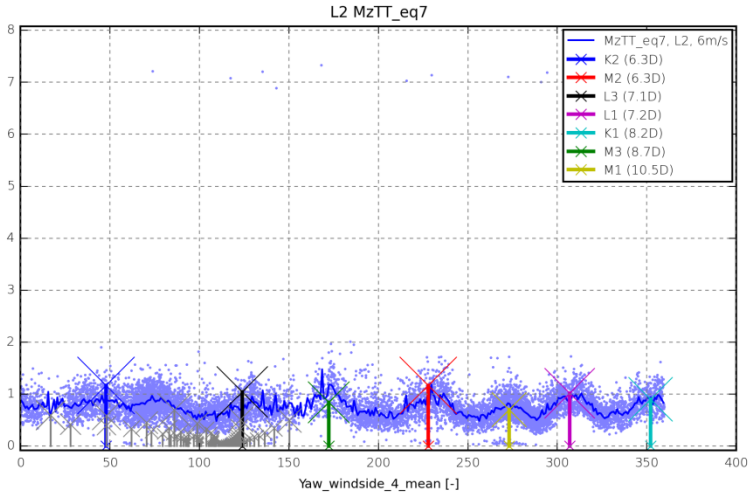

Figure E43: Tower top yaw equivalent moment; WT L2; m = 7; U = 6m/s.

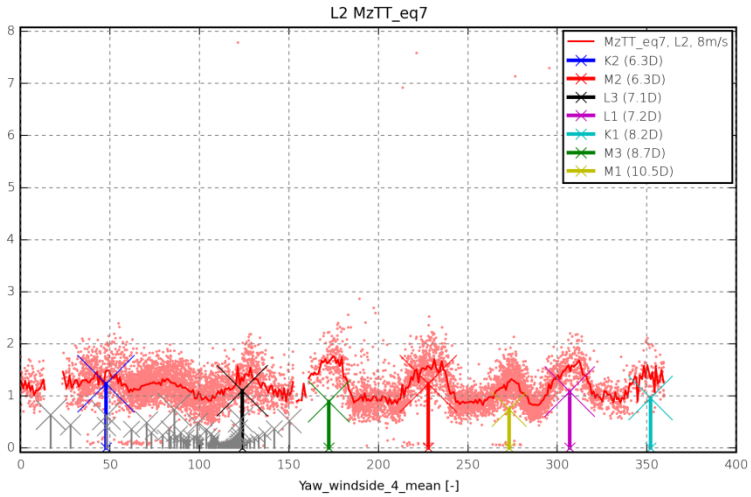

Figure E44: Tower top yaw equivalent moment; WT L2; m = 7; U = 8m/s.

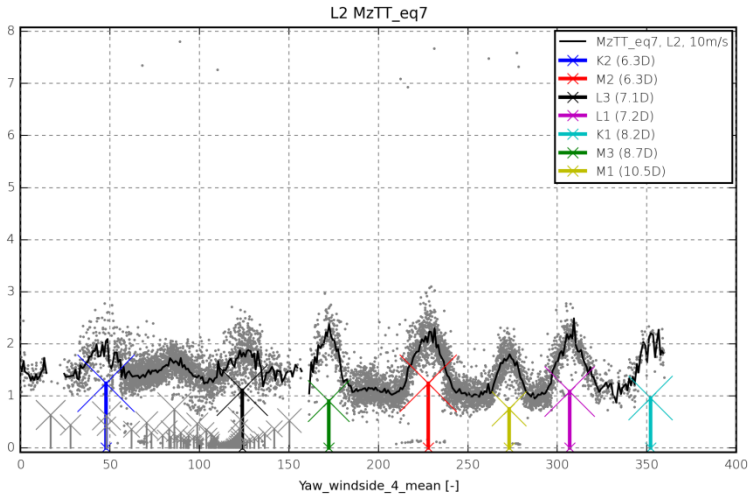

Figure E45: Tower top yaw equivalent moment; WT L2; m = 7; U = 10m/s.

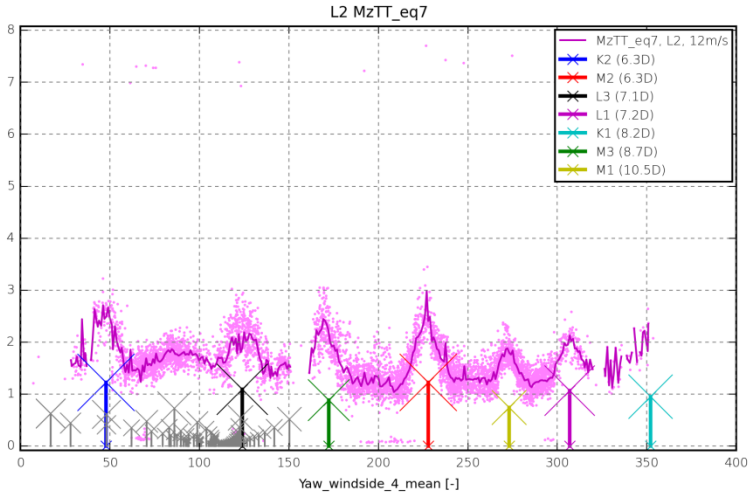

Figure E46: Tower top yaw equivalent moment; WT L2; m = 7; U = 12m/s.

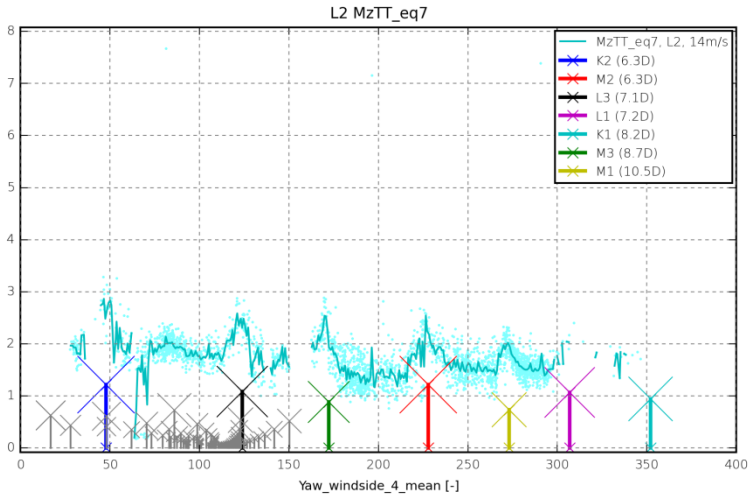

Figure E47: Tower top yaw equivalent moment; WT L2; m = 7; U = 14m/s.

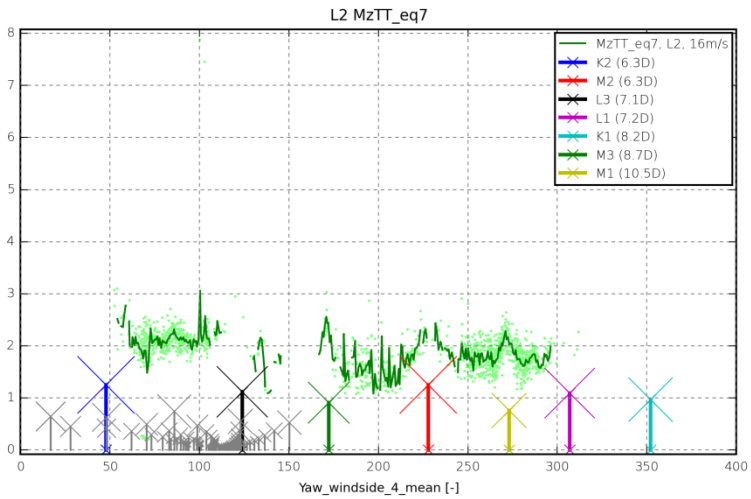

Figure E48: Tower top yaw equivalent moment; WT L2; m = 7; U = 16m/s.

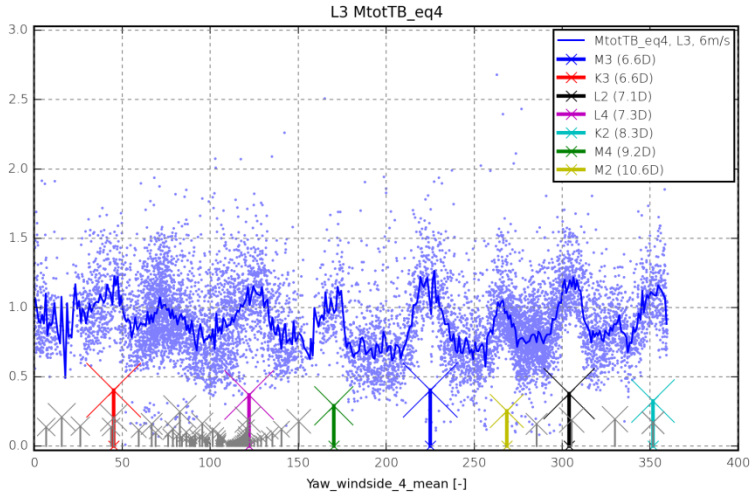

Figure E49: Tower bottom bending equivalent moment; WT L3; m = 4; U = 6m/s.

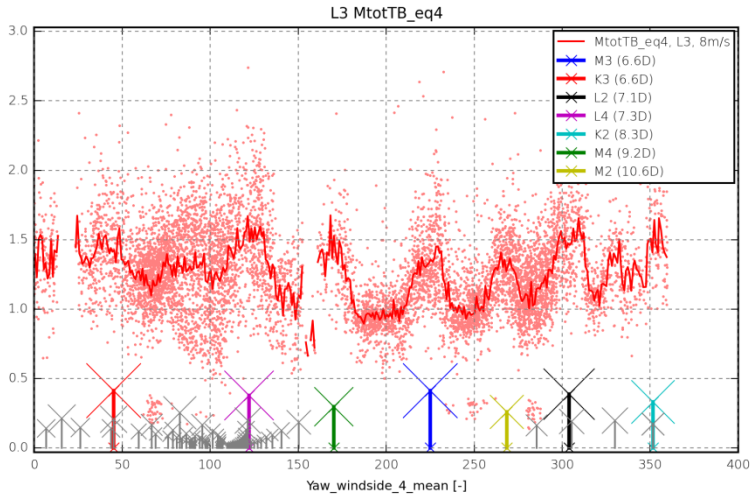

Figure E50: Tower bottom bending equivalent moment; WT L3; m = 4; U = 8m/s.

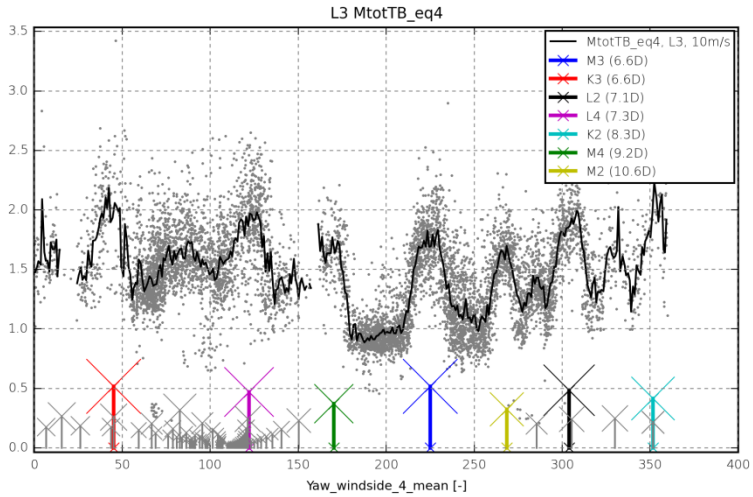

Figure E51: Tower bottom bending equivalent moment; WT L3; m = 4; U = 10m/s.

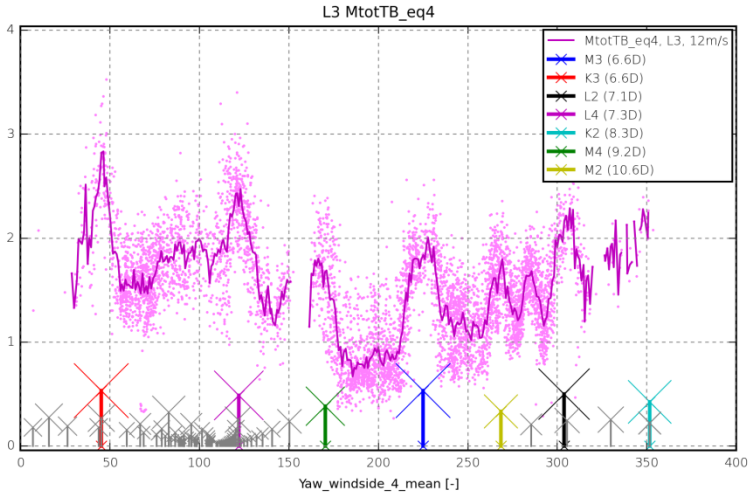

Figure E52: Tower bottom bending equivalent moment; WT L3; m = 4; U = 12m/s.

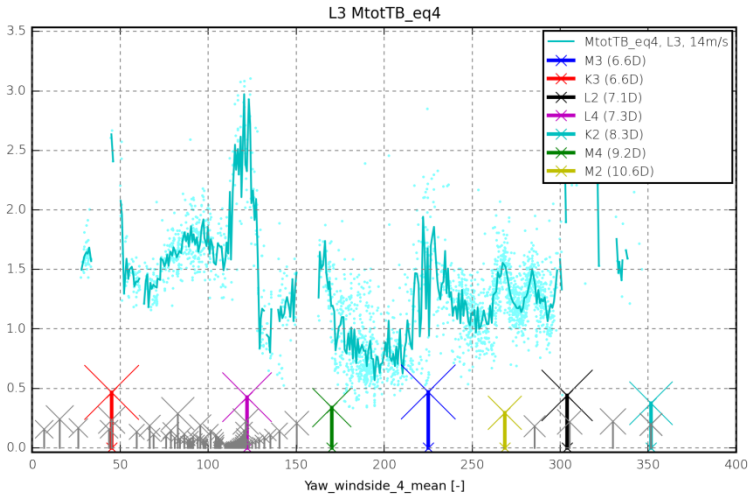

Figure E53: Tower bottom bending equivalent moment; WT L3; m = 4; U = 14m/s.

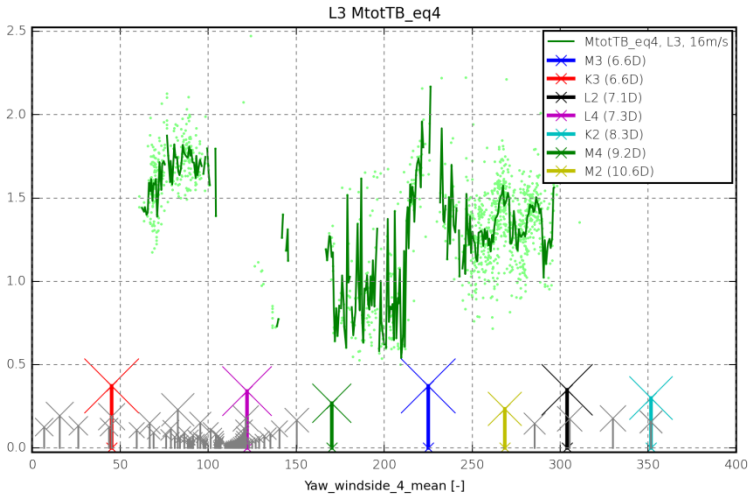

Figure E54: Tower bottom bending equivalent moment; WT L3; m = 4; U = 16m/s.

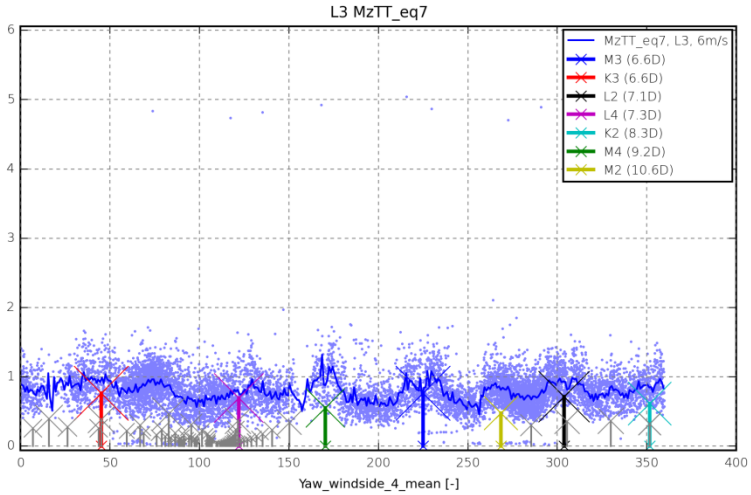

Figure E55: Tower top yaw equivalent moment; WT L3; m = 7; U = 6m/s.

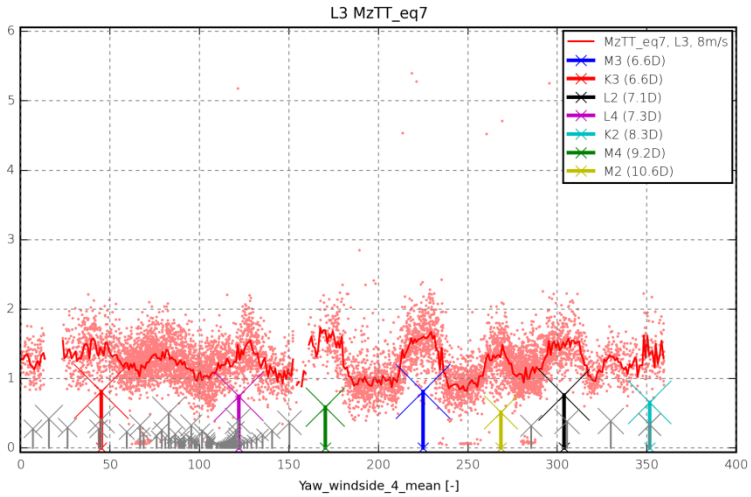

Figure E56: Tower top yaw equivalent moment; WT L3; m = 7; U = 8m/s.

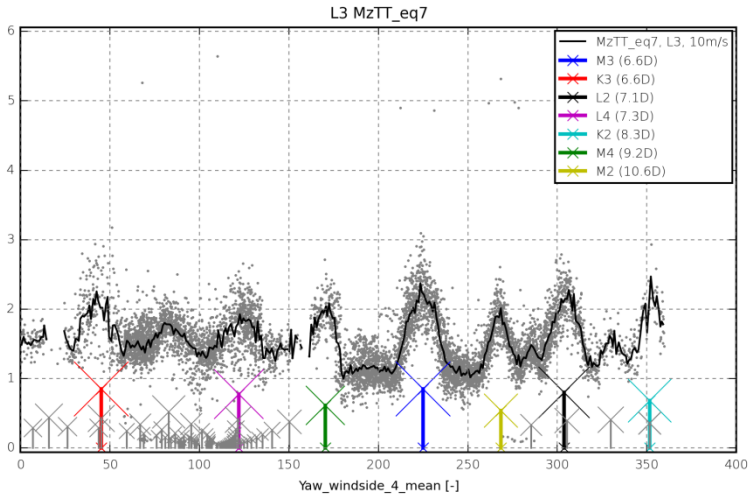

Figure E57: Tower top yaw equivalent moment; WT L3; m = 7; U = 10m/s.

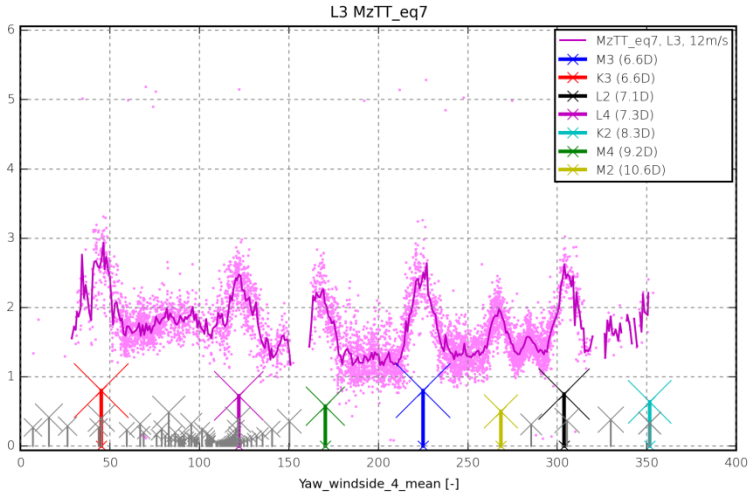

Figure E58: Tower top yaw equivalent moment; WT L3; m = 7; U = 12m/s.

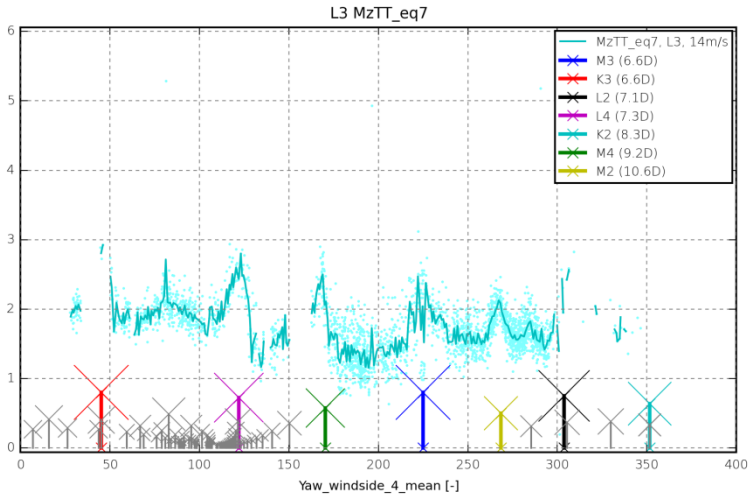

Figure E59: Tower top yaw equivalent moment; WT L3; m = 7; U = 14m/s.

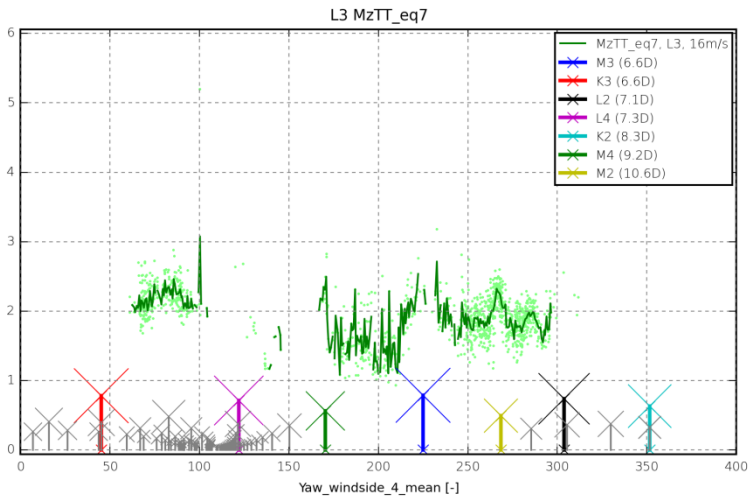

Figure E60: Tower top yaw equivalent moment; WT L3; m = 7; U = 16m/s.